IN-PLANE BEHAVIOUR OF GROUTED CONCRETE MASONRY UNDER BIAXIAL STATES OF STRESS

By

MAGDY MOHAMED SAMIR KHATTAB, B.Sc, M.Sc.

A Thesis

Submitted to the School of Graduate Studies

in Partial Fulfilment of the Requirements

for the Degree

Doctor of Philosophy

McMaster University

IN-PLANE BEHAVIOUR OF GROUTED CONCRETE MASONRY

To my parents

DOCTOR OF PHILOSOPHY (1993) McMASTER UNIVERSITY

(Civil Engineering and Engineering Mechanics) Hamilton, Ontario

TITLE: In-Plane Behaviour of Grouted Concrete Masonry under Biaxial States of Stress

AUTHOR: Magdy Mohamed Samir Khattab, B.Sc. (Ain-Shams University)

M.Sc. (Ain-Shams University)

SUPERVISOR: Professor R. G. Drysdale

NUMBER OF PAGES: xxvii, 402

ABSTRACT

The available literature on the in-plane behaviour of masonry was categorized and reviewed under one of three research approaches; experimental testing of masonry shear walls, microscopic modelling, and macroscopic modelling. The significant differences found in the results obtained from different research programs may leave a wrong impression about the potential of masonry as a structural material. The literature review also pointed out the lack of experimental data on the macro-behaviour of grouted concrete masonry, particularly for reinforced assemblages. Acordingly, the reported investigation provides explanations of behaviours which lead to an improved understanding of the in-plane behaviour of grouted concrete masonry. The experimental part provides a body of test data for North American conditions (practice and material) to form the basis of a macro-behaviour model.

The experimental program in this investigation included two major parts; biaxial tests and auxiliary tests. The biaxial tests involved a total of 36 full scale unreinforced or reinforced panels tested under uniform states of biaxial tension-compression. A biaxial test rig was specially devised to perform these tests. The variables considered covered the bed joint orientation θ, the ratio between principal stresses σ_1/σ_2, and the percentages of reinforcement used parallel and normal to the bed joints. The auxiliary tests comprised 33 prisms tested under

uniaxial compression, 27 prisms tested under uniaxial tension, and 15 couplets tested under direct shear. In addition, a large number of component material tests were performed to determine the physical and mechanical properties of each material used. These also served as control tests.

A macro-model was proposed to predict the in-plane behaviour of grouted concrete masonry. In this model, the masonry assemblage was replaced by an "equivalent material" which consisted of a homogenous medium intersected by two sets of planes of weakness (along the head joint and bed joint planes) and two sets of reinforcement. The macro-behaviour of the "equivalent material" was determined by smearing the influence of these sets, which provided a means for modelling the inherent part of the anisotropic characteristics of masonry assemblages. On the other hand, the behaviour of the homogeneous medium was described by an orthotropic model to account for the induced part of the anisotropic characteristics. The reliability of the proposed model was confirmed using the experimental results from this investigation and others. The model was also used to fill the gaps in the available test results and to provide a more complete picture of the in-plane behaviour of grouted masonry.

ACKNOWLEDGEMENT

The author wishes to express his sincere gratitude to Dr. R.G. Drysdale for his guidance, encouragement, and supervision during the course of this study. The valuable comments offered by Dr. Drysdale during the experimental program and the effort he expended in reviewing the manuscript are greatly appreciated.

The author is greatly in debt to the other supervisor committee members, Dr. F. Mirza and Dr. D.S. Wilkinson for their valuable comments and suggestions. The precious time spent by Dr. Mirza reviewing Chapter 5 is deeply appreciated.

The author wishes to thank Moe Forget, whose enthusiasm and perseverance were the driving forces that helped complete the long experimental program of this study. The collaboration and assistance of Ross McAndrew and Dave Perrett during this program are also appreciated.

Acknowledgement is due to McMaster University and the Natural Science and Engineering Research Council of Canada for financial support. The author appreciates the contribution of the mason's time made available through the Ontario Masonry Contractors Association and the Ontario Masonry Industry Promotion Fund, and he thanks the Ontario Concrete Block Association for their donations of the blocks.

Sincere appreciation is due to the author's best friends, Mr. and Mrs.

Sernie for their kindness, help, and encouragement that helped complete this thesis.

Finally, and most important, a special note of deep, hear-felt appreciation is due to my kind parents and my sister whose continuous support, encouragement, and fruitful care are the backbone of my persistence to excel.

TABLE OF CONTENTS

LIST OF FIGURES

LIST OF TABLES

NOTATION

Given below is a list of the principal symbols and notation used in the thesis. All notations and symbols are defined in the text when they first appear.

A_h and A_b	Cross-section area of the masonry assemblage along the head joint and the bed joint planes of weakness, respectively.
A_{mb} and A_{gb}	Cross-section area, respectively, of the mortar and the grout along the bed joint planes of weakness.
A_{mh}, $A_{k,}$, and A_{in}	Cross-section area, respectively, of the mortar, the block and the grout-block interface along the head joint planes of weakness.
c	Coefficient of cohesion equal to the shear strength with no precompression.
$[D]$	Elasticity matrix.
E and ν	Young's modulus and Poisson's ratio, respectively.
F and Q	Yield surface and plastic potential functions, respectively.
$(f_c')_b$	Compressive strength of block.
f'_m	Ultimate compressive strength of masonry.
f'_t	Uniaxial tensile strength.
f_{tb}	Tensile strength of block.
f_{yp} and f_{yn}	Yield stress of the reinforcement parallel and normal to the bed joint planes, respectively.

$[T_{sn}]_{LG}$	Strain transformation matrix from the global to the local coordinate axes.
$[T_{sr}]_{LG}$	Stress transformation matrix from the global to the local coordinate axes.
t_m and s_m	Thickness and spacing of the mortar joints, respectively.
β	Angle measured between the directions of principal strains and principal stresses.
γ_{pn}	Shear strain in the directions of the mortar joint planes.
$\{\Delta\epsilon\}$ and $\{\Delta\sigma\}$	Vectors of the strain and stress increments, respectively.
$\{\Delta\epsilon\}^e$	Vector of the elastic strain increment.
$\{\Delta\epsilon\}^{ne}$	Vector of the inelastic strain increment.
ϵ_o	Compressive strain associated with the peak compressive stress.
ϵ_1 and ϵ_2	Principal strains.
ϵ_p and ϵ_n	Normal strains acting parallel and normal to the bed joint planes, respectively.
ϵ_{30} and ϵ_{90}	Average strains measured, respectively, in the directions of 30° and 90° from the principal tensile stress orientation.
θ	Bed joint orientation; the angle measured between the bed joint plane and the direction of the principal tensile stress σ_1.
θ_{cs}	Angle measured between the orientations of the crack and the reinforcement parallel to the bed joint plane.
θ_m	Angle measured between the bed joints and σ_{1m} (the principal tensile stress of masonry).
λ	Damage parameter that accounts for the effect of cracking on the strength and stiffness of masonry in the principal compressive stress direction.
ρ_p and ρ_n	Percentages of reinforcement used parallel and normal to the bed joint plane, respectively.

σ_1 and σ_2	Principal stresses.
$(\sigma_1)_{cr}$ and $(\sigma_1)_{ult}$	Values of σ_1 corresponding to the cracking and the ultimate stresses, respectively.
$(\sigma_1)_{yp}$ and $(\sigma_1)_{yn}$	Values of σ_1 corresponding to yielding of the reinforcement parallel and normal to the bed joints, respectively.
σ_p and σ_n	Normal stresses acting, respectively, parallel and normal to the bed joint planes.
σ_{sp} and σ_{sn}	Stresses in reinforcement parallel and normal to the bed joint planes, respectively.
τ_{pn}	Shear stresses acting along the mortar joint planes.
τ_u	Ultimate shear stress.
ϕ	Angle of internal friction along the shear plane.
ψ	Angle of dilation.

CHAPTER 1

INTRODUCTION

1.1 GENERAL

Masonry, as one of the oldest forms of construction, has been built for thousands of years. In spite of its long history, the development of masonry as a modern structural material has lagged behind steel and concrete. This lack of development may be attributed to the required high loading capacity for testing and the lack of research facilities, in the past. Uncertainty about masonry behaviour along with the traditionally thick walls detracted from masonry being an economically viable structural material. Masonry was thought of mainly as useful for cladding, minor buildings or architectural decoration. This attitude was also supported by the poor earthquake performance of "unengineered" masonry structures, (Mayes and Clough, 1975-b). However, the idea of employing masonry walls as structural members and avoiding the need for other structural materials has occupied the attention of civil engineers for a long time.

During the last few decades, concurrent with the improvement of the quality control in the masonry industry, a large number of studies have explored the potential of masonry as a structural material. The principal aim of these studies was to provide enough information to formulate and evaluate masonry

design codes. Even though this task is far from being completed, a better understanding of the major features of masonry behaviour, accompanied by a significant change in the design philosophy for masonry structures, has been achieved. Engineered masonry design principles have been proposed to replace the traditional "rule of thumb" design approach. A very good example is the change in the design philosophy regarding the resistance of masonry due to lateral loads from earthquake or wind.

Traditional masonry walls were planned to be stable on their own. The critical requirement was to keep the line of thrust, under the effect of lateral and axial loads, within the section. This in turn resulted in very thick walls as portrayed in the 16-storey Monadnock Building; a brick loadbearing wall structure built in Chicago during 1889-1891 having, at the base, walls of 6 ft (1.83 m) thickness. In their book, Schneider and Dickey (1980) speculated that if modern design techniques and construction methods had been available at that time, the designers of the Monadnock might have used instead masonry walls one foot (300 mm) or less in thickness. Modern thin masonry walls are composite in their action. To some extent, they evolved from traditional thick walls, but largely they are a development of frame construction. The floors and roofs, acting as rigid diaphragms, transfer lateral loads to the masonry walls, which in turn provide the horizontal shear resistance needed. This kind of structure may be defined as a box system or shear wall system. The design of modern thin masonry walls involves providing enough strength and ductility to resist the in-

plane stresses induced by lateral and vertical, live and dead loads.

A large portion of the masonry research conducted to date has been dedicated to study of the in-plane behaviour of masonry under different combinations of shear and normal stresses. As a result, two load-resisting mechanisms have been recognised; the flexural and the shear mechanisms. Even though there is agreement on the general features of the behaviour of masonry walls, some uncertainty remains because of the discrepancies between different studies especially when the shear mechanism prevails. These discrepancies can be attributed to the wide range of masonry materials, the different ranges of variables covered in different studies, and the dependence on empirical formulae rather than using rational design procedures. Added to these factors, masonry is a material which exhibits distinct directional properties due to the influence of the mortar joints acting as planes of weakness. Its behaviour cannot, therefore, be defined simply in terms of principal stresses at any point. A third variable, the bed joint orientation with respect to the principal stresses, must be considered.

This chapter contains a brief literature review of the available research studies concerned with the in-plane behaviour of masonry. The literature review is then followed by an outline of the objectives and scope of this dissertation.

1.2 IN-PLANE BEHAVIOUR OF MASONRY: LITERATURE REVIEW

The literature review of the in-plane behaviour of masonry would have been lengthy and difficult without the available reviews provided by Mayes and Clough (1975-a and b), Hegemier (1975), Schneider and Dickey (1980), and

Page et al. (1980). It is not meant, therefore, to cover every study conducted, but rather to report the information directly related to this study and to point out the areas of discrepancy between different research programs. The readers can refer to the above mentioned reviews for more complete information.

Among the different research studies, three different approaches can be distinguished as illustrated in Fig. 1.1. Perhaps the most direct approach is to investigate experimentally the overall behaviour of full or model scale masonry shear walls under different loading conditions using various masonry materials. This approach could lead to empirical or semi-empirical formulae for design. On the other extreme, the third approach is to formulate a separate theoretical model for each masonry component. These models can then be combined together in a micro-element model that depicts the overall behaviour of the masonry assemblage. Between these two extremes lies the second approach which is to study experimentally the behaviour of masonry at a macroscopic level under well defined loading conditions. A macro-element model, incorporating the stress-strain relationships and the failure criteria observed in the tests, can then be used to predict the behaviour of masonry shear walls with different geometrical configurations under different loading conditions. The results obtained in previous research studies are grouped and reviewed in the following sections according to these three approaches.

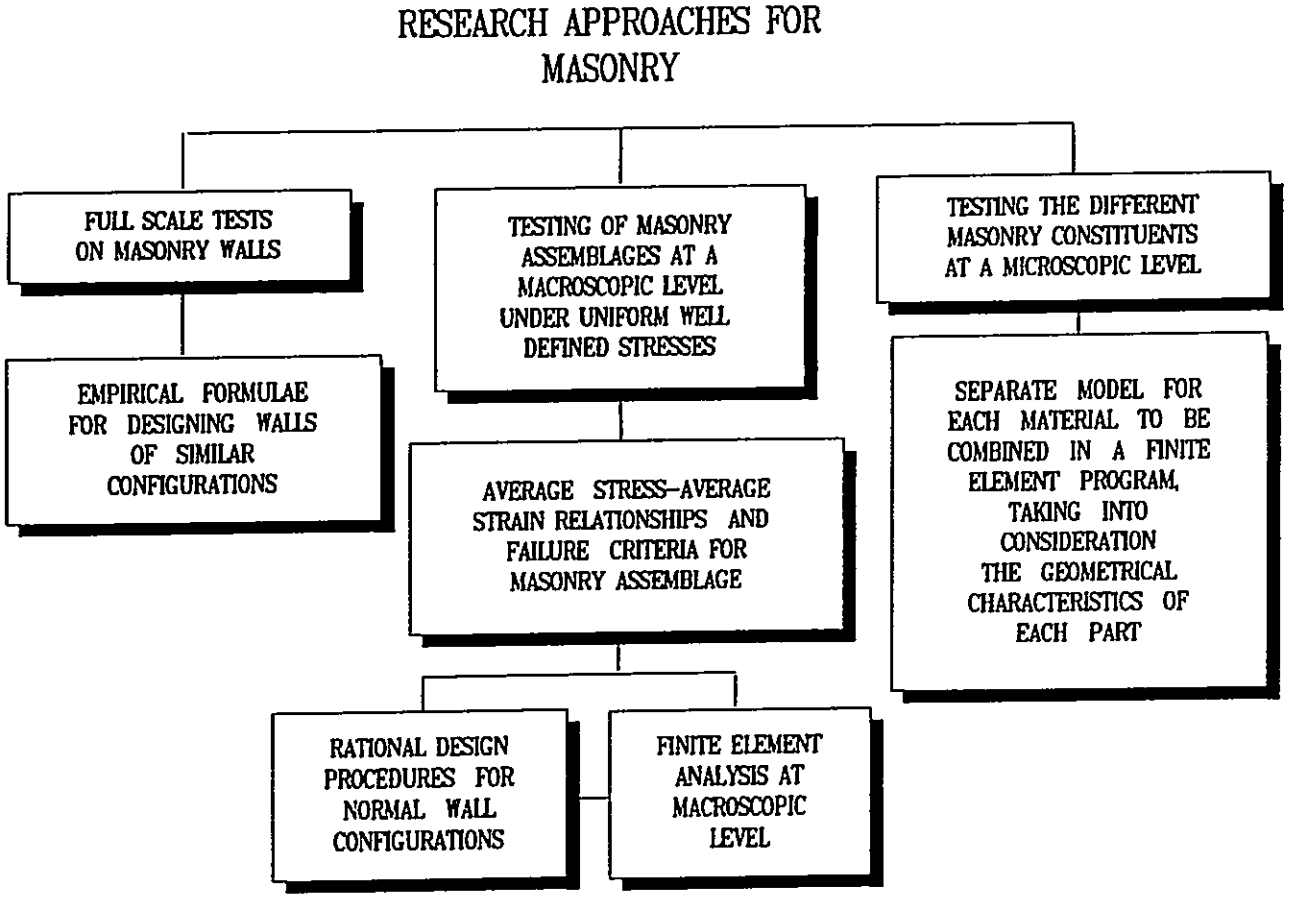

Fig. 1.1 Research approaches for masonry.

1.2.1 Experimental Investigations of Masonry Shear Wall Behaviour

The advent of the masonry shear wall systems was accompanied by a large number of experimental investigations on full scale and model masonry walls. Depending on the research facilities available, different test techniques have been used. The forerunner of the early investigations on masonry walls was conducted by Benjamin and Williams (1958). They performed their tests on one storey unreinforced brick walls loaded as vertical cantilever beams by a concentrated horizontal load at the top without any axial loads. Full scale and model brick walls were tested without bracing frames, and with reinforced concrete or steel bracing frames. Benjamin and Williams concluded that the strengths of plain brick masonry panels are very limited, unless they are properly confined by frames. This conclusion can be attributed to the facts that the walls were tested without any axial loads, on one hand, and the braced frames were designed to be stronger in overturning than the walls in shear, on the other hand.

Another early series of tests was conducted at the University of Southern California by Schneider (1956). In this series, Schneider tested reinforced masonry panels under horizontal shear force. External hold down force was applied on the specimens to resist the overturning moment. This arrangement formed the basis for the racking test. The effect of this external concentrated load on the internal stress distribution is a matter of speculation. Therefore, the results obtained in this kind of test can only be used as a comparative behaviour index. The external hold down force was replaced by an internal anchor in a second

series of tests (Schneider 1959), in an attempt to obtain more realistic boundary conditions. The parameters studied in this series covered the height-to-depth ratio, the mortar mix proportions, and the effect of different sizes of opening. Schneider reported that the mode of failure was essentially diagonal tension. In the case of panels with large height-to-depth ratios, failure was initiated by yielding in the boundary reinforcement. The results obtained pointed out the fallacy of assigning a constant allowable shear stress, independent of the height-to-depth ratio.

A series of racking tests on reinforced concrete masonry panels was also conducted in New Zealand by Scrivener (1966). Among other things, he indicated that a higher shear failure load was achieved by having higher percentages of reinforcement up to 0.3% of the gross area. Above this percentage, additional reinforcing had little effect on the failure load. To predict the flexural capacity of the panels, Scrivener assumed that all the vertical steel bars had yielded and that the compressive force lay at the outside edge of the compression zone. As a result of a second test series, Scrivener (1969) concluded that vertical and horizontal reinforcement are equally effective in providing satisfactory crack control and shear capacity.

In 1969, Schneider carried out another test program on reinforced concrete masonry piers. He used a diagonal loading frame to load the specimens. A definite increase was observed in the shear strength with a decrease in the height - to-depth ratio. The presence of horizontal web reinforcement was reported to have improved the shear capacity of the pier. This effect was found to become more

pronounced as the height-to-depth ratio decreased. Conversely, the presence of the vertical shear reinforcement did not significantly increase the shear capacity of the pier. Comparing the obtained load-deflection curves, Schneider concluded that the vertical reinforcement does not impart as much stiffness to a pier as the horizontal shear reinforcement. Based on the test results, Schneider developed empirical relationships for determining the shear strength in terms of the height-to-depth ratio. He proposed two relationships; one for reinforced and the other for unreinforced piers. In these relationships, Schneider did not consider the effects of applied compressive load and the flexural capacity of vertical reinforcement. It is important to keep in mind that the proposed relationships are only applicable to materials and loading conditions similar to those used in the investigation.

In Scotland, Sinha and Hendry (1969) performed tests on a 1/6-scale model for a storey height brick wall structure. The test model consisted of three panels with a floor above, stiffened by cross walls and having door openings. The failure observed was predominantly due to a breakdown of the bond along the brick-mortar interface, which led to stepped diagonal cracks through a combination of bed and head joints, although the cracks occasionally propagated through the masonry units. Sinha and Hendry proposed three formulae for predicting shear strength of brickwork. Two of these formulae were based on the Coulomb-Mohr friction failure hypothesis to predict the failure along the mortar-brick interface. The third formula was based on the maximum tensile stress

failure criterion to estimate the diagonal tension cracking through both bricks and mortar.

Near the beginning of the 1970's, the availability of research facilities allowed for studying the seismic behaviour of masonry shear walls. At nearly the same time, both Williams (1971), in New Zealand, and Meli (1972), in Mexico, performed tests under pseudo-static cyclic loads to investigate the inelastic behaviour of masonry shear walls. The results obtained by Williams revealed flexural and shear failure mechanisms. The former was characterized by yielding of reinforcement after which the load remained steady until failure was brought about by crushing at the toe of the wall. On the other hand, the shear failure mechanism was initiated by diagonal cracking resulting in a sharp drop in strength and stiffness. Failure in this case was sudden and extensive, mainly due to the disintegration of the masonry at the toe of the wall. These observations correlated with those of Meli. To avoid the brittle shear failure, Williams recommended limiting the amount of flexural reinforcement so that the flexural capacity of a masonry shear wall does not exceed its shear capacity. William was also the first to compare the effects of dynamic and pseudo-static, cyclic loads on the behaviour of masonry walls (Mayes and Clough 1975-b). Out of the four brick walls subjected to dynamic loading, three walls suffered shear failure with substantial load degradation similar to that observed under the effect of the pseudo-static loading. The fourth wall exhibited flexural failure but, in contrast to the satisfactory ductile behaviour noticed under pseudo-static loading, severe

losses in the load carrying capacity and ductility were observed. This behaviour led Williams, at that time, to conclude that, until the structural deterioration revealed in the dynamic tests is prevented, the working stress design approach must be retained for seismic design of reinforced masonry.

Priestley and Bridgeman (1974) performed a series of tests on masonry shear walls under pseudo-static cyclic loading. Contrary to the conclusions drawn by Schneider and by Scrivener, they indicated that shear reinforcement greater than 0.3%, of the gross section, is effective in improving the ultimate shear capacity of masonry provided that sufficient shear reinforcement is used to resist the loads associated with the ultimate flexural capacity. They also demonstrated that horizontal reinforcement is approximately three times as efficient as vertical reinforcement in carrying shear force. This ratio was suggested considering a diagonal tension failure at 45°, which could change with an increase of the axial loads or a change in the wall configuration. A significant improvement in ductility was reported where 1/8 in. (3 mm) plates were introduced into the mortar joints in the vicinity of the toe of the wall. The presence of these plates confined the compression zone and inhibited the tensile splitting associated with the compression failure. This behaviour was also reported by Hamid (1978) and Priestley and Elder (1983) in their tests on three and five course prisms, respectively. Priestley and Bridgeman showed that the flexural capacity of masonry walls can be predicted quite accurately by using the simple bending theory originally developed for reinforced concrete beams.

The disadvantages of adopting elastic theory for designing masonry shear walls was discussed by Priestley (1986-a and b). He presented a capacity design approach that involves ultimate strength design for flexure, detailed assessment of ductility capacity, and protection against shear failure. This proposal was the basis for the design code in New Zealand. Later the strength design approach was introduced in the Unified Building Code (UBC 1991) in the U.S.A. as an alternative for designing reinforced masonry shear walls. The current Canadian Code (CAN3-S304-M84) is being modified to include a limit states design approach. The approaches that involve designing at the ultimate stage have the advantage of providing an explicit consideration to the inelastic behaviour of the structural components so that undesirable failure mechanisms, such as brittle shear failure, can be avoided. This, consequently, leads to a more consistent level of safety for the different components in a structure.

An extensive research program was conducted at the University of California, Berkeley, during the past two decades. Cyclic loading tests were initially conducted on double pier specimens, (Mayes et al. 1976-a and b), chosen to simulate a lower storey in a masonry shear wall perforated by windows. This was followed by a large series of tests on single piers (Hidalgo et al. 1978 and 1979, Chen et al. 1978, and Sveinsson et al. 1981 and 1985) to establish which parameters effectively improve the inelastic behaviour of piers failing in shear. The tests covered the effects of the height-to-depth ratio, the type of construction and grouting, the amount of horizontal and vertical reinforcement, and the level

of axial compression. In addition to the flexural and diagonal tension modes of failure, a sliding mode of failure was reported for piers with high percentages of horizontal reinforcement and with a height-to-depth ratio of 0.5. It was also found that some of the piers, with a height-to-depth ratio of 0.5, exhibited compression failure in the diagonal struts formed between the diagonal cracks. This mode of failure will be referred to in this thesis as "diagonal compression failure". A comparison was made between the load associated with formation of the first diagonal tension crack and the ultimate capacity of panels tested under diagonal compression load. The correlation was described as a "reasonable correlation".

Although a positive correlation was observed between the increase in horizontal reinforcement and the improvement in inelastic behaviour, it was reported that only some of the piers showed this improvement and that it was not consistent. Sveinsson et al. (1985) stated "improved ductility appears to be accomplished by distributing the horizontal reinforcing bars more uniformly over the pier" and "improvement can be expected for horizontal reinforcement ratios up to three to five times the minimum ratio specified in the 1985 UBC (0.07%)". Sveinsson et al. also added "horizontal reinforcement ratios beyond that are not expected to improve the ultimate strength of the masonry piers significantly". The importance of the anchorage of horizontal reinforcement was also emphasised.

The effect of the horizontal reinforcement on strength and ductility of masonry walls, at shear failure, was also investigated by Tomazevic and Zarnic (1985) in Yugoslavia. They carried out cyclic lateral load tests on 1/3-scale model

masonry walls, having different mortar strengths and different percentages of horizontal reinforcement. They concluded that the horizontal reinforcement significantly improved the wall ductility, but had no effect on the shear resistance. It was observed that an amount of reinforcement equivalent to the lateral shear resistance of an unreinforced wall is sufficient for improving ductility. Larger amounts of reinforcement were found not to be fully effective because of, as indicated by Tomazevic and Zarnic, the inadequate bond and anchorage conditions in the case of shear failure. It is important to keep in mind that these tests were performed in the absence of any vertical reinforcement.

A study similar to the foregoing research was conducted in Japan by Matsumura (1987 and 1990) on full scale masonry shear walls. The tests were performed on fully grouted concrete and brick masonry walls, reinforced both vertically and horizontally and designed to fail in shear. Matsumura reported a proportional but low increase in the ultimate shear strength with increased horizontal reinforcement. In an attempt to explain this relatively small effect of shear reinforcement, Matsumura provided a schematic illustration based on the truss analogy in which the reinforcement functions as the tension member while masonry acts as diagonal compression members. He suggested that the increase in the shear reinforcement was accompanied by a reduction in the ultimate contribution of masonry which eventually led to the small improvement observed in the total shear capacity of the wall. He also proposed semi-empirical formulae to predict both ultimate and cracking shear strengths. The ultimate shear strength

formula included axial load and horizontal reinforcement terms along with a masonry term modified by the aspect ratio and the amount of vertical reinforcement. Matsumura stressed the undesirable effect of inadequate grouting, to which the inconsistent effectiveness of the shear reinforcement in one of the test series was attributed.

As a part of the U.S. Coordinated Program for Masonry Building Research, Shing et al. (1989 and 1990) tested twenty two single storey masonry walls. It was found that shear failure often leads to undesirable brittle failure. Similar to Sveinsson et al. (1985) and Tomazevic and Zarnic (1985), Shing et al. indicated that increasing the amount of horizontal reinforcement significantly improved the post cracking ductility, but had an inconsistent influence on the shear strength. Applying simple flexural theory, based on the assumption that plane sections remain plane after bending, Shing et al. were able to predict the flexural strengths of the walls with good accuracy. On the other hand, they concluded that the UBC (1988) specifications for shear strength did not lead to a consistent level of safety. In the 1988 version of the UBC as well as the recent version (UBC, 1991), a semi-empirical formula is adopted for calculating the nominal shear strength of reinforced masonry shear walls as the summation of the residual strength after diagonal cracking and the resistance of horizontal reinforcement. In this formula, the effect of the axial stress and the resistance of flexural reinforcement were neglected. The code specifications were found also to overestimate the contribution of horizontal reinforcement. A semi-empirical

formula, taking into account the influence of axial stress and flexural reinforcement, was proposed by Shing et al..

Anderson and Priestley (1992) discussed the formulae proposed by Matsumura and Shing et al. They provided an alternative formula which is simply the summation of the contributions of masonry, vertical reinforcement, horizontal reinforcement and axial stress. The parameters of this formula were evaluated using test results of masonry shear walls that failed in shear. It was found that the contribution of horizontal reinforcement is only half that normally used for designing reinforced concrete members, whereas the vertical reinforcement has no influence on the shear strength. Anderson and Priestley related these findings to the possibility that the rate at which the presence of reinforcement increases the shear capacity is less than the rate at which the masonry loses strength after the formation of diagonal cracks.

1.2.2 Macro-Modelling of Masonry under In-Plane Stresses

Several attempts have been made to study the in-plane behaviour of masonry assemblage. Johnson and Thompson (1967) carried out diametral tests on brick masonry discs to produce indirect splitting tensile stress. The discs were tested with mortar joints inclined at various angles to the vertical compressive load. This test approach was later the object of a theoretical analysis by Stafford-Smith et al. (1970). They stated that, in the stress analysis of non-homogeneous material such as brickwork, an analysis based on the assumption of homogeneous material may lead to substantial underestimates of maximum stresses. Similar tests

on grouted and ungrouted concrete masonry were performed by Drysdale et al. (1979). Blume and Proulx (1968) conducted diagonal compression tests on square panels in an attempt to simulate the stress induced in a masonry pier between two windows. The same technique, but in the existence of axial compressive load, was used by Borchelt (1970). Yokel and Fattal (1976) proposed failure hypotheses to predict the capacities of Borchelt's panels. In this analysis, they considered masonry as an elastic isotropic material.

The results of the above tests showed clearly the dependence of the behaviour of masonry on the orientation of the mortar joints. However, the nonuniform stress distributions induced in the specimens limited their reliability in representing the actual behaviour of masonry. They can only be used for comparison purposes.

Researchers began to realize that there was a need for tests that produce uniform stress distribution in the specimens. Hegemier et al. (1978-a) studied masonry behaviour under biaxial states of stress. Uniaxial tension and biaxial tension-compression tests were performed on grouted concrete block panels with different bed joint orientations. In the biaxial tests, the normal stress parallel to the bed joints, σ_p, was kept equal to zero. The test results showed a slight change in the tensile strength due to the bed joint orientation. A failure surface very similar to that of concrete was proposed. The authors stated that the material used " by accident " led to an essentially isotropic material, but that the isotropy " can be destroyed by a non-judicious selection of block and grout

strengths". Because no tests on panels with different bed joint orientations were performed under uniaxial compression, no information was available on potential anisotropic characteristics of masonry under uniaxial compression.

Hamid and Drysdale (1980) conducted uniaxial compression tests on both ungrouted and grouted off-axis prisms. The prisms were cut at different bed joint orientations. The test results indicated the dependence of both strength and deformation characteristics on the bed joint orientation. However, the continuity provided by the grout cores helped to decrease the anisotropic characteristics. They pointed out that the failure theories for isotropic materials are not applicable to masonry. Instead of one failure criterion, Hamid and Drysdale (1981) proposed a set of sub-criteria to account for the different possible modes of failure.

A comprehensive experimental program was conducted by Page (1981 and 1983) to define the failure envelope of brick masonry. A total of 180 half scale panels were tested under both biaxial compression-compression and compression-tension states of stresses with different bed joint orientations. It was found that the bed joint orientation affected the failure pattern only when one of the principal stresses dominated. Under the effect of biaxial tension-compression states of stress, the panels exhibited failure along the mortar joints. In this case, the bed joint orientation had a significant effect on the mode of failure. Similar behaviours were observed under biaxial compression-compression states of stress when one of the principal stresses was significantly larger than the other. As the principal compressive stresses get closer to being equal (i.e. σ_1/σ_2=-1/-1), the

panels typically failed by splitting along longitudinal planes parallel to the plane of the panels, regardless of the bed joint orientation. Page (1980) used a micro-model finite element model to define the failure criterion of the same assemblage under biaxial tension-tension states of stress.

Using the results obtained by Page, Dhanasekar et al. (1985-a) developed a complete failure surface for the masonry assemblage tested. They represented this failure surface in terms of the normal stresses and the shear stress along the mortar joints. The failure surface consisted of three distinct regions each represented by an elliptic cone. However, the three cones did not correspond with distinct modes of failure, but rather fitted the experimental results. Dhanasekar et al. (1982) performed a regression analysis on the test results to define the elastic properties of the assemblage which were found, on average, to be nearly isotropic. In contrast, the nonlinear behaviour under biaxial compression-compression was best modelled by power laws in terms of strains and stresses along the mortar joints (Dhanasekar et al., 1985-b). The panels tested under biaxial tension-compression were reported to exhibit only slightly nonlinear behaviour which can be neglected.

Another series of tests was performed by Samarasinghe et al. (1982) to study the failure characteristics of brick masonry under biaxial tension-compression states of stress. In these tests, they used panels built of one-sixth scale clay bricks and 1:0.25:3 mortar (cement:lime:sand). An idealized failure surface, expressed in terms of principal stresses and bed joint orientation, was

derived from the results.

It is important, at this point, to distinguish between two categories of the available macro-failure criteria. The first category includes the phenomenological failure criteria that strictly fit the experimental results. This kind of criteria suffers the same disadvantage of any empirical formulae by being useful only for the conditions used in the tests. The second category covers the failure criteria based on physical interpretations of the masonry behaviour. The failure surface can be defined, in this case, in a closed analytical form or in the form of a numerical model. Use of numerical models has the advantage of predicting the deformation as well as the strength of the masonry assemblage. A physical failure criteria could yield more generalized information which could be used for different masonry assemblages depending on how realistically the effects of the different parameters involved were considered.

Ganz and Thürlimann (1983) suggested a failure surface that can be classified as a physical failure criteria. They presented the failure surface in terms of the stress components along the mortar joints. Four separate failure criteria, each corresponding to a distinct failure mode, were used to define the failure surface. Two of these criteria were defined by the maximum principal compressive stress limit and the no tension limit. The remaining two were defined by the Mohr-Coulomb sliding failure on the bed joint and the splitting failure of the perforated bricks. It is worth noting that the first two criteria were independent of the bed joint orientation, whereas the last two criteria were

functions in the bed joint orientation. Ganz and Thürlimann (1985) used the lower bound theorem along with this failure surface to predict the shear strength of masonry shear walls. They modelled masonry as rigid perfect plastic material. The proposed failure surface was modified later by Ganz (1989) to allow for masonry tensile strength and the stepped mode of failure. The final version of the failure surface showed good agreement with the results obtained by Page (1981 and 1983) and by Samarasinghe et al. (1982). Essawy (1986), used a similar technique and defined three distinct failure criteria for ungrouted concrete block masonry under shear and tensile stresses along the mortar joints. The failure criteria were derived to address the individual failures along bed joints or head joints and the stepped failure through both of them. Masonry, in this analysis, was assumed to behave elastically up to failure.

Mann and Müller (1982) proposed three failure criteria to predict the shear strength of masonry. The failure criteria were based on the assumption that no shear stress can be transferred in the head joints. This in turn alters the normal stress distribution along the bed joint and doubles the shear stresses acting on the masonry unit along the head joint plane. The failure criteria, expressed in terms of normal stress and shear stress acting on the bed joint planes, were shear failure of the bed joint, tension failure in the masonry unit, and compression failure of the masonry assemblage. The effect of the normal stress parallel to the bed joint was neglected in the proposed criteria which, consequently, represents a cross-section in the total failure surface of the masonry assemblage.

A numerical model was proposed by Gerrard and Macindoe (1985) to predict the tensile strength of brickwork. It was based on a multi-laminate model developed by Zienkiewicz and Pande (1977) to study the behaviour of a jointed rock mass. Masonry was considered, in this model, as an elastic continuum intersected by planes of weakness with behaviour described as an elastic viscoplastic material with a Mohr-Coulomb failure envelope. Although the model successfully predicted the effect of the bed joint orientation on the modes of failure, Gerrard and Macindoe reported some divergence between their predictions and the experimental results obtained by Page. They attributed these discrepancies to insufficient information about the properties of the different components of the masonry assemblage. It should also be kept in mind that the masonry was idealized as an elastic continuum.

Antonucci et al. (1992) used the finite element method to model masonry shear walls. To get the advantages of both micro and macro-models, they derived the macro-element stiffness matrix by using a static condensation method applied to the stiffness matrices of a set of sub-elements representing the different constituents of the masonry assemblage. This technique has definite advantages over the micro-modelling for linear elastic analysis where many elements have the same geometric and material properties. However, these advantages diminish in the nonlinear analysis because of the different responses of each sub-element within the macro-elements.

Pietruszczak and Niu (1992) presented a numerical model in which

masonry was regarded as a two-phase composite. The masonry assemblage was idealized as the superposition of two parts; namely the brick matrix with a family of head joints treated as aligned uniformly disperses weak inclusions and the bed joints running continuously through the assemblage and forming the weakest link in the microstructure. The bed joints were modelled as an elastoplastic strain hardening material, whereas the brick matrix was treated as an elastic-brittle material. Assuming perfect bond between the masonry constituents, kinematic and static constraints were used to relate the stresses and strains in each of the two parts to the average values for the assemblage. While the model provides a rational basis for modelling masonry, the idealization of the brick matrix part as elastic material did not allow for predicting the inelastic deformation associated with the compression mode of failure which was noticed under biaxial compression by Dhanasekar et al. (1985-b). The results predicted by the model also did not exhibit any failure along the head joint planes with the variation of the bed joint orientation under the effect of uniaxial compression or tension. This could be attributed to the failure criteria adopted for the brick matrix part.

Maksoud and Drysdale (1992) used kinematic and static constraints similar to the ones used by Pietruszczak and Niu (1992), but in the context of a macro-finite element model. The nonlinear characteristics of the masonry assemblage were determined from those of the mortar and the masonry unit using weighting numbers. In this model, both the mortar and the masonry units were idealized as elastoplastic strain hardening materials. The model was used to predict the

behaviour of four-course prisms of concrete block masonry under uniaxial compression. Good agreement was reported.

In addition to the above models and failure surfaces, a significant number of studies neglected the anisotropic characteristics of masonry (Bernardini et al. 1985, Motta and D'Amore 1985, Qamarunddin et al. 1989-a and b, Ewing et al. 1989, Seible et al. 1990 and Jamal et al. 1992).

1.2.3 Micro-Modelling of Masonry under In-Plane Stresses

A large number of experimental investigations have been conducted on the different constituent materials of the masonry assemblages. These investigations involved specimens of different sizes and shapes tested under compressive stress (Hamid 1978, Essawy 1986, Khalaf 1988, Guo and Drysdale 1989, Chahine 1989, and Sakr and Neis 1989), tensile stress (Pearson 1963, Self 1975, Hamid 1978, Gazzola et al. 1985, and Guo 1991), combined shear and normal stresses (Benjamin and Williams 1958, Haller 1969, Pieper and Trautsch 1970, Hamid 1978, Hegemier 1978-b, Hodgkinson and West 1982, Ali et al. 1986, Guo 1991 and Pluijm 1992), and triaxial states of stress (Khoo and Hendry 1972 and Guo 1991). The results obtained in some of these investigations were implemented in several micro-level analyses to study the distribution of stresses within masonry assemblages, the interactions among the different constituent materials, and their effects on the macro-behaviour. Some of these analyses were based on the linear elastic behaviour (Stafford-Smith et al. 1970 and 1971, Hamid 1978, Atkinson et al. 1987, Shrive 1982 and Simbeya et al. 1986), whereas others were extended

to cover the nonlinear behaviour (Arya and Hegemier 1978, Ali et al. 1986, Page 1978 and 1980 and Guo 1991).

A micro-level analysis provides a chance to consider the detailed mechanical and geometric characteristics of the different constituent materials in the masonry assemblage. This allows study of the influence of the different parameters on the macro-behaviour of the masonry assemblage. There are, however, serious limitations on this kind of analysis. First, the geometric characteristics of the masonry unit and the mortar joints can lead to ill-conditioning or instability of the numerical solution (Pietruszczak and Niu, 1992). Second, very sophisticated and detailed information about the characteristics of each material in the masonry assemblage is required. Third, the micro-level analysis becomes impractical for multi-storey masonry shear walls.

1.2.4 Closing Remarks

The two failure mechanisms identified for masonry shear walls are flexural and shear failure. The former is characterised by yielding of flexural reinforcement or/and crushing of masonry at the wall toe. This mechanism can be reasonably predicted using simple bending theory, such as commonly used for reinforced concrete beams, if the masonry characteristics for bending normal to the bed joints are defined. The situation is more complicated when the shear mechanism governs the behaviour. It involves diagonal tension, diagonal compression and sliding modes of failure. These modes of failure take place over relatively large zones, in which the mortar joints act as planes of weakness.

Depending on the mortar joint orientation, with respect to the principal stresses, masonry exhibits distinct directional properties altering the shear behaviour. Added to all of these difficulties, is the controversial issue of the effectiveness of horizontal and vertical reinforcement in resisting shear stresses after the formation of diagonal cracks. As a result, most design codes have adopted empirical or semi-empirical formulae to evaluate the shear strength of masonry shear walls.

A comparison between the design procedures used to predict the flexural and shear strengths of masonry shear walls may explain the uncertainty associated with the shear behaviour. The flexural design procedure is based on rational flexural theory which satisfies both equilibrium and deformation compatibility requirements. This kind of analysis provides the designers with an idea about the contribution of the different components in a section (such as masonry and flexural reinforcement). The flexural capacity of a section can then be predicted regardless of the reinforcement position in the section or of the strengths of the materials used. On the other hand, the shear design procedure is a collection of empirical or semi-empirical formulae that have been formulated to lead to a conservative design. The empirical formulae usually fall short of explaining the influence of the different parameters and their interactions. For the design of walls outside the range of tests, this lack of understanding could lead to the undesirable situation of inconsistent factors of safety. The use of empirical formulae should be limited to those conditions used in the derivations.

The anisotropic characteristic of masonry due to the mortar joints has been

recognised for a long time. The behaviour of masonry cannot be defined only in terms of the principal stresses, but requires a third parameter; the bed joint orientation with respect to the principal stresses. Studies, conducted neglecting the anisotropic characteristics of masonry, cannot be expected to contribute to the fundamental understanding of masonry.

1.3 OBJECTIVES AND SCOPE

In the light of the discussion and the literature review presented in the previous sections, the investigation reported herein was initiated to achieve the following objectives:

1. **To explore the macro-behaviour of unreinforced grouted concrete masonry under in-plane stresses.** It was decided to investigate the macro-behaviour experimentally under uniform well defined biaxial states of stress with different bed joint orientations. This provides an opportunity to assess the degree of anisotropy in terms of modes of failure, strength characteristics, and deformation characteristics.
2. **To explore the macro-behaviour of reinforced grouted concrete masonry under in-plane stresses.** The experimental investigation of reinforced masonry was intended to cover the effects of the percentages of reinforcement normal and parallel to the bed joints in addition to those aspects covered for unreinforced masonry. These tests were expected to permit the study of the macro-behaviour of cracked masonry.
3. **To develop and verify a macro-behaviour model.** There is a need for

a model that can be described as reasonably simple, yet accurate and able to simulate the full range in-plane behaviour of both unreinforced and reinforced grouted concrete masonry. It was intended that this model be used to predict and explain the effects of various parameters associated with the shear failure mechanism, such as the effectiveness of the reinforcement and the influence of axial stress.

The scope of the research reported in this dissertation was limited to grouted concrete masonry assemblages. It represents a reasonable choice of materials for North American construction practices. The assemblages studied can be used to predict the behaviour at critical sections of masonry shear walls which resist severe stress combinations introduced by lateral and axial loads. The fulfilment of the objectives stated above should help form the foundation on which a rational design approach can be formulated to predict the shear response of masonry assemblages.

The experimental part of this investigation is presented in Chapters 2, 3, and 4. In Chapter 2, the two parts of the experimental test program; namely the biaxial tests and the auxiliary tests, are described together with construction of the biaxial test rig. Chapter 3 deals with experimental results obtained in the auxiliary tests. Finally, the experimental results of unreinforced and reinforced grouted concrete masonry tests are reported and discussed in Chapter 4.

The theoretical study is reported in Chapters 5, 6, and 7. In Chapter 5, the macro-behaviour model, developed in this investigation, is described. In

Chapter 6, the experimental results are used to define the required stress-stain characteristics of grouted concrete masonry and to check the validity of the assumptions made in the macro-behaviour model. The reported test results and some results from other investigations are used in Chapter 7 to confirm the reliability of the proposed model. Some observations are made regarding the shear response of grouted concrete masonry.

Chapter 8 contains a summary of the investigation and presents the final conclusions drawn from this study. It also includes recommended areas for further research related to this study.

CHAPTER 2

DESCRIPTION OF THE EXPERIMENTAL TEST PROGRAM

2.1 INTRODUCTION

The experimental test program was designed to investigate the behaviour of grouted concrete masonry and to provide sufficient information to form the basis of a macro-behaviour model. The required information involved the following areas:

1. The failure criteria of unreinforced masonry.
2. The average stress-average strain relationships of uncracked masonry.
3. The average stress-average strain relationships of cracked masonry extracted from the tests of reinforced masonry.
4. The contributions of horizontal reinforcement, vertical reinforcement and the masonry itself to the response of reinforced masonry.

The experimental test program can be divided into two major parts. The first part consists of two series of unreinforced and reinforced full scale panels tested under states of biaxial tension-compression. A biaxial test rig was specially devised to perform these tests. The second part includes a large number of auxiliary specimens that were tested under different stress conditions. The auxiliary specimens were tested for comparison with the biaxial tests and to serve

as control specimens to define the material characteristics of the masonry assemblages and their constituents (blocks, mortar, grout and steel bars).

In accordance with the outline of the experimental test program, this chapter consists of two main sections after this introduction. Section 2.2 deals with the biaxial tests. It includes the rationale of the test technique and descriptions of the panels, the biaxial test rig, the instrumentation and the test procedures. Finally, Sec. 2.3 covers the specimen configurations, the instrumentation and the test procedures implemented in the different auxiliary tests.

2.2 BIAXIAL TESTS

2.2.1 Rationale of the Test Technique

Although it is relatively easy to perform tests on single-storey masonry shear walls, it is quite difficult to analyze their results. These specimens are subjected to nonuniform stresses due to the loading and support conditions. Calculation of the stresses at any point based on the assumption of elastic isotropic material is inconsistent with the presence of mortar joints and the propagation of cracks. Because of nonuniform stress conditions, it is difficult to relate calculated stresses to the applied loads and measured strains. Consequently, direct use of the results obtained in these tests is limited to situations with similar materials and boundary conditions. They cannot be used in formulating a macro-behaviour model.

To fulfil the objectives of this part of the experimental test program, there

was a need to produce homogeneous and well defined stress distributions in the specimens. A decision was made to test square full scale panels under uniform loads applied in two orthogonal directions. If there are no constraints to deformation along the loaded boundaries, the panel is statically determinate and the induced stresses within it can be determined simply by equilibrium with the applied uniform loads. Having the average strains measured in three (or more) directions, the average stress-average strain relationships can be defined through the different loading stages. In this situation, interpretation of data does not necessitate the assumptions of isotropic or linear elastic behaviour. As indicated in Chapter 1, this technique was used to study the macro-behaviour of plain concrete (Kupfer et al. 1969), brickwork masonry (Samarasinghe and Hendry 1982 and Page 1980/81/83), grouted concrete masonry (Hegemier et al. 1978-a) and recently cracked reinforced concrete (Vecchio and Collins 1982, Kirschner and Collins 1986, Bhide and Collins 1987).

A macro-element (A), in a masonry shear wall, under an arbitrary state of stress is shown in Fig. 2.1. It is subjected to normal stresses parallel and normal to the bed joint plane (σ_p and σ_n) and shear stress (τ_{pn}). Owing to the complexity of applying direct shear forces, a solution was to test the panels in the principal stress orientation under normal stresses (σ_1 and σ_2) as shown by the equivalent macro-element (B) in Fig. 2.1. In this manner, the shear stresses along the mortar joint planes were induced by rotating the bed joints with respect to the direction of the principal tensile stress σ_1. The angle θ, measured between the bed

joint plane and the principal tensile stress σ_1, is referred to in this study as the bed joint orientation. Five angles of θ=0, 22.5, 45, 67.5 and 90° were chosen to cover a wide range of normal and shear stress combinations along the mortar joints.

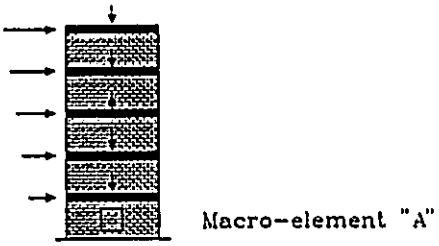

(a) Masonry shear wall

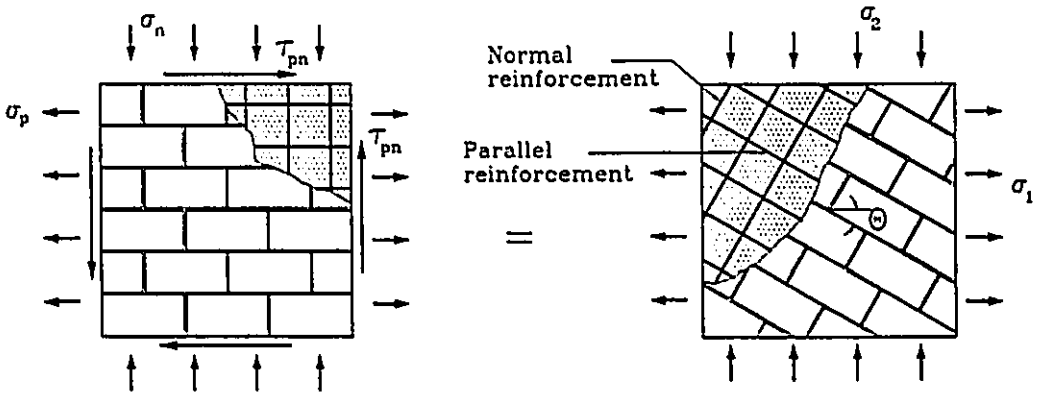

(b) Stress conditions of macro-element "A" and its equivalent macro-element "B".

Fig. 2.1 A macro-element in a masonry shear wall.

To detect the inherent anisotropic characteristics, a large number of tests would be required for a complete mapping of the complete failure surface. However, the situation was alleviated by the following points:

1. A large part of a regular masonry shear wall is subjected to the effect of

biaxial tension-compression states of stress. For example a state of pure shear stress along the mortar joints, τ_{pn}, is equivalent to a state of equal and opposite principal stresses with $\theta=45°$. The existence of normal stress σ_n along with τ_{pn}, which represents the situation in most shear walls, is equivalent to biaxial tension-compression states of stress. These states of stress change in narrow zones, in the vicinity of the loading and support points, to biaxial compression-compression.

2. The anisotropic characteristics of masonry are more apparent under the biaxial tension-compression states of stress. In the extensive test program conducted by Page (1981 and 1983) on brick masonry, failures were observed to occur along the mortar joints under the effect of biaxial tension-compression states of stress, which resulted in different failure stresses depending on the bed joint orientation θ. Conversely, the effect of the bed joint orientation vanished under the states of biaxial compression-compression when the principal stresses were closer to being equal. Under these states of stress, a splitting mode of failure was reported to occur along longitudinal planes parallel to the plane of the panel, regardless of the bed joint orientation. This behaviour was similar to the behaviour observed by Kupfer et al. (1969) in their tests on plain concrete under biaxial compression-compression. The anisotropic characteristics of brick masonry appeared under biaxial compression-compression only when one of the principal stresses was significantly larger than the other, which represented a natural continuation of the anisotropic behaviour observed under biaxial tension-compression.

3. Compared to the response of ungrouted masonry assemblages, the continuity provided by the grout cores of the grouted assemblages, under consideration in this study, was expected to help in decreasing the inherent anisotropic characteristics. This argument is consistent with the conclusion made by Hamid and Drysdale (1980) as a result of uniaxial compression tests on both ungrouted and grouted off-axis prisms.

In the light of the above points along with the main objective of this study which was to investigate the shear response of grouted concrete masonry, all the panels were tested under biaxial tension-compression states of stress.

2.2.2 Description of the Biaxial Panels

The panel dimensions, used in this part of the test program, were chosen to exhibit the macro-behaviour of grouted concrete masonry by including several blocks, grout cores, mortar joints and steel bars. Due to loading capacity limitations, the panel dimensions were set at 1200 mm square by 190 mm thick. The panels tested can be divided into two major series; UNP and RP. The unreinforced series, UNP, consisted of sixteen panels designated UNP1 to UNP16 and tested under the conditions described in Table 2.1. Panels UNP1 to UNP5 were tested to study the effect of the bed joint orientation under the effect of uniaxial compression. Similarly, panels UNP11 to UNP15 were tested to investigate the effect of the bed joint orientation under uniaxial tension. The other six panels were tested under different biaxial tension-compression states of stress. These panels were constructed using standard 190 mm two-cell hollow concrete

blocks. Pouring grout in the hollow cells produced continuous grout cores normal to the bed joints.

Table 2.1 Unreinforced panels of series UNP.

PANEL	θ, (degrees)	σ_1/σ_2
UNP1	0	0/-1
UNP2	22.5	0/-1
UNP3	45	0/-1
UNP4	67.5	0/-1
UNP5	90	0/-1
UNP6	45	1/-6.55
UNP7	45	1/-3.86
UNP8	22.5	1/-1.09
UNP9	45	1/-1.09
UNP10	67.5	1/-1.09
UNP11	0	1/0
UNP12	22.5	1/0
UNP13	45	1/0
UNP14	67.5	1/0
UNP15	90	1/0
UNP16	0	1/-1.09

Table 2.2 Reinforced panels of series RP.

PANEL	θ, (degrees)	σ_1/σ_2	ρ_p, %	ρ_n, %
RP1	0	1/-7.08	0.26	0.26
RP2	22.4	1/-6.22	0.26	0.26
RP3	45	1/-6.49	0.26	0.26
RP4	67.5	1/-7.7	0.26	0.26
RP5	45	0/-1	0.26	0.26
RP6	45	1/-13.5	0.26	0.26
RP7	0	1/-0.98	0.26	0.26
RP8	45	1/-1.08	0.26	0.26
RP9	45	1/0	0.26	0.26
RP10	45	1/-0.98	0	0
RP11	45	1/-0.98	0.53	0.53
RP12	45	1/-0.98	0.79	0.79
RP13	45	1/-1.08	0	0.53
RP14	45	1/-1.08	0.17	0.53
RP15	45	1/-0.98	0.26	0.53
RP16	45	1/-1.02	0.17	0.26
RP17	45	1/-0.98	0.53	0.26
RP18	45	1/-0.98	0.79	0.26
RP19	45	1/-1.08	0.26	0.26
RP20	0	0/-1	0.26	0.26

The reinforced series, RP, consisted of twenty panels designated RP1 to RP20 with test conditions and reinforcement percentages as listed in Table 2.2. This series involved three variables; θ, σ_1/σ_2 and the percentages of reinforcement parallel and normal to bed joint plane (ρ_p and ρ_n). The panels can be grouped in

the following manner to study the effects of these variables:

1. RP1 to RP4 were tested to study the effect of θ under high principal compressive stress, whereas RP7, RP8 and RP19 were tested to study the effect of θ under the effect of almost equal and opposite principal stresses.
2. RP3, RP5, RP6, RP8, RP9 and RP19 were tested to study the effect of σ_1/σ_2 for θ=45°, whereas RP1, RP7 and RP20 were used to investigate the effect of σ_1/σ_2 for θ=0°.
3. RP8, RP10-RP12 and RP19 were tested under pure shear τ_{pn} to study the effect of the percentage of reinforcement, keeping $\rho_p=\rho_n$.
4. RP11 and RP13-RP15 were tested under pure shear τ_{pn} to study the effect of varying ρ_p for a fairly high constant value of ρ_n.
5. RP8 and RP16-RP18 were tested under pure shear τ_{pn} to study the effect of varying ρ_p for a constant moderately low value of ρ_n.

2.2.3 Fabrication of the Test Panels for Biaxial Loading

Fabrication of the panels, especially with θ=22.5, 45 and 67.5°, took a lot of care and time during this study. A total of 36 full scale unreinforced or reinforced panels were constructed. The panel dimensions were set, as mentioned before, to be 1200x1200x190 mm. The panels were built by an experienced mason in a running bond pattern with face shell bedded 10 mm mortar joints. They were all fully grouted. Two options were considered to build the panels at θ=22.5, 45 and 67.5°. The first option was to build large panels and then to cut

them to the chosen dimensions. The other alternative was to build the panels directly at the chosen dimensions which required the following preparation before building the panels:

1. The blocks and the steel bars had to be cut to the correct sizes to ensure a good fit along the perimeter of the panel.
2. Wooden frames oriented at the required bed joint orientation θ had to be prepared and installed. The panels were built in these frames.

The second option was chosen to avoid having to cut large panels. It also facilitated the use of more elaborate details in constructing the reinforced panels, as described in Sec. 2.2.4.4. These details were necessary to permit the loads to be applied simultaneously to both masonry and reinforcement. The procedures followed in constructing the unreinforced and reinforced panels are described in the next two sections.

2.2.3.1 Unreinforced Panels (UNP)

The first step taken to construct the panels was to precut blocks to ensure good fit along the perimeter of the panel. The panel configurations used for the different bed joint orientations are shown in Fig. 2.2. The same panel configuration was used for θ=0 and 90° (or for θ=22.5 and 67.5°) but with reversed principal stress directions. The number and the patterns of the blocks required to be precut were determined. Each block was then marked on both sides and cut as accurately as possible. The blocks were cut using a diamond blade on a moving table saw as shown in Fig. 2.3.

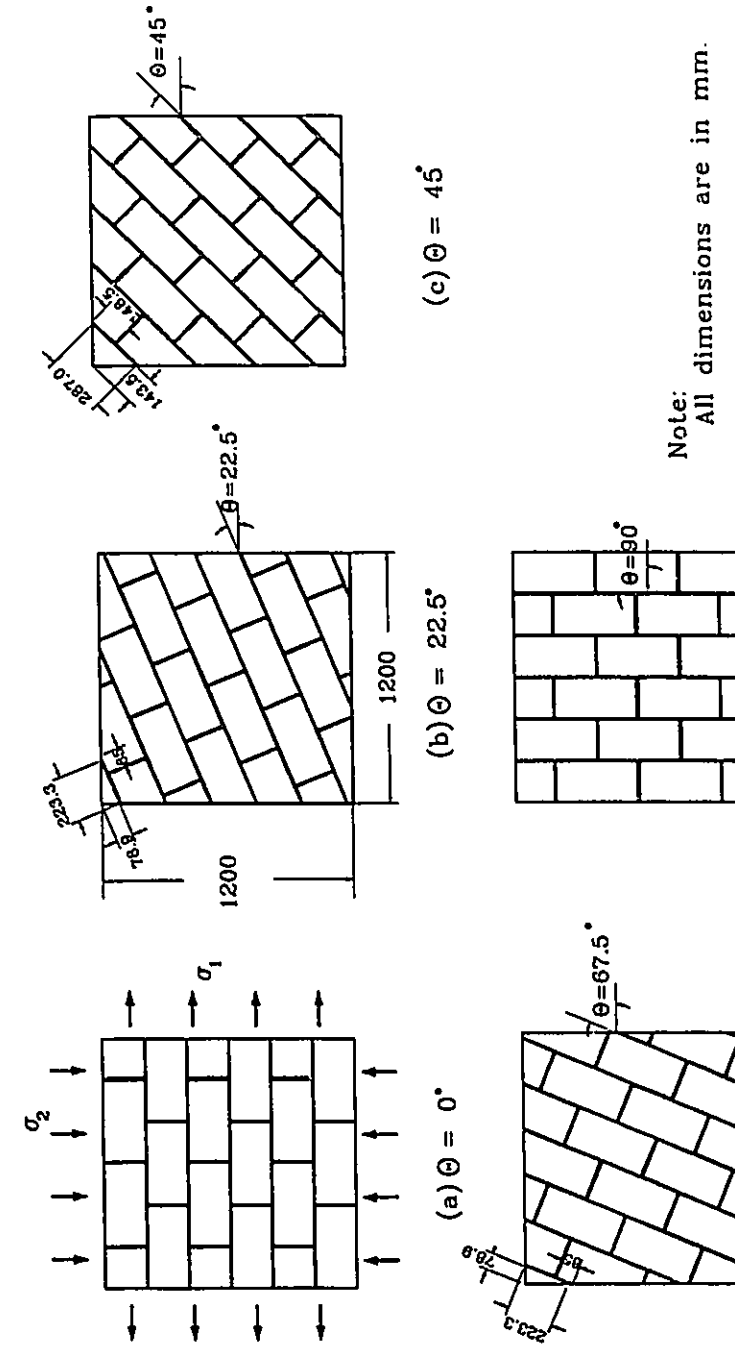

Fig. 2.2 The configurations of the panels of series UNP.

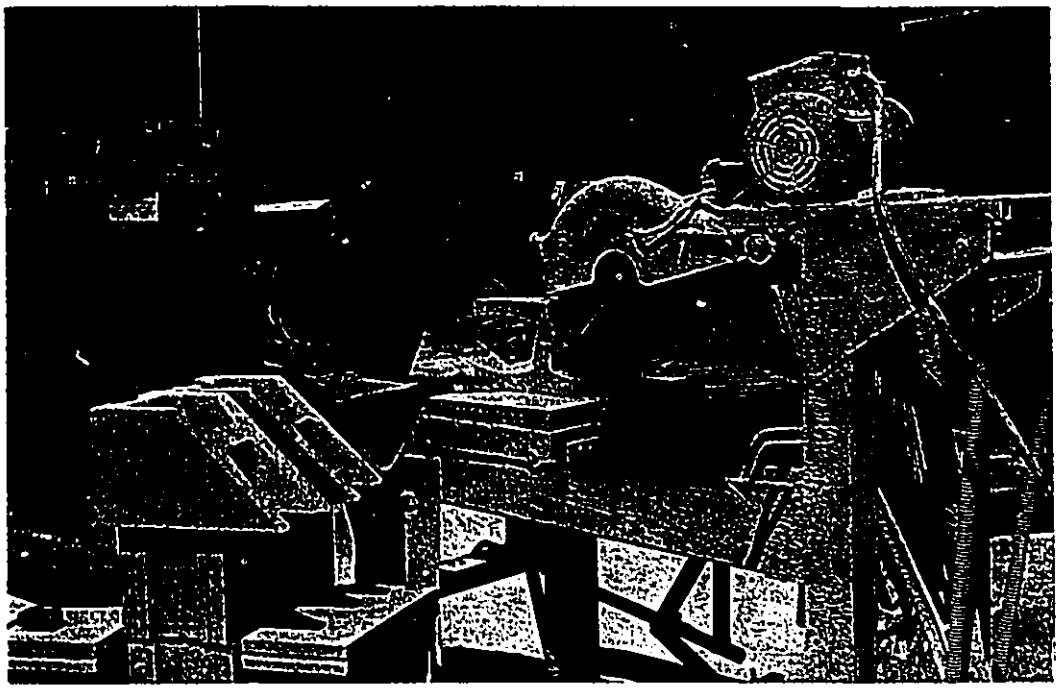

Fig. 2.3 Precutting blocks for panels with different bed joint orientations.

Rigid wooden frames were constructed in the two patterns shown in Fig. 2.4; one for building panels with θ=45° and the other for both θ=22.5 and 67.5°. Each frame consisted of four members; two diagonal and two vertical. These members were pin connected to simplify the installation of the frame and the removal of the panel. Two pieces of 10 mm thick plywood, covered with plastic sheets, were placed on each wooden frame. The frames were installed, levelled and attached to rigid elements in the laboratory to avoid any movement during the construction and curing periods.

The panels were built in the wooden frames, in the conventional manner

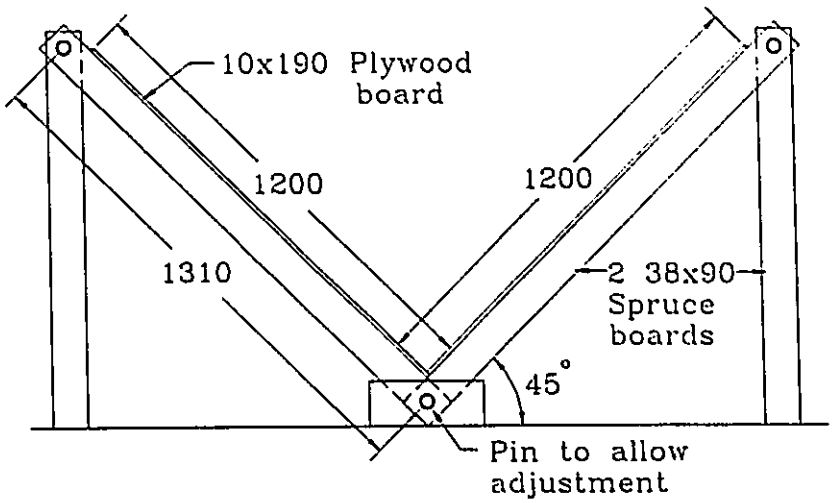

(a) Θ =45°

Note: All dimensions are in mm.

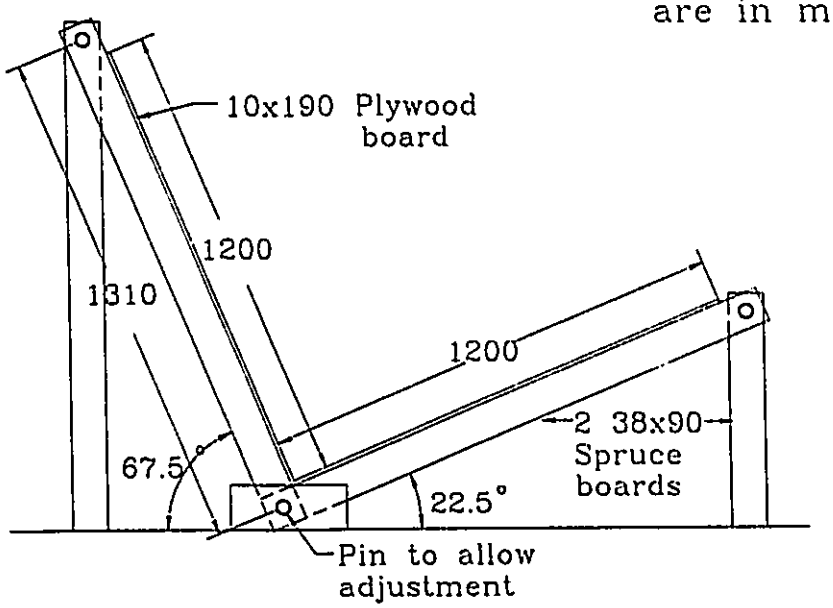

(b) Θ =22.5° or 67.5°

Fig. 2.4 Wooden frames for constructing panels with θ=22.5, 45 and 67.5°.

(with horizontal bed joints), using the precut blocks along the perimeter. An experienced mason, who had worked with patterned walls before had no trouble with the odd-shaped blocks and followed the patterns with ease. All the walls were square and true to line. One day after building the panels, grout was poured into the cores and consolidated using an internal poker type vibrator. Figure 2.5 shows several walls after completion of construction. Two weeks later, the panels were taken off the support frames and stored until tested. The laboratory temperature was kept steady at 21°C +/-2°C and the relative humidity was 50% +/-20%.

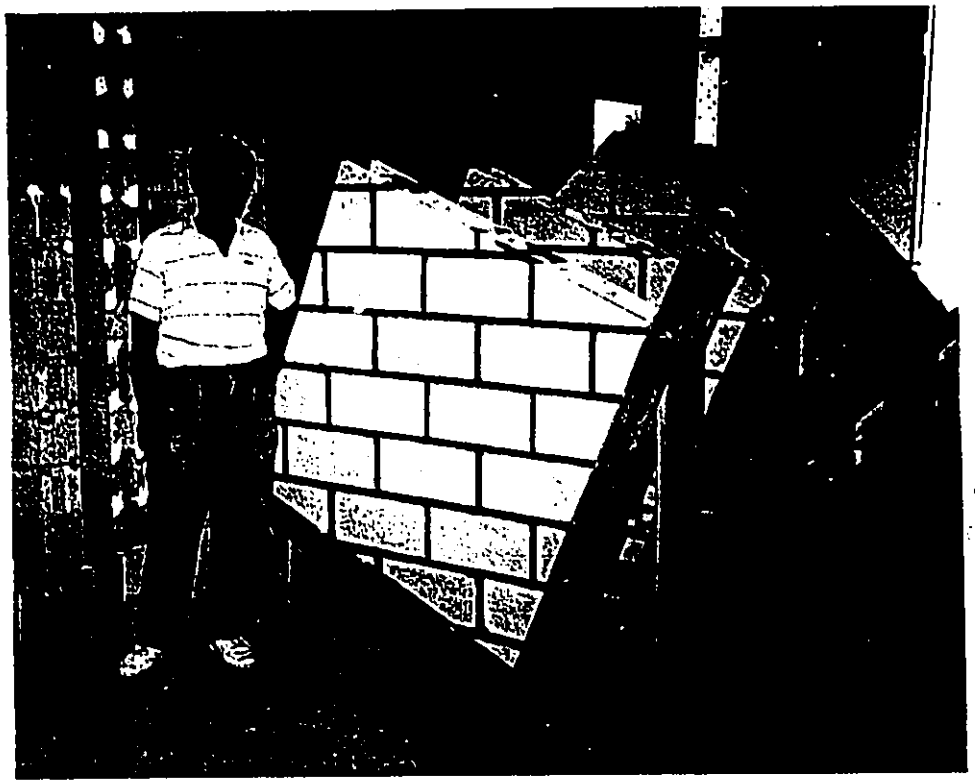

Fig. 2.5 Test panels of series UNP.

2.2.3.2 Reinforced Panels (RP)

The construction procedure for the reinforced panels was similar to that for the unreinforced panels except that additional steps were required because of the reinforcement. The webs of the blocks were saw cut then knocked-out to a depth of 100 mm to accommodate placing the horizontal bars. The configurations of the reinforced panels constructed with different bed joint orientations θ are shown in Fig. 2.6. The bars were cut to the required lengths. Each bar was welded to a 25.4 mm (1 in.) thick steel plate, designated by R, in the manner illustrated in Fig. 2.7. A hole of a diameter ϕ matching the steel bar was drilled through plate R. The hole was then widened by 12 mm in diameter through a depth of 10 mm. The bar was inserted in the hole from the narrow side and the gap between the bar and the plate, on the wide side, was filled by the welding material as shown in Fig. 2.7(c). This technique provided more weld area to transfer the forces between the plate and the bar.

The reinforcement layouts for the panels of series RP are shown in Fig. 2.8. In the case of θ=0°, both ends of each horizontal bar were pre-welded to plate R. The plates were pre-welded to the vertical bars only at the bottom ends to leave room for pouring grout from the top. The vertical and horizontal bars were placed and tied in their locations as the mason laid each course. Immediately after grouting, the pre-drilled plates (R), having the wide side of the hole on the top, were positioned over the top ends of the vertical bars and pushed into solid bearing with the fresh grout. Each plate was later welded

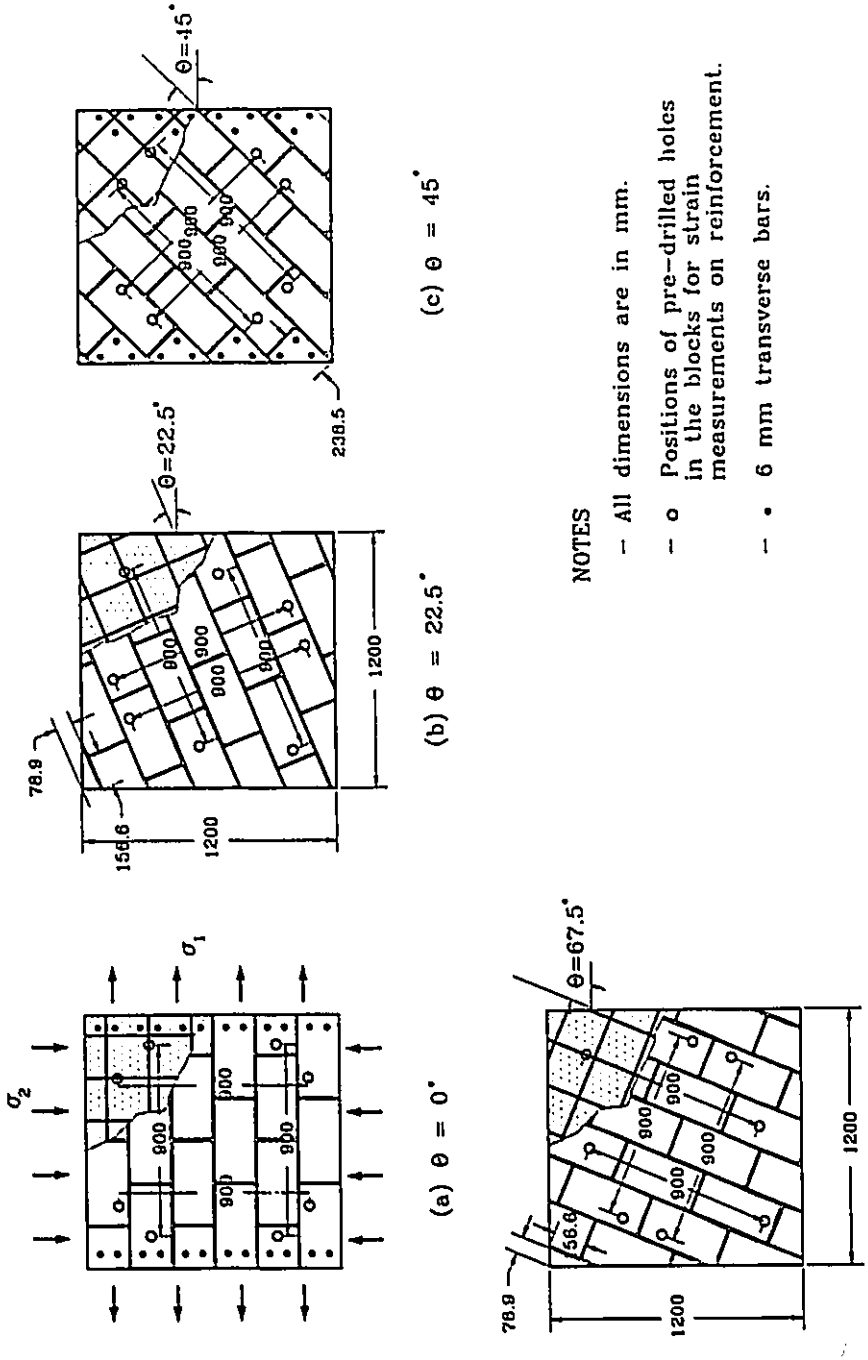

Fig. 2.6 Configurations of the panels of series RP.

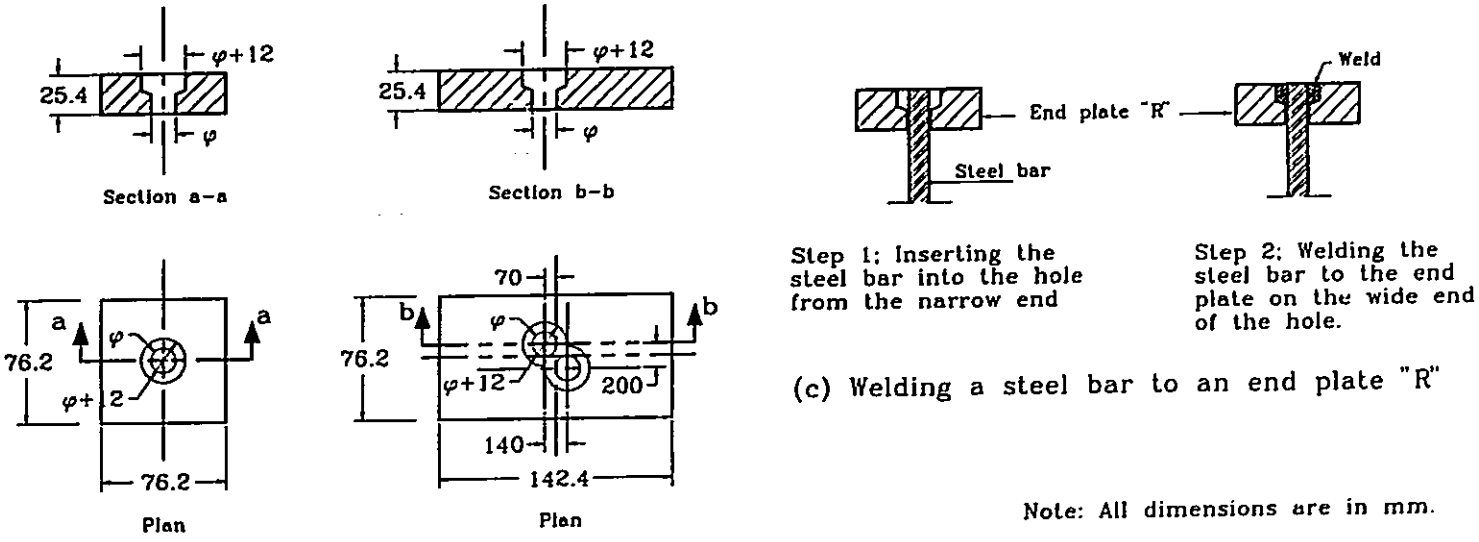

Fig. 2.7 Details of welding steel bars to end plates R.

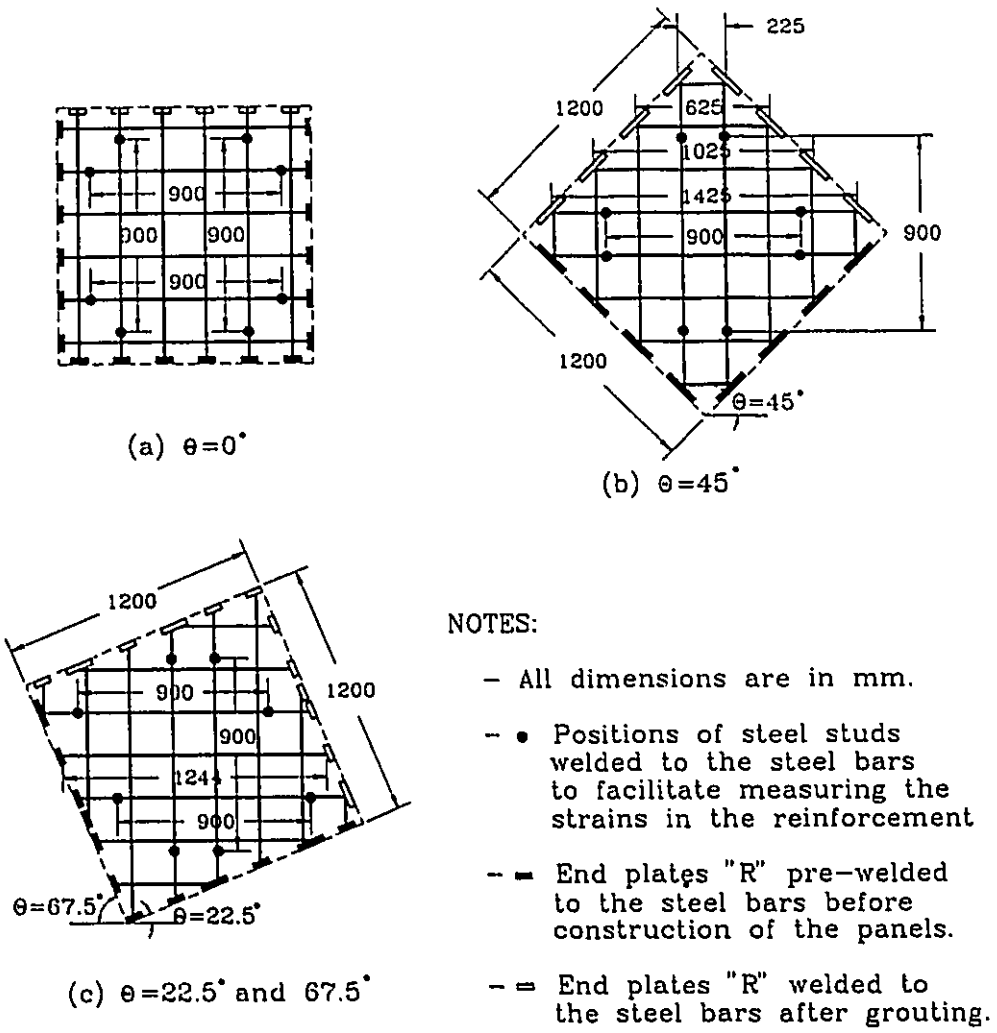

Fig. 2.8 Reinforcement layouts for the panels of series RP.

to the corresponding bars as shown in Fig. 2.7(c).

A more elaborate procedure was followed to prepare the steel bars in the cases of θ=22.5, 45 and 67.5°. The end plates R could be only pre-welded to the bars along the supported edges of the panel. The plates along the top two edges had to be left without welding to allow for grouting. The ends of the bars were also bent to fit in the holes of plates (R). The panels were drawn to full scale on

plywood sheets which were used as templates to lay out the exact dimensions and patterns of the bars. The end plates R were positioned along the two edges to be supported on the wood frames. Both these plates R and the bars were clamped in their exact positions on the templates. This arrangement facilitated the welding of the bars to the plates at the chosen angles as shown in Fig. 2.9.

Before building the panels, the positions of plates R were marked on the wooden frames. The vertical and horizontal bars were placed and tied in their locations as the mason laid each course in the manner shown in Fig. 2.10. Similar to the case of $\theta=0°$, the pre-drilled plates R for the top edges, having the wide side of the hole on the top, were positioned over the top ends of the bars just after grouting. They were later welded together. Two high strength steel bolts were welded on the exterior side of each plate R. (These bolts were included so that the plates could be prestressed to the tension loading saddles at the same time as the latter were glued to the panel sides. This procedure is more fully described in Sec. 2.2.4.4.) In addition, transverse 6 mm diameter steel bars were placed along the two sides of the panels that were to be attached to the tension loading plates. The transverse steel bars were used, in the positions indicated in Fig. 2.6, to help prevent splitting between the grout and the blocks near the loading points. Holes were pre-drilled in the block face shells. After building the walls and before pouring the grout, the transverse bars were inserted through the holes and glued in place. They were then encased in the grout when it was poured.

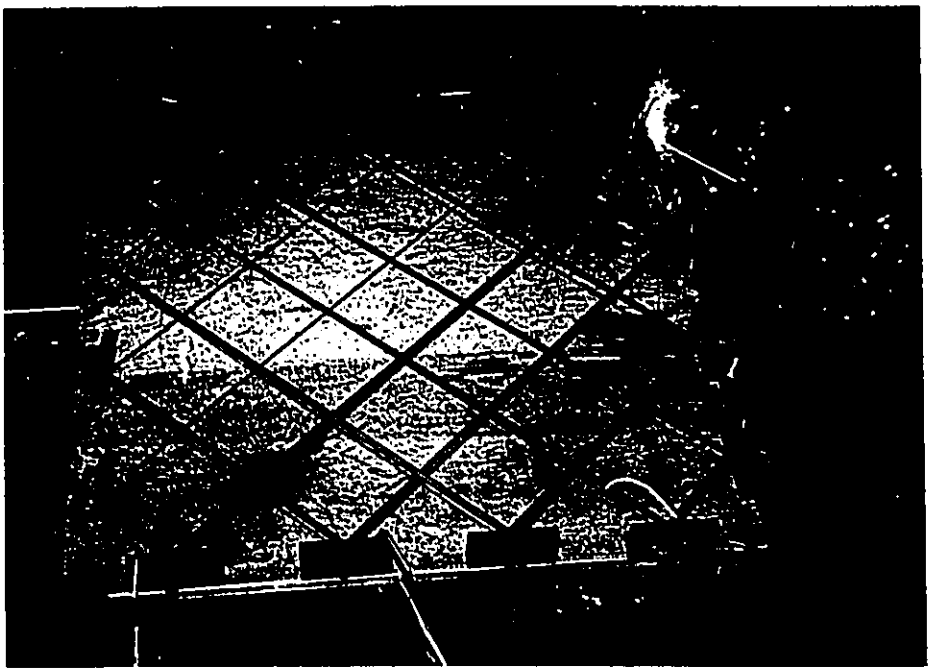

Fig. 2.9 Preparing reinforcement for the panels of series RP.

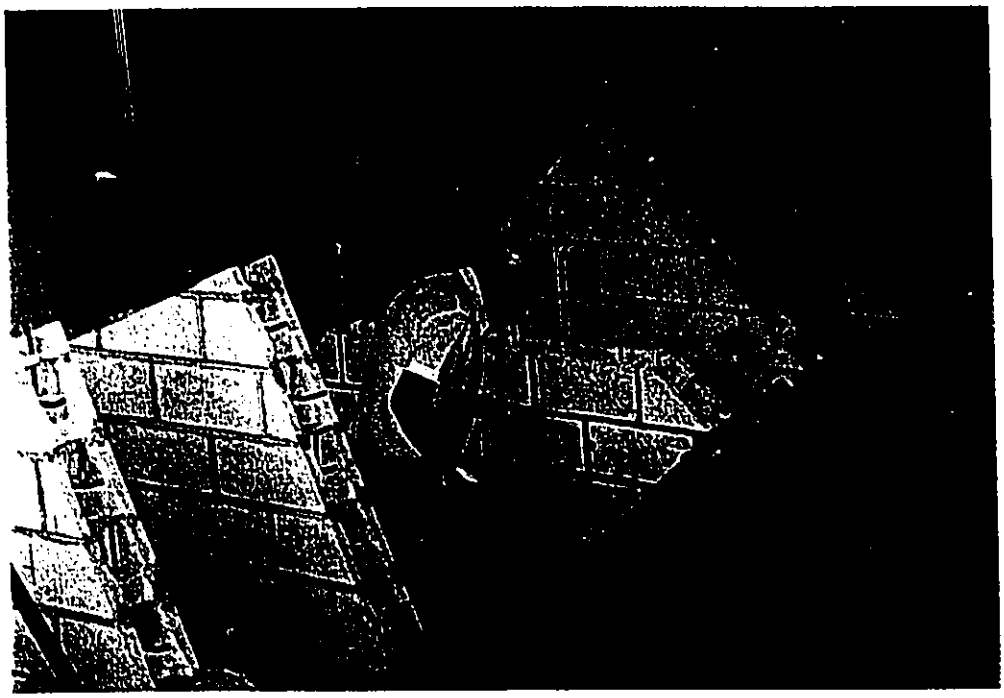

Fig. 2.10 Constructing reinforced panels of series RP.

To be able to measure the average strains experienced by reinforcement inside the panels, 25.4 mm diameter holes were drilled in the blocks at the positions marked in Fig. 2.6 which defined 900 mm gauge lengths between pairs of holes. Steel studs of 6 mm diameter were also welded perpendicular to the bars to protrude to the surface of the panels. These studs were shielded from contact with the grout or blocks by hollow plastic tubes of 19 mm diameter while the grout was being poured in the cores. The plastic tubes were covered with teflon to facilitate removing them after the grout had hardened.

2.2.4 Biaxial Test Rig

A biaxial test rig was specially devised and constructed for this investigation. It was designed to test full scale panels under uniform well defined states of stress. The test rig consisted of the supporting frame, the compression loading fixture, the tension loading fixture, the specimen interface with the test rig, and the load control system. An overall view and a sketch of the test rig are shown in Figs. 2.11 and 2.12, respectively. More details are presented in the following sections.

2.2.4.1 Supporting Frame

The specimen along with the tension and compression loading fixtures were housed in a steel frame. The frame was designed to support a 900 MN (100 ton) jack, used to apply tensile load on the panel in the horizontal direction, and

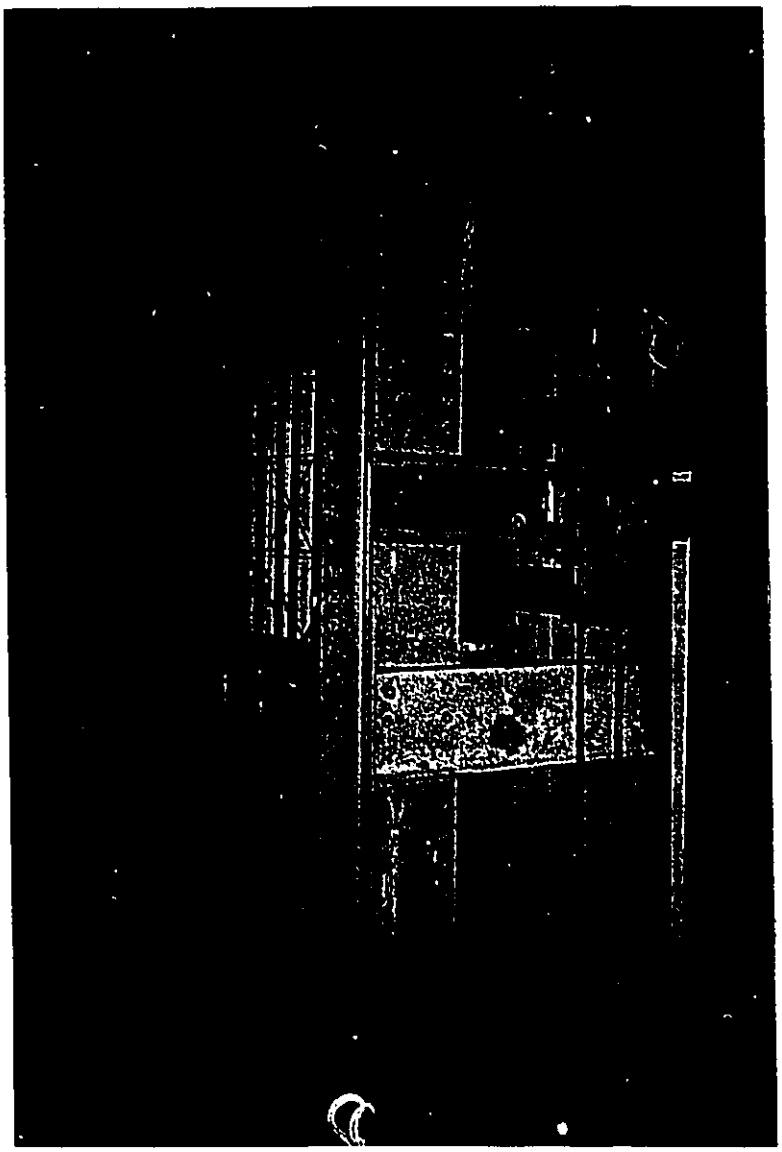

Fig. 2.11 Overall view of the biaxial test rig.

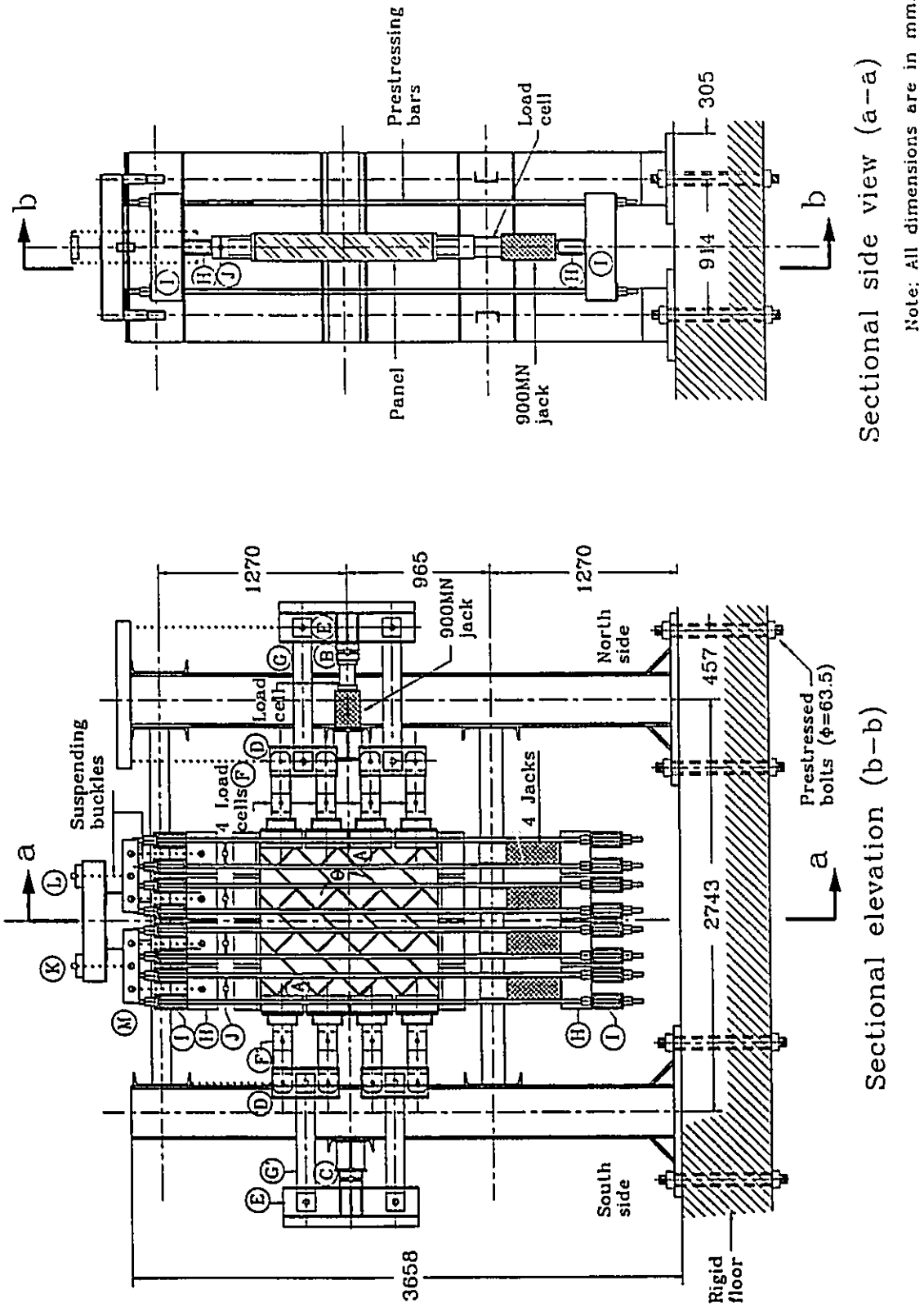

Fig. 2.12 The biaxial test rig.

to suspend the compression loading fixture. Different views of the supporting frame are shown in Fig. 2.13. It consisted of the following members.

1. Four W360x134 columns, designated by (S1), were bolted to the rigid floor.
2. Five C380x50 beams, designated by (S2), were used to connect the pairs of columns in the transverse direction. Three of them were bolted across the tops of the columns, whereas the other two were bolted to the columns at a height of 1270 mm from the floor.
3. Two parallel HSS127x63.5x9.53 beams, designated by (S3), were welded at the centres of the top channels (S2) along the centre lines of the columns (S1). They linked the columns in the longitudinal direction to form a closed frame. They also provided a support for a set of two cross beams (S4) and a longitudinal beam (S5) from which the compression loading fixture was suspended at two points (K) and (L).
4. Two parallel MC150x24.3 beams, designated by (S6), were welded at the centres of the lower channels (S2) along the centre lines of the columns (S1). They were used to increase the stiffness of the frame and to provide support for the panel during the handling and capping stages.
5. Two beams, designated by (S7), were built up of W200x59 and C310x37. They were bolted to the columns in the transverse direction at a height of 2235 mm above the floor. The horizontal 900 MN jack was fastened to the beam on the north side.

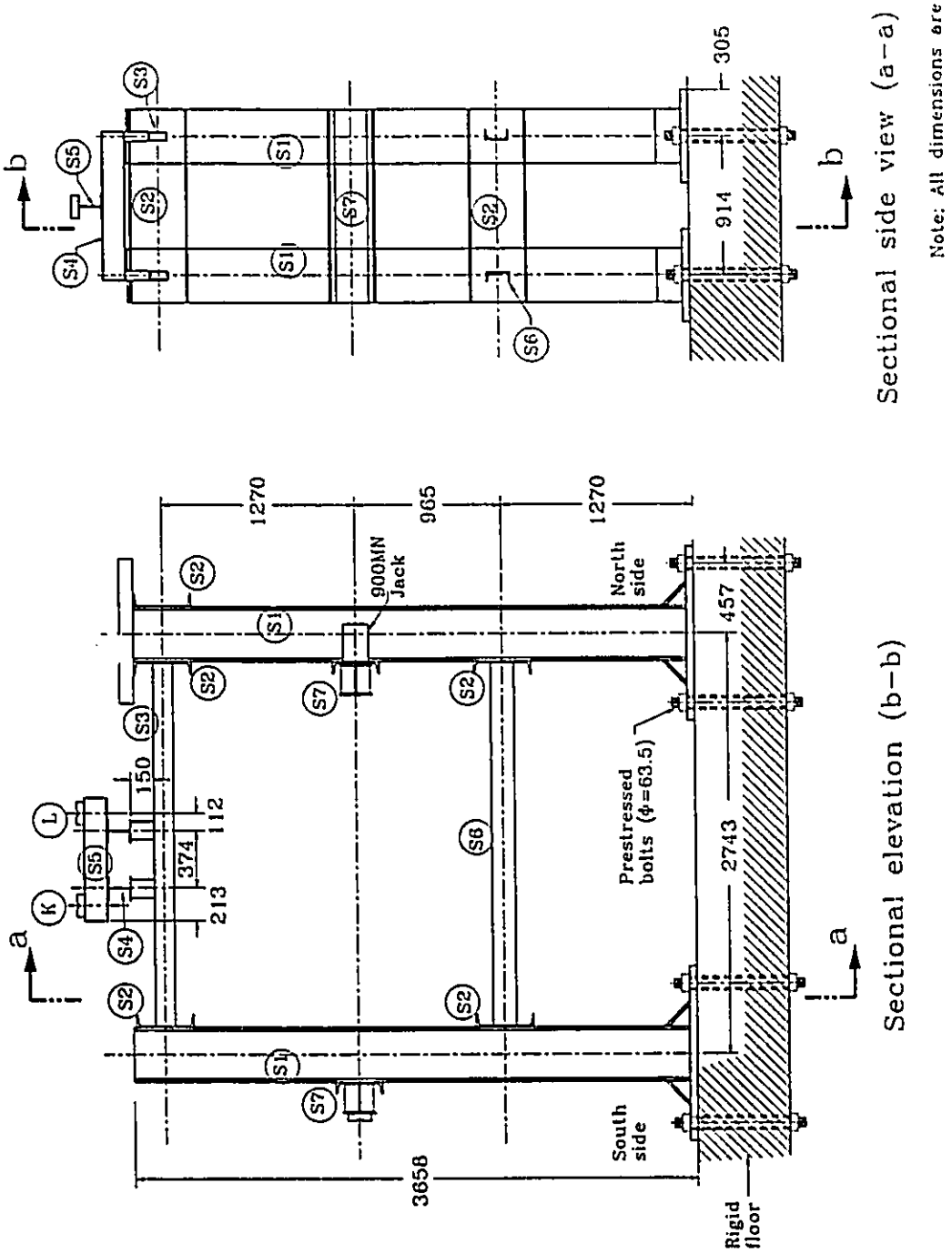

Fig. 2.13 The supporting frame of the biaxial test rig.

2.2.4.2 Tension Loading Fixture

The tensile load was applied in the horizontal direction. This part of the test rig included eight loading saddles (A), four of them were glued to the north end of the panel and connected to the hydraulic jack at point (B), as shown in Fig. 2.12. The other four saddles, glued to the south side of the panel, were connected to the supporting point (C). The applied force was distributed into four equal forces through a set of three beams (D and E) and six links (F and G or F´and G´) on each side. Each beam was built of two C200x28, back to back, leaving a gap of 41 mm to fit the links. The links were 12.7 mm thickness and increased to 38.1 mm at the joints. The details of the tension loading members on the south side are shown in Fig. 2.14.

The beams and the links were pin connected by means of high strength bolts. In addition, a roller and a spherical seat were included at (B) and (C), respectively. These connections were meant to allow rotation to take place individually at any loading point or globally along the two sides. The elements of the tension loading part were suspended along the centre of the support frame to eliminate the effect of their weight.

2.2.4.3 Compression Loading Fixture

The compression load was applied vertically by four 900 MN (100 ton) hydraulic jacks. The jacks along with the panel were housed in four compression

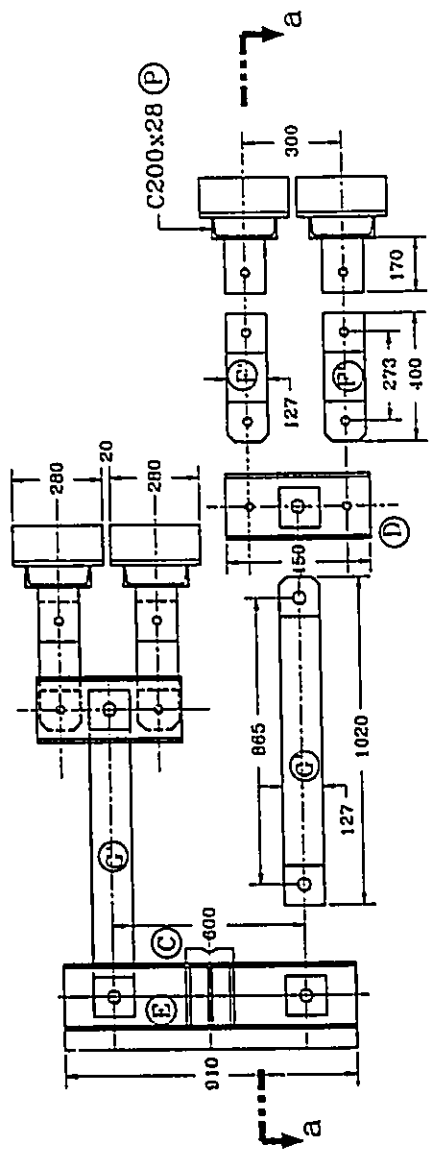

(a) Elevation

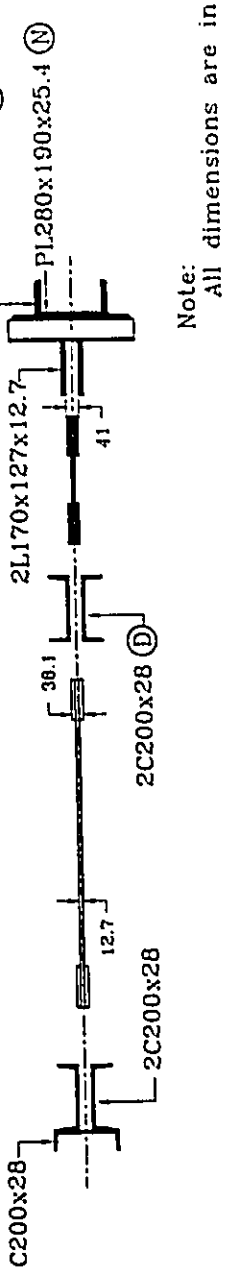

(b) Sectional plan (a–a)

Note:
All dimensions are in mm.

Fig. 2.14 Tension loading fixture on the south side.

frames. The jack in each frame was fastened, at the bottom, to three HSS 203.2x101.6x12.7 crossed beams (H) and (I), as shown in Fig. 2.12. These beams were connected to identical beams on the top of the panel by means of four DY-WI-DAG deformed prestressing bars. The compressive forces were transmitted to the loading plates on the top of the panel through four spherical seats (J), one at each loading point. These spherical seats were included to allow rotation at the loading points.

The four compression frames were suspended in the centre of the supporting frame. Divided into two groups, the compression frames were suspended from two separate beams (M) by the means of turnbuckles. The beams were then hung from points (K) and (L). Having the compression frames suspended minimized any resistance to deformation in the horizontal direction. Moreover, it allowed, in the presence of the spherical seat (C), the panel to move transversely to fit exactly along the line between (B) and (C). This eliminated any out-of-plane moment due to eccentricity in the horizontal direction.

2.2.4.4 Panel Interface with the Test Rig

The major obstacle in performing biaxial tests has been to eliminate the constraints on deformations along the loaded boundaries. Kupfer et al. (1969) used brush platens to test 200x200x50 mm plain concrete specimens. Samarasinghe and Hendry (1982) glued four similar steel blocks to each of two opposite edges of 150x150x18 mm one-sixth scale brickwork panels to apply the

tensile loads. They applied the compressive loads through a friction reducing packing between spreader beams and the other panel edges. Hegemier et al. (1978-a) tested unreinforced and reinforced full scale panels of 1625x1625x203 mm dimensions. They used polysulfide bonding agent with a low shear modulus to transfer the loads between the load fixtures and the edges of unreinforced panels. They had to add a layer of epoxy 203 mm wide to both faces of each tensile edge in order to force the crack into the panel centre. In the reinforced panels, each bar was welded to a steel plate and then the entire tensile edge was bonded to one steel plate which was attached to the load distribution fixture. Page (1980/81/83) used brush platens to test 360 mm square half-scale brick masonry panels. Vecchio and Collins (1982) applied both shear and normal forces to 890x890x70 mm reinforced concrete panels. The forces were applied through five individual shear keys on each edge. Kirschner and Collins (1986) increased the panel size to 1627x1627x285 mm and performed the tests under normal forces applied also by five individual plates on each edge.

In this investigation, the loads were applied by eight individual and similar compression loading plates along with eight individual and similar tension loading saddles. Gaps of 20 mm were left between the adjacent loading plates (or saddles). A decision was made to apply the loads through individual plates (or saddles) because this arrangement has some advantages over using single spreader beam along each edge. It is virtually impossible to avoid introducing edge restraint when continuous spreader beams are used. Introducing a low friction

sliding surface or a soft capping material can reduce these effects, but cannot eliminate them. Although the amount of friction can be estimated, changes in the mechanical properties of the interface material and of the panel at different loads results in the stress distributions being highly indeterminate. Also, although the spreader beam may be fairly stiff, it cannot maintain a plane condition along the edge nor does it allow free deformation. This adds to the indeterminacy of the system. The individual loading plates and saddles adopted in this investigation have the same fault, but limited to a much smaller length along the edges of the panels. Therefore, the effects of these localized restraints were thought to be acceptable because relatively small effects near the edges would have little effect on the overall behaviour of the panel. The gaps left between these loading areas accommodate in-plane deformations and thus reduces the restraint. These gaps also ensure that the load distribution system does not reinforce the edges of the panels.

The details of one of the compression loading plates and one of the tension loading saddles are shown in Fig. 2.15. Each compression loading plate consisted of four parts; a 280x190x25.4 mm horizontal plate (Q1), two identical 280x152.4x25.4 mm vertical webs (Q2) and a 152.4x152.4x50.8 mm horizontal plate (Q3). The four parts were welded to form the shape shown in Fig. 2.15(a). Plate (Q1) is the load bearing plate which was in contact with the panel, whereas plates (Q2) were used to increase the stiffness of the loading plate and to insure full contact of plate (Q1) with the panel under the effect of high

compressive loads. Each of the compression loading plates on the top of the panel, plate (Q3) had a spherical seat to accommodate a ball at (J), as indicated in Fig. 2.15. At the bottom of the panel, plates (Q3) of the four compression loading plates were attached directly to the load cells on the tops of the compression jacks. Before placing the panel in the test rig, the top compression

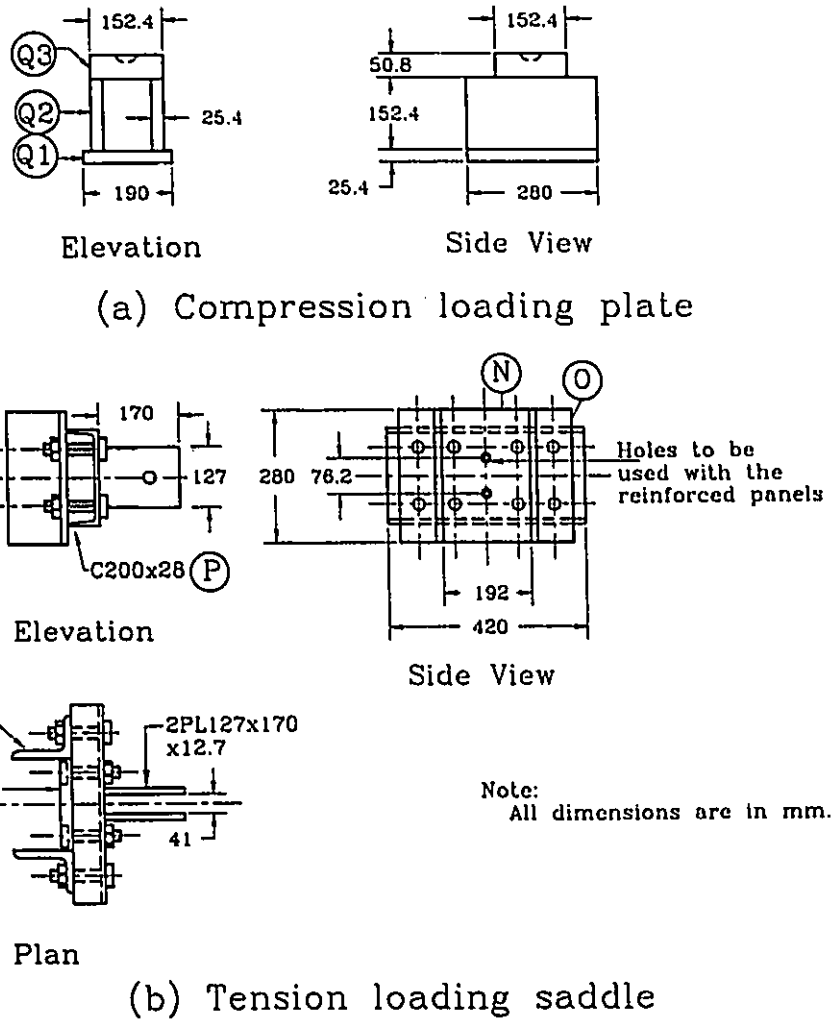

Fig. 2.15 Panel interfaces with the biaxial test rig.

loading plates were capped on the top of the panel using hydrostone to ensure full contact. The panel was then moved inside the test rig, where the bottom compression loading plates were fastened in their exact positions, having plates (Q1) on the top. The panel was lowered onto these loading plates, on which a layer of hydrostone had been just spread.

Each tension loading saddle, as shown in Fig. 2.15(b), consisted of a 25.4 mm thick plate (N), two L125x90x13 side angles (O) and a C200x28 channel (P). The channel was welded to two 12.7 mm plates which were pin connected to link (F), shown in Fig. 2.14. The saddles were glued to the panel sides using an epoxy resin known by the brand name SIKADUR 31. The interior side of plate (N) and the two angles (O) provided a ratio of 1:2 between the panel cross-section area and the glued area. This ratio was selected to avoid premature failure at the loading points.

As shown in Fig. 2.15(b), holes were drilled in plate (N). These holes were used with the reinforced panels to fit the bolts welded to the exterior side of plates (R) (see Fig. 2.7). Plate (N) was prestressed to plate (R) and glued to the end of the panels at the same time. The side angles (O), which were attached to channel (P), were then glued to a side of the panel and, at the same time, bolted to plate (N). The combination of bolting of the saddle to the reinforcement and gluing it to the masonry ensured that the tensile load was applied simultaneously to both masonry and reinforcement. The sequence of these steps are further illustrated in Fig 2.16.

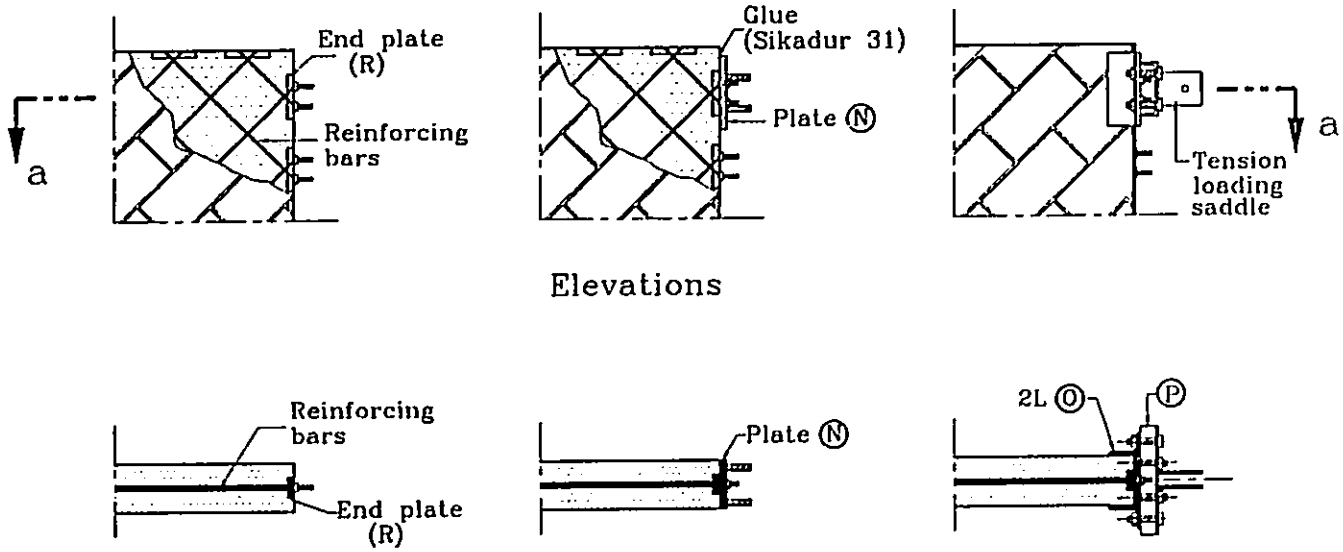

Step (1)
Weld bolts to the end plates (R) along the tension sides.

Step (2)
Glue plate (N) to the panel and have it prestressed to the end plate (R).

Step (3)
Glue the side angles (O) and prestress the rest of the saddle to plate (N).

Fig. 2.16 Procedures for fastening a tension loading saddle to a reinforced panel of series RP.

2.2.4.5 Load Control System

To control the test loads and to maintain the selected ratio between the principal stresses (σ_1/σ_2), the oil pressure was simultaneously applied to all five jacks by a hydraulic hand pump. The oil was pumped into a six-way manifold, as indicated in Fig. 2.17. Four lines out of this manifold were connected directly to the four compression jacks. Having the fifth output line connected to the tension loading jack directly, a ratio of σ_1/σ_2=1/-6.22 was maintained during the test of panel RP2. In other tests, the fifth output line was connected to a double acting jack with different push-pull piston areas. This jack acted as a pressure regulating device out of which different oil pressure was supplied to the tension loading jack. In this manner, ratios of σ_1/σ_2=1/-3.86 and 1/-13.5 were successfully maintained during the tests of panels UNP7 and RP6, respectively, as indicated Table 2.2.

The double acting jack had to be replaced by a pressure distributing frame to provide the other ratios of σ_1/σ_2 listed in Tables 2.1 and 2.2. The pressure distributing frame consisted of a rigid beam connected to the rigid floor of the laboratory by two DY-WI-DAG deformed prestressing bars. Inside this frame three jacks were arranged as shown in Fig. 2.18. Having the oil supplied with pressure P_1 to the bottom jacks (BJ1 and BJ2), different oil pressure P_2 was developed in the top jack (TJ), depending on the ratio between the cross-sections of the top jack and the bottom jacks. The oil pressure P_2 was applied to the horizontal tension jack. Using this arrangement, with different jacks and

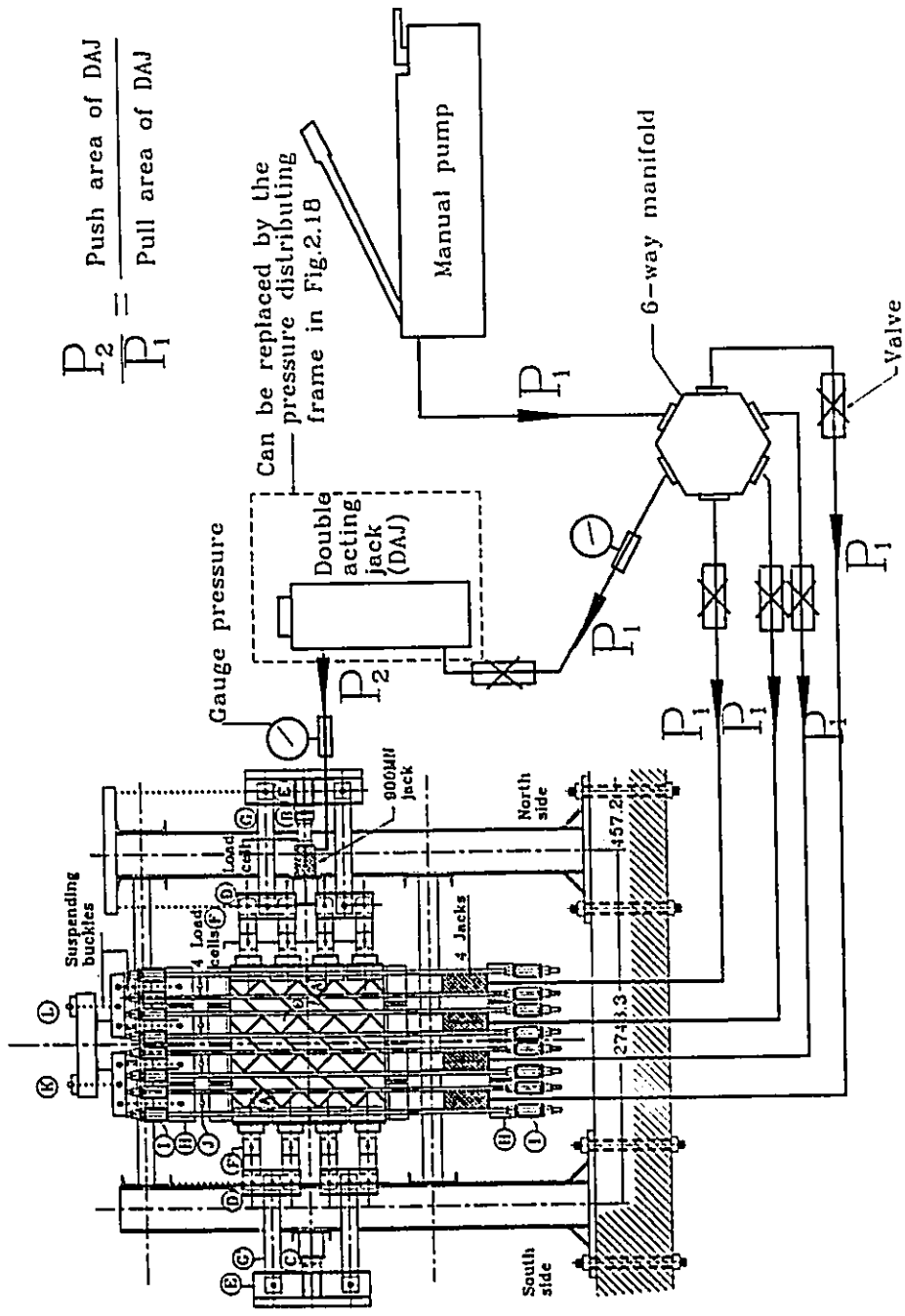

Fig. 2.17 Hydraulic system to maintain constant ratios of σ_1/σ_2.

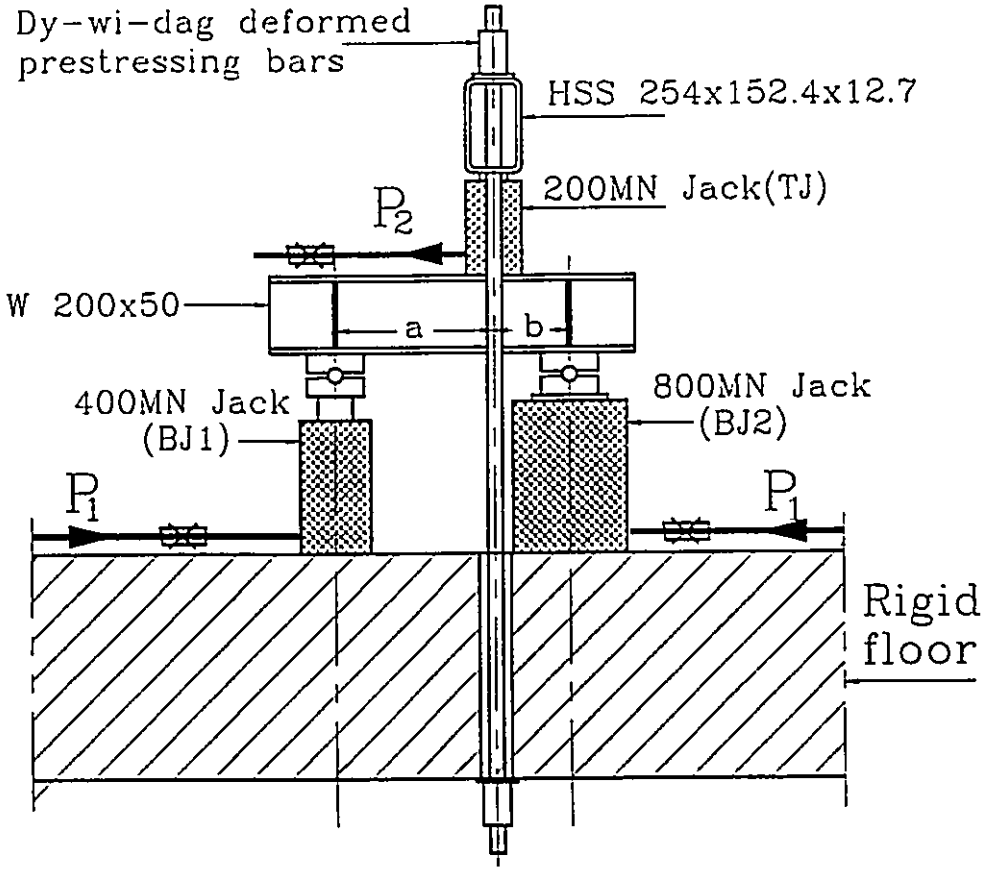

Fig. 2.18 Pressure distributing frame.

corresponding different ratios of a/b, the principal stress ratios of σ_1/σ_2=1/-1.09 and 1/-0.98 were developed.

Five valves were introduced in the circuit to facilitate placing the different jacks into positions before the test. The valves were all left opened during the test.

2.2.5 Instrumentation and Data Acquisition

The average strains of both masonry and reinforcement were monitored during the tests. Six LPDTs (linear potentiometer displacement transducers) were

mounted on each face of the panel in the positions shown in Fig. 2.19. They were used to measure the average displacement of masonry over the gauge lengths in four directions which provided enough data to draw Mohr's circles of strain at the different loading stages. The measurements were taken over a 900x900 mm area at the centre of the panel. Each LPDT was mounted on the panel surface at one end of the gauge length, as indicated by point 3 in Fig. 2.19, whereas an aluminium rod was attached to the panel at the other end, as indicated by point 1. This aluminium rod was then attached to the tip of the LPDT at point 2. Four more LPDTs were used to monitor the average strains along the steel bars on gauge lengths of 900 mm. Two of these LPDTs were attached to vertical bars and the other two were attached to horizontal bars at the positions indicated in Fig. 2.6. As illustrated in detail (V) in Fig. 2.19, each LPDT was mounted on a steel tube which was glued to the steel stud already welded to the steel bar. The LPDTs used in this investigation had 25.4 and 50.8 mm gauge lengths with accuracies of 0.8×10^{-3} to 1.6×10^{-3} mm, respectively.

A load cell was used on the top of each compression jack to measure the applied forces. The four links (F), of the tension loading fixture on the north side, were also instrumented with electric strain gauges and calibrated to work as load cells. A fifth load cell was inserted in front of the horizontal jack to determine the total applied tensile force. Almost uniform force distributions were recorded among the different loading points. The readings of the tensile forces showed differences of 1.2 to 7.2% between the maximum and the minimum tensile

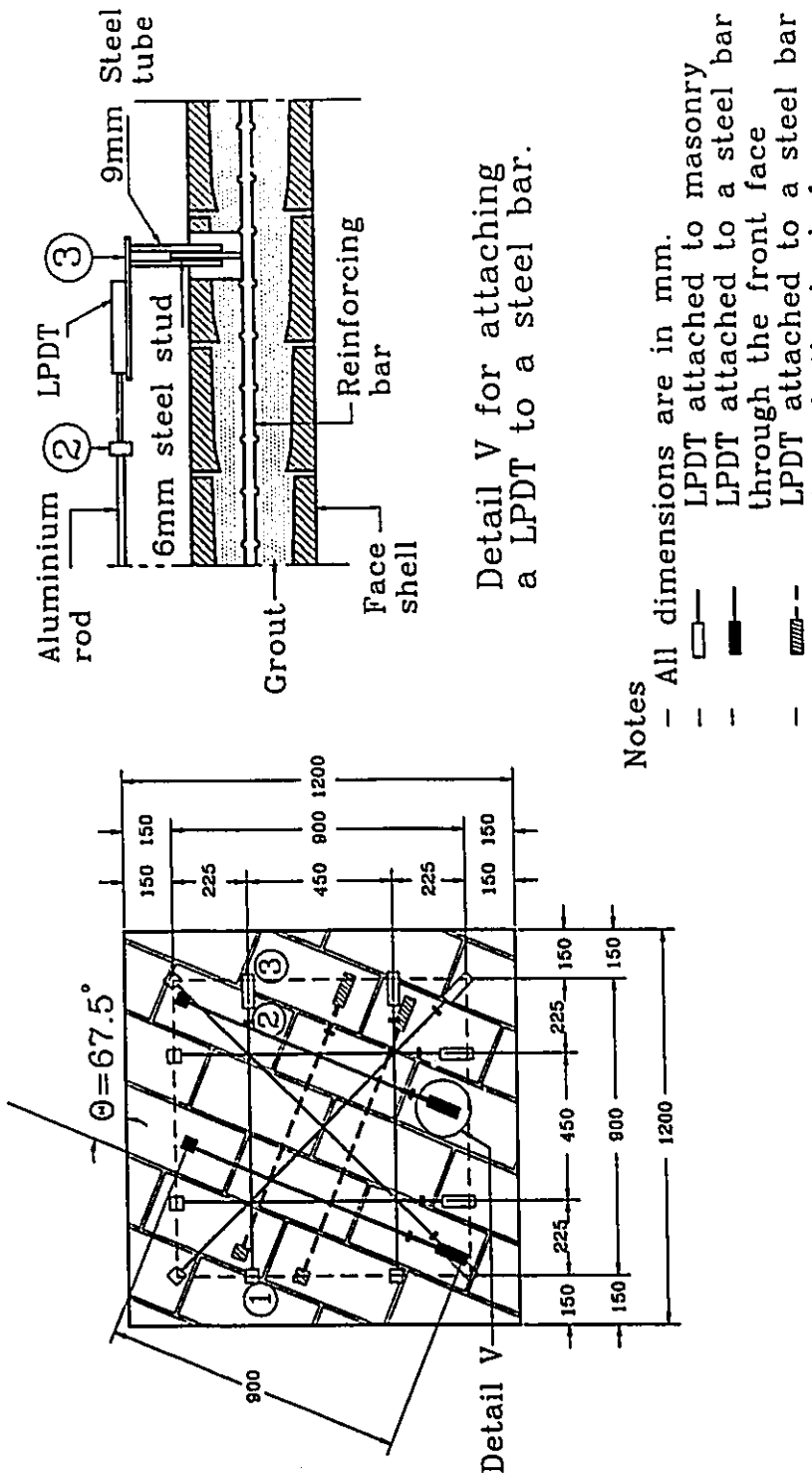

Fig. 2.19 Position of LPDTs for measuring the deformations of masonry and reinforcement.

forces. The higher value occurred at low loading ranges. Similarly, the measurements of the compressive forces showed a difference between the maximum and the minimum compressive forces as high as 9.4% at low loading ranges. This difference dropped to a maximum of 2.4% as the oil pressure was increased to the failure range of the specimens.

The readings of the LPDTs and the load cells were recorded in a quasi-continuous manner using a computer controlled OPTILOG data acquisition system. One of the compression load cells and one of the tension load cells were connected to strain gauge boxes to monitor and control the load during the test. Also, a continuous plot of the overall displacement from an additional horizontal LPDT versus the total tension force was drawn on an X-Y plotter. It provided an immediate visual check on the response of a panel during the course of a test.

During a typical test, the loads were increased monotonically until failure. At each load stage, the loading was halted, the readings of the LPDTs and the load cells were recorded more than once. The initiation and propagation of cracks were marked and photographed, and any pertinent observations were noted. The tests took two to three hours and consisted of 15 to 20 load increments. Smaller load increments were applied as the cracks propagated to be able to document the stress redistribution between the masonry and the reinforcement. Failure of the panels was declared when one of the following conditions existed:

a. The panel split into two (or more) pieces.

b. The panel displayed very large deformations under constant or decreasing

loads.

c. The load dropped dramatically due to crushing of masonry.

2.3 AUXILIARY TESTS

A large number of auxiliary tests were performed before and during the biaxial test program. These tests can be classified under two categories; component material tests and assemblage tests. The tests performed under these two categories are summarized in the following sections.

2.3.1 Tests of Component Materials

As mentioned before, the test program was restricted to one set of component materials to reduce the number of variables. However, the materials selected for this test program are commercially available and similar to those commonly used in North America. The component materials included blocks, mortar, grout and steel bars. A sufficient number of specimens for each component material were prepared, cured and tested with the associated test panels. Physical as well as mechanical tests were performed. These tests were used to determine the properties of the materials and served as control tests.

The physical properties determined for the concrete blocks included the weight, dimensions, density and initial rate of absorption (IRA). Mechanical tests were performed to determine the compressive and tensile strengths using full blocks, half blocks and parts cut out of the blocks. Each type of test included 5 to 10 repetitions. Some of the tests were repeated, during the course of the test program, to investigate the effect of age on the block characteristics.

Unit weights and sieve analyses of fine sand, coarse sand and pea gravel were required to design the mortar and the grout mixes. For every batch of mortar, the initial flow was measured and three 2 inch cubes were prepared to determine the compressive strength. For each batch of grout, the slump was monitored and six (or more) block moulded prisms were prepared. Half of these prisms were tested under uniaxial compression and the other half were used to determine the splitting tensile strength.

Three 500 mm coupons randomly cut from the reinforcing bars were tested to determine the yield stress and the failure stress for each of the different bar sizes used.

The details of the tests performed and their results are presented in Chapter 3.

2.3.2 Assemblage Tests

Some tests of masonry assemblages were conducted for direct comparison with the biaxial tests, whereas others provided data about the basic properties and behaviour of grouted concrete masonry. Uniaxial compression, uniaxial tension and direct shear tests were included.

2.3.2.1 Uniaxial Compression Tests

Test Specimens

Two series of prisms were tested under uniaxial compression. The first, designated as series UCU, was constructed at the same time as the unreinforced panels and similarly had grout cores only normal to the bed joints. The second

series, designated by UCR, was constructed with the reinforced panels and, due to the knocked-out webs, similarly had grout cores both normal and parallel to the bed joints. Each series consisted of fifteen prisms prepared with three specimens for each of the bed joint orientations of θ=0, 22.5, 45, 67.5, and 90°. The configurations of the prisms constructed in the first series (UCU) are shown in Fig. 2.20. (It should be kept in mind that the bed joint orientation θ is the angle between the bed joint and the principal tensile stress σ_1 which is equivalent in the case of the compression prisms to the angle between the head

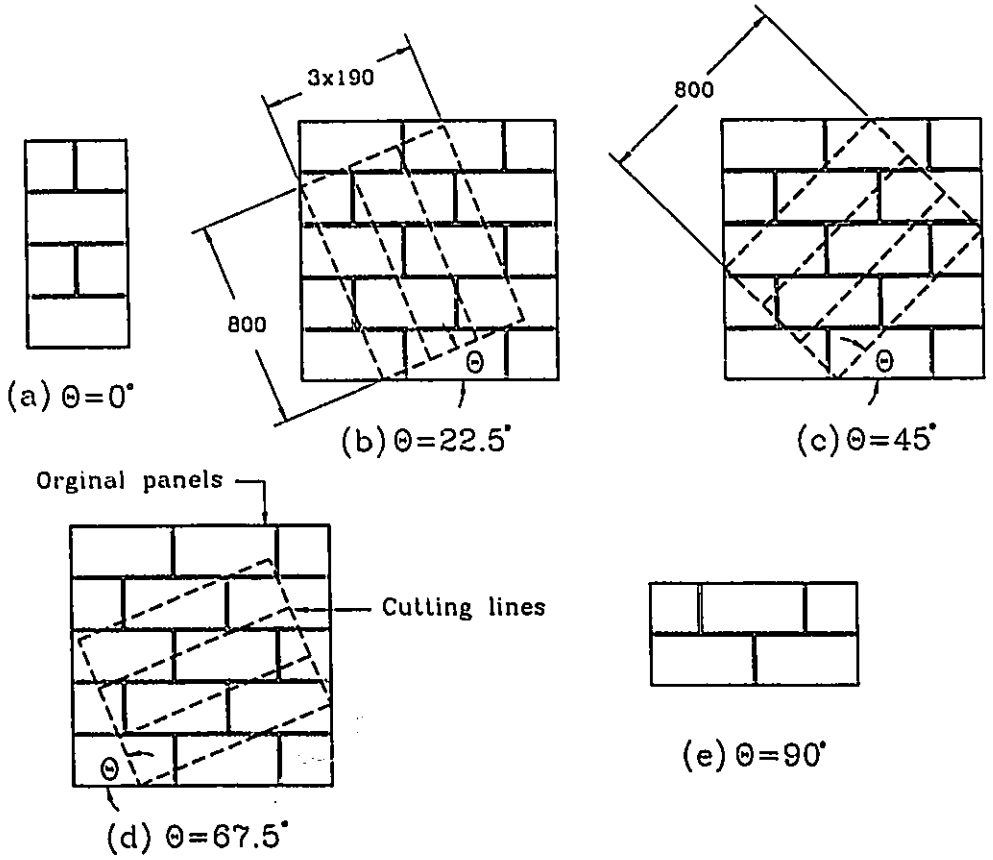

Fig. 2.20 Configurations of the prisms of series UCU.

joint and the principal compressive stress σ_2.) Three 1000 mm square panels were constructed to prepare the prisms with θ=22.5, 45 and 67.5°. They were all built in exactly the same way as the biaxial panels of the corresponding series. Twenty eight days after grouting these panels, each was cut to produce three prisms with bed joints oriented at the required angles. The panel size was increased to 1200 mm square in series UCR. This allowed for the preparation of wider prisms (800x390x190 mm). The increased width was thought to be more representative of the average masonry behaviour as it allowed for a larger number of mortar joints and grout cores in the specimen. Three additional prisms were constructed with series UCR. They were four-course prisms with θ=0°, but they were built using blocks with no webs knocked-out. These prisms were included to investigate the effect of knocking-out the webs of the blocks on the compressive strength and to relate series UCU and UCR which were tested at different times.

In addition to the above series of prisms, a four course prism was constructed in running bond pattern with each biaxial panel. These prisms were tested at the same time as the corresponding panels to identify any significant change in the compressive strengths of the masonry assemblages.

Test Procedure and Instrumentation

Each prism was capped top and bottom using hydrostone to create uniform bearing on 76.2 mm thick steel plates. It was then moved for testing in a Riehle universal testing machine with a 2500 KN capacity. The prisms were tested between a roller at the bottom and the machine head with a spherical seat

at the top. Another 76.2 mm steel plate was used between the roller and the bottom of the prism to assure uniform stress distribution. The rate of loading was set to comply with ASTM C140 (1991).

Average deformations were monitored along 200 mm gauge lengths over the mid-hight of the prism. In the cases of θ=0 or 90°, four LPDTs, two vertical and two horizontal, were mounted on each face as shown in Fig. 2.21(a). In the cases of θ=22.5, 45 and 67.5°, the deformations were measured in three directions. Three LPDTs, forming a 60° strain rosette, were mounted on each face as shown in Fig. 2.21(b). These LPDTs provided enough data to draw Mohr's strain circle at any loading stage. The horizontal deformation across the end webs of the blocks, over the mid-height of the prism, were also recorded. All deformations and load outputs were recorded using the computer controlled OPTILOG data acquisition system.

2.3.2.2 Uniaxial Tension Tests

Test Specimens

Similar to the uniaxial compression prisms, two series of prisms were prepared and tested under uniaxial tension. The first, designated as series UTU, was prepared at the same time as the unreinforced panels. It consisted of twelve prisms cut to produce bed joint orientations of θ=22.5, 45, 67.5, and 90°, measured between the bed joint and the principal tensile stress σ_1. The second series, designated by UTR, was prepared with the reinforced panels. It consisted

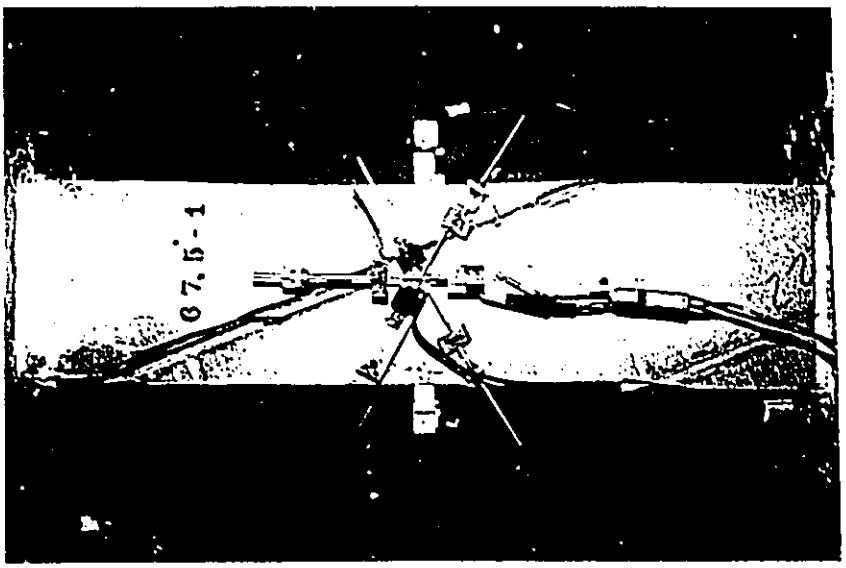

(b) For θ=22.5, 45 or 67.5°

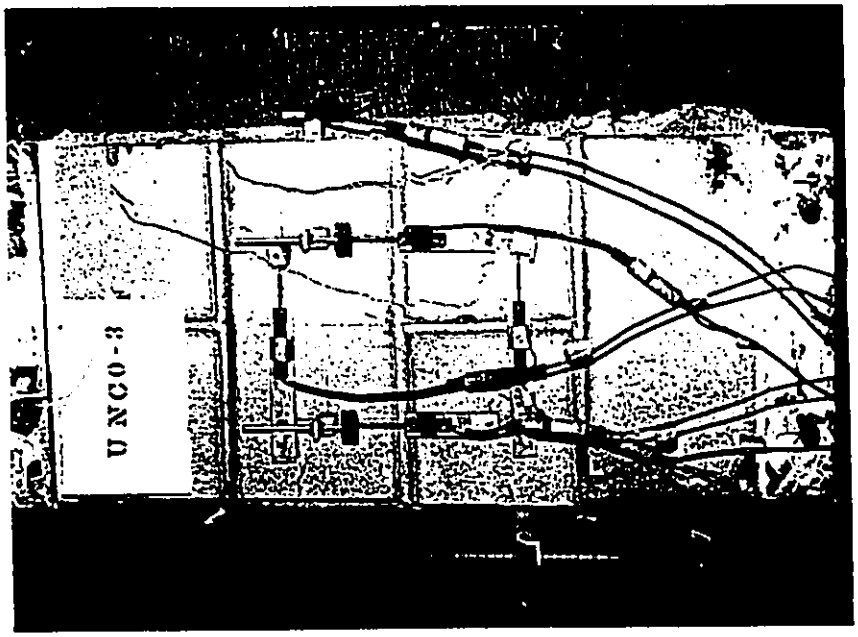

(a) For θ=0 or 90°

Fig. 2.21 Positions of LPDTs for measuring deformations on the prisms.

of fifteen prisms with θ=0, 22.5, 45, 67.5, and 90°. The configurations of the different prisms tested are similar to those shown in Fig. 2.20.

Test Procedure and Instrumentation

Tension loading saddles were glued top and bottom to each prism, as shown in Fig 2.22. The glue was allowed to harden for at least 24 hours. The loading saddles were then attached to the centres of the upper and lower heads of the Tinius-Olsen test machine. A roller and a pin connection were used between the top loading saddle and the upper head of the test machine to allow rotation to take place around two orthogonal axes. Two similar connections were also used

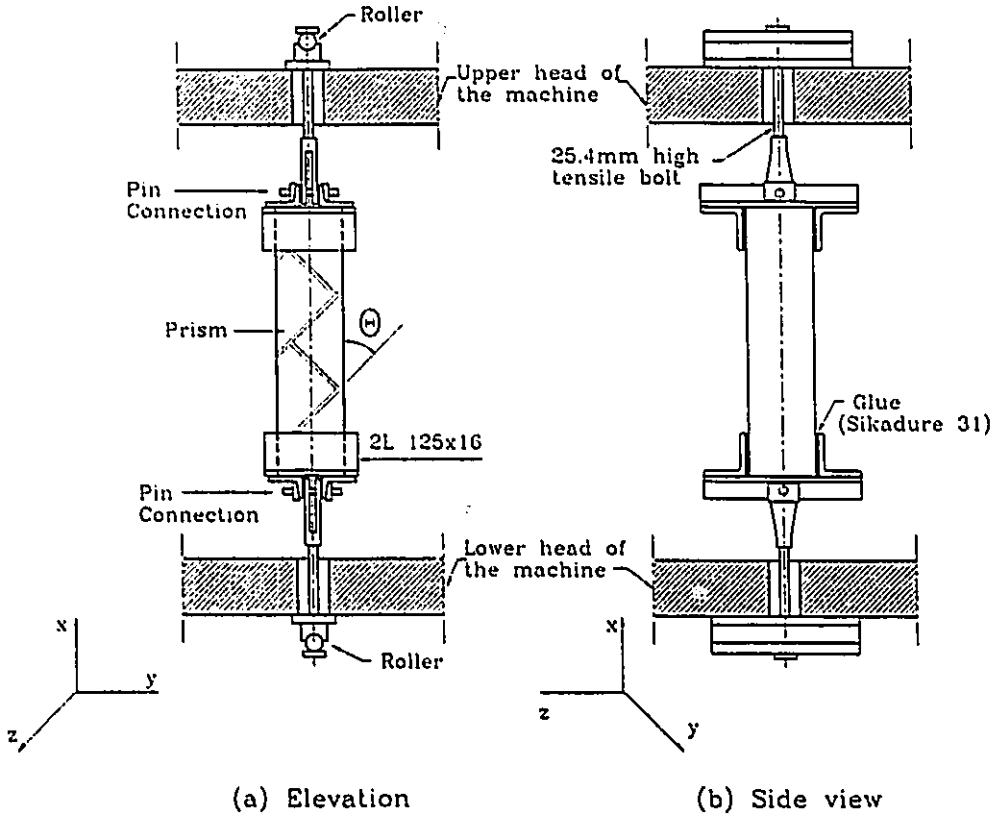

Fig. 2.22 Set-up for the uniaxial tension tests for series UTU and UTR.

between the bottom loading saddle and the lower head of the machine. These four connections eliminated transfer of moment to the ends of the prism and ensured that only axial load was applied.

The average deformations were measured along 200 mm gauge lengths over the mid-height of the prism. Four LPDTs, one on each side, were mounted to record the vertical deformation. The deformations in the horizontal direction were too small to be measured accurately. All deformations and load outputs were recorded using the computer controlled OPTILOG data acquisition system.

2.3.2.3 Direct Shear Tests

Background

Several types of specimen and loading configurations have been developed to study the shear behaviour of masonry joints. Some of the test techniques used are illustrated in Fig. 2.23. These test techniques can be classified into three categories according to the specimen configuration; triplet, four-unit, and couplet specimens. The triplet specimen has been widely used in different shapes (Haller 1969, Hodgkinson and West 1982, Hegemier 1978-b, Ali et al. 1986). However, the mortar joints, in this specimen, are subjected to flexural stresses which may significantly affect the shear capacity of the joint. The four-unit specimen, shown in Fig. 2.23-d, was used by Hamid (1978). It is a statically indeterminate structure which could lead to stress redistribution between the different joints in the assemblage. Whereas no eccentricity exists between the loading and support points, the joints are still subjected to flexural stresses. The

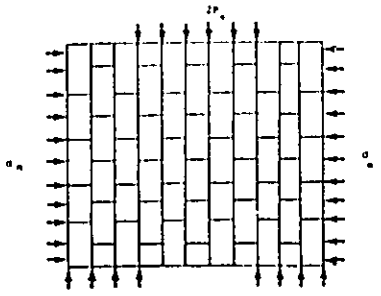

(a) Haller (1969)

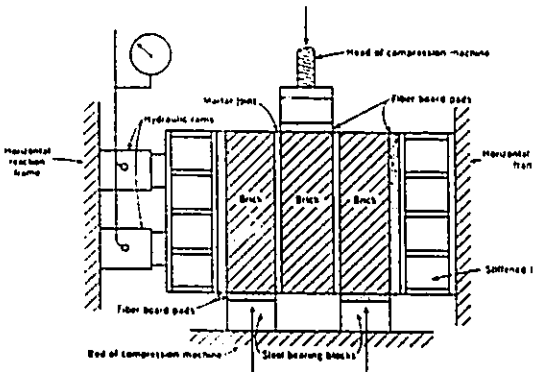

(b) Hodgkinson and West (1982)

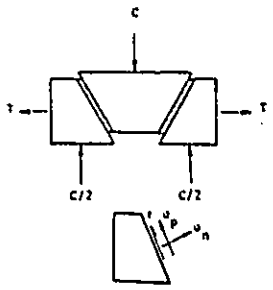

(c) Ali and Page (1986)

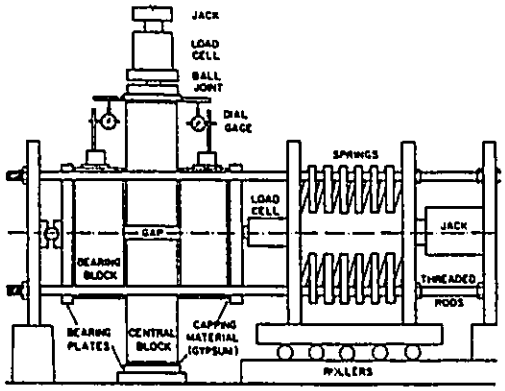

(d) Hamid (1978)

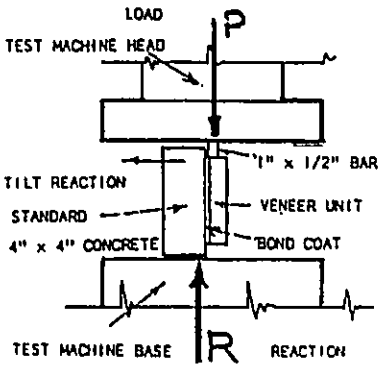

(e) Dickey (1982)

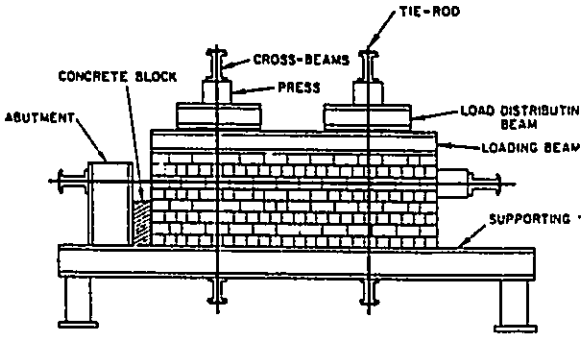

(f) Piper and Trautsch (1970)

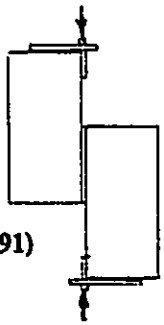

(g) Guo (1991)

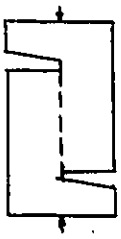

(h) Hofbeck et al. (1969)

Fig. 2.23 Review of the configurations of the direct shear specimens.

couplets used by Dickey (1982) and Pieper and Trautsch (1970) suffered also from the effect of flexural stresses along the joint.

Test Specimens

The couplet specimen shown in Fig. 2.23(g) was used by Guo (1991). It is similar to the specimen used in reinforced concrete by Hofbeck et al. (1969). This couplet specimen was chosen to be used in this test program. It has the following advantages over the triplet or the four-unit specimens.

1. The specimen is loaded through two round bars which are aligned with the joint. This eliminates the flexural stresses along the joint.
2. The specimen is statically determinate and the average shear stress can be evaluated simply by equilibrium.
3. The specimen is easy to prepare and to test. It can also be used to study the interaction between shear and normal stresses along the joint.

Three series of shear couplet specimens were constructed with series UNP. Each series consisted of nine couplets tested under three levels of pre-compression, each with three repetitions. The three series can be described as follows;

1. Series (M) was tested to study the behaviour of mortar bed joints.
2. Series (GM) was tested to study the behaviour of grouted bed joints with mortar.
3. Series (G) was tested to study the behaviour of grouted bed joints without mortar.

The couplets were built with the bed joint in the horizontal position. Two blocks were placed on the top of the couplet after laying the upper block to provide some weight on the bed joint during setting of the mortar. For the construction of series G, pieces of 10 mm thick plywood were used in the place of the mortar joint. They were removed before testing.

Test Procedure and Instrumentation

As shown in Fig. 2.24, the shear load P was applied along the centre line of the mortar joint through two plates (C), which were capped to the top and the bottom of the couplet. In the case of the couplets tested under precompression stresses, the normal load was applied by a 540 MN horizontal jack. The jack was attached to a horizontal frame as illustrated in Fig. 2.24. This frame consisted of

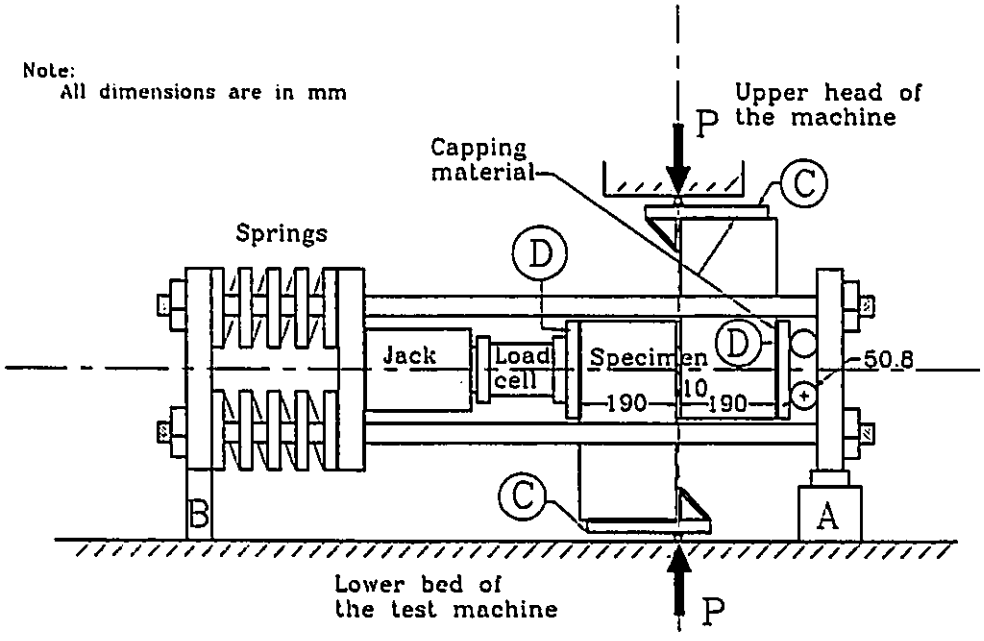

Fig. 2.24 Set-up for the direct shear tests.

a series of steel plates connected by four 25.4 mm steel rods. The precompression load was transferred to the couplet through two 25.4 mm plates (D); one capped to each end of the couplet to assure full contact and uniform stress distribution. A load cell was used between the precompression jack and the couplets. Two 50.8 mm rollers were also placed between the couplets and the frame to allow the upper block to slip without transferring load to the horizontal frame. A commercial load cell was used at point A which confirmed that no shear load was transferred through the precompression frame during the test. In this manner, the shear force along the joint remained in equilibrium with the applied load.

The couplets were tested in a Tinius Olsen test machine. Each couplet was carefully aligned with the centre of the upper and lower heads of the machine and the centre of the loading frame. The desired precompression load was first applied and maintained while the shear force was gradually increased. A valve was used to control the oil pressure in the precompression jack to avoid any increase in the precompression force due to dilation of the joint.

Two LPDTs were mounted on each side to measure the average slip and dilation along the joint. All deformation and load outputs were recorded using the computer controlled OPTILOG data acquisition system.

2.4 CLOSING REMARKS

Having selected the second research approach indicated in Fig. 1.1 to study the in-plane behaviour of grouted concrete masonry at a macroscopic level, an extensive experimental test program was conducted to provide a body of test

data for North American conditions (practice and material). This data was required to formulate and verify the proposed macro-behaviour model.

Development of the biaxial test method, reported in this chapter, was necessary to gain an understanding of the fundamental behaviour of masonry subject to biaxial states of stress. A major part of the work in this research was to design an apparatus which would produce well defined loading conditions and exclude the indeterminate effects of external boundary conditions. All of this, of course, had to be accomplished within budget limitations. As will be discussed further in Chapter 4, the apparatus and the test method satisfied the design criteria and provided suitably accurate and detailed data to contribute toward a further understanding of the in-plane behaviour of grouted concrete masonry.

The two series of panel tests differ in the degree of anisotropy because of the presence of continuous horizontal grout cores in the second series. This is of added interest and permits investigation of the influence of anisotropy on overall behaviour.

The data from the auxiliary tests are presented and discussed in the following chapter, whereas the biaxial tests of the panel assemblages are discussed in Chapter 4.

CHAPTER 3

EXPERIMENTAL RESULTS OF THE AUXILIARY TESTS

3.1 INTRODUCTION

The auxiliary tests, which included the tests of component materials and of assemblages, were conducted at the same time as the biaxial tests. It took two years, beginning in February 1990, to complete the experimental test program. During this time, some of the auxiliary tests were repeated to facilitate the comparison of the results obtained at different phases of the test program. In this chapter, the results of the auxiliary tests are presented and discussed.

3.2 COMPONENT MATERIAL TESTS

Masonry is a composite material composed of several components; masonry units, mortar, grout, and steel bars. Each component has its own physical, mechanical, and geometrical characteristics, which influence the global behaviour of the masonry assemblage. Understanding, or even comparing, the behaviour of different masonry assemblages requires that the characteristics of these components are defined. Several tests were conducted in this experimental program to define both the physical and the mechanical characteristics of the component materials used. They provided part of the data required for the macro-behaviour model and for the comparison with the results obtained in other investigations. These tests were also used as control tests to monitor the

consistency of the materials.

All the component materials selected for this test program were commercially available and similar to those commonly used in North America.

3.2.1 Concrete Blocks

The same concrete blocks were used throughout the experimental program. They were manufactured at the same time and stored under the same conditions. Tests were performed on the blocks at several ages to define the block characteristics at the different phases of the test program. For panel series RP, the shape of the block had to be modified by knocking out parts of the webs to allow for placing horizontal reinforcement in the reinforced specimens.

3.2.1.1 Physical Characteristics

Autoclaved, standard 190 mm normal weight hollow concrete blocks were used throughout this test program. They had the nominal dimensions of 200x200x400 mm. The standard shape and dimensions of this type of block are shown in Fig. 3.1. Two similar half blocks were prepared by cutting these blocks along the central web. The average net cross-sectional area, specified by the manufacturer, was 41500 mm^2 which resulted in 56% solid volume.

To allow for placing the horizontal reinforcement in the reinforced panels, the blocks were modified according to the dimensions shown in Fig. 3.2. Two vertical groves of 100 mm depth and 102 mm apart were cut in the three webs using a dry cutting diamond saw. The top parts of the webs were then carefully knocked-out. In addition, the thicker ends of the face shells were trimmed to a

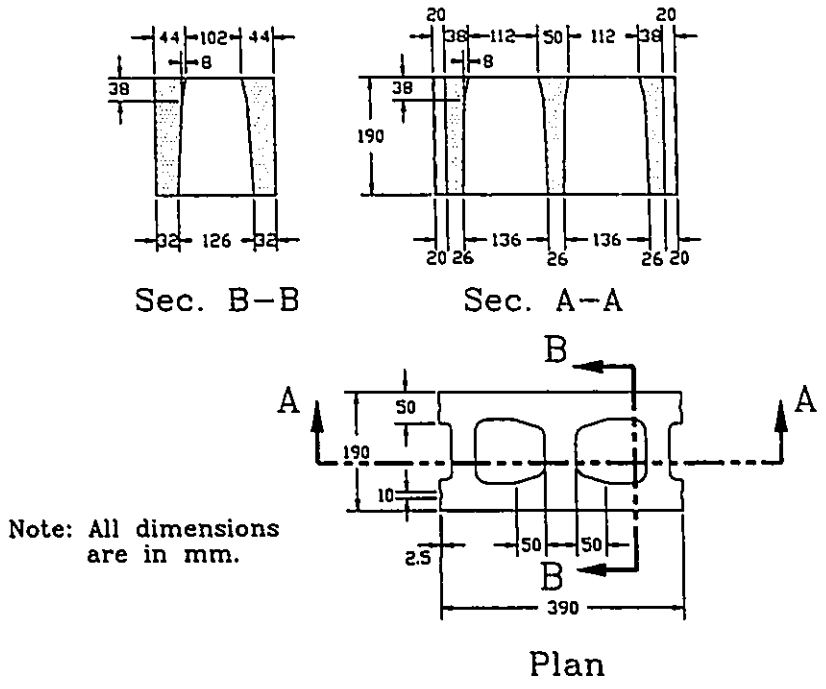

Fig. 3.1 Dimensions of the full concrete block used.

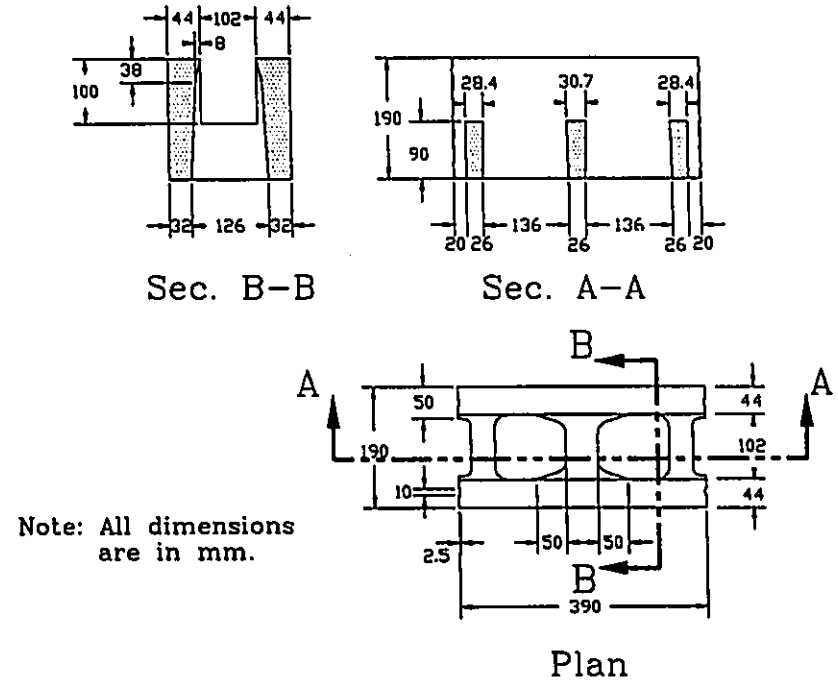

Fig. 3.2 Dimensions of a block with knocked-out webs.

thickness of 44 mm over the cut depth. Because it facilitated comparisons between the results of the unreinforced and reinforced specimens, it was preferred to prepare the blocks in this shape, rather than to use another type of block, which might have different material properties.

The initial rate of absorption (IRA) was determined by performing the ASTM C67 (1991) test on five blocks. In this test, the IRA is defined as the amount of water initially absorbed by a dry block when it is immersed in water to a depth of 3.2 mm (1/8 inch) for a period of one minute. Accordingly, the mean IRA determined for the top surfaces of the blocks was 1.52 kg/m^2/min. with a coefficient of variation of 18.6%. The average density of the dry units, based on weighting five blocks, was 2080 kg/m^3 with a coefficient of variation of 2.2%.

3.2.1.2 Mechanical Characteristics

Compressive Strength

The compressive strength of the blocks was determined for different block configurations, loading directions, and capping areas. Compression tests were performed on full blocks loaded flat wise (C1) and end wise (C2). Half blocks were tested with full capping (C3) and face shell capping (C4). Cores (C5) of 50.8 mm (2 in.) diameter and 101.6 mm (4 in.) height were also drilled out of the corners of the blocks. They were prepared and tested according to ASTM C42 (1991). The compressive strength of the blocks with knocked-out webs was determined by testing both full blocks (C6) and half blocks (C7). All of the

specimens were hard capped using Hydrostone. The results obtained in these tests are summarized in Table 3.1.

Table 3.1 Summary of the compression tests on blocks

Series	Description	Age (Day)	No. of specimens	Mean strength (f'_m) (MPa)	C.O.V (%)	Area used for calculating (f'_m) (mm)	Secant modulus of elasticity* (GPa)	Poisson's ratio+
C1	.Full blocks .Flat wise .Full capping	90	10	20.6	7.8	Average net area	-	-
		270	5	20.3	4.1			
C2	.Full blocks .End wise .Face shell capping	90	10	18.9	4.4	Minimum face shell area	24.3	0.48
C3	.Half blocks .Flat wise .Full capping	90	10	18.8	5.6	Average net area	12.8	0.32
C4	.Half blocks .Flat wise .Capping of bedded area of 32mm width	90	10	24.9	6.0	Bedded area	15.1	0.15
C5	.Cores .Full capping	100	12	18.6	5.8	Cross-section	15.3	-
C6	.Full blocks with knocked-out webs .Flat wise .Full capping	570	5	21.9	5.0	Minimum cross-section	-	-
C7	.Half blocks with knocked-out webs .Flat wise .Full capping	570	5	21.1	6.6	Minimum cross-section	29.8	-

* Determined at stress equal to half the failure stress.
+ Determined as the mean value of Poisson's ratios corresponding to compressive strains less than 1 mm/m.

The deformations parallel and normal to the loading direction were measured on the test specimens using a mechanical strain indicator. The gauge lengths were set to be 100 mm (4 in.) for series C2, C3, C4, and C7, whereas gauge lengths of 50 mm (2 in.) were used for series C5. The average stress-strain relationships obtained for the blocks used in preparing the unreinforced and reinforced specimens are shown in Figs. 3.3 and 3.4, respectively. The strain measurements were used to determine the values of secant modulus of elasticity and the Poisson's ratios which are given in Table 3.1. Photographs of the specimens after failure are shown in Figs. 3.5 to 3.8.

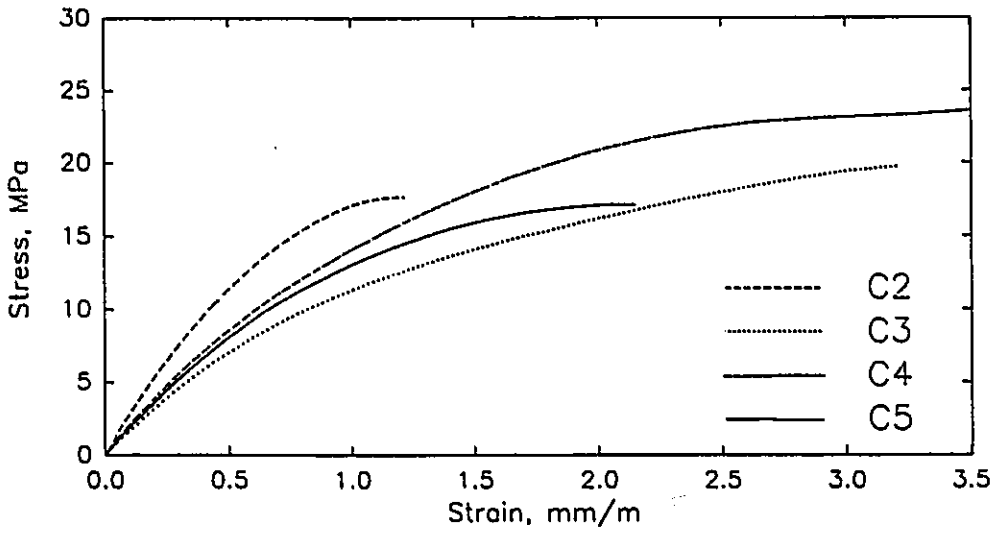

Fig. 3.3 Average stress-strain relationships for blocks tested under uniaxial compression.

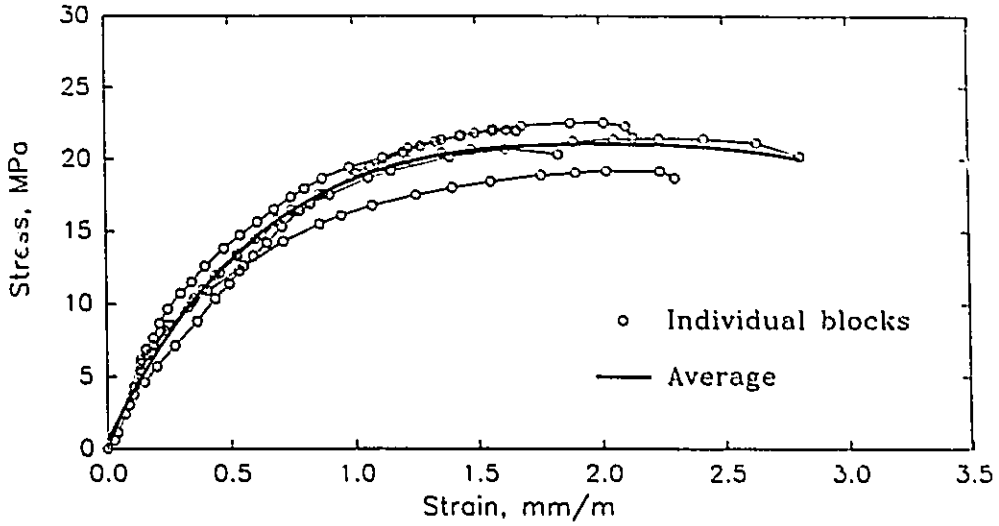

Fig. 3.4 Stress-strain relationships for blocks with knocked-out webs (series C7) tested under uniaxial compression.

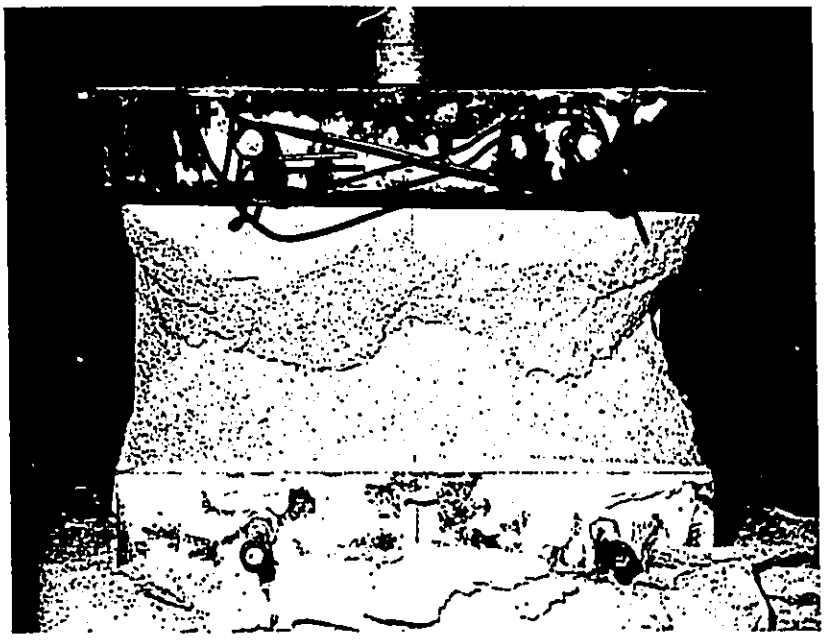

Fig. 3.5 Failure of a full block (C1) tested flat wise with full capping.

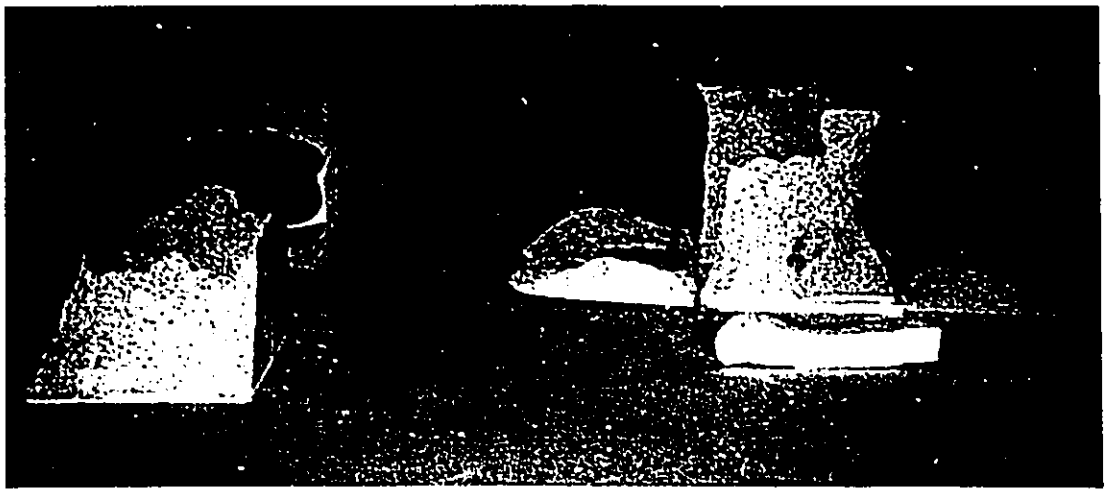

(a) Series C3
(Full capping)

(b) Series C4
(Face shell capping)

Fig. 3.6 Failures of half blocks.

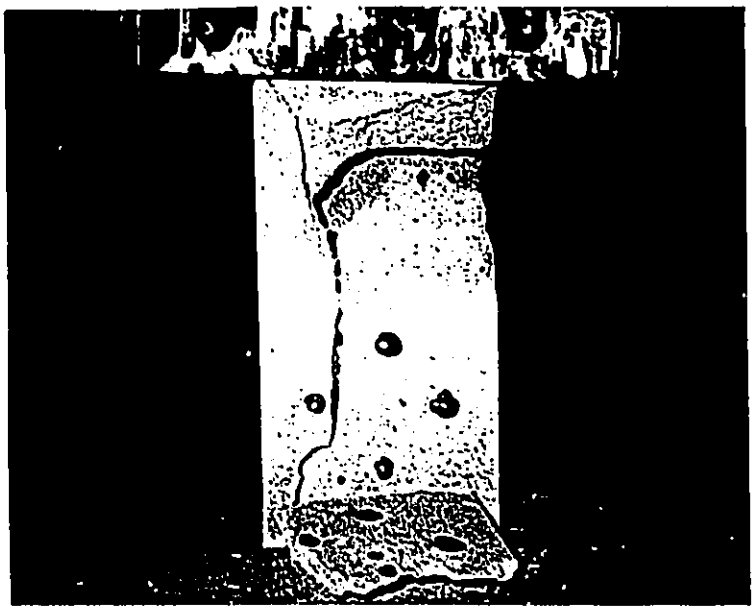

Fig. 3.7 Failure of a full block (C2) tested end wise.

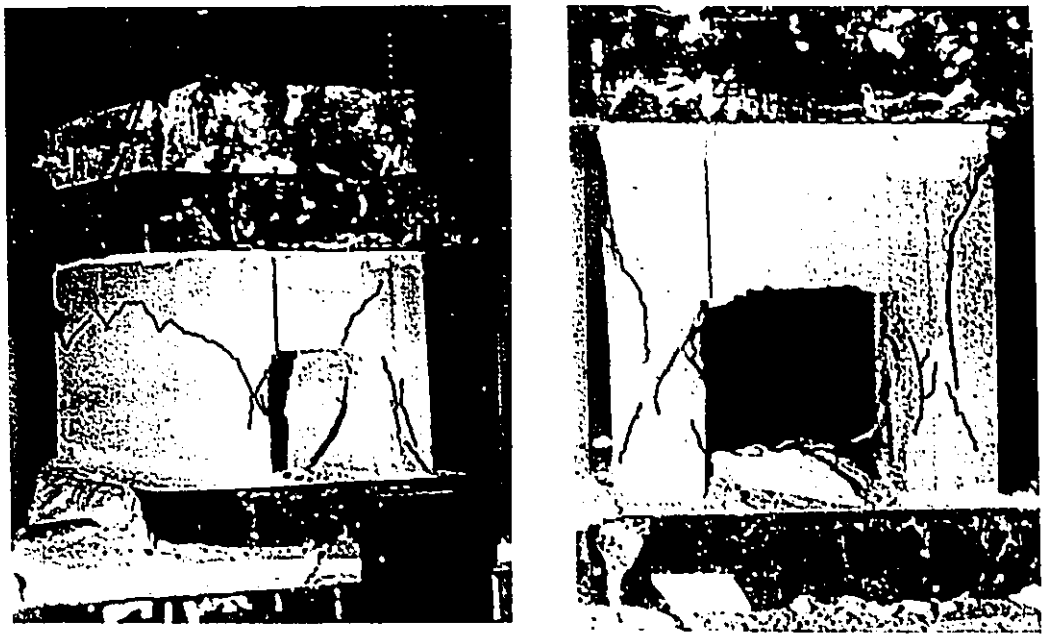

(a) Full block (C6)

(b) Half block (C4)

Fig. 3.8 Failures of blocks with knocked-out webs.

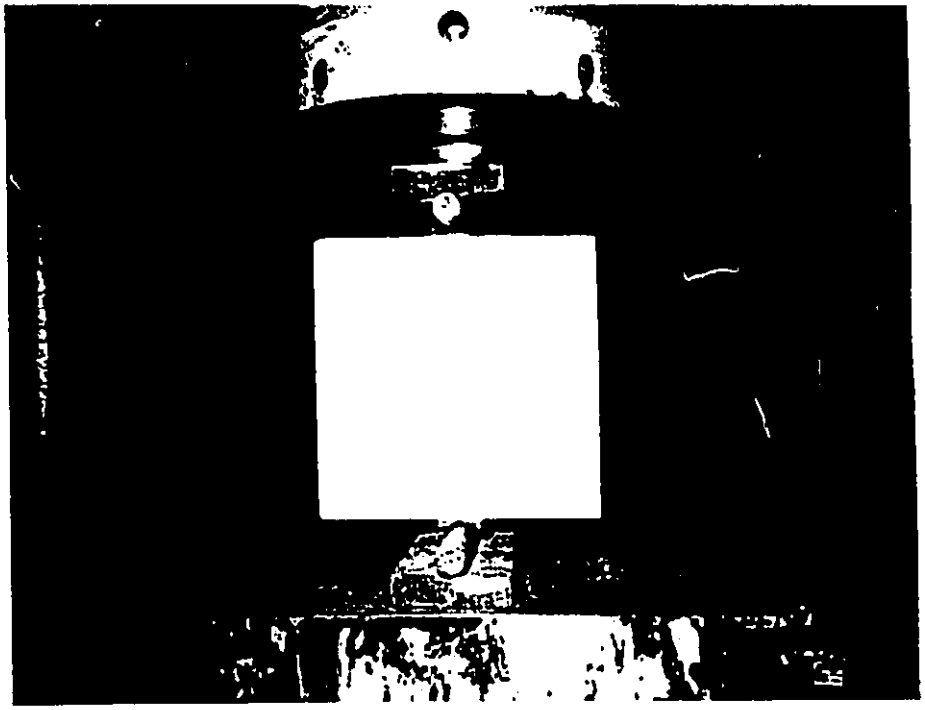

Fig. 3.9 Splitting test on block face shells.

Tensile Strength

Splitting tension tests were performed on both face shells (T1) and webs (T2). Two opposite compressive line loads were applied through 15 mm diameter bars as shown in Fig. 3.9. Strips of plywood were used between the bars and the block to minimize the stress concentration along the loading line. The mode of failure was splitting along the loaded plane. The tensile strength of the block, f_{tb}, was calculated using the following relationship adopted by Self (1975) and Hamid (1978).

$$f_{tb} = \frac{2P}{\pi A_n} \qquad \ldots(3.1)$$

where P is the splitting failure load and A_n is the sectional area along the splitting plane.

The flexural tensile strength of the block face shells was determined by in-plane bending tests on specimens (T3). Each specimen was made of two blocks glued end-to-end by the means of an epoxy resin (SIKADUR 31). The specimen was simply supported and tested under the effect of two point loads as shown in Fig. 3.10.

The results obtained in the different tests are summarized in Table 3.2.

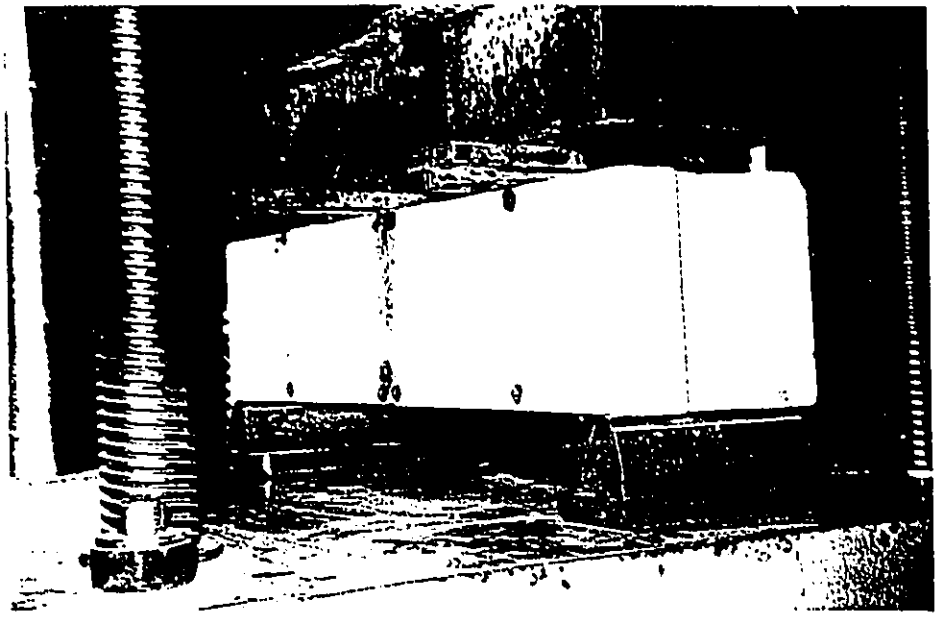

Fig. 3.10 Flexural test on block face shells.

Table 3.2 Summary of the tension tests on the blocks

Series	Description	Age (Days)	No. of specimens	Mean Strength f_{tb} (MPa)	C.O.V. (%)	Area used for calculating f_{tb} (mm)
T1	.Splitting of face shell	90	10	1.86	6.1	Minimum area along the splitting plane
		235	5	1.89	11.3	
		570	5	2.22	8.4	
T2	.Splitting of webs	90	10	1.73	5.2	Minimum area along the splitting plane
		235	5	1.67	7.3	
		570	5	2.01	9.4	
T3	.Flexural test on face shells	100	10	2.87	9.6	Minimum cross-section of face shells

Observations

Based on the results of the block tests, the following observations are noted:

1. The block specimens (C1 to C5) tested under uniaxial compression exhibited different modes of failure depending on the geometry of the specimen, the loading pattern, and the capping area. Both the full and half blocks (C1 and C3), tested with full capping, exhibited conical modes of failure as shown in Fig. 3.6 due to the friction between the specimen and the loading plates. In this case, the failure did not occur at the minimum cross-section area, but rather at the mid-height of the block. Therefore, the failure stresses of these specimens were calculated using the average net areas as recommended in ASTM C140 (1991). In the case of the half blocks (C4) tested with face shell capping, similar conical modes of failure took place in the face shells leaving the webs almost intact as shown in Fig. 3.6(b). Splitting cracks were also observed between the face shells and the webs as a result of the stress transfer from the face shells to the webs. The mode of failure was different in the full blocks loaded end-wise (C2). Splitting cracks occurred in the webs along with inclined shear cracks in the face shells as shown in Fig. 3.7. The cores (C5) failed by the typical vertical splitting cracks indicating no effect of the friction with the loading plates.

2. Both the full and half blocks with knocked-out webs (C6 and C7) exhibited the same mode of compression failure. Most of the cracks were observed in the two face shells along the section of minimum area as shown in Figs. 3.8(a) and (b). The failure, in this case, took place in the form of a conical

mode of failure in each face shell.

3. The stress-strain relationships as well as the failure stresses were also influenced by the test methods. An increase of 10% in the failure stress was observed in the test results of the full block loaded flat wise (C1), in comparison with the test results of the cores (C5). The failure stresses obtained from the half blocks with full capping loaded flat wise and the full blocks loaded end-wise were in agreement with the results obtained from the tests on cores (C5). This observation supports the conclusion drawn by Hamid (1978), Essawy (1986), and Guo (1991) that testing half blocks flat wise with full capping or testing full blocks end-wise can be used to represent the strength of the block material. On the other hand, the failure stresses obtained from the half and full block with knocked-out webs were almost the same. This could be attributed to the fact that the compressive stresses applied in these tests were mainly resisted by the face shells, regardless of the length of the specimen.

4. The webs had slightly lower splitting tensile strength compared to the face shells. This could be attributed to less compaction in the web zones or the existence of small cracks near the top of the webs. This observation is in agreement with the conclusion drawn by Essawy (1986).

5. The fact that the flexural tensile strength was larger than the values obtained in the splitting tests of the face shells or webs could be attributed to the stress gradient in the flexural tests.

6. No significant change was observed in the compressive or the splitting tensile strengths obtained at the block ages of 90, 235, and 270 days. During this

period, the panels of series UNP were prepared and tested. An increase in the order of 15 to 20% was found in the splitting tensile strength at the age of 570 days, compared to the test results at the age of 90 days. The panels of series RP were constructed and tested in the period between the block ages of 400 and 700 days. As a result, it is more appropriate to define the mechanical characteristics of the blocks used in each series from the tests conducted in the same period.

3.2.2 Mortar

Code designated type S mortar was used in the fabrication of all specimens tested in this experimental program. It was prepared using type 10 portland cement, type N hydrated finishing lime and masonry sand. The gradations of the available masonry sand along with the limits of CSA A82.56M-1976 are given in Table 3.3. The results of the sieve analyses lay between the limits except at the sieve of 0.6 mm size openings, which had 2% over the upper limit. This difference was thought not to be sufficiently significant to reject the available masonry sand.

Table 3.3 Sieve analysis of masonry sand for mortar.

Sieve size (mm)	Percentage passing			
	Masonry sand for group		CSA A82.56M-1976	
	1 and 2	3	Minimum	Maximum
5	99.97	100	100	100
2.5	99.60	99.70	95	100
1.25	98.00	97.49	60	100
0.6	82.00	82.30	35	80
0.3	36.44	49.56	15	50
0.149	7.77	14.34	2	15

The above materials were mixed in the proportions of 1.0:0.5:4.0 parts by volume (or 1.0:0.21:4.39 parts by weight) of portland cement, lime, and dry sand, conforming to CSA A179M-1976. A water-cement ratio of 0.95 was established to satisfy the mason's requirements for workability. The mortar was prepared in batches of 50 kg, which was small enough to be well mixed by hand in a wheelbarrow and not to last longer than 40 minutes. Any mortar left after this period was discarded rather than allowing retempering. The fabrication of all of the specimens required 115 batches of mortar.

The mortar's initial flow was measured for each batch using the flow table according to ASTM C109 (1991). The mean initial flow measured for the different batches was 128% with a C.O.V. of 1.64%.

Three 50.8 mm (2 inch) mortar cubes were prepared as control specimens for each batch. They were air cured in the laboratory under the same conditions as the assemblage specimens. The mortar cubes associated with each panel, prism, or shear couplet were tested on the same day or the day following the assemblage test. The specimens were fabricated in three groups. The first group included the unreinforced panels tested under uniaxial compression, the prisms of series UCU, and the shear couplets. The second group included the rest of the unreinforced panels, which were tested under uniaxial tension and biaxial tension-compression, and the prisms of series UTU. All the reinforced panels of series RP and the prisms of series UCR and UTR were constructed in the third group. The mean compressive strengths of the mortar used in each group are summarised in Table 3.4. The mean strength of the mortar used in the first group was

significantly lower than the values obtained in the other two groups. This could be attributed to the unfortunate use of cement, that had been stored for some time, in fabricating the specimens of the first group. The mortar compressive strengths for the different panels, prisms and shear couplets are given later in the corresponding sections.

Table 3.4 Compressive strength of mortar cubes.

Group	Compressive strength	
	Mean (MPa)	C.O.V. (%)
1	8.2	26.4
2	19.3	15.9
3	16.8	20.3

3.2.3 Grout

Code designated "Coarse Grout" was chosen for this experimental program. It represents the normal practice. The grout was prepared using type 10 portland cement, concrete sand and 10 mm (3/8 inch) pea gravel. The gradations of the concrete sand and pea gravel are given in Tables 3.5 and 3.6, respectively. Both aggregates met the specifications of ASTM C404 (1991). The above materials were mixed dry in the proportions of 1.0:3.0:2.0 parts by volume (or 1.0:3.69:2.25 parts by weight) of portland cement, concrete sand, and pea gravel, conforming to CSA A179M-1976. The water-cement ratio of 0.8 was selected to achieve an average slump of 250 mm (10 in.).

The control specimens of the first two groups, which included the panels of series UNP, were prepared in two different manners. Absorbent prisms, in the dimensions of 75x75x150 mm, are moulded as four blocks according to CSA A179M-1976. These prisms are referred to as "block moulded" prisms. In addition, grout was poured to fill the block cells which were then sawn to provide absorbent prisms in the above dimensions. The prisms prepared in the latter manner were referred to by "cell moulded" prisms which was suggested by Guo (1991) to provide more representative specimens. The main merit of the cell moulded prisms, over the block moulded prisms, is that the volume to surface area ratio, and consequently the water-cement ratio of the prism, after absorption of water by the block, is identical to grout in masonry walls. Also, the preparation of cell moulded prisms requires less space during the fabrication of the walls. However, the cell moulded prism has the drawback of the need to saw

Table 3.5 Sieve analysis of concrete sand for grout.

Sieve size (mm)	Percentage passing			
	Masonry sand for group		ASTM C404	
	1 and 2	3	Minimum	Maximum
12.5	100	100	100	100
9.5	100	100	100	100
4.75	99.50	99.75	95	100
2.36	85.34	85.83	80	100
1.18	67.62	66.29	50	85
0.6	42.17	41.83	25	60
0.3	22.04	20.29	10	30
0.149	10.16	9.31	2	10
0.053	1.43	0		

Table 3.6 Sieve analysis of pea gravel for grout.

Sieve size (mm)	Percentage passing		
	Coarse aggregate for all groups	ASTM C404	
		Minimum	Maximum
12.5	100	100	100
9.5	99.29	85	100
4.75	33.56	10	55
2.36	3.92	0	30
1.18	1.81	0	10
0.6	0.85	0	5
0.3	0.2	0	0

the prisms out of the grouted blocks. Both block moulded and cell moulded prisms were prepared with the first and second groups of specimens, whereas only cell moulded prisms were prepared with the third group of specimens.

Grout batches of 300 kg were mixed in a mechanical mixer. Six block moulded prisms and/or six cell moulded prisms were prepared from each batch of grout. All of the grout prisms were air-cured and tested at the same time with the corresponding specimens. Half of the prisms were hard capped by Hydrostone and tested under uniaxial compression. The vertical deformations at the mid-height of the prisms were measured using a mechanical strain indicator over gauges lengths of 50 mm (2 in.). A typical stress-strain relationship is shown in Fig. 3.11. The second half of the prisms were used for splitting tension tests and the failure stresses were calculated according to Eq. 3.1. A summary of the mechanical properties of the grout used with the different groups is given in Table 3.7. No significant difference can be noticed between the mean compressive strengths obtained from the block moulded prisms and the cell moulded prisms.

Details of the grout strengths for each panel or assemblage specimen are provided later in the corresponding sections.

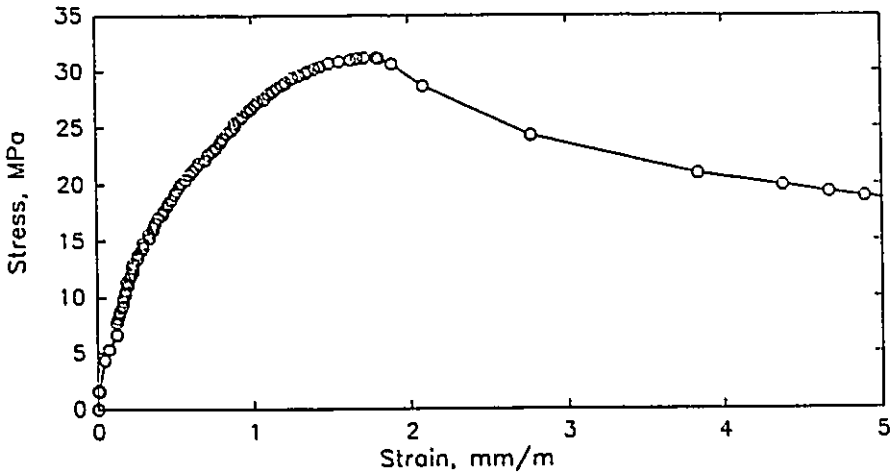

Fig. 3.11 Typical stress-strain relationship for a grout prism.

Table 3.7 Mechanical properties of grout

Group	Compressive strength				Splitting tensile strength			
	Block moulded		Cell moulded		Block moulded		Cell moulded	
	Mean (MPa)	C.O.V. (%)	Mean (MPa)	C.O.V. (%)	Mean (MPa)	C.O.V. (%)	Mean (MPa)	C.O.V. (%)
1	28.6	11.1	29.5	13.0	3.3	17.3	-	-
2	31.3	13.8	32.0	17.2	-	-	4.3	10.7
3	-	-	31.9	10.9	-	-	4.3	17.4

3.2.4 Reinforcement

Keeping the spacing of reinforcement constant at 200 mm in all of the reinforced panels, bars of 6, 10, 15, and 20 mm nominal diameters were used to achieve the percentages of reinforcement of 0.17, 0.26, 0.53, and 0.79%, respectively. Three 500 mm long coupons were cut randomly for each of the bar sizes. They were tested under uniaxial tension in a 600 kN capacity Tinius Olson machine. The longitudinal deformations were measured over a gauge length of 50 mm by means of a clip-on gauge. The average stress-strain relationships obtained for the different bar diameters are shown in Fig. 3.12. The values of the yield stresses and the failure stresses determined for these bars are also summarized in Table 3.8. In contrast to the other bars, the 6 mm diameter bars did not exhibit a yield plateau and, therefore, the stress corresponding to 0.2% inelastic strain was used as the yield stress.

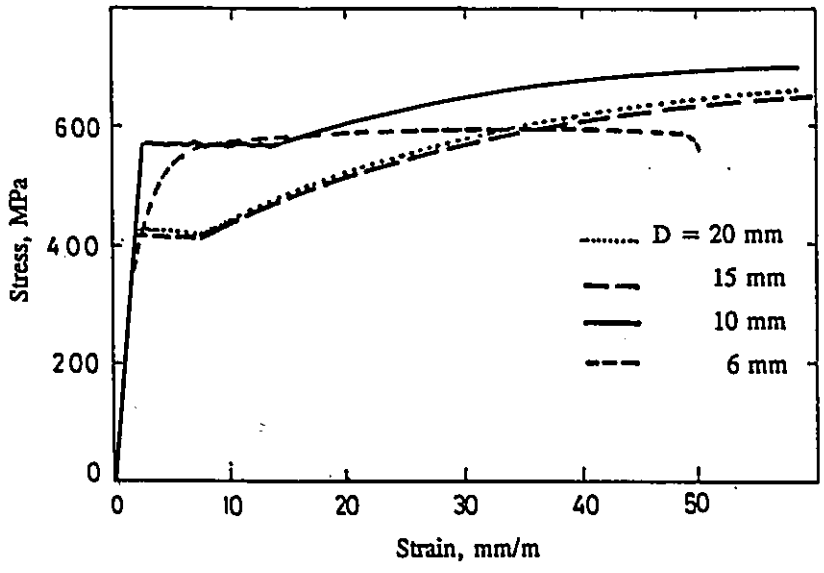

Fig. 3.12 Stress-strain relationships for reinforcement.

Table 3.8 Mechanical properties of reinforcement

Bar diameter (mm)	Yield stress (MPa)	Failure stress (MPa)
20	419.6	694.8
15	415.0	672.1
10	568.3	733.3
6	531.0*	580.2

*Stress corresponding to 0.2% inelastic strain.

3.3 ASSEMBLAGE TESTS

The tests of auxiliary assemblages were conducted according to the procedures discussed in Chapter 2. The results obtained in these tests are presented and discussed in the following sections. The auxiliary assemblage specimens included four series of prisms; two of them were tested under uniaxial compression,whereas the other two were tested under uniaxial tension. The prisms of each series were prepared with five different bed joint orientations θ. In addition, three series of couplet specimens were tested under direct shear.

3.3.1 Uniaxial Compression Tests

As stated before, two series of fifteen prisms were tested under uniaxial compression. The first series (UCU) was constructed with the unreinforced panels, having grout cores normal to bed joints. The second series (UCR) was constructed with the reinforced panels using blocks with knocked-out webs which resulted in continuous grout cores normal and parallel to bed joints. In addition

to the fifteen prisms, series UCR included three more prisms constructed using normal blocks (without knocked-out webs) for testing with compression normal to bed joints (θ=0°). These three prisms were meant to investigate the effect of having the webs of the blocks knocked-out and to relate the test results of series UCU and UCR, which were constructed and tested at different times. The test results obtained in series UCU and UCR are presented in the following sub-sections in terms of modes of failure, strength characteristics, and deformation characteristics.

3.3.1.1 Modes of Failure

The prisms exhibited different modes of failure depending on the bed joint orientation θ. The modes of failure observed in the two series of prisms are shown in Figs. 3.13 to 3.17.

At θ=0° (compression normal to bed joint), the failures of the prisms of series UCU and UCR were similarly initiated by vertical splitting cracks in the webs of the two middle blocks. As the applied load was increased, additional splitting cracks were observed in the face shells. This kind of cracking has been attributed to the lateral expansion of grout and mortar as they approached their strengths as well as wedging action due to the tapered and flared shapes of the grout in blocks. As shown in Fig. 3.13, some of the cracks in the face shells tended to propagate diagonally. This behaviour could be attributed to the fact that the grout cores normal to bed joints are not strictly aligned in the running bond

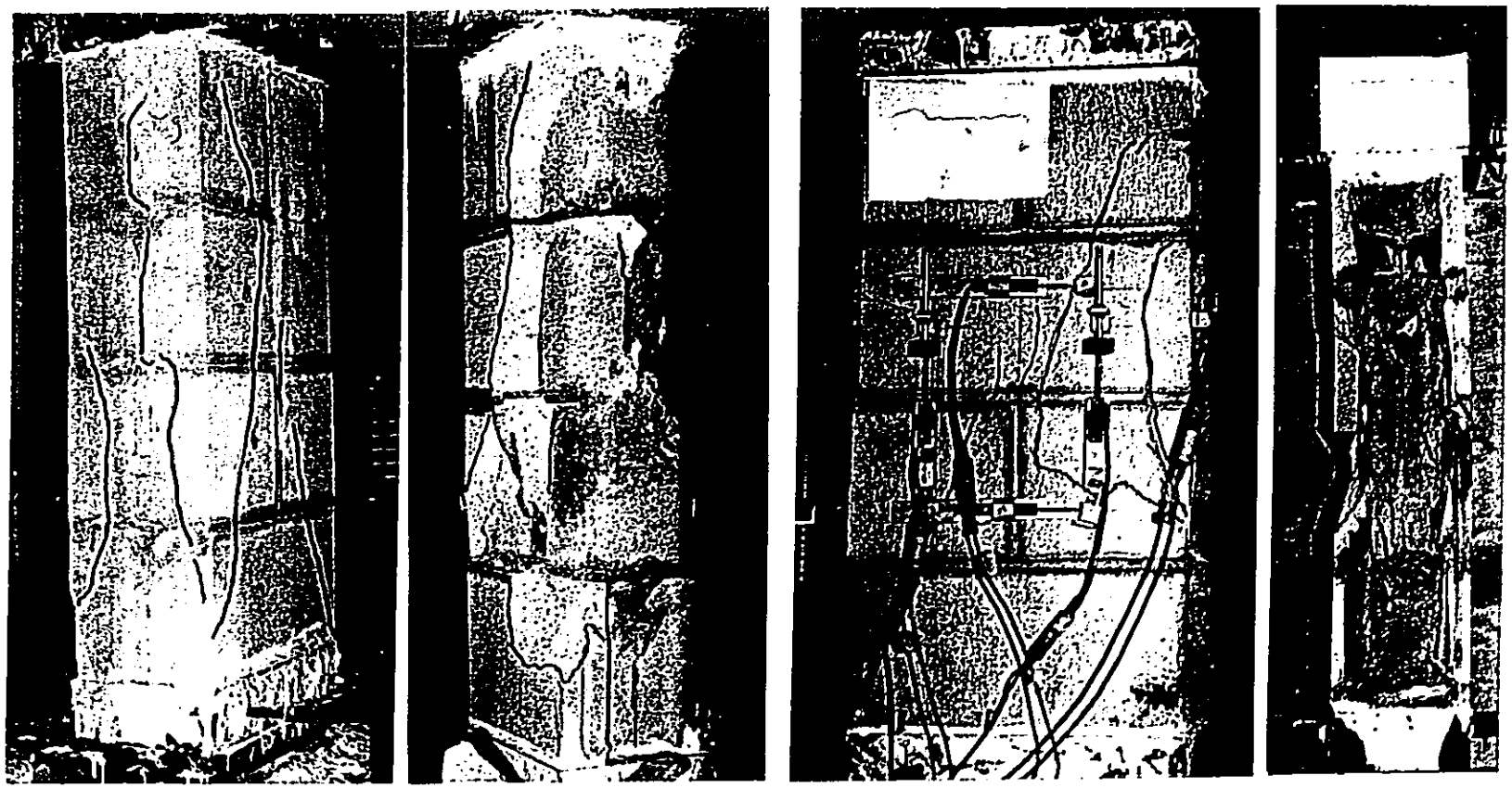

(a) Series UCU

(b) Series UCR

Fig. 3.13 Typical failures of prisms with θ=0° under uniaxial compression

construction pattern. Also, near the top and bottom, the friction with the loading plates restricts the vertical crack growth. Eventually, the load began to drop and parts of the block face shells spalled. Splitting cracks were also noticed in the grout cores as indicated in Fig. 3.13(a).

The failures of the prisms with θ=90° (compression parallel to bed joint) occurred suddenly. As shown in Fig. 3.14, splitting cracks occurred along the block-grout interfaces and through the webs, which represented the minimum resisting sections under the effect of the lateral tensile stresses due to the lateral expansion of grout and mortar. The splitting cracks isolated the face shells and allowed them to deform independently with high slenderness ratios. Cracks were also observed along the bed joints as shown in Fig. 3.14. This is the weakest plane for vertical cracking through the face shell planes. Finally, entire face shells spalled and the remaining parts of the prisms of series UCU became unstable mechanisms as shown in Fig. 3.14(a). In the prisms of series UCR, spalling of the face shells was accompanied by a shear failure in the grout cores as shown in Fig. 3.14(b).

Different modes of failure were observed in the prisms tested with θ=22.5°. With this angle, the head joint planes were subjected to a high shear-to-normal stress ratio. As a result, shear failures along the head joint planes were observed in the prisms of series UCU, as shown in Fig. 3.15(a). The planes of failure followed the head joints and passed through the block face shells thus

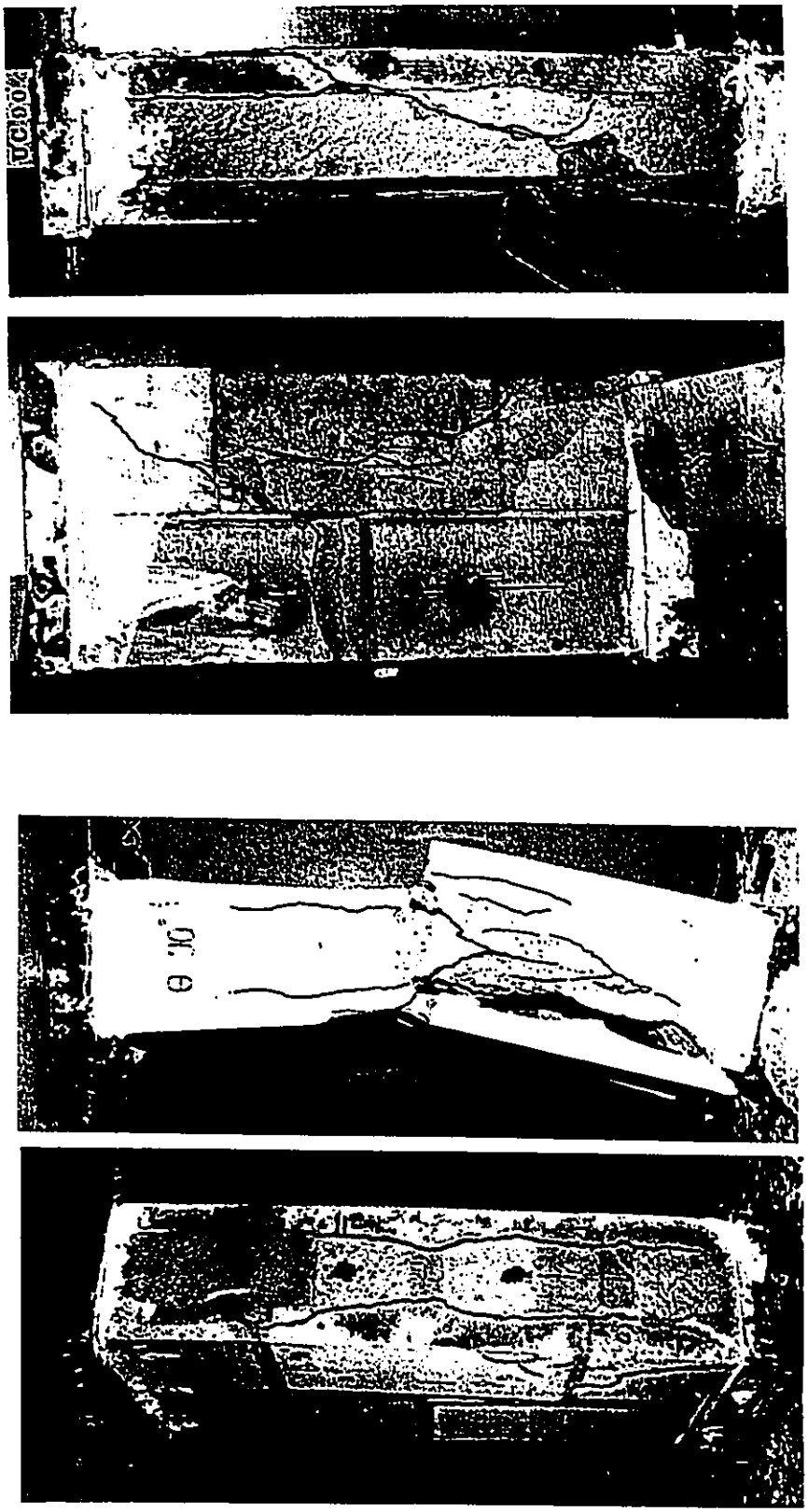

(a) Series UCU

(b) Series UCR

Fig. 3.14 Typical failures of prisms with θ=90° under uniaxial compression

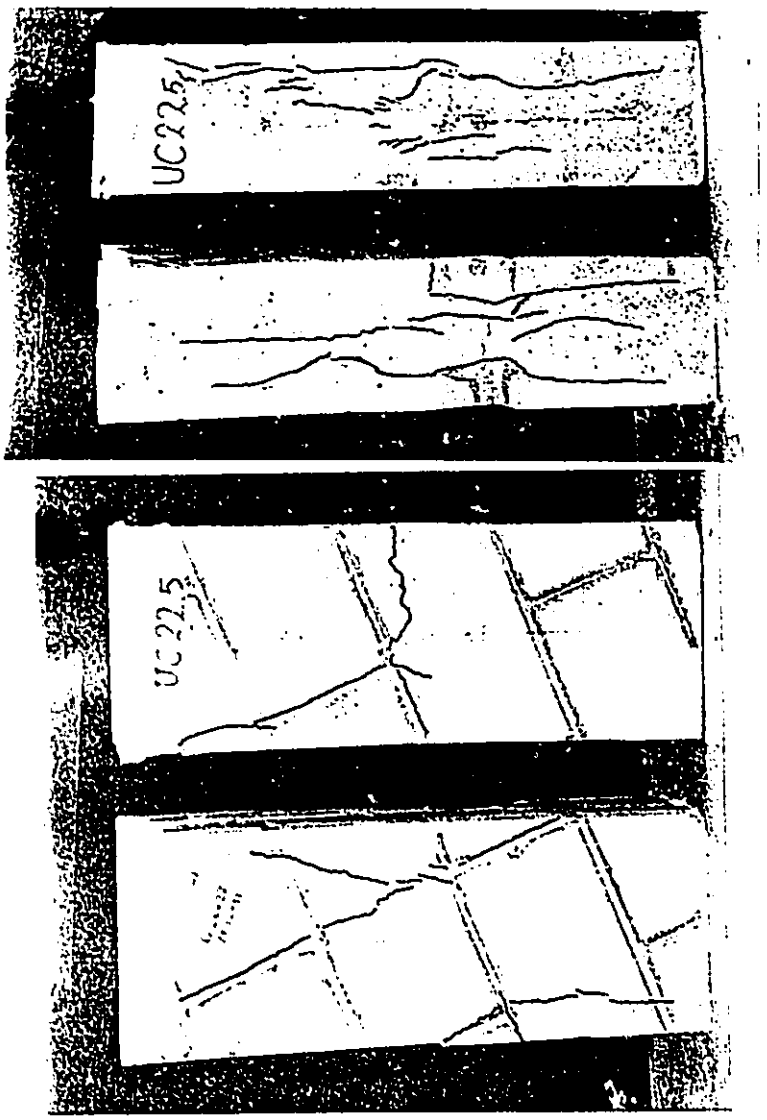

(a) Series UCU

(b) Series UCR

Fig. 3.15 Typical failures of prisms with θ=22.5° under uniaxial compression

avoiding the grout cores. Very few splitting cracks were found on the prisms' sides. In the prisms of series UCR, the grout cores parallel to the bed joints helped stop the propagation of the shear cracks through the block face shells. Instead, vertical splitting cracks, similar to those which occurred with $\theta=0°$, were observed on the prisms' sides as shown in Fig. 3.15(b).

At $\theta=67.5°$, the head joint planes were subjected to compressive normal stress high enough to prevent their failure in shear. On the other hand, the bed joints were subjected to a high shear-to-normal stress ratio. As a result, the prisms of series UCU and UCR exhibited shear failures along the bed joints as shown in Figs. 3.16(a) and (b), respectively. At $\theta=67.5°$, the grout cores parallel to bed joints did not have a significant effect on the mode of failure of the prisms of series UCR, which could be explained by the fact that the planes of failure did not cross these grout cores. The failure planes did cross the grout cores normal to the bed joints.

At $\theta=45°$, equal shear and normal stresses acted along the bed and head joint planes. As a result, the failure of the UCU prisms was a mixed mode of shearing along bed joints, shearing along head joints and splitting in the block face shells and grout, as shown in Fig. 3.17(a). In the prisms of series UCR, as shown in Fig. 3.17(b), most of the cracks were splitting cracks rather than following the mortar joints.

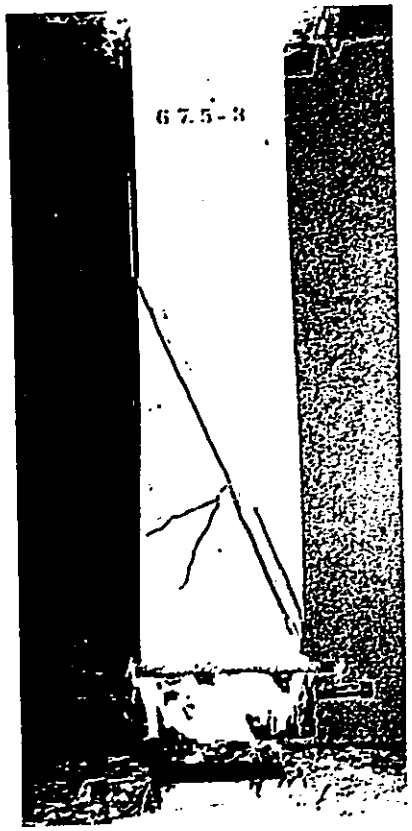

(a) Series UCU

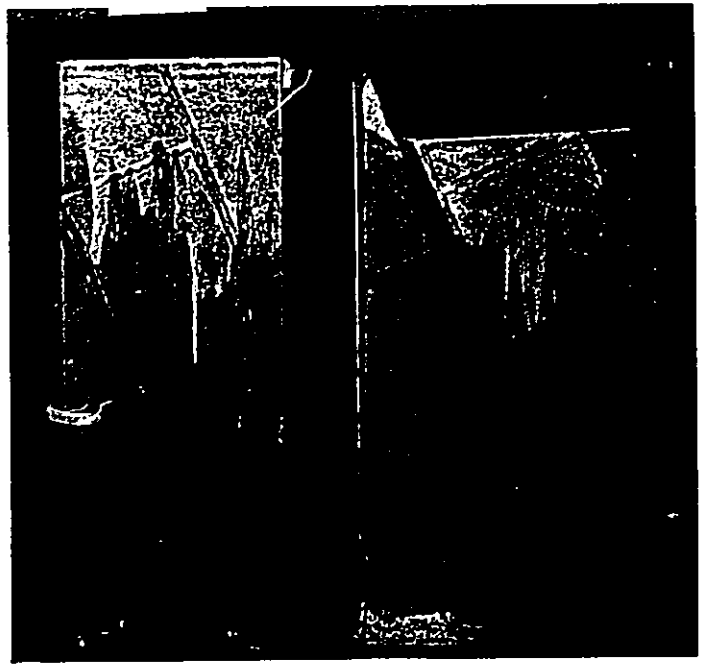

(b) Series UCR

Fig. 3.16 Typical failures of prisms with θ=67.5° under uniaxial compression

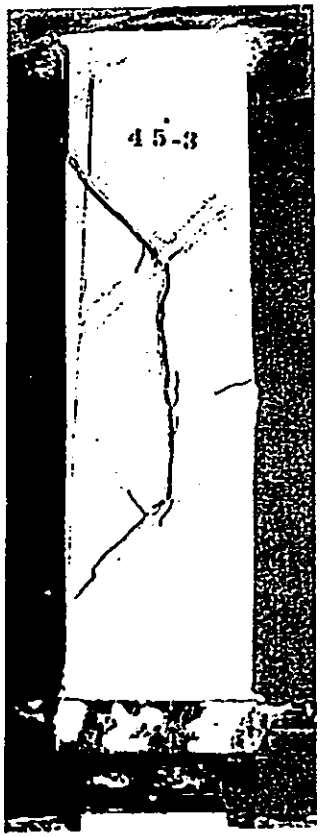

(a) Series UCU

(b) Series UCR

Fig. 3.17 Typical failures of prisms with θ=45° under uniaxial compression

3.3.1.2 Strength Characteristics

The test results of series UCU and UCR, along with their control specimens, are summarized in Tables 3.9 and 3.10, respectively. The variations of the compressive strength with the bed joint orientation θ are also shown in Fig. 3.18. The dependence of the compressive strength on the bed joint orientation is very obvious in the results of the two series.

The mean compressive strength of the three prisms constructed in series UCR with $\theta=0°$, using blocks without knocked-out webs, was 16.1 MPa with a coefficient of variation (C.O.V.) of 14.0%. On the other hand, the mean compressive strength of the similar prisms, constructed at the same time using blocks with knocked-out webs, was 17.0 MPa with a C.O.V. of 10.5%. These values imply that the grout cores parallel to bed joints resulted in an increase of only 5.6% of the compressive strength at $\theta=0°$. Larger differences can be observed between the compressive strengths of the corresponding prisms in series UCU and UCR. These differences could be attributed to the different constituent materials used in preparing the mortar and the grout used in each series. However, in the light of the small effect of the grout cores parallel to bed joint on the compressive strength at $\theta=0°$, the comparison can still be made between the test results of series UCU and UCR using the strengths obtained at $\theta=0°$ as the reference points. The straight lines drawn in Figs. 3.18(a) and (b) represent the compressive strengths at $\theta=0°$.

Table 3.9 Prism test results for series UCU

θ (Degrees)	Mortar strength (MPa)	Grout strength (MPa)		Prism strength		
		Block moulded	Cell moulded	Individual (MPa)	Mean (MPa)	C.O.V (%)
0	9.75	30.3	26.1	11.3 10.8 11.3	11.1	2.9
22.5	7.90	29.6	31.9	6.5 7.0 6.1	6.5	6.5
45	8.34	29.2	26.1	6.8 8.7 8.0	7.8	12.6
67.5	7.36	28.4	28.8	6.2 7.1 5.7	6.3	11.4
90	9.75	30.3	26.1	16.3 15.2 15.0	15.5	4.5

Table 3.10 Prism test results for series UCR

θ (Degrees)	Mortar strength (MPa)	Grout strength (Cell moulded) (MPa)	Prism strength		
			Individual (MPa)	Mean (MPa)	C.O.V. (%)
0	14.9	30.8	16.5 19.0 15.5	17.0	10.5
22.5	17.4	37.3	14.3 13.2 14.4	14.0	3.7
45	21.1	33.2	16.7 17.9 17.3	17.3	2.9
67.5	22.3	32.2	12.5 14.8 16.2	14.5	10.4
90	15.7	33.3	18.6 18.2 19.4	18.8	2.6

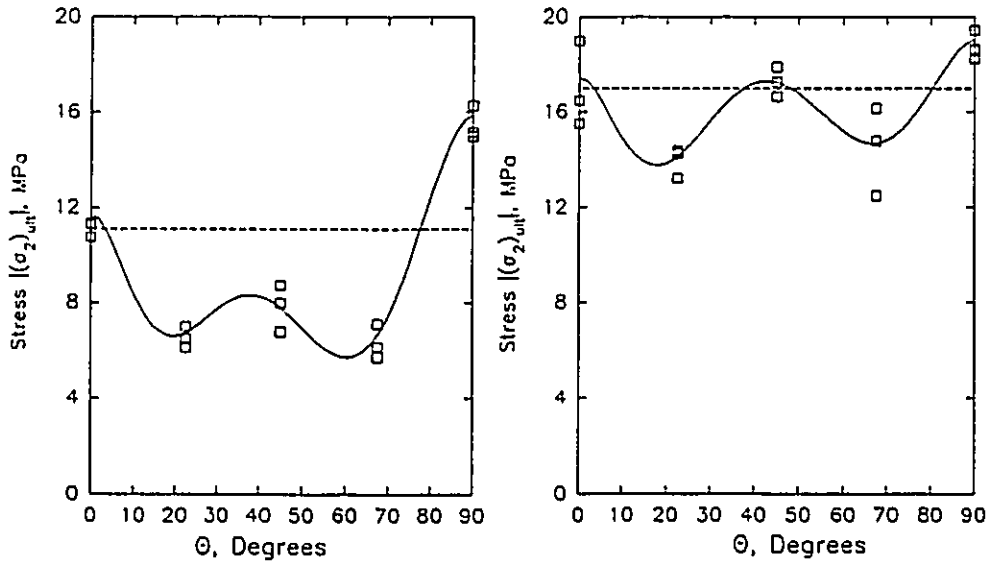

Fig. 3.18 Variations of uniaxial compressive strengths with θ.

As shown in Table 3.9 and Fig. 3.18(a), the prisms of series UCU suffered a 41.4% reduction in the compressive strength at θ=22.5°, compared to the compressive strength at θ=0°, due to the shear failure along the head joint plane. This reduction was 2.35 times the corresponding reduction in series UCR as shown in Table 3.10 and Fig. 3.18(b). This difference could be attributed to the effect of the grout cores parallel to bed joints in changing the mode of failure from a shear failure to a compression failure as described in the previous section. At θ=45°, the reduction in the compressive strength of series UCU was in the order of 29.7%, whereas no reduction was found in series UCR. Again, this could be also attributed to having continuous grout cores normal and parallel to the bed joints. While the prisms of series UCU and UCR with θ=67.5° failed

similarly in shear along the bed joints, the reductions in their compressive strengths, compared to the values obtained at $\theta=0°$, were respectively 43.2% and 14.7%. The difference in this case can be related to the grouted areas along the bed joint planes. Using blocks with knocked-out webs resulted in an increase in the percentage of the minimum grouted area along the bed joints from 22.6% in series UCU to 35.2% in series UCR.

The prisms of series UCU with $\theta=90°$ exhibited significantly higher failure stresses compared to the other prisms in the same series. This difference can be explained by considering the configurations of the different prisms shown in Fig. 2.20. The prisms prepared with $\theta=90°$ were two course high, for which it was easy to fill the frogged ends in the head joints with grout. On the other hand, examinations of the prisms prepared with $\theta=0$, 22.5, 45, and 67.5° revealed that the coarse grout did not fill these locations in the case of series UCU, even though a poker vibrator was used for compaction. Conversely, no voids were found in the head joints of the prisms of series UCR where blocks with knocked-out webs were used.

The failure stresses of the two series are also presented in Fig. 3.19 in terms of τ_{pn} (shear stress along mortar joints) and σ_n (normal stress acting normal to bed joints). Similar graphs were used by Hamid (1978) and Guo (1991) to represent their results. This figure was considered here only for comment. The experimental results included in the figure, for each series, were obtained at different ratios of σ_p/σ_n (the ratio between normal stress acting parallel to bed

joints and normal stress acting normal to bed joints). Because of the anisotropic characteristics of masonry due to the existence of the mortar joints, a complete failure surface of a masonry assemblage has to be expressed in terms of σ_1, σ_2, and θ or σ_p, σ_n, and τ_{pn} Dhanasekar et al. (1985) and Ganz and Thurlimann (1985). Drawing a single curve through the results of each series could leave the wrong impression that failure of masonry is a function of only τ_{pn} and σ_n. In fact, changing the ratio σ_p/σ_n could lead to totally different failure stresses. The results shown in Fig. 3.19, therefore, are only cross-sections in the failure surfaces, and their use is limited to those cases when the masonry assemblage is subjected to uniaxial compression.

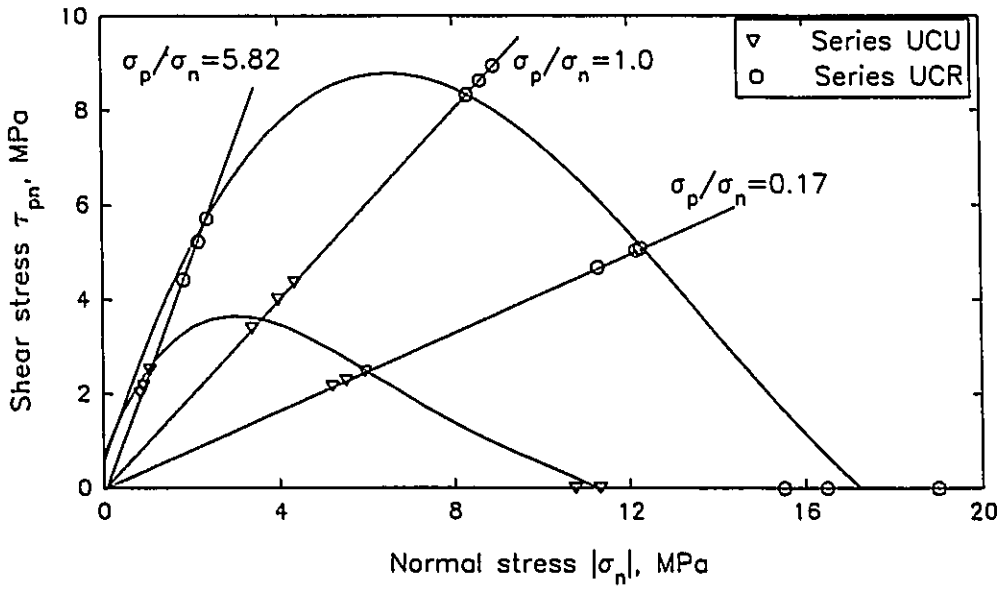

Fig. 3.19 Variations of shear strengths with normal stress σ_n for series UCU and UCR.

3.3.1.3 Deformation Characteristics

The deformations of the prisms tested with θ=22.5°, 45°, and 67.5° were measured on the prism face shells in three directions forming a 60° strain rosette, as shown in Fig. 2.21. The readings were reduced to the average strains ϵ_{30}, ϵ_{90}, and ϵ_{150} corresponding to the directions of 30°, 90°, and 150° from the horizontal direction (x-axis). These strains were then used to draw Mohr's circles for the average stains, as illustrated in Fig. 3.20, at the different loading stages. From these circles, the following parameters could be determined.

1. Principal tensile strain ϵ_1.
2. Principal compressive strain ϵ_2.
3. The angle β between the directions of principal strains and principal stresses.
4. Strains ϵ_p and ϵ_n acting, respectively, parallel and normal to bed joints.
5. Shear strain γ_{pn} acting along mortar joints.

The applied load was also used to determine the principal compressive stress σ_2 (in the vertical direction). The principal tensile stress, in these tests, was equal to zero. Drawing Mohr's circles for stress at the different loading stages yielded the normal and shear stresses (σ_p, σ_n, and τ_{pn}) acting along the mortar joint planes. Having defined these stresses together with the corresponding strains, the average stress-average strain relationships could be determined.

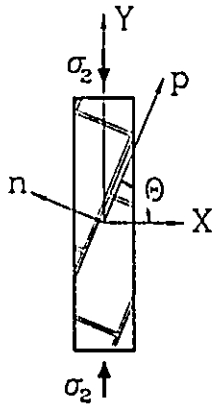

(a) A prism of series UCU with Θ=67.5°.

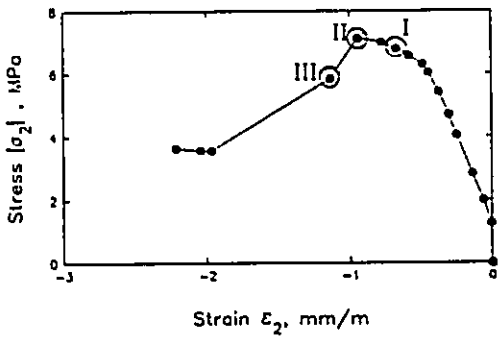

(b) $\varepsilon_2 - \sigma_2$

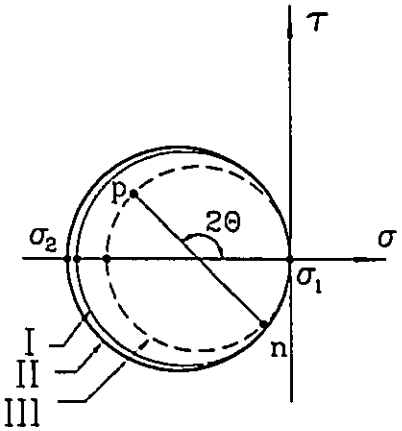

(c) Mohr's circles of stress.

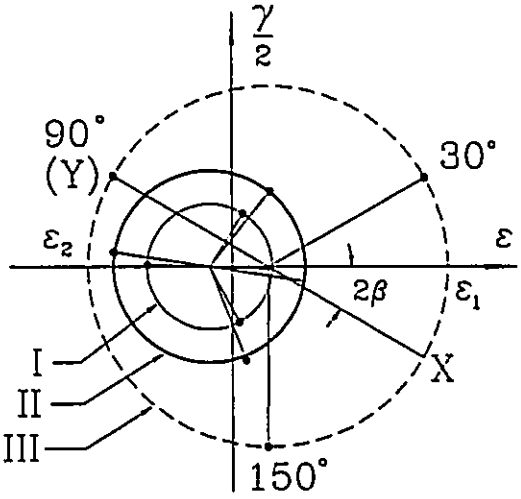

(d) Mohr's circles of strain.

Fig. 3.20 Mohr's circles for stresses and strains of a prism with θ=67.5° of series UCU.

The average stress-average strain relationships determined in the principal directions for series UCU and UCR are shown in Figs. 3.21 and 3.22, respectively. A good agreement can be observed between the initial slopes for the prisms tested with θ=0° and 90° in the two series. In series UCU, softer stress-strain relationships can be noticed in cases of the prisms tested with θ=22.5°, 45°, and 67.5°. This could be attributed to the shear deformations taking place along the mortar joints. Having continuous grout cores normal and parallel to bed joints in series UCR helped reduce the difference between the stress-strain curves obtained for θ=22.5°, 45°, and 67.5° and those determined for θ=0°. The prisms that suffered shear failures along the mortar joints, showed a sudden drop in the stresses followed by a horizontal plateau. The slope of the falling branch and the position of the horizontal plateau depended on the residual shear resistance along the planes of failure. The prisms of series UCR exhibited flatter falling branches and higher plateaus compared to the prisms of series UCU.

Acting as planes of weakness, the mortar joints altered not only the failure stresses, but also the average stress-average strain relationships. With the increase of the applied loads, more deformation took place along the mortar joints, which consequently resulted in a deviation between the orientations of the principal stresses and the principal strains by an angle β. The stress and strain measurements were used to define the variations of angle β with the principal compressive stress σ_2 for series UCU and UCR which are presented, respectively,

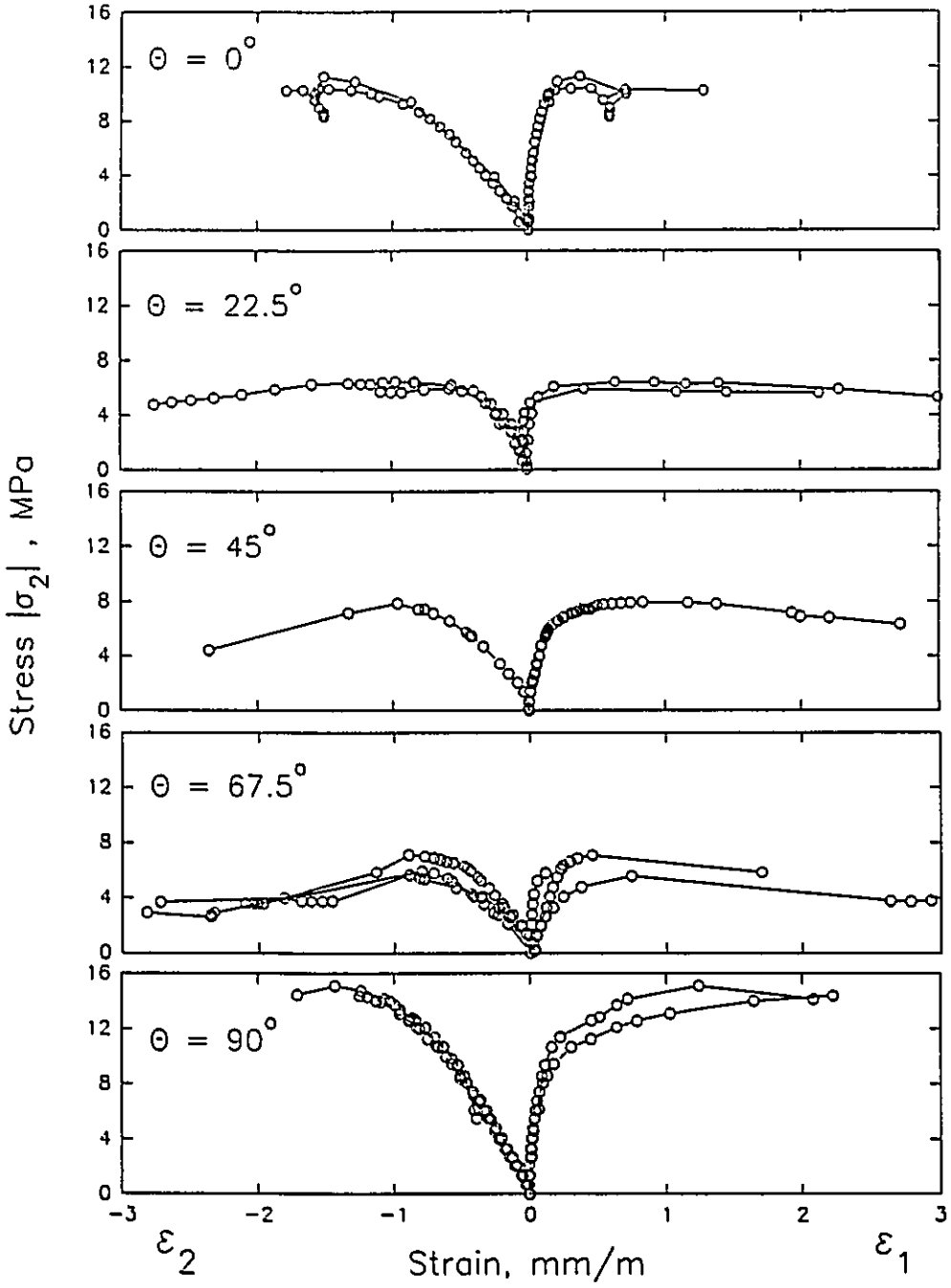

Fig. 3.21 Average stress-average strain relationships for series UCU.

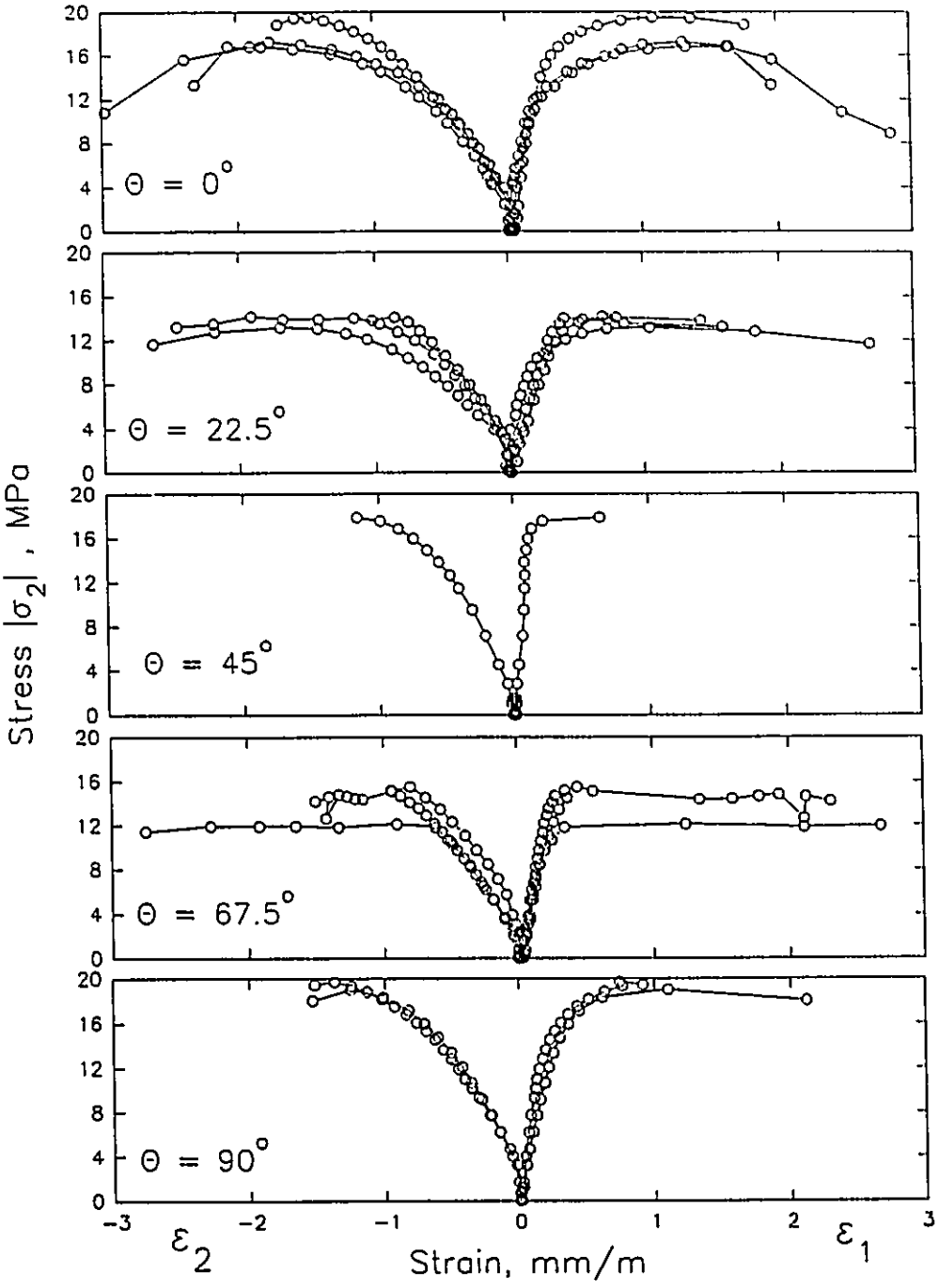

Fig. 3.22 Average stress-average strain relationships for series UCR.

in Figs. 3.23 and 3.24. Depending on the bed joint orientation θ (or, in other words, on the stress combinations acting along the mortar joints), different values of angle β were observed. These angles remained almost constant prior to failure. As the loading approached the shear capacity of one of the mortar joints, higher deformations took place along this plane leading to a significant increase in β. The ranges and the mean values of β prior to failure are summarized in Table 3.11. These values were determined using the strain measurements corresponding to the values of σ_2 between 25% and 80% of the failure stresses. The results reported in Table 3.11 together with Figs. 3.23 and 3.24 clearly indicate the significant effect of having continuous grout cores parallel to bed joints on reducing the anisotropic characteristics of masonry which are brought about by the presence of the mortar joints. For example, the maximum absolute value of angle β dropped from 25.8° for series UCU to 7.9° for series UCR.

Table 3.11 Angles β for series UCU and UCR

Series	θ (degrees)	Angle β, (degrees)	
		Range	Mean
UCU	22.5	-25.8 to -2.23	-10.64
	45	-1.86 to 0	-0.78
	67.5	-10.08 to 3.4	-3.1
UCR	22.5	-1.2 to 4.5	1.16
	45	-2.69 to 2.07	-0.41
	67.5	-7.94 to 3.18	-0.05

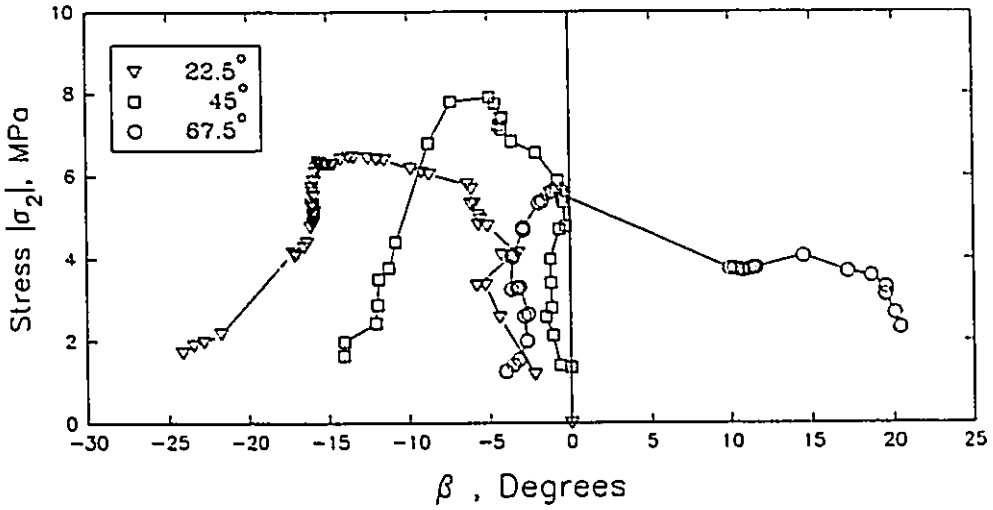

Fig. 3.23 Variations of angle β with principal stress σ_2 for series UCU.

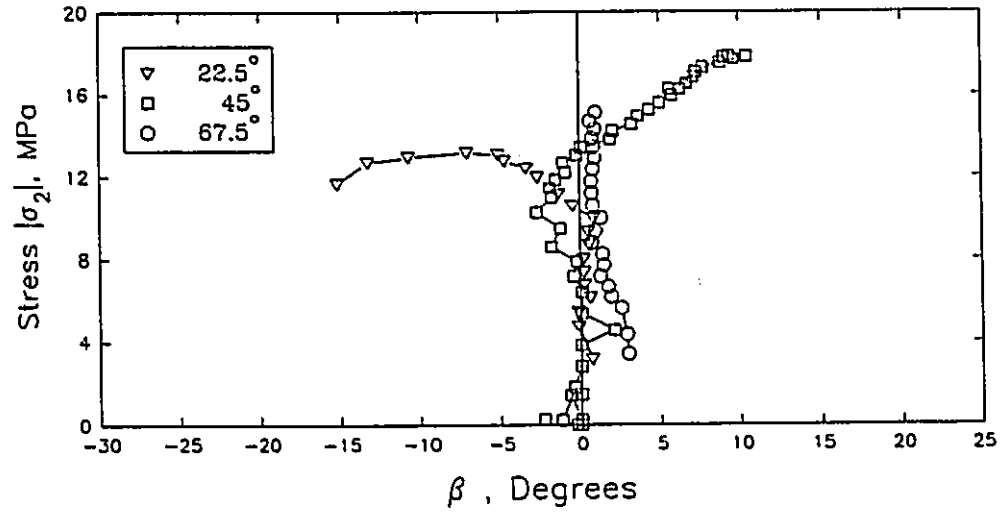

Fig. 3.24 Variations of angle β with principal stress σ_2 for series UCR.

3.3.2 Uniaxial Tension Tests

Two series of prisms, UTU and UTR, were tested under uniaxial tension with different bed joint orientations θ=0, 22.5, 45, 67.5, and 90°. Similar to the compression prisms, the prisms of series UTU and UTR were constructed at the same time as the unreinforced and the reinforced panels, respectively. Series UTU represents the case of having grout cores normal to bed joints only, whereas series UTR represents the case of having continuous grout cores both normal and parallel to bed joints.

3.3.2.1 Modes of Failure

All of the prisms exhibited tension modes of failure, but in different patterns depending on θ. The fracture planes tended to follow the weakest cross-sections. Series UTU did not include prisms tested at θ=0° (tension parallel to bed joints). The prisms of series UTR with θ=0° failed along the head joint planes as shown in Fig. 3.25. The straight line fracture plane followed the head joints and crossed the block face shells as well as the grout cores parallel to the bed joints. Similar failure patterns were observed in the prisms prepared with θ=22.5° in both of series UTU and UTR, as shown in Fig. 3.26.

At θ=45°, both the bed and head joint planes were subjected to the same tensile and shear stresses. A stepped fracture pattern was observed in the prisms of series UTU through the bed and the head joints as shown in Fig. 3.27(a). Having continuous grout cores parallel and normal to bed joints, in series UTR, improved the tensile capacity of the mortar joint planes. As a result, the fracture

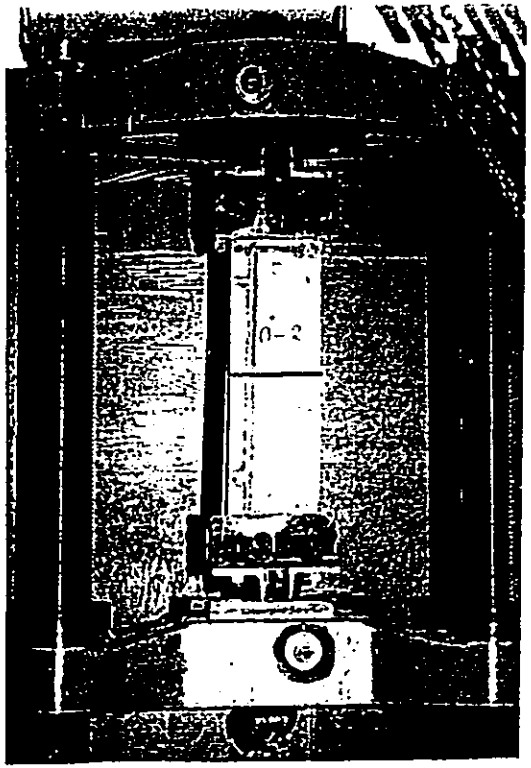

Series UTR

Fig. 3.25 Typical failures of prisms with $\theta=0°$ under uniaxial tension.

(a) Series UTU (b) Series UTR

Fig. 3.26 Typical failures of prisms with $\theta=22.5°$ under uniaxial tension.

planes followed the weakest sections which were normal to the principal tensile stress σ_1, Fig. 3.27(b), rather than following the mortar joints. This change in the fracture pattern, between series UTU and UTR, illustrates the additional contribution of having continuous grout parallel to the bed joints, toward minimizing the anisotropic characteristics of masonry.

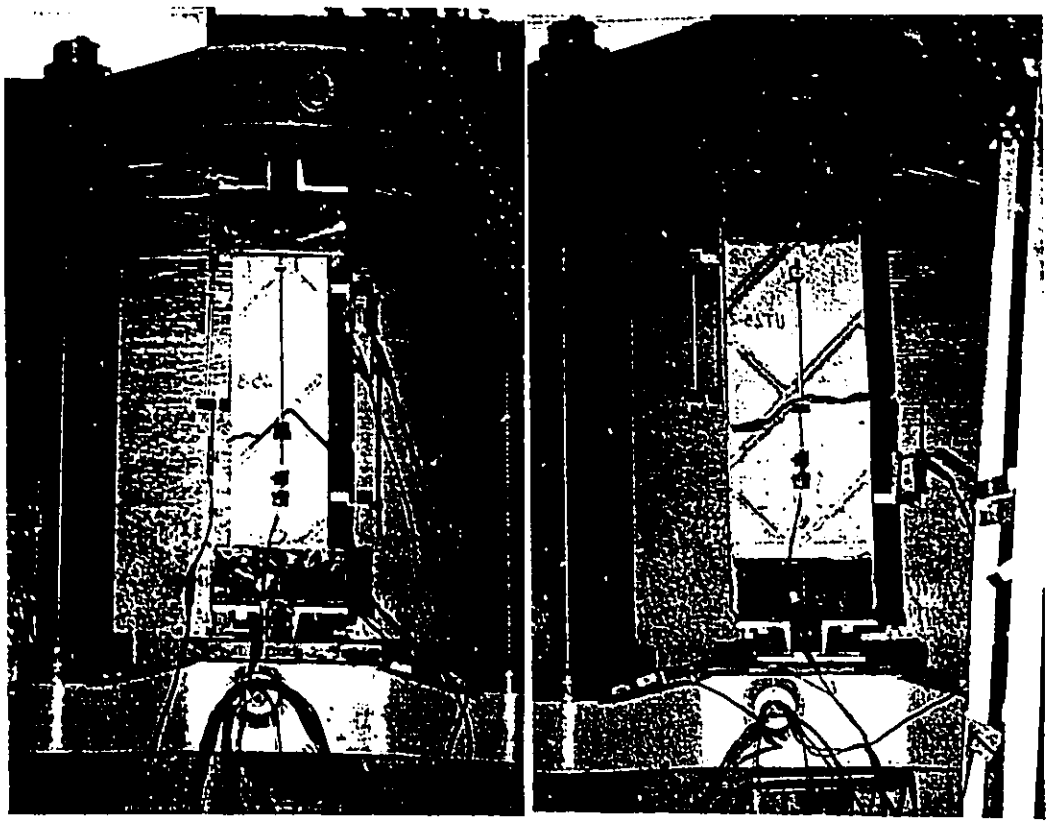

(a) Series UTU (b) Series UTR

Fig. 3.27 Typical failures of prisms with θ=45° under uniaxial tension.

For θ=67.5 and 90°, the fracture planes followed the bed joints through the grout cores. As shown in Figs. 3.28 and 3.29, the same failure patterns were observed in both of series UTU and UTR.

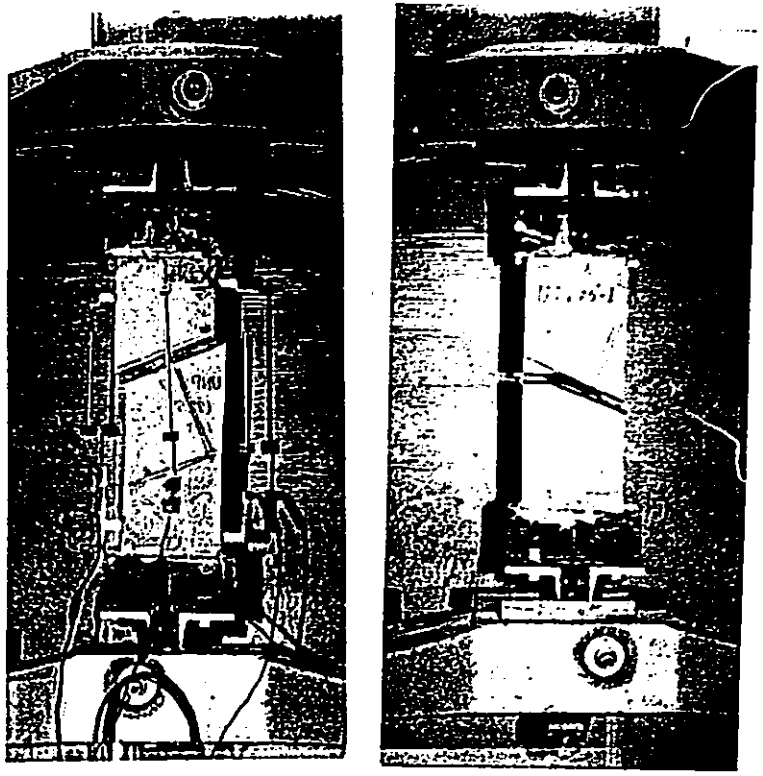

(a) Series UTU (b) Series UTR

Fig. 3.28 Typical failures of prisms with θ=67.5° under uniaxial tension.

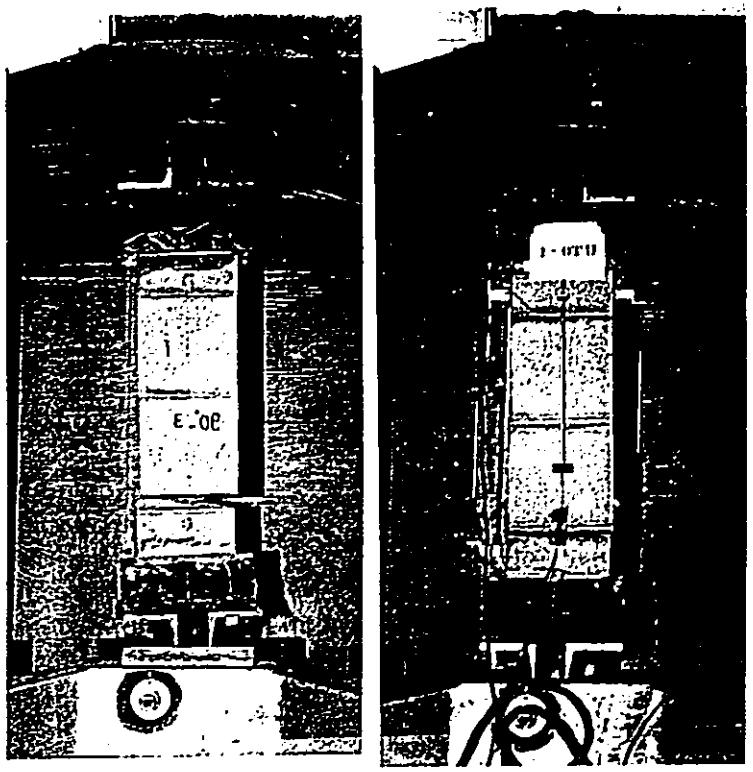

(a) Series UTU (b) Series UTR

Fig. 3.29 Typical failures of prisms with θ=90° under uniaxial tension.

3.3.2.2 Strength Characteristics

The variations of the tensile strengths of the masonry assemblages of series UTU and UTR, with the bed joint orientation θ, are shown in Figs. 3.30(a) and (b). The value of the tensile strength shown in Fig. 3.30(a) at θ=0°, for series UTU, was calculated based on the assumption that the fracture plane will follow a head joint plane. Neglecting the small bond strength of the mortar head joints, this tensile strength was determined as the product of the net cross-section area of the face shells, along the head joint plane, times the splitting tensile strength of the block face shells. The failure stresses of the prisms of series UTU and UTR, along with their control specimens, are summarized in Tables 3.12 and 3.13, respectively.

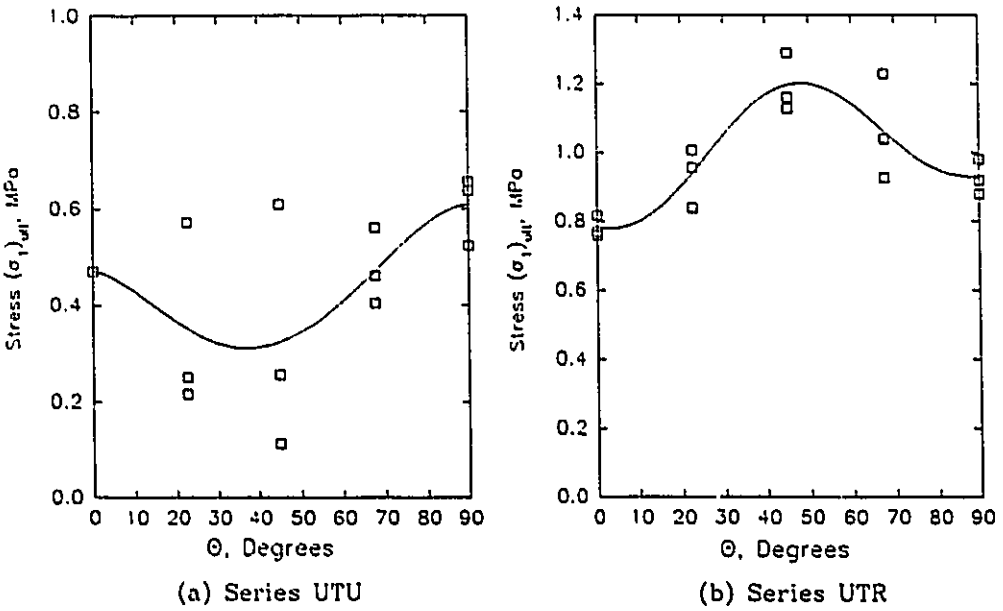

Fig. 3.30 Variations of uniaxial tensile strengths with θ.

Table 3.12 Prism test results of series UTU

θ (Degrees)	Mortar strength (MPa)	Grout splitting strength, Cell moulded (MPa)	Grout compressive strength (MPa)		Prism strength		
			Block moulded	Cell moulded	Individual (MPa)	Mean (MPa)	C.O.V. (%)
22.5	19.5	3.64	29.6	30.8	0.57 0.25 0.22	0.35	46.0
45	20.8	4.03	29.2	32.9	0.26 0.11 0.61	0.33	64.0
67.5	19.5	3.73	28.4	31.1	0.47 0.40 0.56	0.48	13.8
90	22.7	3.48	30.3	32.8	0.64 0.52 0.65	0.61	11.8

Table 3.13 Prism test results of series UTR

θ (Degrees)	Mortar strength (MPa)	Grout (cell moulded)		Prism strength		
		Splitting tensile strength (MPa)	Compressive strength (MPa)	Individual (MPa)	Mean (MPa)	C.O.V. (%)
0	18.2	4.70	33.8	0.82 0.76 0.77	0.78	3.1
22.5	23.9	4.60	31.6	1.01 0.84 0.96	0.93	9.0
45	22.2	5.16	35.7	1.29 1.16 1.13	1.19	5.9
67.5	21.7	4.99	37.1	0.93 1.04 1.24	1.07	14.6
90	18.9	4.69	33.6	0.92 0.98 0.88	0.87	13.8

As shown in Fig. 3.30(a), the failure stresses obtained in series UTU were significantly scattered, even for the same θ. The coefficients of variation (C.O.V.) for θ=22.5 and 45° were, respectively, 46.0% and 64.1%. At these angles, the fracture planes propagated through the head joints along with the block face shells or the bed joints. On the other hand, at θ=67.5 and 90°, where the fracture planes followed the bed joints only, the C.O.V. dropped to 13.8% and 11.8% respectively. The values of the C.O.V. of series UTR were noticeably smaller than the corresponding values of series UTU which could be attributed to having continuous grout normal and parallel to bed joints. The maximum C.O.V. obtained in series UTR was equal to 14.6% for θ=67.5°.

The large values of the C.O.V. that were found for series UTU raised a question about the reliability of testing narrow prisms, with different θ, under uniaxial tension. In an attempt to answer this question, the configurations of three prisms prepared with θ=22.5°, but having different widths, are sketched in Fig. 3.31. The three prisms are assumed to have grout cores normal to the bed joints only (i.e., they belong to series UTU).

As observed in the tests at θ=22.5°, the failure is expected to take place along the head joint planes which are designated by sections a-a in Fig. 3.31. In this case, the fracture planes cross both head joints and block face shells as indicated in the plan views. The greater tensile strength of the block face shells, compared to the bond strength along the block-mortar interface, could result in an eccentricity "e" between C_r (the point through which the resultant of the

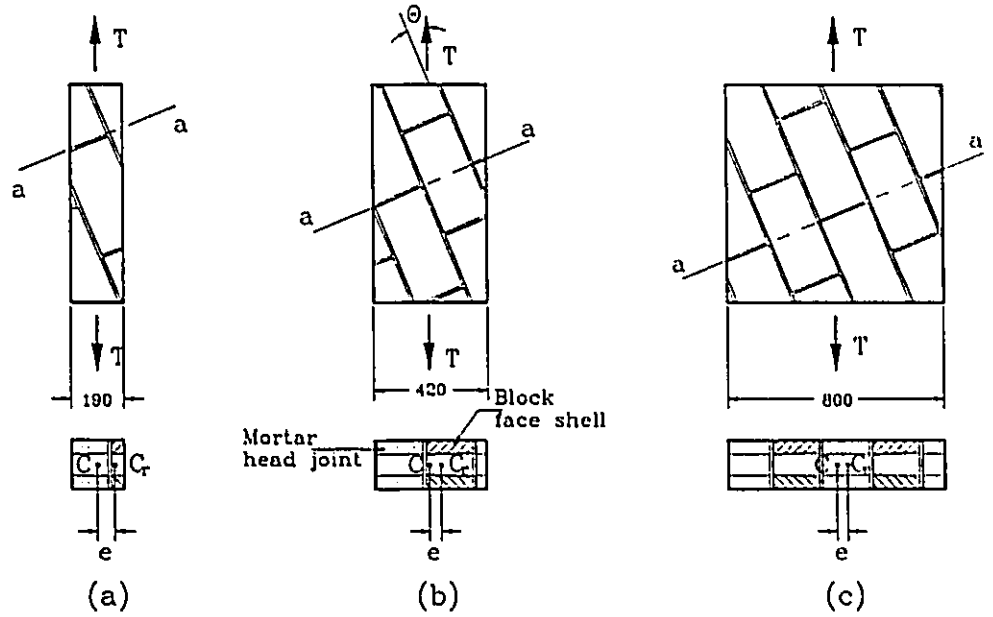

Fig. 3.31 Effect of prism width on the internal forces under uniaxial tension.

ultimate resistance of section a-a acts) and C (the centre of the gross area of section a-a). Having the test load T applied through C, section a-a acts under the effects of not only T, but also a moment M=T.e. The value of the moment M changes with the configuration and the width of the prism, which explains the large C.O.V. obtained for θ=22.5°. In a 190 mm wide prism, a small eccentricity could be large enough to alter the stress distribution and consequently the test results. In this case, none of the test results obtained could realistically represent the average tensile strength of the assemblage.

Increasing the width of the prism improves the reliability of the specimen in representing the macro-behaviour of masonry in more than one way. First, increasing the prism width "w" reduces the ratio "e/w" and its effect on the

stress distribution and on the test results. Second, as demonstrated in Figs. 3.31(b) and (c), the larger the prism width is, the more head joints and blocks are included in the specimen and, consequently, along the fractures planes. Testing narrow prisms with one head joint, even with no eccentricity, does not reflect the average characteristics of the masonry assemblage, but rather it reflects the tensile strength of this joint. Increasing the number of mortar joints along the fracture plane allows for stress redistribution to take place between the weakest joint and the adjacent parts of the section until a complete failure occurs for the whole section, representing the macro-behaviour of the masonry assemblage. However, it should be kept in mind that testing large specimens is not an easy task. It requires higher tensile forces and more details to eliminate the effect of the constraints along the loaded boundaries; the points that were discussed earlier in Chapter 2 for the biaxial tests.

The same argument considered for θ=22.5° is also applicable for the prisms prepared with different bed joint orientations. Therefore, the results of series UTU cannot be used to accurately judge the anisotropic characteristics of masonry assemblages under uniaxial tension. The variations among the results obtained for the same θ are too large to be able to distinguish between the change in the tensile strength of the assemblage due to θ and the variability in the test results. On the other hand, the C.O.V. obtained for the prisms of series UTR were reasonably small (max. C.O.V. was found for θ=22.5° in the order of 14.6%). As a result, the failure stresses of series UTR can be used to judge the

anisotropic characteristics of the assemblage. Based on the results shown in Fig. 3.30(b) and given in Table 3.13, an increase in the order of 52.6% can be detected in the mean failure stress of the prisms with θ=45°, compared to the value found for θ=0°, which reveals the dependence of the prism failure stresses on the bed joint orientation θ.

3.3.2.3 Deformation Characteristics

The average stress-average strain relationships, obtained in the direction of the principal tensile stress σ_1, are drawn in Figs. 3.32 and 3.33 for series UTU and UTR, respectively.

A high variability can be noticed among the average stress-average strain curves obtained for series UTU. However this variability cannot be attributed solely to θ, since significant differences can be observed among the curves obtained for the same bed joint orientation θ. As indicated before, testing narrow prisms under tension, especially with grout cores only normal to bed joints, does not reflect the average characteristics of the masonry assemblage.

In contrast to the above observations, the stress-strain relationships obtained for series UTR were in good agreement. This agreement can be observed among the results obtained at the same θ, which gives confidence in the tension tests of the masonry prisms with continuous grout cores normal and parallel to the bed joints. The agreement extended also to cover the initial slope of the stress-strain relationships at different values of θ, revealing an almost isotropic deformation characteristic for the masonry assemblages of series UTR.

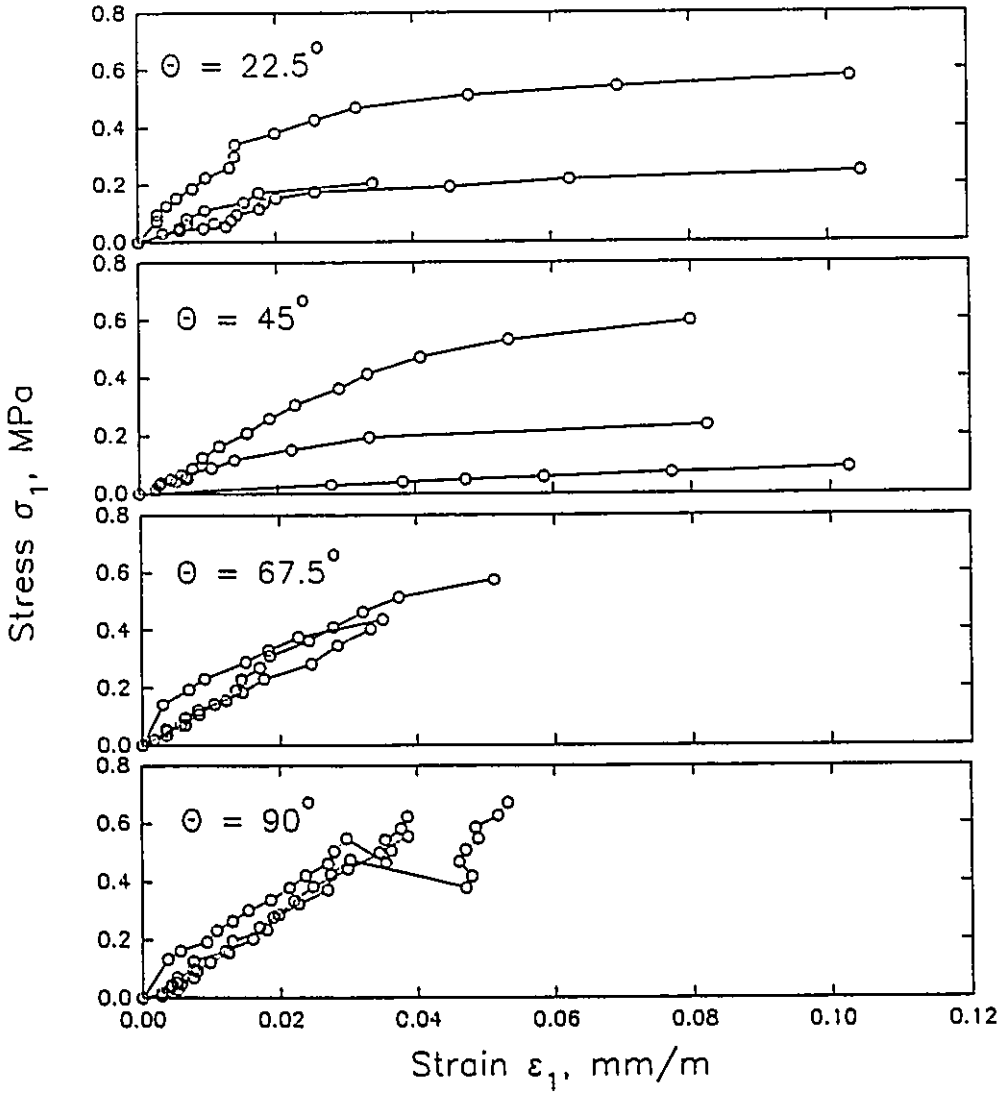

Fig. 3.32 Average stress-average strain relationships for series UTU.

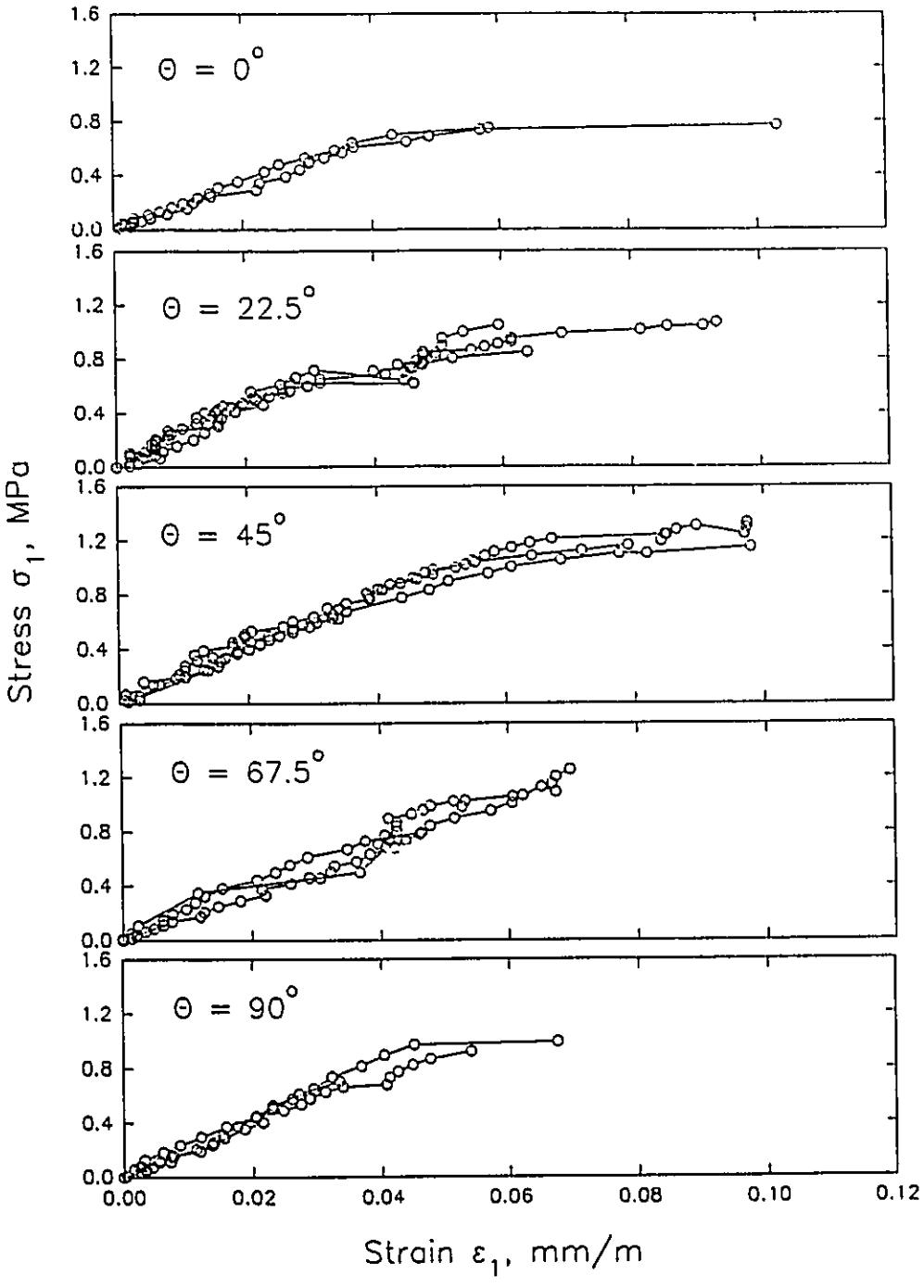

Fig. 3.33 Average stress-average strain relationships for series UTR.

At stresses approaching failure, a significant change in the slope can be observed in most of the average stress-average strain curves. This behaviour could be attributed to the stress redistribution taking place between the weak mortar joints and the adjacent grout cores or blocks, when the joints reached their tensile capacities. It is interesting to indicate, at this point, that no cracks in the mortar joints were observed, during the tests, prior to the final failures of the prisms.

3.3.3 Direct Shear Tests

Three series of shear couplets (M, GM, and G) were constructed with the unreinforced panels. Each series consisted of 9 shear couplets tested under three levels of precompression, each with three repetitions. Series M, GM, and G were tested to investigate the shear behaviour of mortar bed joints, mortar bed joints with grout, and bed joints with grout but without mortar, respectively.

3.3.3.1 Modes of Failure

All the couplets tested exhibited shear modes of failure along the joints. In series M under no precompression, debonding failure took place in a brittle manner along the weakest block-mortar interface. Under the effect of precompression, the failure occurred along the two block-mortar interfaces with inclined cracks through the mortar joints. Increases in the precompression stress led to higher failure loads with more ductile behaviour.

In series G as well as series GM, the failure stresses were governed by the shear capacity of the grout cores. The observed conical shape of the failure is shown in Fig. 3.34. The wide base of the conical surfaces coincided with the flared tops of the blocks where the grout cores had the smallest cross-section. The conical shape was observed in the tests with precompression, but the couplets tested without precompression had much deeper conical surfaces. Under the effect of high precompression, the failure was also accompanied by dislocation of some of the aggregate. The conical shape of the failure plane could be attributed to the presence of shrinkage cracks, which are discussed later in Chapter 4. Also, similar to the behaviour of concrete under direct shear stresses, the planes of failure of the grout are likely to be roughly perpendicular to the diagonal tension. As shown in Fig. 3.34, the grout areas across the failure surfaces were marked to reveal how the actual grout cross-sections were much smaller than the size of the block void. This reduction in the grout area results from the fact that, in the running bond pattern, the block webs are not aligned in the vertical direction. In addition, during the construction, mortar fins flow in and hang over the bottom blocks reducing the void cross-section. The grout areas, A_{gt}, across the failure surface were measured. An average ratio between this area and the gross area, A_g, was found to be in the order of 19.4%, instead of the expected ratio of 22.6%. It is worth noting that the blocks used in this investigation had a 44% void volume.

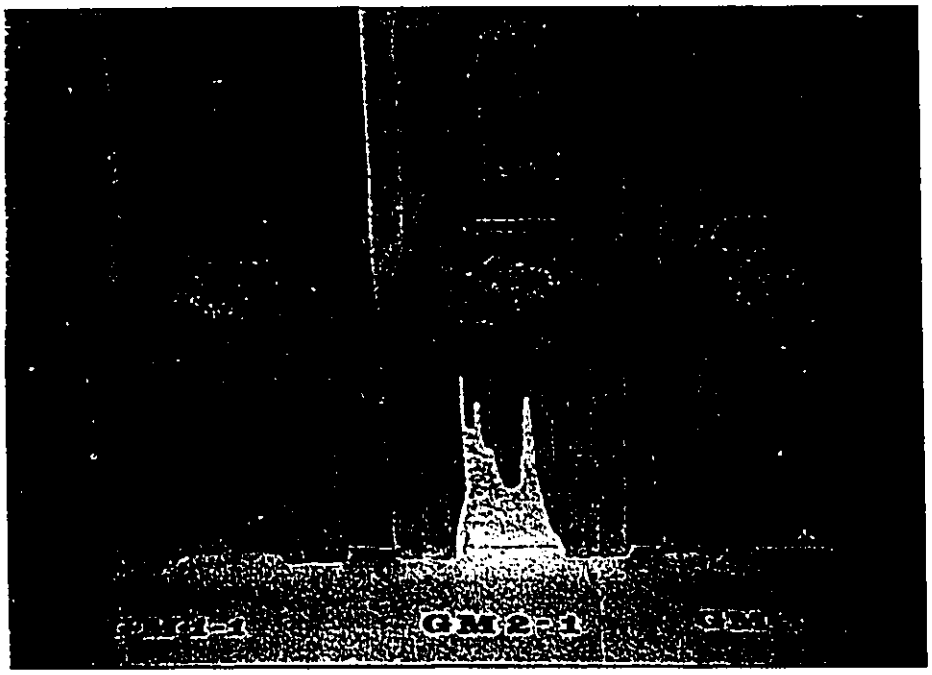

Fig. 3.34 Failed grouted couplets of series GM.

3.3.3.2 Strength Characteristics

The test results obtained for series M, GM, and G are listed in Table 3.14. The shear strengths for series M and G were calculated using the minimum net areas along the block-mortar interface and across the grout core, respectively. The gross area, A_g, was used for calculating the shear strengths of series GM. The variations of the shear strengths with the precompression level are also presented graphically in Fig. 3.35.

Table 3.14 Direct shear test results

Series	σ_n (MPa)	Mortar strength (MPa)	Grout strength (MPa)	Shear strength	
				Mean (MPa)	C.O.V. (%)
M	0	10.1		0.25	21.0
	1.0			0.83	11.6
	2.0			1.52	0.9
G	0		28.2	2.25	18.2
	0.5			2.73	18.9
	1.0			3.41	16.7
GM	0	10.1	28.2	0.88	16.8
	0.55			1.23	3.5
	1.1			1.9	8.1

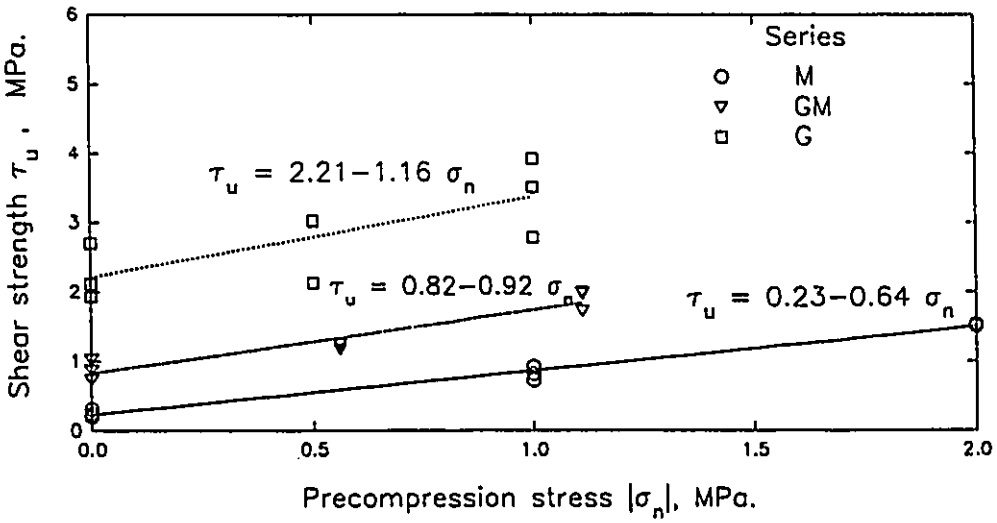

Fig. 3.35 Variations of shear strengths of bed joints with the precompression level.

The test results, shown in Fig. 3.35, reflect a strong correlation between the increase in the shear strength and the increase in the precompression level. This correlation suggested the use of Coulomb's hypothesis of internal friction to predict the shear strength of the bed joints at these low levels of precompression. This hypothesis has been used for masonry by many researchers (Benjamin and Williams (1958), Sinha and Hendry (1969), Yokel and Fattal (1976), Hamid (1978), and Hegemier et al. (1978)). It is based on the assumption that the shear strength is the summation of the contributions of shear bond and internal friction along the shear plane:

$$\tau_u = c - \sigma_n \tan\phi \qquad \ldots(3.2)$$

where τ_u = the average shear strength,

c = the coefficient of cohesion or the shear strength with no precompression,

σ_n = the precompression stress normal to the bed joint (negative value), and

ϕ = the angle of internal friction along the shear plane.

The negative sign in Eq. 3.2 resulted from considering compressive stress as a negative stress. Performing linear regression analyses on the test results yielded the following equations:

For ungrouted bed joints (series M),

$$(\tau_u)_m = 0.23 - 0.64\,\sigma_n \qquad \ldots(3.3.a)$$

For grouted bed joints (series GM),

$$(\tau_u)_{gm} = 0.82 - 0.92\,\sigma_n \qquad \ldots(3.3)$$

For grouted bed joints with no mortar (series G),

$$(\tau_u)_g = 2.21 - 1.16\,\sigma_n$$

The contribution of the internal friction, in these equations, implies a more pronounced effect of the precompression on the shear strength of grouted joints, compared to ungrouted joints. This can be explained by the shear transfer mechanism proposed by Nawy (1983) for reinforced concrete. He suggested that all shear resistance is initially provided by intrinsic bond, but after slip has started, resistance is developed through friction, aggregate interlock, and dowel action as illustrated in Fig. 3.36. In the case of ungrouted specimens, where failure occurs along the block-mortar interface, the increase in shear strength with precompression is mainly attributed to friction. On the other hand, the rough conical surface through grout allows both friction and aggregate interlock.

The difference between the shapes of the failure surfaces observed in mortar and grout raises a question about the possibility of predicting the shear strength of grouted joints, within a range of low compressive stress (10% of the compressive strength of the assemblage), using a linear superposition of the individual shear strengths of grout and mortar. A comparison was made between the experimental values and those predicted by linear superposition. The results of this comparison are presented in Fig. 3.37. The linear superposition was

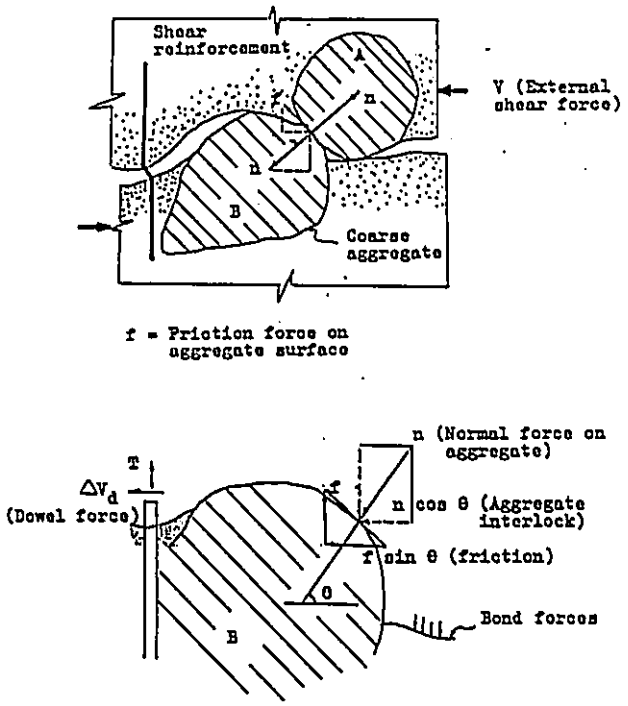

Fig. 3.36 Shear transfer mechanism for reinforced concrete (Nawy 1983).

performed according to the following equation.

$$(\tau_u)_{gm} = \frac{1}{A_g} [A_{gt}\ \tau_g + (1-A_{gt})\ \tau_m] \qquad ...(3.4)$$

It was observed that the failure in grouted joints occurred at the critical section of the grout cores. This section was associated with the largest block-mortar interface. The term $(1-A_{gt})$ in the above equation, allows for this increase in the block-mortar interface as well as the bond between grout and the unaligned webs. The average ratio of the predicted strengths to the observed values was 0.91 with

a C.O.V. of 10.4%. This ratio confirms the general validity of adopting the principle of linear superposition, within a range of low compressive stress (10% of the compressive strength of the assemblage), to predict the shear strength of grouted joints from the shear strengths of their constituents. Similar results were reported by Hamid et al. (1979) on specimens having different grout strengths.

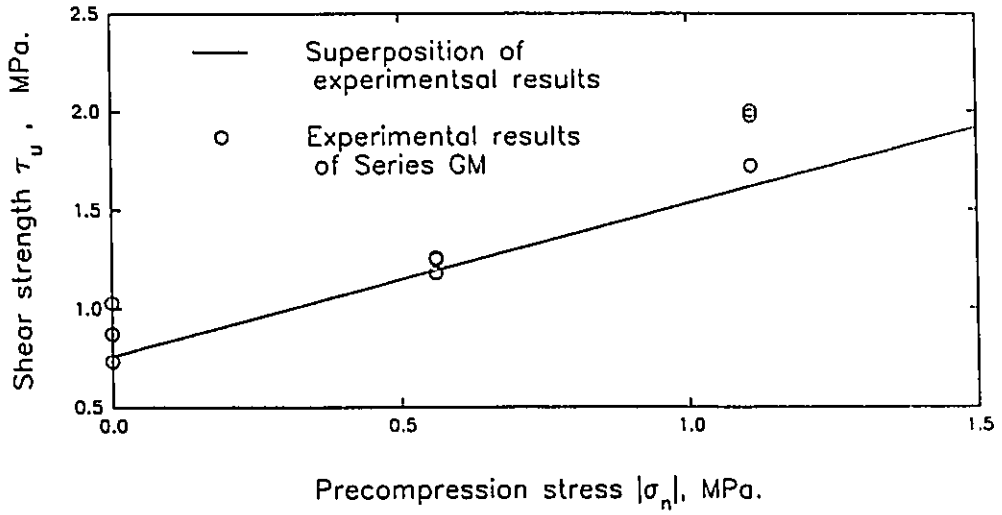

Fig. 3.37 Linear Superposition of shear strengths of grout and mortar in a bed joint.

3.3.3.3 Deformation Characteristics

Typical shear stress-slip curves for series M and GM are shown in Fig. 3.38. The corresponding shear stress-dilation curves are given in Fig. 3.39. The slip and dilation measurements were taken along gauge lengths of 160 mm and 30 mm, respectively. These measurements included the deformations that occurred in the joints as well as in parts of the blocks. Although the block

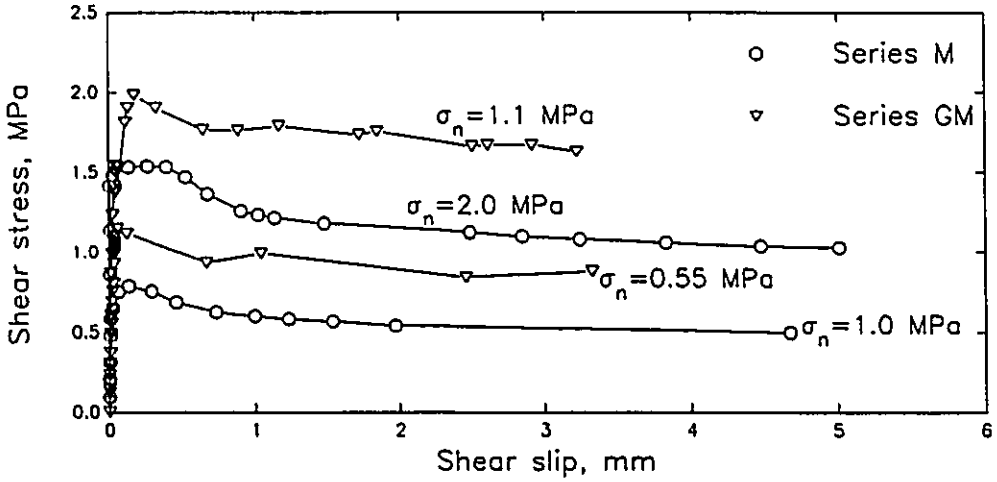

Fig. 3.38 Typical shear stress-slip relationships.

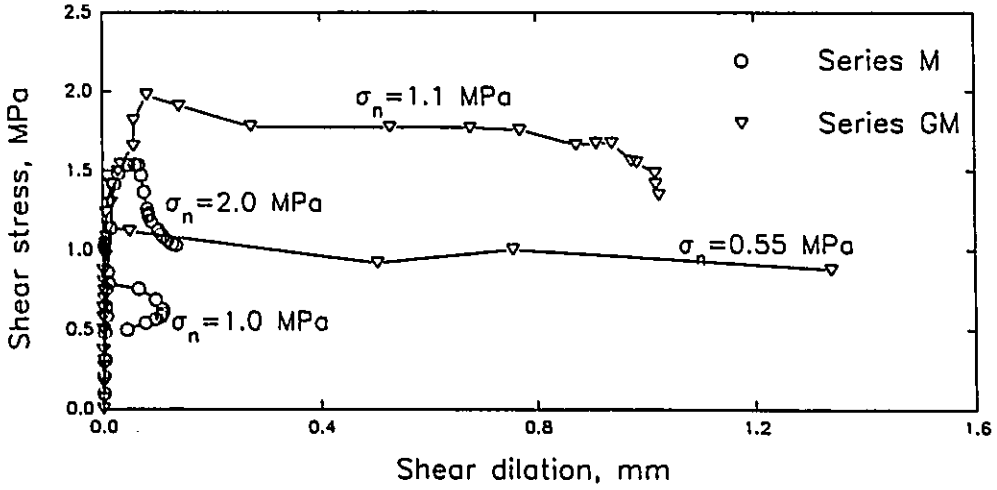

Fig. 3.39 Typical shear stress-dilation relationships.

deformations could contribute to the measured deformations at low shear stresses, this effect is very minor as the shear deformations in the joint increased dramatically near and beyond the peak stress.

Increases in the precompression level led to higher shear strengths and flatter descending branches. This effect is more pronounced in the grouted joints of series GM. The desirable effects of precompression extended to cover the residual shear strength. The higher the precompression level was, the more shear strength the couplet sustained beyond the peak value.

The couplets exhibited significant increases in shear dilation under loading conditions near and beyond the peak shear stresses. The measured values of shear dilation were higher in the grouted joints of series GM, compared to the ungrouted joints of series M. This difference could be attributed to the larger size of the aggregate used in grout, in comparison with that used in mortar. The increase in the aggregate size could result in a rougher failure plane leading to more dilation as the shear slip takes place.

3.4 CLOSING REMARKS

Based on the observations and the results of the different auxiliary tests reported in this chapter, the following conclusions can be drawn:

1. Grouted concrete masonry is a composite material built up of several components. Each has its own physical, mechanical, and geometrical characteristics. Therefore, tests on each component material as well as the assemblage are necessary to achieve an understanding of the factors affecting the

response of masonry.

2. The tests of blocks under compression do not necessarily reflect the characteristics of the block material. The modes of failure and the failure stresses determined in these tests depend on the geometry of the specimen, the loading condition, and the capping area. However, the results of testing half blocks flat wise with full capping or full blocks end-wise were found to be representative of the compressive strength of the block material.

3. Different from the method stated in the CSA A 179M-1976, grout prisms can be prepared by filling the block cells with grout and later sawing the grout cores to the desired dimensions. The prisms prepared in this manner are more representative of the grout in a masonry wall than block moulded grout prisms because they have the same original volume to surface area ratio, and consequently the same water-cement ratio, as actually exists in the grout in masonry walls. Furthermore, less space is required for preparation of the prisms during construction.

4. The behaviour of grouted concrete masonry under uniaxial compression is dependent on the bed joint orientation θ. Both the mode of failure and the compressive strength change significantly with θ. For an assemblage with continuous grout only normal to bed joints, a reduction in the compressive strength, compared to the strength at $\theta=0°$, was found in the order of 41.4% at $\theta=22.5°$, where shear failures took place along the head joint planes.

5. Using blocks with knocked-out webs results in continuous grout both

normal and parallel to bed joints. This grout pattern helps reduce the anisotropic characteristics of masonry. For example, the reduction in the compressive strength at θ=22.5°, compared to that at θ=0°, was found to be only 17.6%.

6. No significant difference, in the mode of failure or the compressive strength at θ=0°, was found between the masonry assemblage with continuous grout normal to bed joints only and that with continuous grout both parallel and normal to bed joints.

7. Due to the anisotropic characteristics of grouted concrete masonry, a complete definition of its failure criteria requires a three dimensional failure surface in terms of σ_1, σ_2, and θ (or σ_p, σ_n, and τ_{pn}).

8. Acting as planes of weakness, the mortar joints undergo larger deformations in comparison with the adjacent blocks or grout. These deformations result in a deviation, of angle β, between the orientations of the principal stresses and the principal strains. The value of the angle β depends on the bed joint orientation θ (or in other words on the ratio between the stresses acting along the mortar joints). Having continuous grout both normal and parallel to bed joints reduces the values of angle β.

9. Testing narrow prisms under uniaxial tension does not reflect the average characteristics of the masonry assemblage but, rather, it represents the characteristics of the weakest joint. Furthermore, the composite nature of the grouted masonry assemblages could result in an eccentricity between the test force and the resultant of the ultimate capacities of the components across the

fracture plane. The value of this eccentricity is not a characteristic of the assemblage; it changes with the configuration of the prisms. Testing wide specimens with a large number of mortar joints, blocks, and grout cores improves the reliability of the test results. The wider the specimen, the smaller the effect of the eccentricity on the test results. Including larger numbers of mortar joints, blocks, and grout cores allows for stress redistribution to take place between the weakest mortar joint and the adjacent parts until a complete failure takes place. Also, a more representative section is tested.

10. The ratio between the tensile strength of grouted concrete masonry and its compressive strength was found to range between 3.9% and 7.6%. This small ratio may justify, in some cases for the sake of simplicity, neglecting the effect of the bed joint orientation θ on the tensile response of masonry.

11. The shear strengths of bed joints increase with the normal compressive stress acting on these joints. Within a range of low compressive stress (approximately 10% of the compressive strength of the assemblage), the relationship between the shear strength and the compressive stress was found to be almost linear. The effect of the compressive stress is more pronounced in the case of grouted masonry, compared to ungrouted specimens.

12. For low levels of compression, the shear capacity of a grouted block specimen can be predicted with reasonable accuracy by linear superposition of the shear capacities of the grout and mortar components across the joint.

13. Using hollow blocks with two cells results in unaligned webs in the

running bond pattern. The unaligned webs, along with the flared tops of the blocks and the frogged ends, lead to small grout areas along the bed joint planes, which in turn limit the effectiveness of the grout in reducing the anisotropic characteristics of masonry. Therefore, it is not advisable to use blocks with frogged ends and flared tops in preparing grouted concrete assemblages.

CHAPTER 4

EXPERIMENTAL RESULTS OF THE BIAXIAL TESTS

4.1 INTRODUCTION

Thirty-six block panels were tested under biaxial tension-compression states of stress to explore the behaviour of grouted concrete masonry. These tests have the merit of explicitly defining the stresses and strains experienced by the specimens without the need to adopt any assumption of isotropic or elastic behaviour. Both unreinforced and reinforced panels were tested under different states of stress with different bed joint orientations to cover a wide range of the combinations of shear and normal stresses acting along the mortar joint planes. Different percentages of reinforcement, normal and parallel to the bed joints, were also used in the reinforced panels to investigate the contribution of reinforcement in resisting the in-plane stresses.

The results of the biaxial tests of the unreinforced panels of series UNP, followed by those of the reinforced panels of series RP, are reported in this chapter. The observed modes of failure, strength characteristics, and deformation characteristics are presented and discussed.

4.2 TEST RESULTS OF UNREINFORCED PANELS (SERIES UNP)

In Table 4.1, the unreinforced panels of series UNP are arranged in sub-sections according to states of stress of uniaxial compression, biaxial tension-

compression, and uniaxial tension. The test conditions, ultimate stresses, and the properties of the mortar and grout are summarized in Table 4.1.

Table 4.1 Results of the unreinforced panel tests

Panel	θ (°)	σ_1/σ_2	Mortar comp. strength (MPa)	Grout compressive strength (MPa)		f'_m 4-Course prism strength (MPa)	Grout splitting strength, Cell moulded (MPa)	Ultimate stresses $(\sigma_1/\sigma_2)_{ult}$ (MPa)
				Block moulded	Cell moulded			
UNP1	0	0/-1	7.3	28.08	34.4	10.8	3.33	0/-9.52
UNP2	22.5	0/-1	10.9	23.64	31.95	11.3	3.40	0/-8.15
UNP3	45	0/-1	7.25	33.3	31.42	12.4	3.60	0/-9.49
UNP4	67.5	0/-1	6.22	25.4	33.55	11.1	2.99	0/-6.08
UNP5	90	0/-1	8.07	29.89	34.95	10.3	3.24	0/-9.83
UNP6	45	1/-6.55	20.75	32.45	32.52	15.1	4.03	0.73/-4.76
UNP7	45	1/-3.86	20.84	33.49	31.42	12.2	2.96	0.95/-3.67
UNP8	22.5	1/-1.09	18.29	32.5	30.33	13.1	3.46	0.70/-0.76
UNP9	45	1/-1.09	19.48	32.26	31.87	13.4	3.98	0.79/-0.85
UNP10	67.5	1/-1.09	19.52	32.19	30.77	13.2	3.64	0.72/-0.78
UNP16	0	1/-1.09	22.35	33.14	32.83	17.7	3.48	0.74/-0.68
UNP11	0	1/0	17.43	30.29	29.07	13.7	4.58	0.48/0
UNP12	22.5	1/0	14.35	26.7	34.8	15.7	-	0.53/0
UNP13	45	1/0	19.73	29.35	27.47	14.4	4.19	0.67/0
UNP14	67.5	1/0	15.2	29.4	33.67	14.3	4.74	0.80/0
UNP15	90	1/0	16.1	22.91	29.06	12.7	3.88	0.78/0

4.2.1 Uniaxial Compression

4.2.1.1 Modes of Failure

The unreinforced panels tested under uniaxial compression exhibited different modes of failure depending on the bed joint orientations θ, as shown in Fig. 4.1. The dependence of the mode of failure on the bed joint orientation reveals the anisotropic characteristics of grouted masonry, which are brought

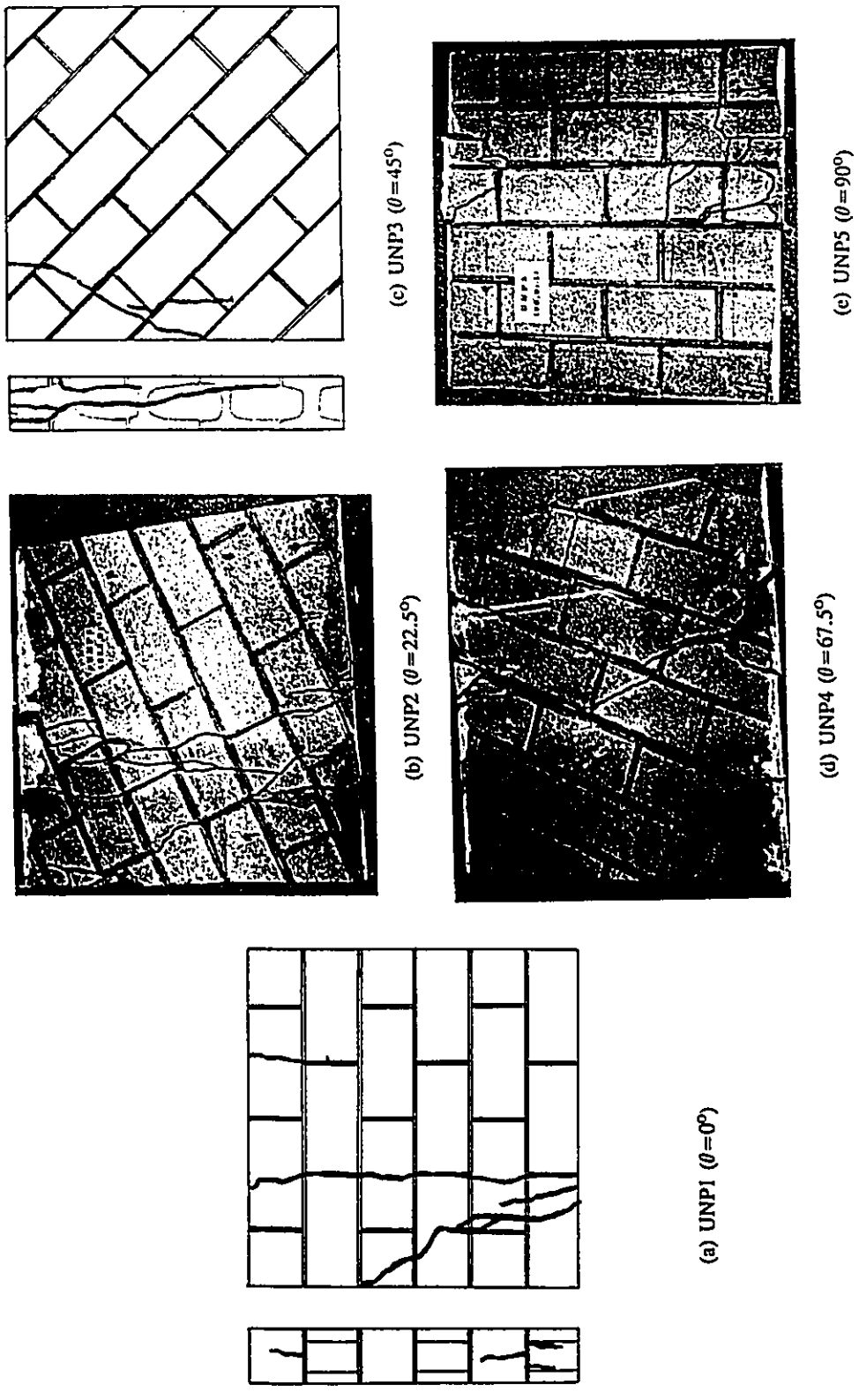

Fig. 4.1 Modes of failure under uniaxial compression.

about by the mortar joints acting as planes of weakness. In general, these modes of failure are consistent with those reported for the prism tests of series UCU.

Panel UNP1, which was tested with the bed joints normal to the applied compression (θ=0°), exhibited splitting cracks in the webs and the face shells, as shown in Fig. 4.1(a). The final failure occurred by spalling of face shells which was similar to the failure observed on the corresponding prisms of series UCU.

For panel UNP5, which was tested with the compression applied parallel to the bed joints (θ=90°), splitting cracks were observed along longitudinal planes coinciding with the grout-block interfaces and crossing the block webs, which seem to be the sections with minimum resistance to lateral tensile stresses (Hamid and Drysdale 1980). The direction of these cracks was parallel to the applied compression. In addition, more cracking took place along the bed joints which were also parallel to the applied compression, as shown in Fig. 4.1(e). Similar to the case with θ=0°, the final failure of the panel occurred by spalling of face shells.

Panel UNP2, which was tested with θ=22.5°, exhibited a shear mode of failure along the head joint planes as shown in Fig. 4.1(b). The planes of failure followed the head joints and passed through the block face shells in alternate courses, thus avoiding the grout cores. Another shear failure was observed in panel UNP4 (θ=67.5°) along the bed joints as shown in Fig. 4.1(d). Compared to the failures of panels UNP1 and UNP5, the shear failures of panels UNP2 and UNP4 occurred at lower loads and were more dramatic.

Although panel UNP3, which was tested with θ=45°, failed near a corner without significant development of other cracks, the observed mode of failure was in agreement with that observed in the corresponding prisms of series UCU. As sketched in Fig. 4.1(c), the cracks occurred through both mortar joints and block face shells. In addition, splitting cracks in the block webs, similar to those observed for θ=0°, were found across the ends of the panel. It is worth noting that the failure of panel UNP3 occurred at a load almost the same as that recorded for UNP1 (θ=0°).

Aside from the panel tested at θ=45°, the panels exhibited fairly widely distributed cracking with more than one potential failure plane. The modes of failure and their agreement with those observed in the prism tests of series UCU demonstrate the effectiveness of the loading arrangement designed to study the macro-behaviour of grouted concrete masonry. Edge conditions did not have any noticeable effect on panel behaviour.

For the comparison with the theoretical results, as reported later in Chapter 7, the failures observed for θ=0° and 90°, which initiated by splitting cracks parallel to applied compression and ended with spalling of face shells, are referred to as compression modes of failure. On the other hand, the failures observed for θ=22.5° and 67.5° are described as shear modes of failures along the head and the bed joint planes, respectively. The failure observed for θ=45° is referred to as a mixed mode of failure.

4.2.1.2 Strength Characteristics

The variation of the ultimate stress $(\sigma_2)_{ult}$ with the bed joint orientation θ, for the grouted concrete masonry assemblages under uniaxial compression, is presented in Fig. 4.2. The ultimate stresses found for θ=0, 45, and 90°, where compression failures took place alone or together with shear failures along mortar joints, were almost the same. Alternatively, significant reductions in the ultimate stresses can be noticed in Fig. 4.2 and Table 4.1 for θ=22.5 and 67.5°. The ultimate stresses $(\sigma_2)_{ult}$ obtained for these angles were limited by the shear capacities along the mortar joint planes. Reductions in the ultimate stresses of 14.4% and 36.1%, of the ultimate stress obtained for θ=0°, were found for θ=22.5 and 67.5°, respectively. These results demonstrate clearly the dependence of the compressive strength on the bed joint orientation.

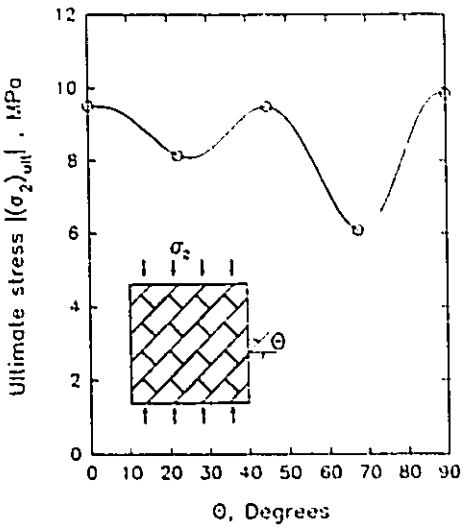

Fig. 4.2 Variation of ultimate stress under uniaxial compression with θ.

4.2.1.3 Deformation Characteristics

The average deformations of each panel were measured in four directions on each face shell. These readings were reduced to average strains and used to draw Mohr's circle of strains. In this manner, the principal strains ϵ_1 and ϵ_2, along with the strain components along the mortar joint planes ϵ_p, ϵ_n, and γ_{pn},

were determined over the range of loading. The applied loads were also used to define the principal compressive stress σ_2 (σ_1=0 for the state of uniaxial compression), as well as the stress components along the mortar joints σ_p, σ_n, and τ_{pn}. Having these stresses defined along with their corresponding strains, the average stress-average strain relationships were drawn in Fig. 4.3.

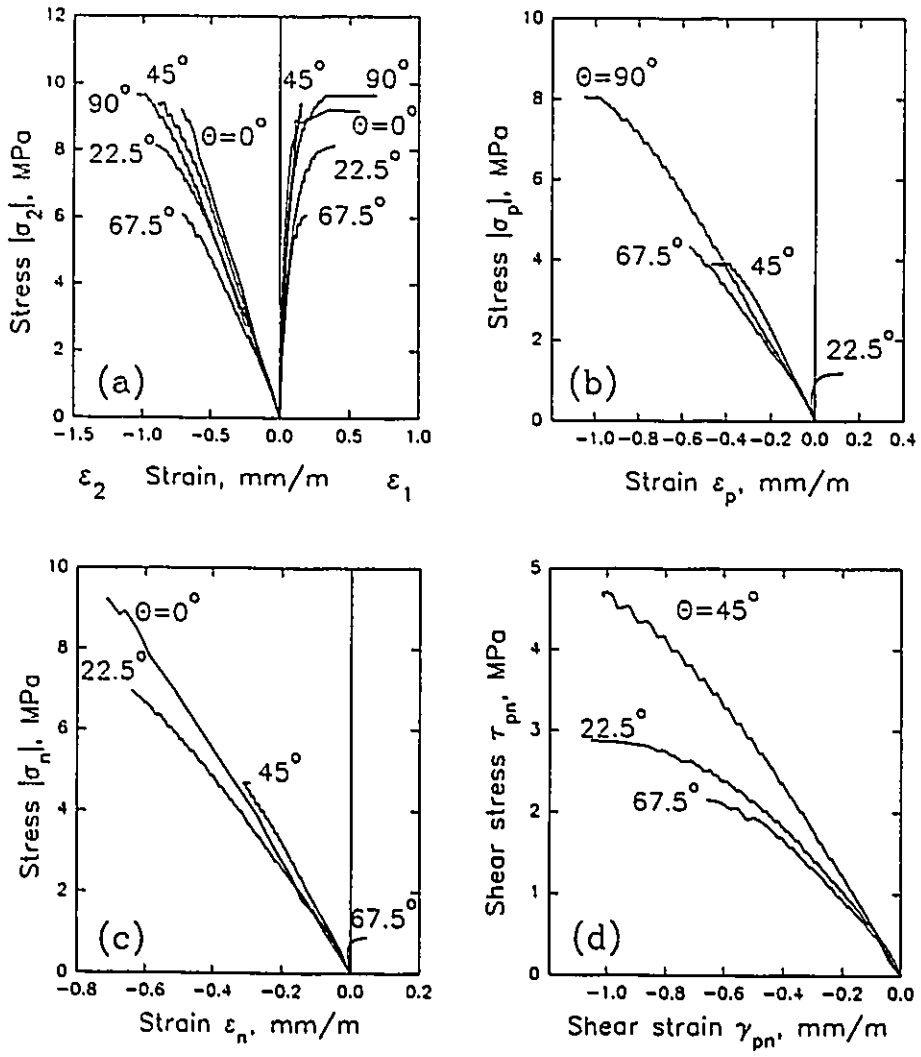

Fig. 4.3 Average stress-average strain relationships for panels UNP1-UNP5 (tested under uniaxial compression).

Figure 4.3 shows the average stress-average strain relationships obtained for the five panels tested under uniaxial compression with different bed joint orientations. In Fig. 4.3(a), the stress-strain relationships are presented in terms of the variations of the principal strains ϵ_1 and ϵ_2 with the principal compressive stress σ_2. The initial slopes of the different curves in the two principal strain directions are similar. However, increases in the applied stresses are accompanied by proportionally higher strains especially for θ=22.5° and 67.5°, compared to the values obtained for θ=0°. This could be attributed, as mentioned before in Sec. 3.3.1.3, to the shear deformations taking place along the mortar joints.

The same stress-strain data used in Fig. 4.3(a) are reproduced again in Figs. 4.3(b), (c), and (d), but in terms of the stress and strain components along the mortar joints. Representing the results in this manner reveals the change in ϵ_p from compression to tension due to the dilation taking place parallel to the bed joint planes for θ=22.5°, as shown in Fig. 4.3(b). With this bed joint orientation, the head joint planes were subjected to a high ratio of shear to compressive stress. Similar behaviour can be observed in the ϵ_n-σ_n relationship obtained for θ=67.5°, as shown in Fig. 4.3(c). In comparison with the normal stress-normal strain relationships, the shear stress-shear strain relationships shown in Fig. 4.3(d) are highly nonlinear and depend on the bed joint orientation. The panel tested with θ=45°, where equal compressive stresses act parallel and normal to bed joints (σ_p=σ_n), exhibited less shear strain and consequently higher shear stiffness in comparison with the values found for the panels tested with θ=22.5° or 67.5°.

The variations of angles β, between the orientations of the principal stresses and the principal strains, are shown in Fig. 4.4 for θ=22.5, 45, 67.5, and 90°. These angles reflect the effect of the deformations taking place along the mortar joints on the average deformation characteristics of the grouted masonry assemblage. For each bed joint orientation θ, the values of angle β remained almost constant until just prior to failure, when the shear deformations taking place along the mortar joints increased significantly as shown in Fig. 4.3(d), altering the values of β. The determined values of angle β ranged from -4 to 2°, depending on the bed joint orientation θ; or in other words on the ratio of the stresses acting along the mortar joint planes. Compared to the test results of the prisms of series UCU summarized in Table 3.11, the values of angle β from the panel tests are smaller. This difference is likely a result of the size and the cutting configuration of the prisms. For example, different cut locations could result in different areas of grout along the bed joint planes and consequently different shear capacities. This effect diminishes as the number of grout cores increases along the failure plane or, in other words, as the specimen size increases.

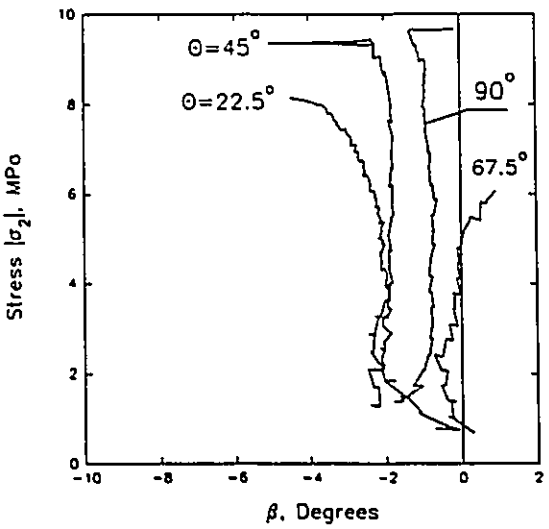

Fig. 4.4 Angles β for panels UNP1-UNP5 (tested under uniaxial compression).

4.2.2 Uniaxial Tension

4.2.2.1 Modes of Failure

All the panels tested under uniaxial tension (see Table 4.1) exhibited tensile modes of failure, but with fracture planes having different configurations, depending on the bed joint orientation θ. Photos of the panels after failure are shown in Fig. 4.5. Unlike the panels tested under uniaxial compression, each panel tested under uniaxial tension failed by the formation of a single major crack.

For panel UNP11, which was tested with bed joints parallel to the applied tensile loads (θ=0°), the failure took place on a plane normal to the loaded direction. As shown in Fig. 4.5(a), the fracture plane occurred along the head joints and passed through the block face shells at alternate courses. The fracture plane crossed the block face shells along the interface between the centre webs and the grout which left both the centre webs and the grout cores basically intact.

The failure of panel UNP15, which was tested with bed joints normal to the applied tensile loads (θ=90°), followed a bed joint as shown in Fig. 4.5(e). Because the blocks had face shells and webs with flared tops, the fracture plane occurred along the bottom of the bed joint which represented the section with minimum grouted area and consequently minimum resistance to the tensile force. It is worth noting that the fracture plane was also normal to the applied tension.

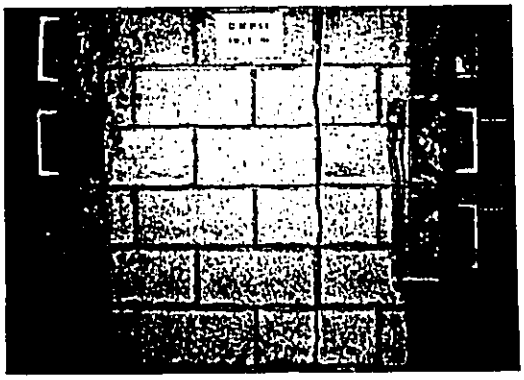

(a) UNP11 (θ=0°)

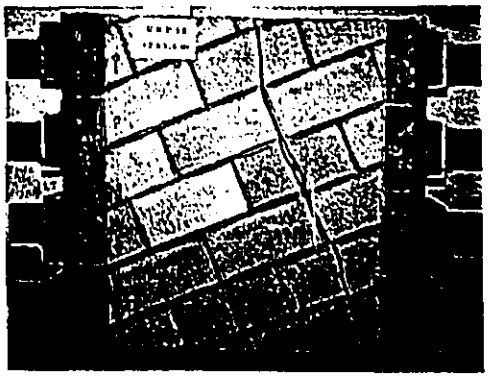

(b) UNP12 (θ=22.5°)

(c) UNP13 (θ=45°)

(d) UNP14 (θ=67.5°)

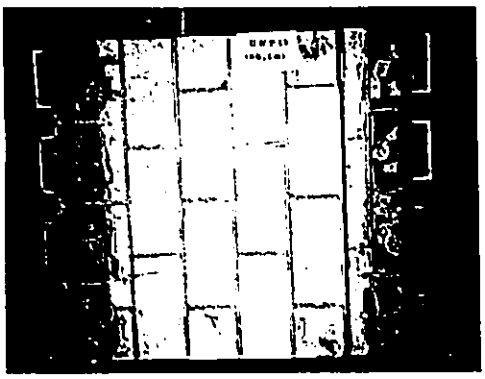

(e) UNP15 (θ=90°)

Fig. 4.5 Modes of failure under uniaxial tension.

For panels UNP12 and UNP14, which were tested, respectively, with θ=22.5 and 67.5°, the fracture planes did not occur along planes normal to the applied tension, but rather they followed the mortar joint planes. As shown in Fig. 4.5(b), the fracture plane took place along the head joint plane for θ=22.5°, whereas it followed the bed joint plane for θ=67.5° (Fig. 4.5(d)).

For panel UNP13, which was tested with θ=45°, the bed and head joints were subjected to equal shear and normal stresses. A stepped fracture pattern was observed through a combination of bed and head joints as shown in Fig. 4.5(c).

4.2.2.2 Strength Characteristics

The variation of the ultimate stress $(\sigma_1)_{ult}$ with the bed joint orientation θ, for the grouted concrete masonry assemblage under uniaxial tension, is presented in Fig. 4.6. The panels that failed along the bed joint planes (θ=67.5 and 90°) exhibited higher tensile strengths, in comparison with those panels that failed along the head joint planes (θ=0 and 22.5°). This could be attributed to the higher tensile strength of the grout,

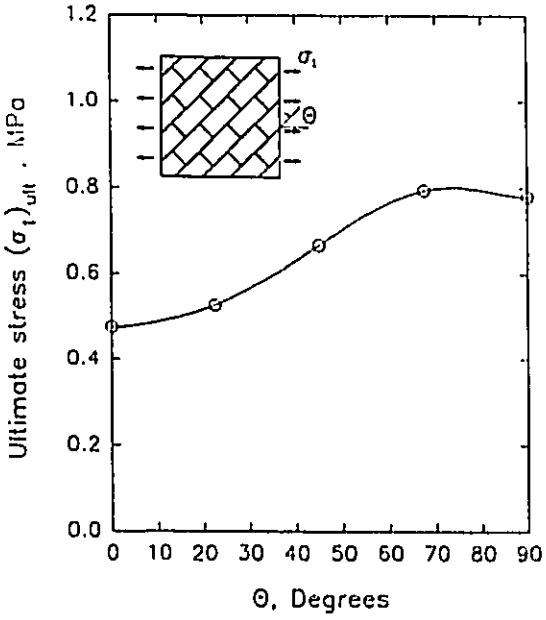

Fig. 4.6 Variation of ultimate stress under uniaxial tension with θ.

compared with that of the block face shells. The ratio between the maximum and the minimum tensile strengths was 1.67.

The tensile strengths of the masonry assemblage under consideration ranged from 5.0 to 14.5% of the compressive strengths obtained at the corresponding bed joint orientations.

4.2.2.3 Deformation Characteristics

The average stress-average strain relationships obtained for the panels tested under uniaxial tension are presented in Fig. 4.7. The curves shown in this figure illustrate the dependence of the deformation characteristics of grouted

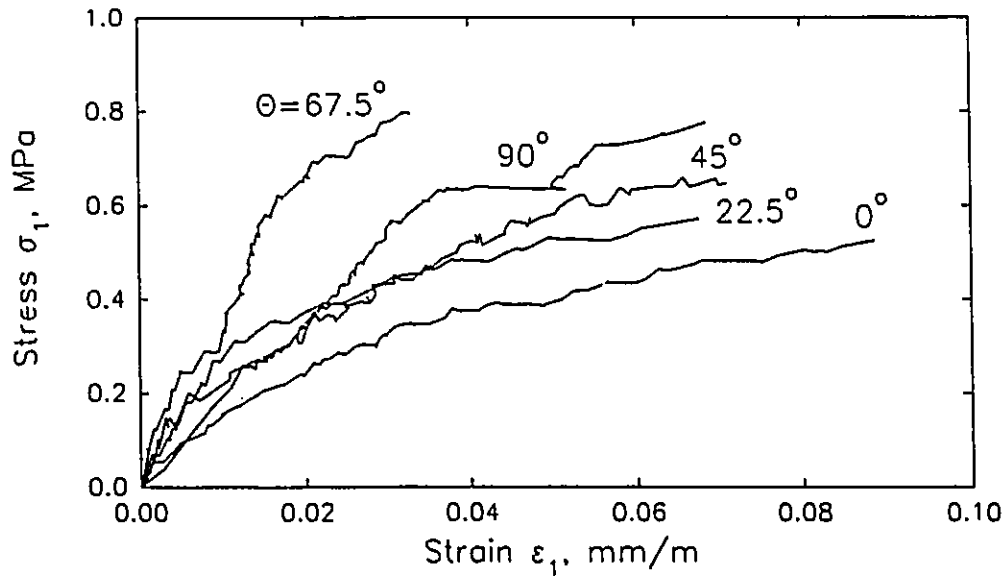

Fig. 4.7 Average stress-average strain relationships for panels UNP11-UNP15 (tested under uniaxial tension).

concrete masonry under uniaxial tension on the bed joint orientation. The panels that failed with fracture planes along the bed joint planes (θ=67.5 and 90°) exhibited stiffer stress-strain relationships, in comparison with the panels that failed with fracture planes along the head joint planes (θ=0 and 22.5°). The stress-strain relationship obtained for θ=45°, where a stepped fracture pattern was observed, lies in the centre between these two groups.

Approaching the failure stresses, noticeable changes in the slopes of the stress-strain relationships can be observed for the different bed joint orientations. This trend of behaviour may be the result of the stress redistribution taking place between the weak mortar joints and the surrounding grout cores or blocks, when the former reach their tensile capacities. However, it should be kept in mind that no cracks could be detected visually in the mortar joints prior to failure of the panels.

4.2.3 Biaxial Tension-Compression

4.2.3.1 Modes of Failure

As indicated in Table 4.1, Six unreinforced panels (UNP6-UNP10 and UNP16) were tested under biaxial tension-compression with different principal stress ratios. Four of these panels, UNP8-UNP10 and UNP16, were tested under the effect of the same state of stress of σ_1/σ_2=1/-1.09, but with different bed joint orientations. Under this state of stress, the behaviours were governed by the tensile characteristics of the assemblages. Panel UNP16, which was tested with

$\theta=0°$, failed in tension as the fracture plane followed a head joint plane as shown in Fig. 4.8(a). This mode of failure was identical to that observed under uniaxial tension for panel UNP11. Compared to the uniaxial tension tests, the existence of the principal compressive stress with $\theta>0°$, reduces the normal tensile stress acting on the mortar joint planes. As a result, the fracture planes observed for panels UNP8 and UNP10 ($\theta=22.5$ and $67.5°$ respectively) occurred along the mortar joints and passed through the blocks, as shown in Figs. 4.8(b) and (d). Panel UNP9, which was tested with $\theta=45°$, represents a case of almost pure shear along the mortar joints. A stepped failure, similar to that observed under uniaxial tension, was observed in this case, as shown in Fig. 4.8(c) .

Panels UNP6 and UNP7 were tested, respectively, under the effect of $\sigma_1/\sigma_2=1/-6.55$ and $1/-3.86$ having $\theta=45°$. A comparison of the modes of failure observed for these two panels with those of panels UNP9 and UNP13 reveals the effect of the principal stress ratio on the modes of failure. With the increase in the principal compressive stress σ_2, the mortar joint planes of panels UNP6 and UNP7 were subjected to normal compressive stresses. As a result, the failures of panel UNP6 and UNP7 took place along almost straight fracture planes passing through both blocks and grout, as shown in Figs. 4.9(a) and (b). The planes of failure in these cases were normal to the orientation of σ_1, rather than following the mortar joints.

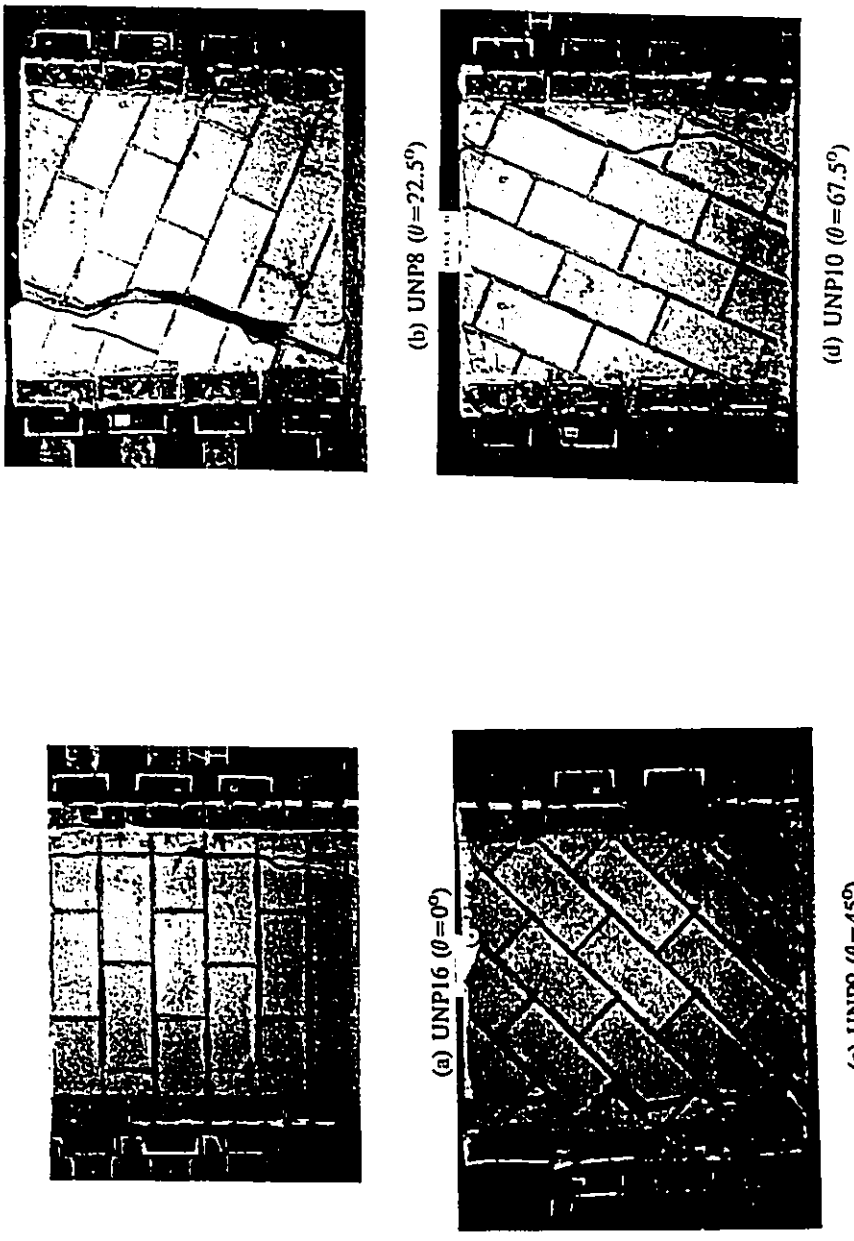

Fig. 4.8 Modes of failure under biaxial tension-compression (σ_1/σ_2=1/-1.09).

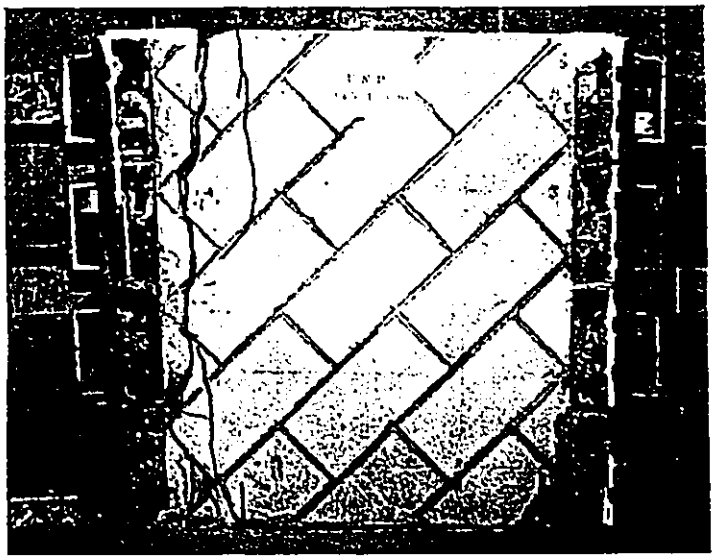

(a) UNP6 (θ=45° and σ_1/σ_2=1/-6.55)

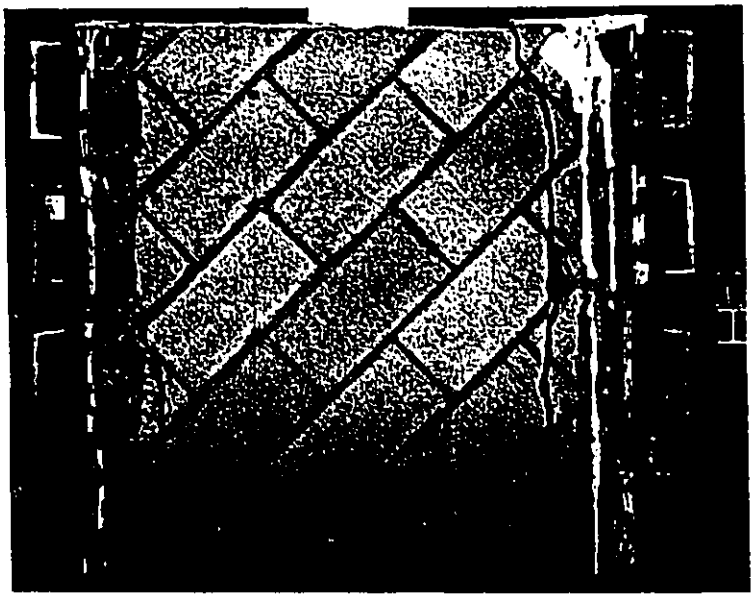

(b) UNP7 (θ=45° and σ_1/σ_2=1/-3.86)

Fig. 4.9 Modes of failure under biaxial tension-compression for θ=45°.

4.2.3.2 Strength Characteristics

The variation of the ultimate principal tensile stress of the masonry assemblage with the bed joint orientation, under the effect of σ_1/σ_2=1/-1.09 is shown in Fig. 4.10. The existence of the principal compressive stress σ_2 seems to reduce the effect of the bed joint orientation on the strength of the assemblage. The ultimate stresses obtained for the different bed joint orientations were almost the same.

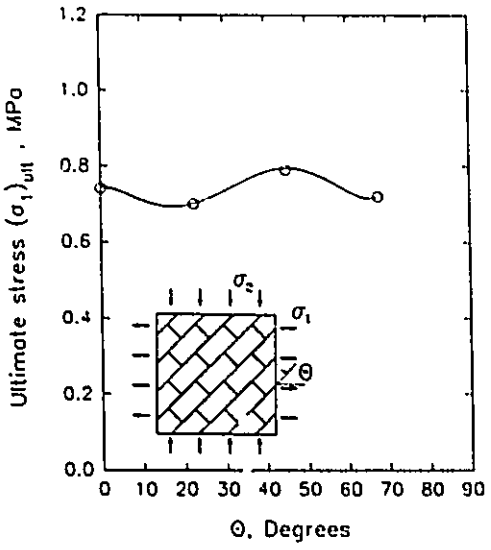

Fig. 4.10 Variation of ultimate stress with θ under σ_1/σ_2=1/-1.09.

The effect of the principal stress ratio on the masonry strength for θ=45° is shown in Fig. 4.11. Unlike concrete, the reduction in the algebraic ratio of σ_1/σ_2 from 1/0 to 1/-1.09 or to 1/-3.86 has led to an increase in the tensile strength. This increase can be attributed to the stepped pattern of failure, as the increase in the principal compressive stress counteracted part of the tensile stress acting along the mortar joints. As a result, the failures occurred at higher principal tensile stresses. Under the effect of σ_1/σ_2=1/-3.86 and 1/-6.55, where almost straight planes of failure normal to the principal tensile stress direction were observed, the reduction in the ratio σ_1/σ_2 resulted in a slight drop in the

tensile strength which was similar to the behaviour reported by Kupfer et al. (1969) for concrete.

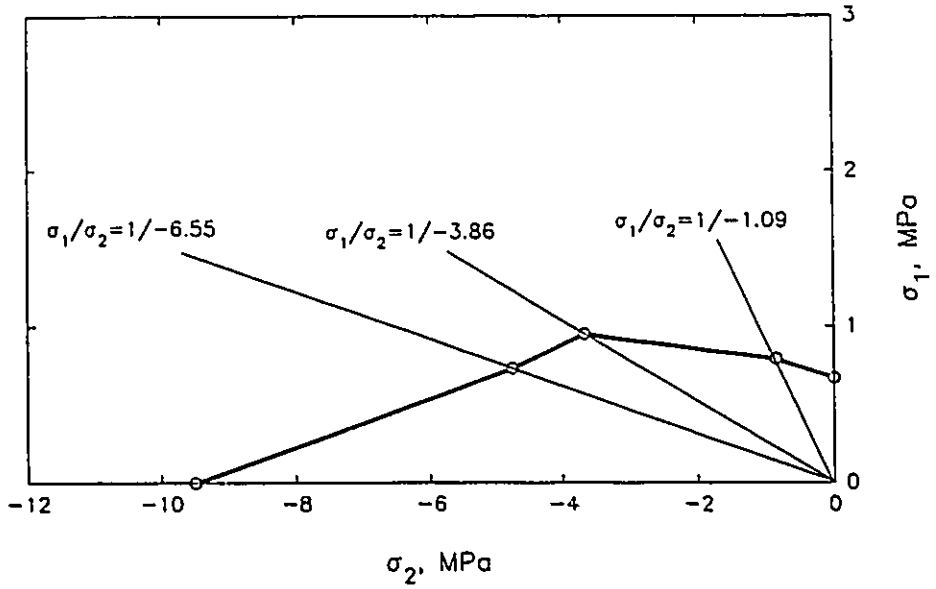

Fig. 4.11 Failure envelope of grouted masonry assemblage under biaxial tension-compression for θ=45°.

4.2.3.3 Deformation Characteristics

The average stress-average strain relationships obtained for the panels tested under the effect of σ_1/σ_2=1/-1.09 with different bed joint orientations are plotted in Fig. 4.12. The stress-strain relationships are presented in terms of the variations of the principal strains ϵ_1 and ϵ_2 with the principal tensile stress σ_1. Similar to the results obtained under uniaxial tension, the stress-strain relationships, especially in the principal tensile direction, were dependent on the bed joint orientation θ.

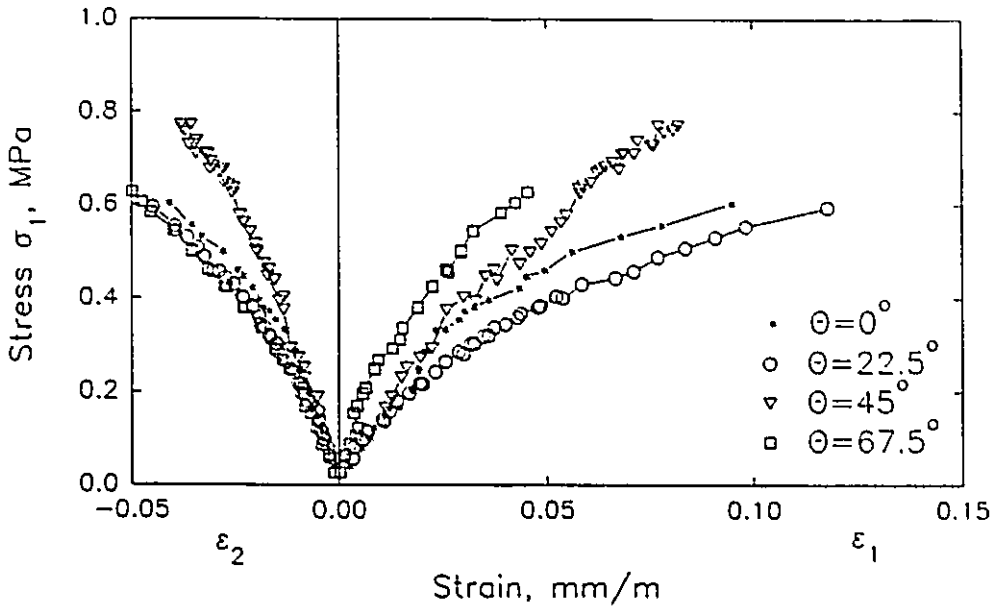

Fig. 4.12 Average stress-average strain relationships for panels UNP8-UNP9 and UNP16 (σ_1/σ_2=1/-1.09).

Figure 4.13 shows the stress-strain relationships obtained under different states of stress for θ=45°. Increases in the principal compressive stress σ_2 resulted in stiffer responses in the principal tensile stress direction. This behaviour could be attributed to the effect of the compressive principal stress in reducing the normal tensile stresses acting along the mortar joints, which consequently led to a change from the stepped failure pattern to a failure along straight planes normal to the principal tensile stress σ_1. The existence of the principal tensile stress did not seem to cause a significant change in the stiffness in the principal compressive stress direction. However, the compressive strain corresponding to the ultimate stress dropped with the increase in the principal tensile stress σ_1.

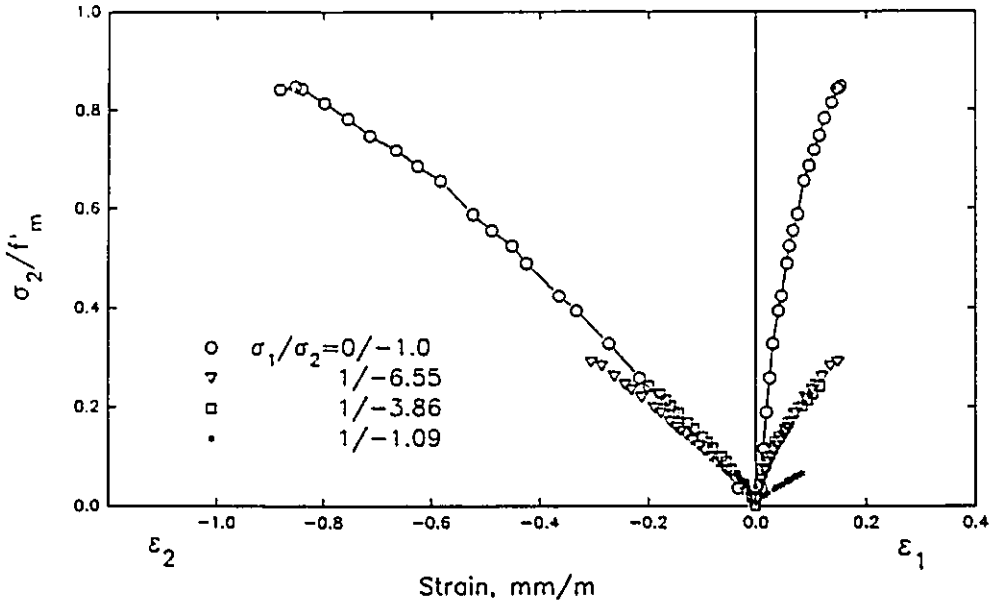

Fig. 4.13 Effect of principal stress ratio on average stress-average strain relationships for θ=45°.

4.3 TEST RESULTS OF REINFORCED PANELS (SERIES RP)

Series RP includes twenty reinforced panels that were tested under biaxial tension-compression states of stress to investigate the macro-behaviour of reinforced grouted concrete block masonry. The variables considered covered the bed joint orientation θ, the ratio between principal stresses σ_1/σ_2, and the percentages of reinforcement used parallel and normal to the bed joints. The results obtained along with the observations made regarding the different tests are arranged in the following sections. A summary of the results obtained is presented in Table 4.2. The properties of the corresponding control specimens are listed in Table 4.3.

Table 4.2 Test results of series RP

Panel	θ	σ_1/σ_2	ρ_p %	ρ_n %	$(\sigma_1)_{cr}$ MPa	$(\sigma_1)_{yp}$ MPa	$(\sigma_1)_{yn}$ MPa	$(\sigma_1)_{ult}$ MPa	Failure modes
RP1	0	1/-7.08	0.26	0.26	1.12	1.52	-	1.77	YP+C
RP2	22.5	1/-6.22	0.26	0.26	1.04	1.28	-	1.45	YP+C
RP3	45	1/-6.49	0.26	0.26	0.95	-	1.02	1.13	YP+C+SBJ
RP4	67.5	1/-7.7	0.26	0.26	0.86	-	1.09	1.16	SBJ+YN
RP5	45	0/-1	0.26	0.26	-	-	-	[s]	-
RP6	45	1/-13.5	0.26	0.26	0.72	-	-	0.76	C
RP7	0	1/-0.98	0.26	0.26	1.22	1.49	-	1.69	YP
RP8	45	1/-1.08	0.26	0.26	1.00	1.24	1.30	1.35	YP+YN
RP9	45	1/0	0.26	0.26	1.15	1.16	1.35	1.5	YP+YN
RP10	45	1/-0.98	0	0	1.37	-	-	1.37	L
RP11	45	1/-0.98	0.53	0.53	1.25	1.68	1.64	1.93	YP+**
RP12	45	1/-0.98	0.79	0.79	1.13	-	-	1.64	**
RP13	45	1/-1.08	0	0.53	1.22	-	-	1.22	L
RP14	45	1/-1.08	0.17	0.53	1.34	1.26	-	1.34	FP+L
RP15	45	1/-0.98	0.26	0.53	1.13	1.48	1.7	1.78	YP+YN
RP16	45	1/-1.02	0.17	0.26	1.29	1.07	-	1.29	FP+L
RP17	45	1/-0.98	0.53	0.26	1.30	1.43	1.40	1.72	YP+YN+**
RP18	45	1/-0.98	0.79	0.26	1.00	1.57	1.37	1.88	YP+YN
RP19	45	1/-1.08	0.26	0.26	1.37	1.26	1.32	1.55	YP+YN
RP20	0	0/-1	0.26	0.26	-	-	-	[ss]	-

$(\sigma_1)_{cr}$, $(\sigma_1)_{yp}$, $(\sigma_1)_{yn}$, and $(\sigma_1)_{ult}$ are the values of σ_1 corresponding to cracking, yield of reinforcement parallel to bed joints, yield of reinforcement normal to bed joint, and ultimate stress.

**	premature failure of steel bars.
C	Compression failure; characterized by spalling of block face shells.
L	Local failure along a single crack before developing a uniform crack pattern.
SBJ	Shear failure along bed joints.
YP and YN	Yield of reinforcement parallel and normal to the bed joints, respectively.
FP	Fracture of reinforcement parallel to bed joints.
[s] and [ss]	The tests were stopped at σ_2=14.4 and 13.5MPa respectively, because the ultimate stresses were larger than the loading capacity of the compression jacks.

Table 4.3 Material Properties for Series RP

Panel	Mortar compressive strength MPa	Grout compressive strength* MPa	Grout tensile splitting strength* MPa	f'_m 4-Course prism strength MPa
RP1	13.3	34.6	4.60	19.5
RP2	14.8	29.6	4.25	15.9
RP3	14.2	29.4	3.61	16.9
RP4	14.4	30.8	4.20	14.6
RP5	12.9	33.3	3.59	16.1
RP6	15.3	27.9	4.15	15.9
RP7	18.8	32.5	4.87	14.6
RP8	18.3	31.8	3.59	17.0
RP9	13.3	30.1	3.28	14.5
RP10	18.5	34.1	4.94	17.4
RP11	18.7	34.1	5.12	17.1
RP12	16.3	29.4	3.90	15.1
RP13	15.0	28.2	4.78	19.7
RP14	15.9	31.8	4.02	13.8
RP15	20.7	32.0	4.60	15.1
RP16	14.2	33.1	3.99	15.1
RP17	14.7	33.6	4.68	16.5
RP18	17.5	31.8	3.98	14.0
RP19	11.5	30.3		14.1
RP20	13.3	34.6	4.62	19.5
Mean	15.6	31.6	4.25	16.1
C.O.V	15.6%	6.7%	12.4%	11.3%

* The tests were performed on absorbent prisms cell moulded.

4.3.1 Effect of Bed Joint Orientation θ

A total of seven panels were tested to study the effect of θ on the behaviour of reinforced masonry. (It is worth noting that angle θ represents, in the case of reinforced masonry, the orientation of the reinforcement as well as the orientation of the mortar joints with respect to the principal stresses.) These panels were all reinforced equally parallel and normal to bed joints with $\rho_p=\rho_n=0.26\%$. Three of these panels (RP7, RP8, and RP19) were tested under ratios of biaxial stresses close to $\sigma_1/\sigma_2=1/-1$ to investigate the effect of θ when a tensile mode of failure dominates behaviour. Panel RP7 was prepared with $\theta=0°$, whereas panels RP8 and RP19 were prepared with $\theta=45°$. Panel RP19 was identical to RP8 and was used as a pilot test before fabricating the other reinforced panels. The other four panels consisting of RP1, RP2, RP3, and RP4 were prepared with $\theta=0$, 22.5, 45, and 67.5°, respectively. They were tested under biaxial states of stress with ratios of σ_1/σ_2 varying between 1/-6.22 and 1/-7.7 with an average of $\sigma_1/\sigma_2=1/-6.87$. These panels were used to investigate the effect of θ when a compression mode of failure controls the behaviour.

4.3.1.1 Observed Behaviour

The behaviours of the three panels (RP7, RP8, and RP19) tested under $\sigma_1/\sigma_2=1/-1$ were similar. As shown in Figs. 4.14 and 4.15, most of the cracks were vertical and normal to the principal tensile stresses even at $\theta=45°$. This behaviour could be attributed to the effect of having continuous grout cores both

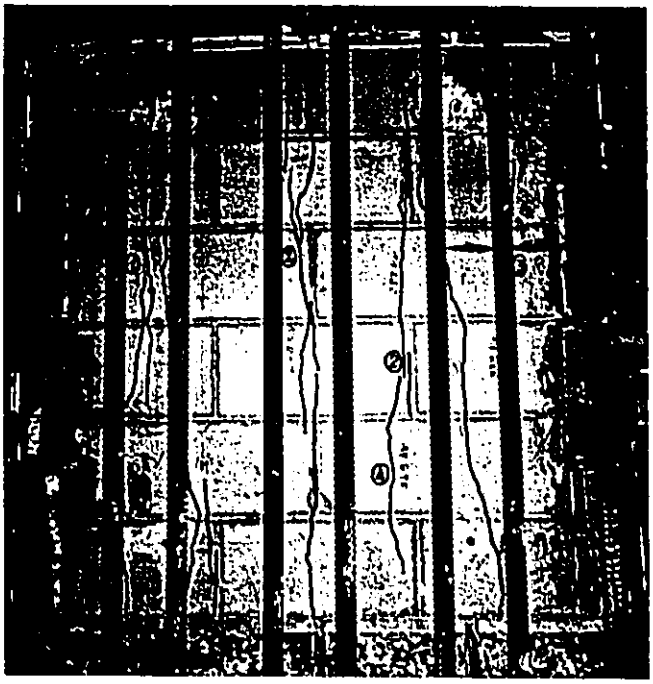

Fig. 4.14 Panel RP7 after failure
(θ=0°, σ_1/σ_2=1/-0.98, and $\rho_p=\rho_n$=0.26%).

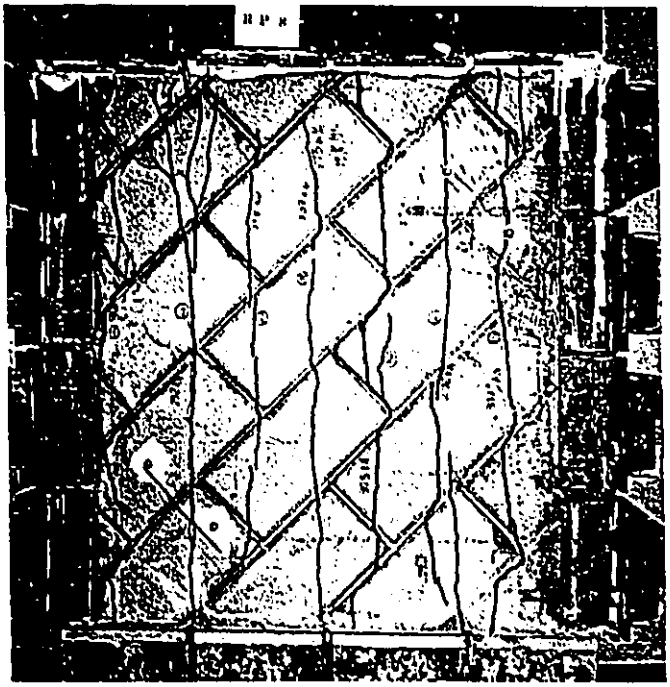

Fig. 4.15 Panel RP8 after failure
(θ=45°, σ_1/σ_2=1/-1.08, and $\rho_p=\rho_n$=0.26%).

normal and parallel to the bed joints. The appearance of the first crack was accompanied by a slight drop in the load along with a significant increase in the measured deformations. These increased deformations indicated the stress redistribution taking place between masonry and reinforcement. The panels were then able to resist higher load until other cracks formed. As the load was increased, the cracks increased in both number and width until extensive yielding of the reinforcement took place. The failure was characterized by a rapid increase in deformations under constant load. The number of cracks remained constant after yielding.

As shown in Fig. 4.14, most of the cracks observed in panel RP7 occurred along the head joint planes, which were normal to the principal stress direction (θ=0°). These planes represent the cross-sections with minimum resistance to tensile stress. In panel RP8, whereas the overall direction of the cracks was vertical, as shown in Fig. 4.15, a few of the cracks tended to propagate for short distances along the mortar joints especially in the locations where the cross-section of the continuous grout cores parallel to the bed joints was reduced by the block webs. The average crack spacing of panel RP8 was about 140 mm, compared to the 200 mm spacing of panel RP7.

Figures 4.16 to 4.19 show photos of panels RP1 to RP4, respectively. Each figure includes two photos; one taken in the test rig shortly after cracking and the second taken outside the test rig after failure. These photos

(a) After the formation of the first crack.

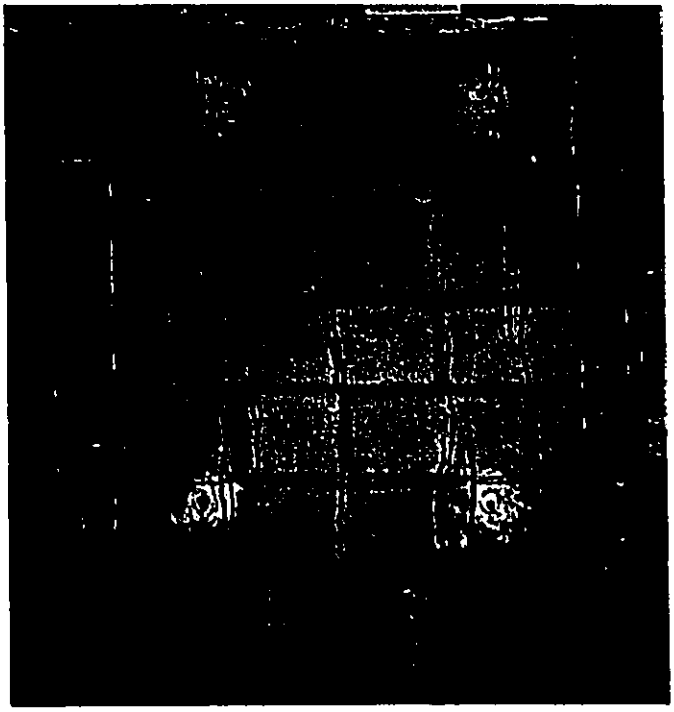

(b) After failure.

Fig. 4.16 Panel RP1; (θ=0°, σ_1/σ_2=1/-7.08, and $\rho_p=\rho_n$=0.26%).

(a) After the formation of the first crack.

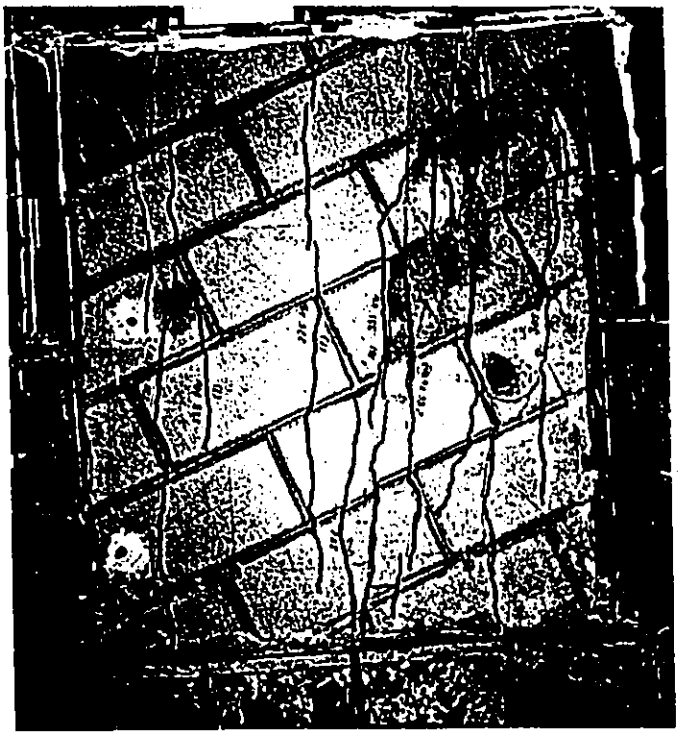

(b) After failure.

Fig. 4.17 Panel RP2; (θ=22.5°, σ_1/σ_2=1/-6.22, and $\rho_p=\rho_n$=0.26%).

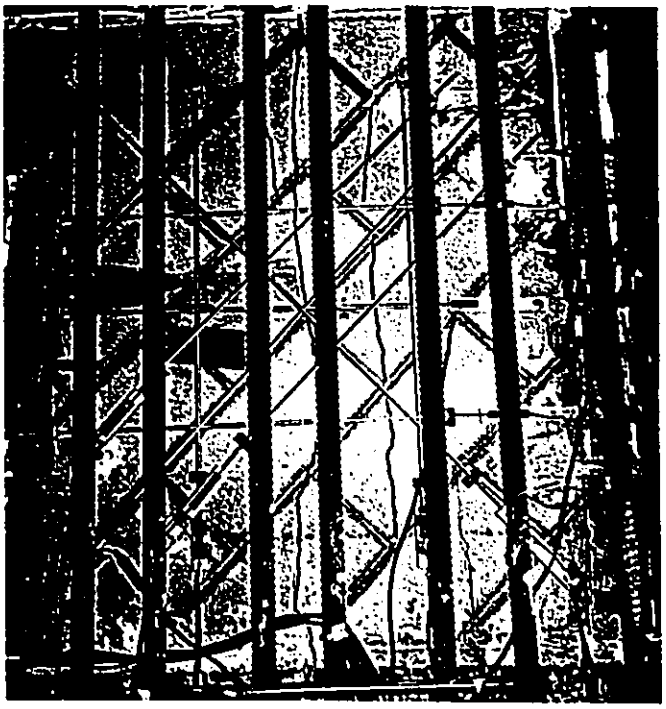

(a) After the formation of the second cracks.

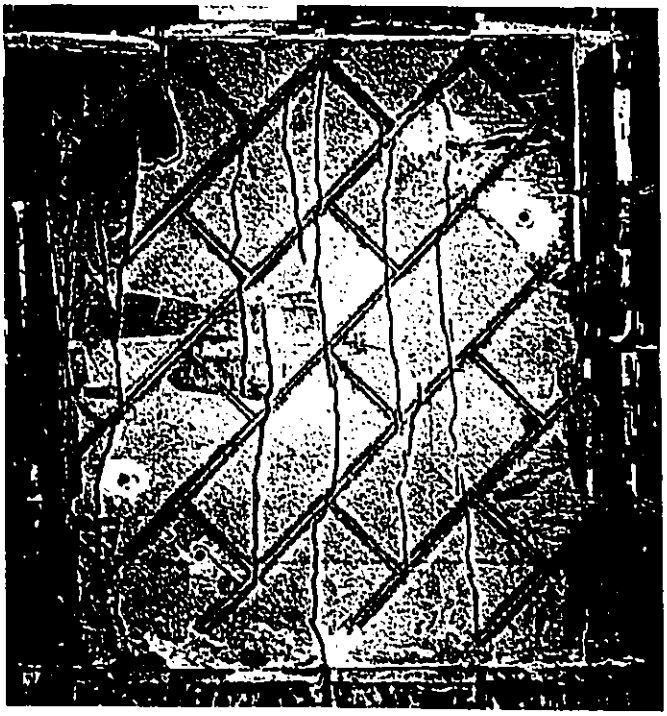

(b) After failure.

Fig. 4.18 Panel RP3; (θ=45°, σ_1/σ_2=1/-6.49, and $\rho_p=\rho_n$=0.26%).

(a) After the formation of the first cracks.

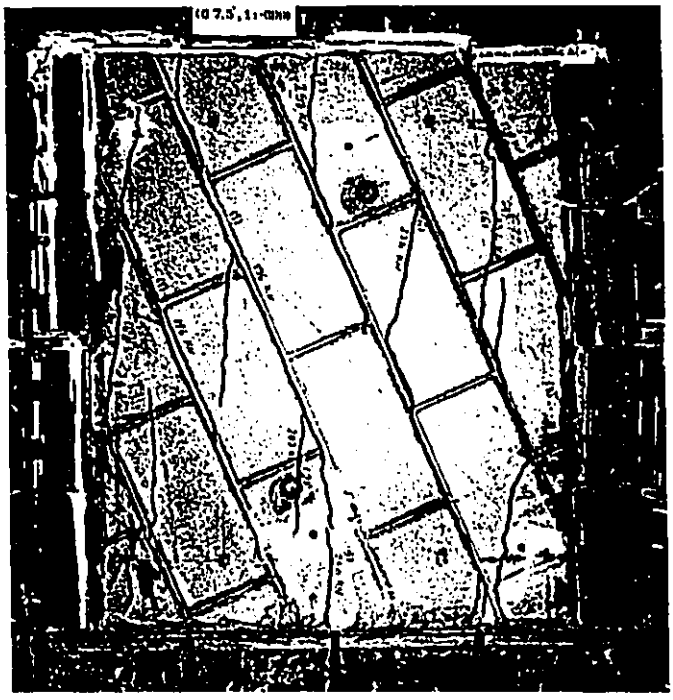

(b) After failure.

Fig. 4.19 Panel RP4; (θ=67.5°, σ_1/σ_2=1/-7.7, and $\rho_p=\rho_n$=0.26%).

reveal the effect of θ on the orientation and propagation of the cracks.

Whereas panels RP1, RP2, and RP3 exhibited cracks normal to the principal tensile stress direction, the first cracks in RP4 formed along the bed joints. The post cracking behaviours of these four panels were quite different, depending on the bed joint orientation θ. The cracks of panel RP1 (θ=0°) tended to follow the head joints as shown in Fig. 4.16(b). Yielding of the reinforcement parallel to bed joints resulted in greatly increased deformation in the principal tensile stress direction. This deformation was accompanied by a softer response in the principal compressive stress direction. Signs of distress and potential failure planes were observed in several regions in the panel. The onset of failure of the panel was signalled by spalling of face shells, as shown in Fig. 4.16(b). The spalling of the face shells left the grout cores to resist the applied compressive loads alone, leading to a dramatic drop in the load carrying capacity of the panel. The behaviour of RP2, with θ=22.5°, was similar to that observed for panel RP1 except that cracks were not necessarily associated with head joints. The compression failure was again initiated by spalling of the block face shells as shown in Fig. 4.17(b) after yielding of the reinforcement parallel to the bed joints.

As indicated before, the first cracks in panel RP4 formed along the bed joints. The cracking load in this case was lower than the value observed for panels RP1 and RP2. The reinforcement held the panel together and it was able

to resist a slight increase in the applied loads after initial cracking. As the load was increased, the cracks shown in Fig. 4.19(b) tended to propagate in the direction normal to the principal tensile stress. The shear deformation along the bed joints was accompanied by dilation which produced tensile stress in the reinforcement normal to the bed joints. Under the effects of this stress as well as the applied tensile force, the reinforcement normal to bed joints reached the yield strain. Reaching the yield stress limit allowed sliding shear failure to occur along the bed joints, as shown in Fig. 4.19(b), leading to a dramatic drop in the load carrying capacity.

Panel RP3, which was tested with θ=45°, exhibited a combination of the modes of failure observed in panels RP1 and RP4. The cracks were initially normal to the principal tensile stress direction as indicated in Fig. 4.18(a). Then, as the loads were increased, the cracks showed some tendency to follow the mortar joints. The measurements indicate that yielding occurred in the reinforcement normal to the bed joints. The average strain measured along the reinforcement in the other direction was close to the yield strain when failure took place in the form of sliding along the bed joints as well as spalling of the block face shells as shown in Fig. 4.18(b).

4.3.1.2 Strength Characteristics

The stresses at cracking and at yielding of the reinforcement as well as the ultimate stresses are summarized in Table 4.2 for the seven panels tested to investigate the effect of θ on the behaviour of masonry. In this table, yielding is

defined, at a macroscopic level, as occurring when the measured strains along the longitudinal directions of the steel bars reached the yield strains determined from the tension tests on the corresponding bars (Chapter 3). The properties of the control specimens corresponding to each panel are listed in Table 4.3.

A comparison between the cracking stress of panel RP7 (θ=0°) and the average of the corresponding values for panels RP8 and RP19 (θ=45°) does not show a significant effect of the bed joint orientation θ. The same remark can be made regarding the ultimate stresses. It should be kept in mind that these three panels were tested under biaxial state of stress of σ_1/σ_2=1/-1, so that the ultimate stresses were governed by yielding of reinforcement, as the principal compressive stresses were far from reaching the compressive strengths of the assemblages.

Figure 4.20 shows the variations of the cracking and ultimate stresses with the bed joint orientation θ, under biaxial states of stress with an average ratio of σ_1/σ_2=1/-6.87. Under this state of stress, the dependence of the masonry strength characteristics on θ is apparent, but more pronounced in terms of the ultimate stresses. Panels RP3 and RP4, which were tested with θ=45 and 67.5° respectively, exhibited significant reductions in the ultimate stresses, compared to the corresponding value of panels RP1, which was tested with θ=0°. These reductions in the ultimate stresses could be attributed to the shear failures observed in panels RP3 and RP4 along the bed joints, before the reinforcement achieved their full capacities.

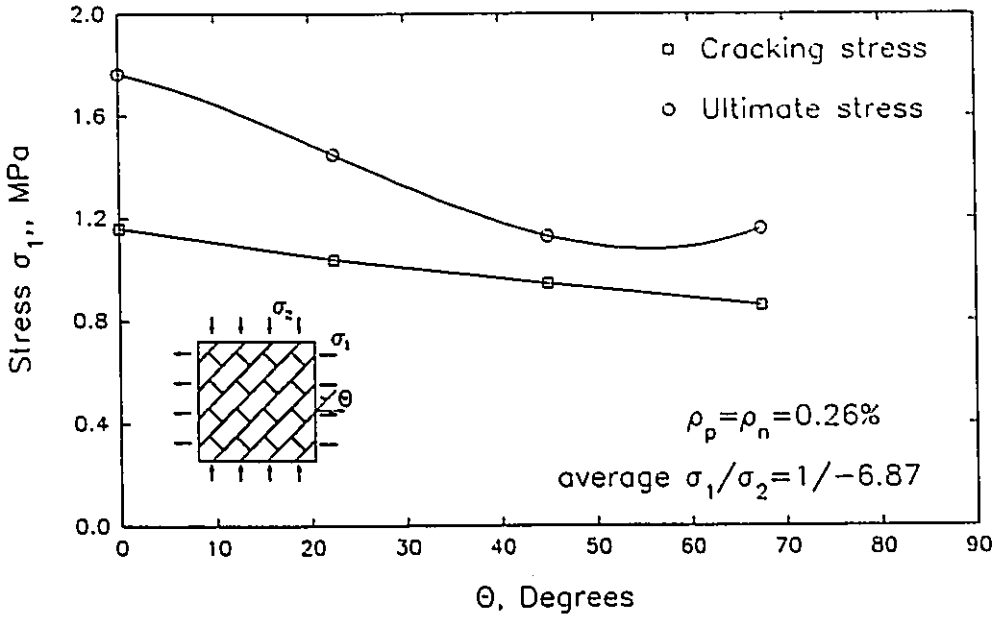

Fig 4.20 Variations of cracking and ultimate stresses with θ.

4.3.1.3 Deformation Characteristics

The average stress-average strain relationships for panels RP1-RP4, which were tested under biaxial states of stress with an average ratio of $\sigma_1/\sigma_2=1/-6.87$, are shown in Fig. 4.21. The initial parts of the principal tensile stress-strain relationships before cracking are magnified in Fig. 4.21(a). In this range of stress, the bed joint orientation θ does not seem to have a significant effect on the observed responses. The relationships for the four bed joint orientations are linear with the same slope which reflects an almost isotropic behaviour before cracking. This behaviour could be attributed to the effect of having continuous grout cores normal and parallel to the bed joints.

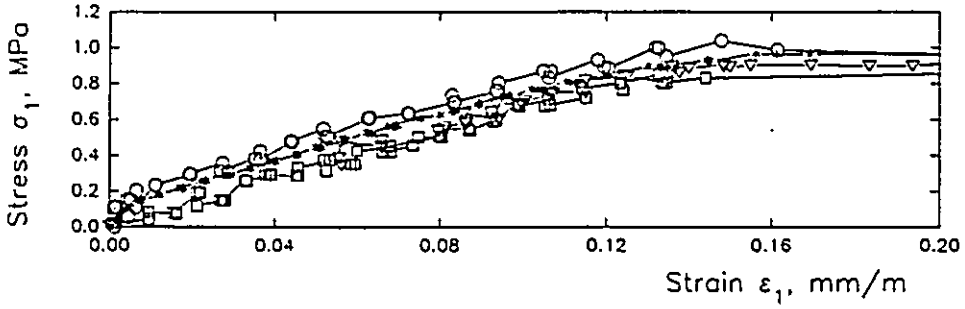

(a) Principal tensile stress vs principal tensile strain.

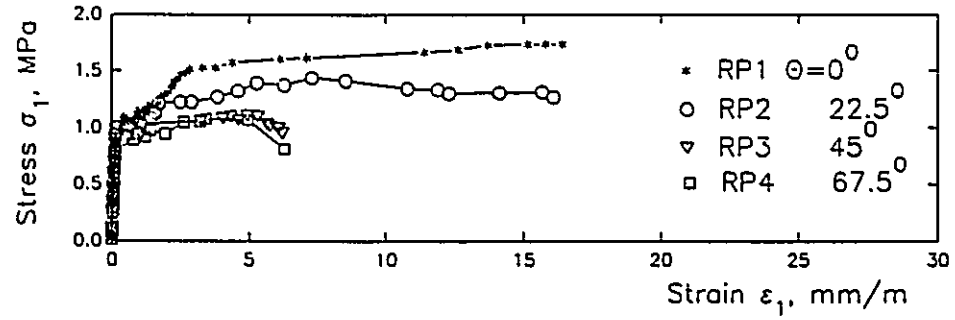

(b) Principal tensile stress vs principal tensile strain.

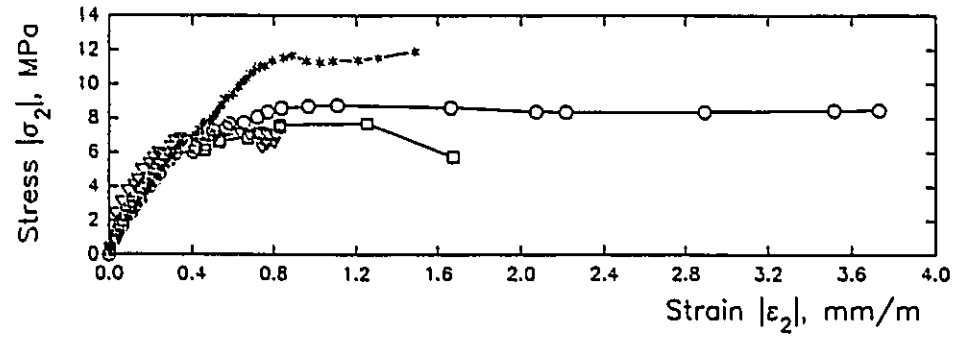

(c) Principal compressive stress vs principal compressive strain.

Fig. 4.21 Average stress-average strain relationships for different θ values (average σ_1/σ_2=1/-6.87).

The complete principal tensile stress-strain relationships for panels RP1-RP4 are presented in Fig. 4.21(b). The initiation and propagation of cracks, for each of these panels, are accompanied by significant reductions in the slopes of the curves. In this range of stress, the effect of the bed joint orientation θ on the stress-strain relationships is obvious. The stress-strain relationship of panel RP2, which was tested with θ=22.5°, reveals a higher stiffness degradation after cracking compared to panel RP1, which was tested with θ=0°. The stiffness degradation after cracking is much more apparent in the stress-strain relationships of panels RP3 and RP4, which were tested with θ=45 and 67.5° respectively.

The complete principal compressive stress-strain relationships are also shown in Fig. 4.21(c). Similar to the principal tensile stress-strain relationships, the bed joint orientation θ does not have a noticeable effect on the initial parts of the principal compressive stress-strain relationships before cracking. This changes with cracking, after which the slopes of the stress-strain relationships decrease significantly to values that depend on the bed joint orientation θ. The post-cracking stiffness of Panel RP1 is the highest followed by that of panel RP2 and then those of panel RP3 and RP4. The effect of cracking on reducing the stiffness in the principal compressive direction was also observed by Vecchio and Collins (1982 and 1986) in the results of their tests on reinforced concrete panels.

The anisotropic behaviour observed after cracking for panels RP1-RP4 can be attributed to the effect of the bed joint orientation θ on the value of the principal strain ϵ_1 associated with yielding of the reinforcement. As discussed in

Sec. 6.3.3, the principal tensile strain ϵ_1 associated with yielding of the reinforcement, for example, at θ=22.5° is higher than that at θ=0°, which consequently results in lower stiffness in the former case. In addition, both panels RP3 and RP4, as shown respectively in Figs. 4.18 and 4.19, exhibited cracks along the bed joints along with the cracks formed normal to the principal tensile stress direction. The deformations which took place along the cracked joints caused the reinforcement in panels RP3 and RP4 to yield at principal stresses lower than those of panels RP1 and RP2, resulting in higher stiffness degradations.

4.3.2 Effect of Principal Stress Ratio (σ_1/σ_2)

Eight panels can be used to study the effect of the principal stress ratio, σ_1/σ_2. They were all equally reinforced parallel and normal to bed joints with $\rho_p=\rho_n$=0.26%. Five of these panels (RP3, RP5, RP6, RP8, and RP9) were fabricated with θ=45°, whereas the other three (RP1, RP7, and RP20) were built with θ=0°. The ratios between the principal stresses applied on these panels are presented in Table 4.2.

4.3.2.1 Observed Behaviour

The observed behaviours and modes of failure changed significantly with the principal stress ratio σ_1/σ_2.

The behaviour of panel RP9 which was tested under σ_1/σ_2=1/0 was similar to that of panel RP8 (Fig. 4.15) which was tested under σ_1/σ_2=1/-1. However, in the absence of the principal compressive stress in RP9, there was much more

of a tendency for the cracks to propagate along the mortar joints, as shown in Fig. 4.22. The failures of these two panels were characterized by extensive yielding of the reinforcement placed both normal and parallel to the bed joints.

As mentioned in the previous section, failure of panel RP3 (Fig. 4.18), which was tested under σ_1/σ_2=1/-6.49 took the form of sliding shear along the bed joints accompanied by spalling of the block face shells. In this case, only the reinforcement normal to the bed joints reached the average yield strain. For panel RP6, which was tested under σ_1/σ_2=1/-13.5, the first crack was observed at a lower principal tensile stress than for either RP8 or RP9. This was a result of the existence of high principal compressive stress. Only a relatively few cracks were observed before the failure of panel RP6 occurred. Similar to RP3 and the prisms tested under uniaxial compression, a mixed mode of shear failure along the mortar joints and spalling of the block face shells took place as shown in Fig. 4.23. In this test, neither the reinforcement placed parallel nor normal to the bed joints reached the yield strain. The test performed on RP5 under uniaxial compression had to be stopped before failure. The load reached more than 80% of the capacity of the compression jacks without any sign of distress or cracking. However, the deformation measurements indicated that the panel loading was beyond the range of the linear behaviour at the principal compressive stress σ_2 of 10.4 MPa.

Panels RP7, RP1, and RP20, fabricated with θ=0°, were tested under biaxial states of stress of σ_1/σ_2=1/-7.08, 1/-1 and 0/-1, respectively. Failure of

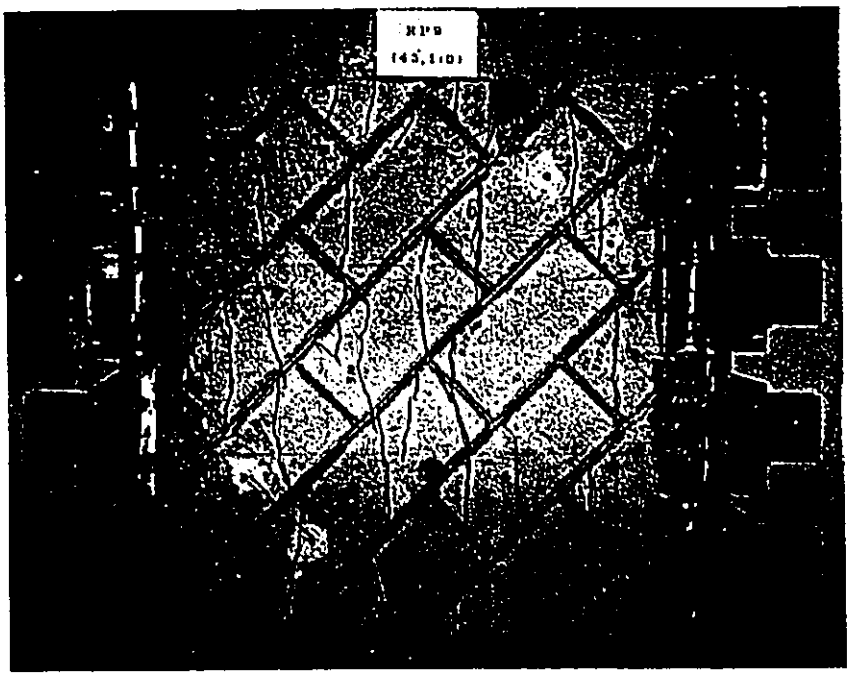

Fig. 4.22 Panel RP9 after failure; (θ=45°, σ_1/σ_2=1/0, and $\rho_p=\rho_n$=0.26%).

Fig. 4.23 Panel RP6 after failure; (θ=45°, σ_1/σ_2=1/-13.5, and $\rho_p=\rho_n$=0.26%).

panel RP7 was characterized by extensive yielding of the reinforcement parallel to the bed joints, whereas failure of panel RP1 occurred by spalling of the block face shell after the yielding of the reinforcement parallel to the bed joints. Similar to panel RP5, the compression failure load of panel RP20 was higher than the capacity of the compression jacks. The test was stopped when the principal compressive stress reached a value of 13.5MPa.

4.3.2.2 Strength Characteristics

The stresses at cracking and at yielding of the reinforcement as well as the ultimate stress are included in Table 4.2 for each of the eight panels tested to study the effect of σ_1/σ_2. In addition, the tension-compression failure envelope for $\theta=45°$ and $\rho_p=\rho_n=0.26\%$ is shown in Fig. 4.24. Because the ultimate stress of panel RP5 was higher than the loading capacity of the compression jacks, the

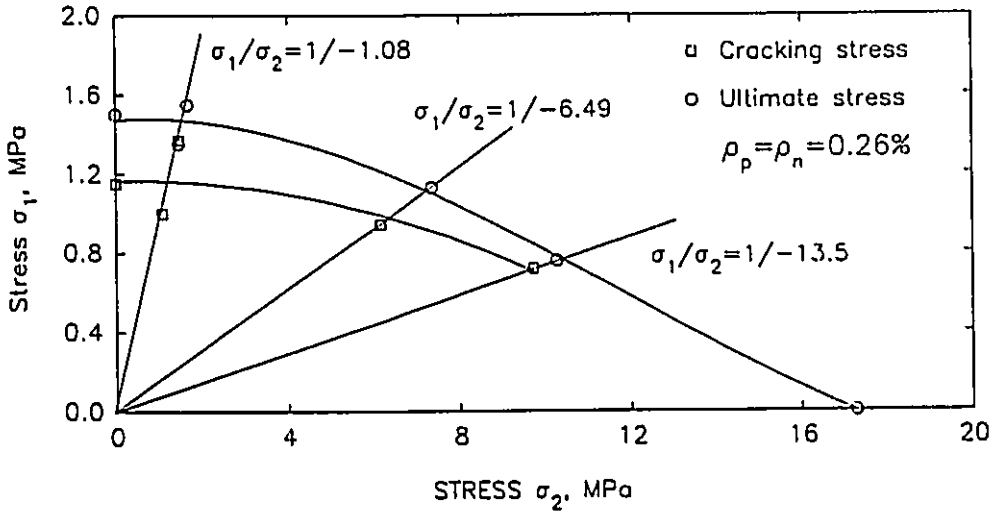

Fig. 4.24 Envelopes of the cracking and the ultimate stresses of reinforced masonry assemblage with $\theta=45°$.

ultimate compressive stress under uniaxial compression in Fig. 4.24 was taken equal to the average compressive strength of three prisms tested with θ=45°. The envelope of the cracking stress is also presented in this figure. The change of the principal stress ratio from σ_1/σ_2=1/0 to 1/-1 did not seem to have a significant effect on either the cracking or ultimate stress. The lack of effect on the ultimate stress could be attributed to the fact that the same yielding of reinforcement mode of failure occurred under both states of stress. Further increase in the algebraic ratio σ_1/σ_2 (moving towards the state of uniaxial compression) resulted in reductions in both the cracking and ultimate stresses, as the failures changed from the tensile mode of failure, characterized by yielding of reinforcement, to the compression modes of failure, characterized by spalling of block face shells. The difference between the ultimate stress and the cracking stress envelopes provides an indication of the contribution of reinforcement to the capacity of reinforced masonry. The contribution of reinforcement was maximum under uniaxial tension where the tensile mode of failure prevailed. The contribution of reinforcement decreased with the increase of the compressive stress, where compression failure occurred before the reinforcement yielded.

4.3.2.3 Deformation Characteristics

The average stress-average strain relationships obtained for the five panels RP3, RP5, RP6, RP8, and RP9, which were tested with θ=45°, are plotted in Fig. 4.25. Changes in the principal stress ratio σ_1/σ_2 can be seen to have significantly affected the post-cracking tensile stress-strain relationships.

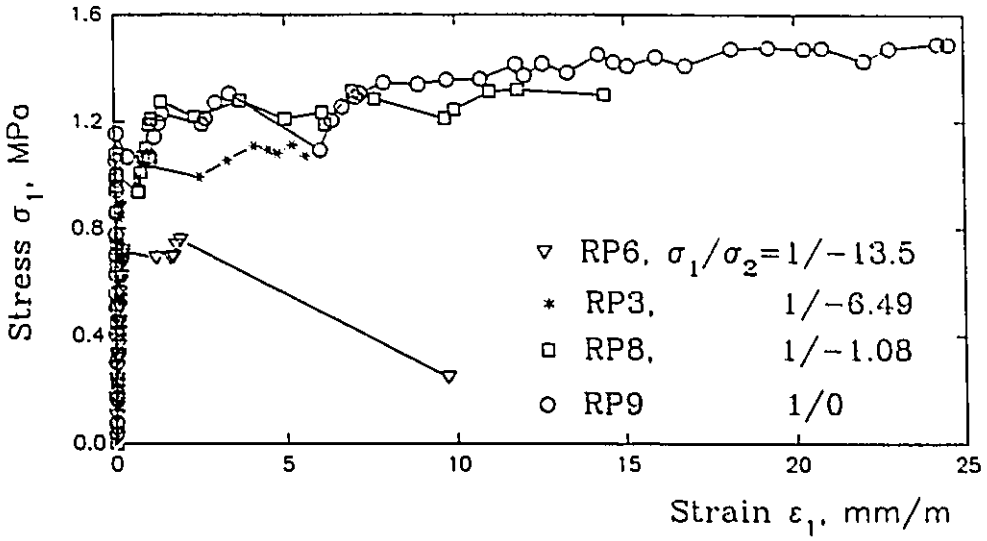

(a) Principal tensile stress vs principal tensile strain.

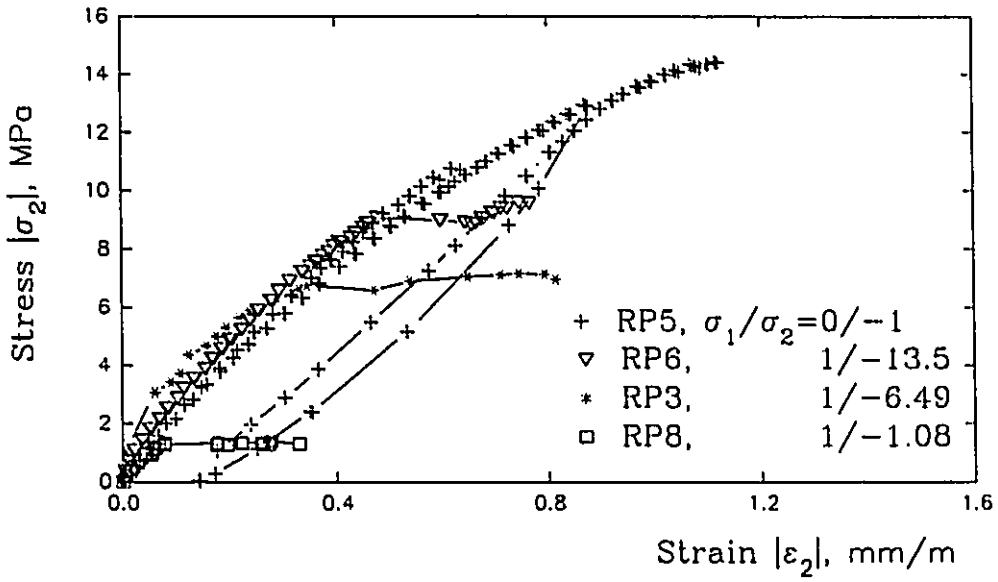

(b) Principal compressive stress vs principal compressive strain.

Fig. 4.25 Average stress-average strain relationships for different σ_1/σ_2 (θ=45° and $\rho_p=\rho_n$=0.26%).

Increasing the compressive stress was accompanied by reductions in the ultimate tensile stress and the associated tensile strain, as shown in Fig. 4.25(a). Increasing the compressive stress was also accompanied by increases in the ultimate compressive stress and the compressive strains associated with the cracking and ultimate stresses, as shown in Fig. 4.25(b). In the same figure, the effect of cracking on reducing the stiffness of the masonry assemblage in the principal compressive stress direction is obvious.

4.3.3 Effect of Percentage of Reinforcement

Eleven reinforced panels were tested under opposite and almost equal principal stresses with θ=45°, which produced a state of pure shear along the mortar joints (the directions of the reinforcement). This loading arrangement permits the effect of reinforcement on the shear response to be investigated without any interference from axial stresses. As a result, all the reinforcement used in these panels, parallel and normal to bed joints, is considered as shear reinforcement.

Five of these panels (RP8, RP19, RP10, RP11, and RP12) were equally reinforced parallel and normal to the bed joints. Panels RP13, RP14, and RP15 were unequally reinforced so that ρ_p= 0, 0.17, and 0.26% respectively, whereas ρ_n was kept constant at 0.53%. On the other hand, panels RP16, RP17, and RP18 were reinforced so that ρ_p=0.17, 0.53, and 0.79% respectively, whereas ρ_n was kept constant and equal to 0.26%.

4.3.3.1 Observed Behaviour

Panel RP10, which was not reinforced ($\rho_p=\rho_n=0$), failed by formation of a single crack oriented basically normal to the principal tensile stress direction. A closer examination of the crack pattern shown in Fig. 4.26 reveals that the crack was normal to the principal tensile stress σ_t over the zone where the grout cores normal and parallel to the bed joints intersect. Aside from that, the crack followed the mortar joints in a stepped manner where the grout cores parallel to the bed joints were intercepted by the block webs.

Panels RP8, RP19, RP11, and RP12 were equally reinforced parallel and normal to bed joints, so that $\rho_p=\rho_n=0.26$, 0.26, 0.53, and 0.79%, respectively. Panels RP8, RP11, and RP12 exhibited uniform well developed cracks as shown respectively in Figs. 4.15, 4.27, and 4.28. Failures of panels RP8 and RP19 were similarly characterized, as mentioned before, by yielding of reinforcement in the two directions. Unfortunately, both RP11 and RP12 suffered premature failures, before the reinforcement reached its ultimate stresses, due to the fracture of some of the steel bars close to the loading plates. These premature fractures could be attributed to the stresses developed in the bars, near their ends, as they were bent and welded to the ends plates R (see Fig. 2.9). However, these tests showed considerable improvement in the capacity of the panels after cracking, due to the existence of the reinforcement.

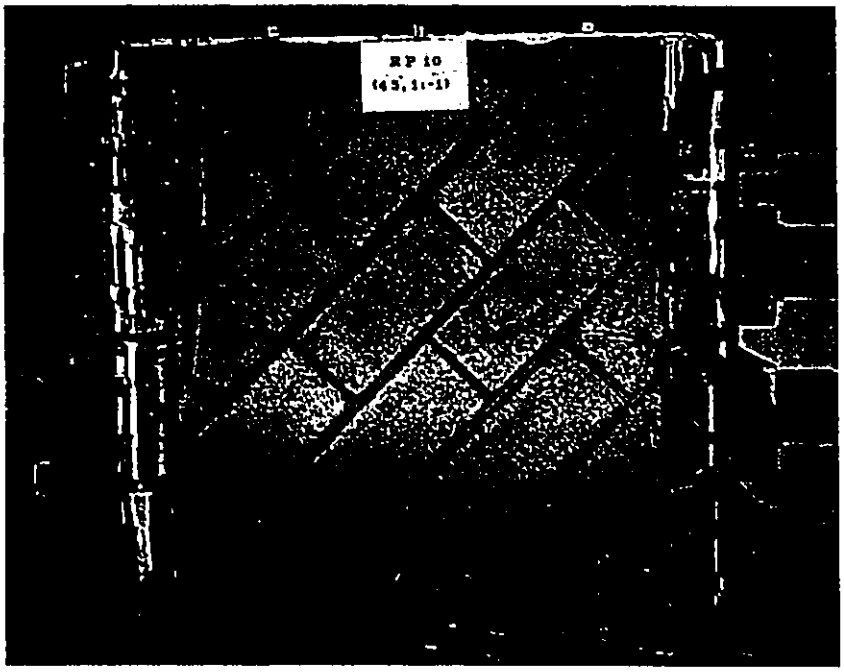

Fig. 4.26 Panel RP10 after failure; (θ=45°, σ_1/σ_2=1/-0.98, and $\rho_p=\rho_n$=0 %).

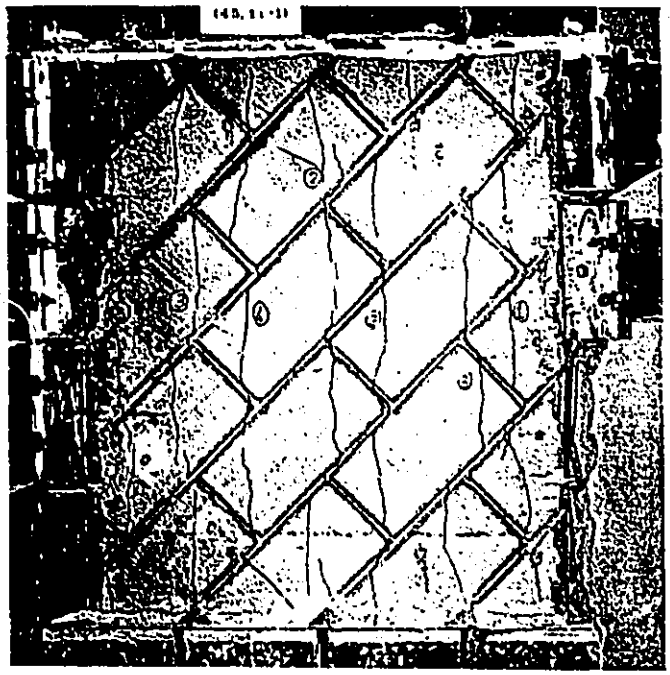

Fig. 4.27 Panel RP11 after failure
(θ=45°, σ_1/σ_2=1/-0.98, and $\rho_p=\rho_n$=0.53%).

Fig. 4.28 Panel RP12 after failure
(θ=45°, σ_1/σ_2=1/-0.98, and $\rho_p=\rho_n$=0.79%).

It is worth noting that the amount of reinforcement provided in panel RP13 was equal to the total amount of reinforcement used in RP8. In spite of this, panel RP13 could not resist even the cracking load after the first crack occurred. The load carrying capacity dropped almost to zero as secondary cracks formed parallel to the direction of the steel bars, as shown in Fig. 4.29. These cracks reduced the contribution of the dowel action of the reinforcement normal to the bed joints so that the reinforcement was not effective in resisting the applied stresses and in controlling the crack widths.

Although the total amount of reinforcement used in panel RP14 was even larger than the corresponding amount used in panel RP8, panel RP14 failed in a

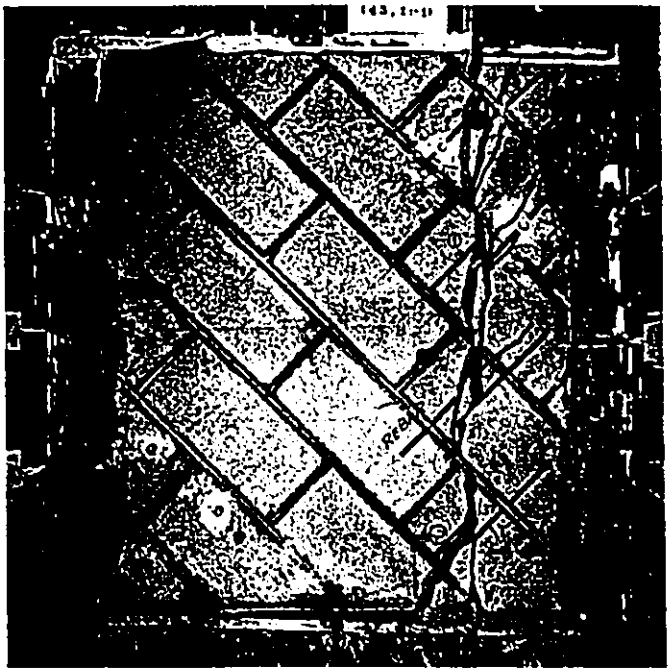

Fig. 4.29 Panel RP13 after failure
(θ=45°, σ_1/σ_2=1/-1.08, ρ_p=0, and ρ_n=0.53%).

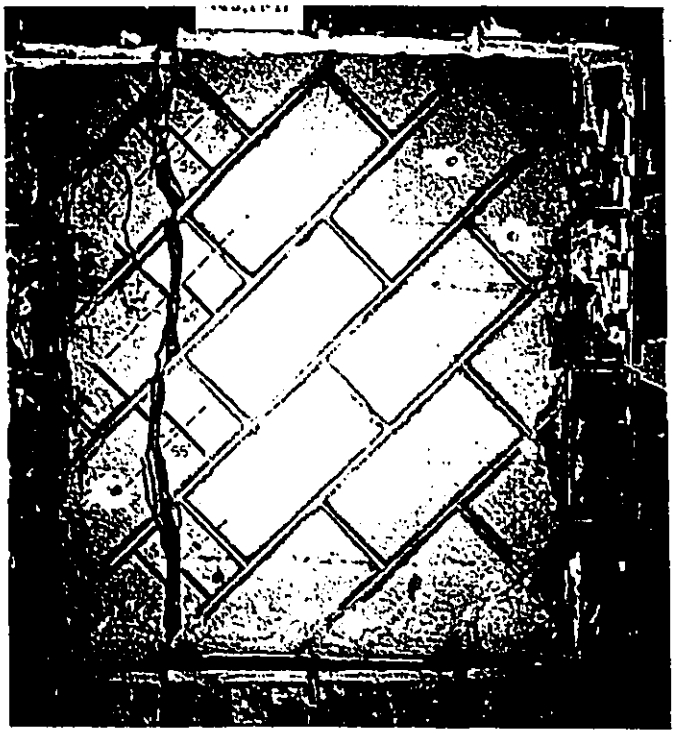

Fig. 4.30 Panel RP14 after failure
(θ=45°, σ_1/σ_2=1/-1.08, ρ_p=0.17, and ρ_n=0.53%).

brittle manner similar to RP13. As shown in Fig. 4.30, panel RP14 did not exhibit a uniform distribution of cracks, instead only two cracks were observed. This behaviour was similar to that of panel RP16 as shown in Fig. 4.31. These brittle behaviours could be related to the fact that the steel bars placed parallel to bed joints in panels RP14 and RP16 had limited ductility. As a result, the brittle rupture of the steel bars parallel to the bed joints occurred without significant stress redistribution, leaving the steel bars normal to bed joints to resist the applied stresses in a manner similar to that observed in panel RP13.

Although panels RP15, RP17, and RP18 were reinforced unequally normal and parallel to the bed joints, their behaviour was similar to the ductile behaviour of RP8. The three panels exhibited uniform well developed cracks in the direction normal to the principal tensile stress as indicated in Figs. 4.32 to 4.34. The steel bars in the two directions reached their yield strains which resulted in considerable increases in their load carrying capacity after cracking. Panel RP17 suffered fracture of two bars at their connection to the end plates, but this happened after reaching the yield strains. The steel bars used in these panels in the direction of the lower percentage of reinforcement had enough ductility to allow full stress redistribution to take place so that the steel bars in the other direction were able to reach their yield strains. The stress redistributions were accompanied by considerable shear deformations along the existing cracks as well as the formation of cracks along the mortar joints.

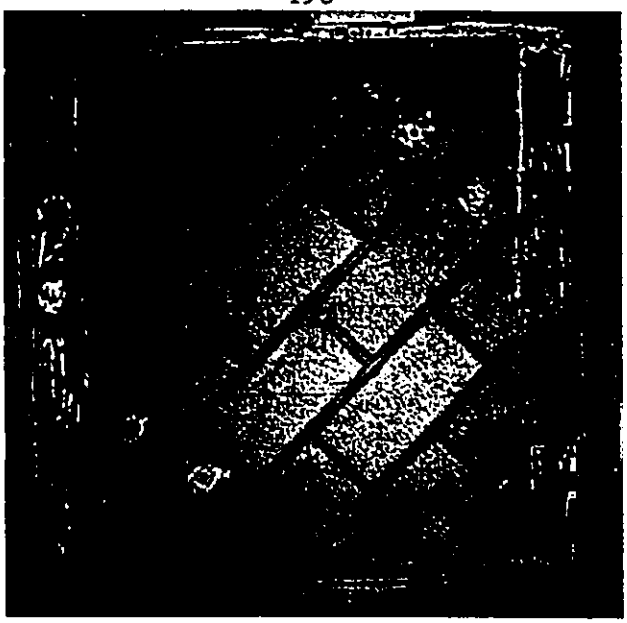

Fig. 4.31 Panel RP16 after failure
(θ=45°, σ_1/σ_2=1/-1.02, ρ_p=0.17, and ρ_n=0.26%).

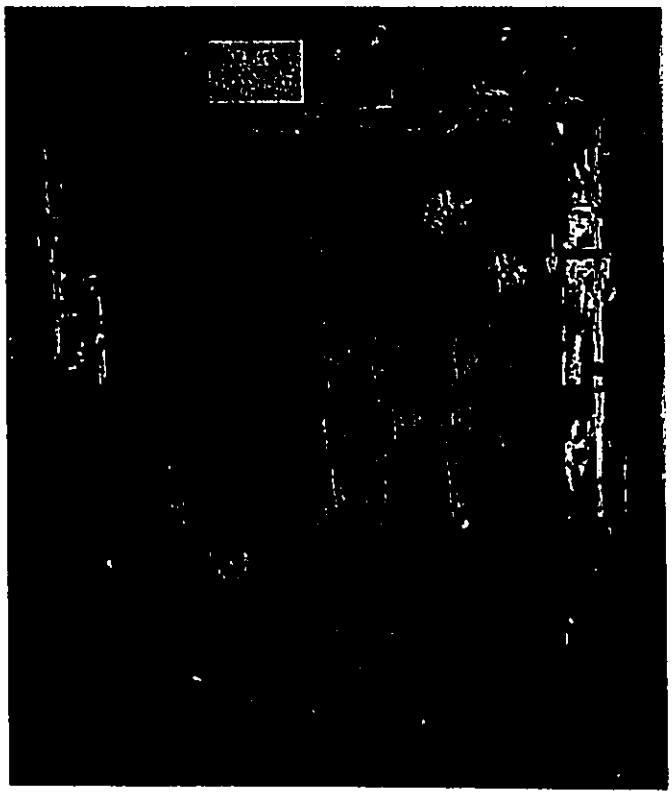

Fig. 4.32 Panel RP15 after failure
(θ=45°, σ_1/σ_2=1/-0.98, ρ_p=0.26, and ρ_n=0.53%).

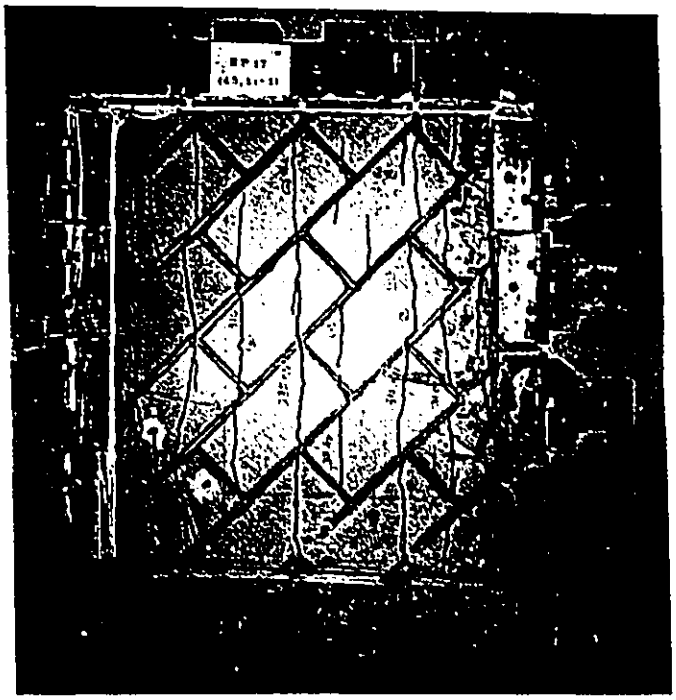

Fig. 4.33 Panel RP17 after failure
(θ=45°, σ_1/σ_2=1/-0.98, ρ_p=0.53%, and ρ_u=0.26%).

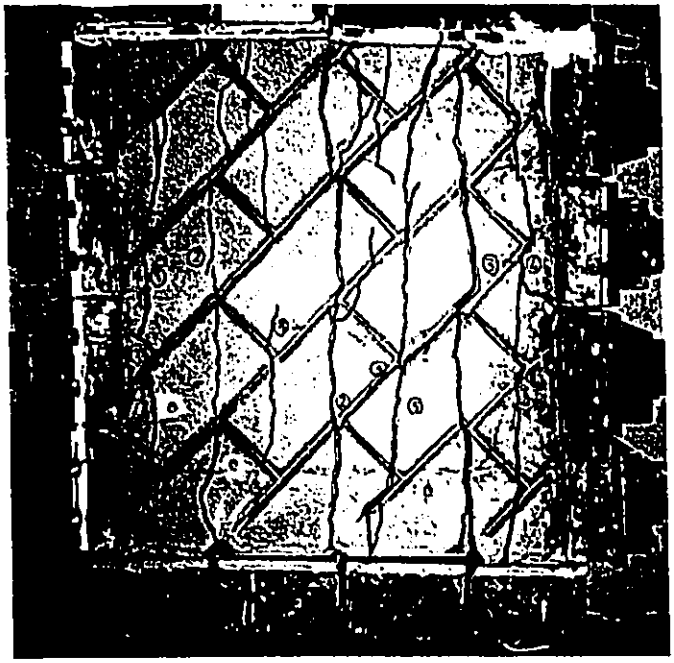

Fig. 4.34 Panel RP18 after failure
(θ=45°, σ_1/σ_2=1/-0.98, ρ_p=0.79%, and ρ_u=0.26%).

The behaviours observed for the above panels indicate the importance of having reinforcement in the two directions to resist the applied shear stresses. The ductility of the steel bars plays a significant role in the case of unequal percentages of reinforcement in the orthogonal directions. Ductility is required in the direction of the low percentage of reinforcement. This allows deformations and consequently stress redistribution to take place until the steel bars in the other direction reach their yield stress.

4.3.3.2 Strength Characteristics

The stresses at cracking and at yielding of the reinforcement as well as the ultimate tensile stresses recorded for the eleven panels tested under the state of pure shear along the mortar joint planes are summarized in Table 4.2. The mean cracking stress is 1.22 MPa, which is equivalent to $0.303\sqrt{f'_m}$. The C.O.V. is 15.6%. This mean strength is slightly lower than the value determined according to the formula adopted in the ACI code (1989) for predicting the diagonal tensile strength of the webs of reinforced concrete beams ($0.33\sqrt{f'_c}$ MPa).

The cracking stress and the ultimate stress are graphically illustrated in the bar chart in Fig. 4.35 for each panel. Where the ultimate stress is greater than the cracking stress, the difference between them, shown as a cross hatched area, represents the contribution of the reinforcement in resisting the increased loads after cracking. It is obvious that the contribution of the reinforcement to resisting the shear stresses along the mortar joints does not increase in proportion to the

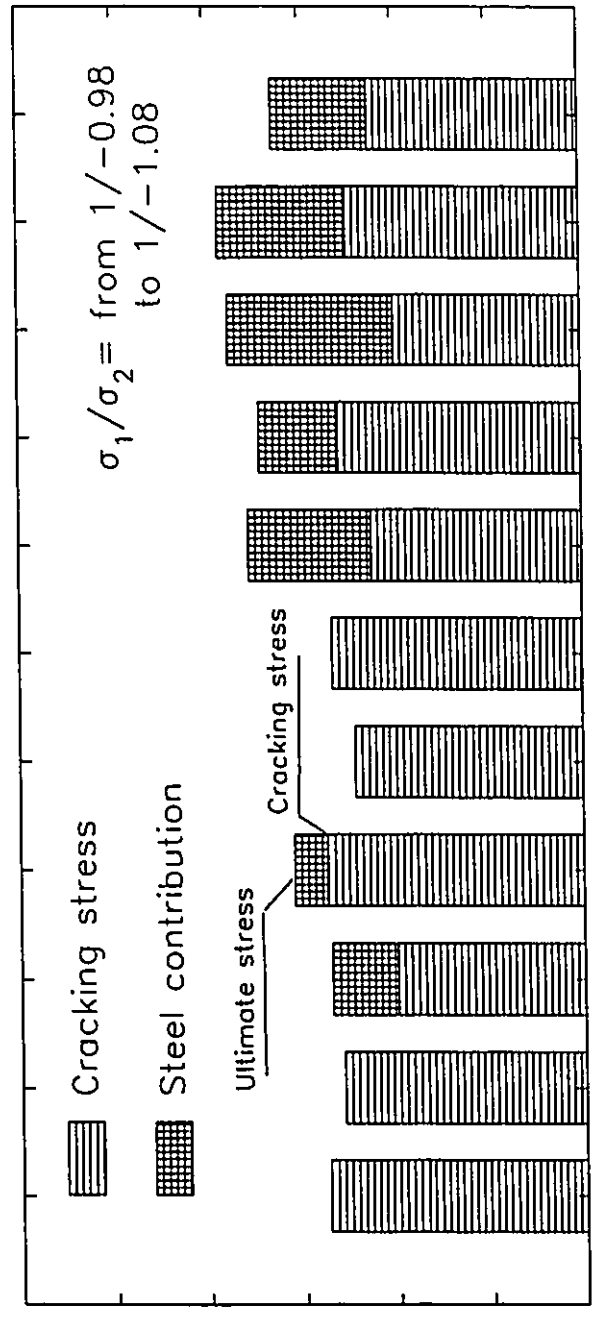

PANEL	RP10	RP16	RP8	RP19	RP13	RP14	RP15	RP17	RP18	RP11	RP12
ρ_p, %	0.0	0.17	0.26	0.26	0.0	0.17	0.26	0.53	0.79	0.53	0.79
ρ_n, %	0.0	0.26	0.26	0.26	0.53	0.53	0.53	0.26	0.26	0.53	0.79
$\rho_p+\rho_n$, %	0.0	0.43	0.52	0.52	0.53	0.70	0.79	0.79	1.05	1.06	1.58

Fig. 4.35 Cracking stresses and ultimate stresses under a state of pure shear along the mortar joints.

total percentage of reinforcement. Instead, it depends also on the distribution of the steel bars normal and parallel to bed joints as well as the ductility of the steel bars used in the direction of the lower percentage of reinforcement. Increases in the ultimate stress beyond the cracking stress were observed for panels RP8, RP19, RP11, and RP12 which had equal percentages of reinforcement in the two directions.

Although panels RP13 and RP14 contained total percentages of reinforcement equal to or greater than the total percentage of reinforcement used in panel RP8, the cracking load could not be sustained. The load carrying capacities of panel RP13 dropped dramatically with the development of the first crack, whereas panel RP14 was able to maintain loading near to the cracking load until the relatively brittle steel bars used parallel to the bed joints began to fail. Following rupture of these steel bars, panel RP14 behaved similar to panel RP13. These details of reinforcement did not allow stress redistribution to take place so that the steel bars in the other direction could achieve their capacity. As indicated in Table 4.2, the reinforcement normal to the bed joints of panels RP13, RP14 and RP16 did not yield. Conversely, panels RP15, RP17, and RP18, which were reinforced by ductile steel bars in the direction of the lower percentage of reinforcement, exhibited full yielding of the steel bars in the two directions at stresses higher than those of RP8. In this case, the contribution of the reinforcement increased with the increase in the total percentage of reinforcement.

It is worth noting that panels RP8, RP11, RP12, RP15, RP17, RP18, and RP19 contained total percentages of reinforcement much higher than the 0.2 and 0.3% that were suggested respectively by Schneider (1959) and Scrivener (1967) as upper limits, beyond which the reinforcement was not found to be effective in resisting shear forces.

4.3.3.3 Deformation Characteristics

The average stress-average strain relationships obtained for the panels tested under pure shear stresses along the mortar joints are shown in Figs. 4.36 and 4.37. The stress-strain relationships are presented in terms of the principal tensile stress and strain. Figure 4.36 includes the results for panels RP8, RP11, and RP12 which were equally reinforced parallel and normal to the bed joints, whereas Fig. 4.37 includes panels RP13-RP18 which were unequally reinforced parallel and normal to the bed joints. These two figures reveal the importance of paying attention to the details of reinforcement to be able to improve both strength and ductility of reinforced masonry compared to unreinforced masonry. This is demonstrated by the post-cracking response of panels RP8, RP11, RP12, RP15, RP17, and RP18 where the reinforcement yielded in the two directions achieving higher strength and more ductile behaviour. As observed for panels RP13, RP14, and RP16, simply increasing the amount of reinforcement without paying proper attention to the details can result in little, if any, improvement in the behaviour compared to unreinforced masonry.

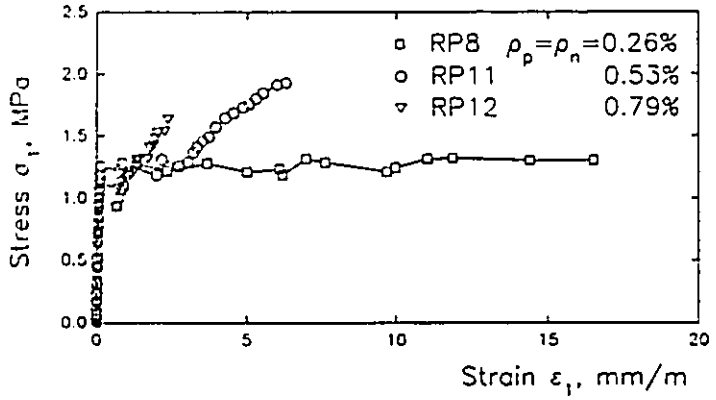

Fig. 4.36 Average stress-average strain relationships with $\rho_p=\rho_n$.

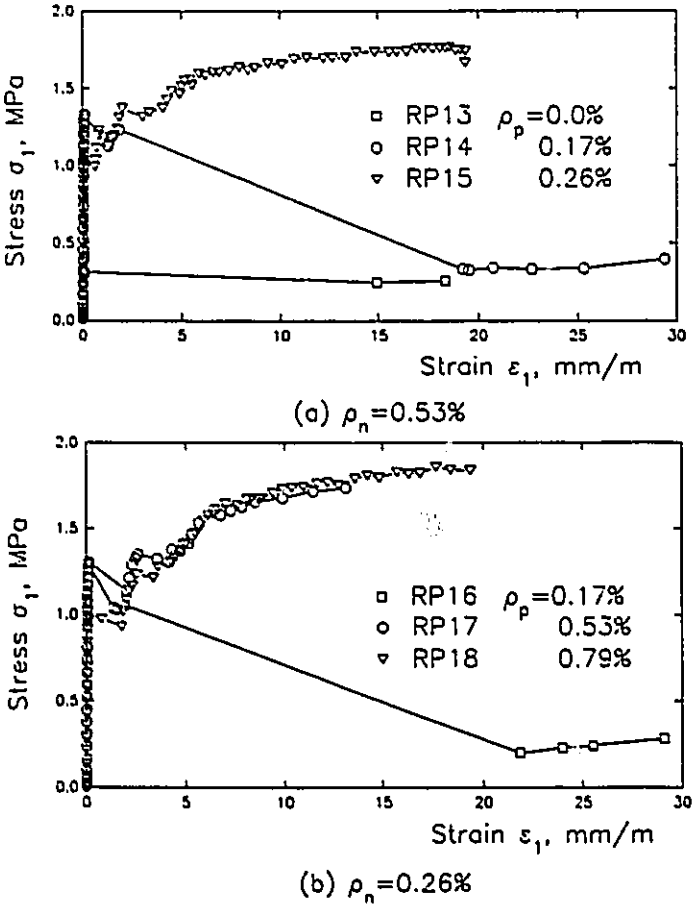

Fig. 4.37 Average stress-average strain relationships with $\rho_p\neq\rho_n$.

4.4 CROSS-SECTIONS IN GROUTED CONCRETE MASONRY

The panels of series UNP had continuous grout cores only normal to bed joints, whereas the panels of series RP had continuous grout cores both normal and parallel to the bed joints. The continuous grout cores parallel to the bed joints were the result of using blocks with knocked-out webs for a depth of 100 mm as illustrated in Fig. 3.2. Sketches of the in-plane cross-sections of the masonry assemblages used in the two series are presented in Fig. 4.38. This figure reveals how the unaligned webs of the blocks in the vertical direction leads to a smaller continuous grout cross-section at the bed joints. This effect is more pronounced in the case of using blocks having flares as well as tapered face shells and webs. Using the block dimensions, the grout cores in series UNP were calculated to have a minimum area along the bed joints in the order of 22.6% of the gross area. The minimum areas increased respectively to 35.2% and 29.5% normal and parallel to the bed joints in series RP where knocking-out the webs opened up the core cross-sections.

Several saw-cuts were made through the panels, during the course of the experimental program, to explore the possible existence of incomplete filling or other flaws in the grout. It should be remembered that the grout in these panels was compacted using a poker vibrator. Figure 4.39 shows marked locations of the shrinkage cracks observed along the vertical saw-cuts in panels UNP2 and UNP3 (cut normal to the bed joints through grout cores). The mortar joints and the shrinkage cracks were marked for clarity. It is observed that mortar fins

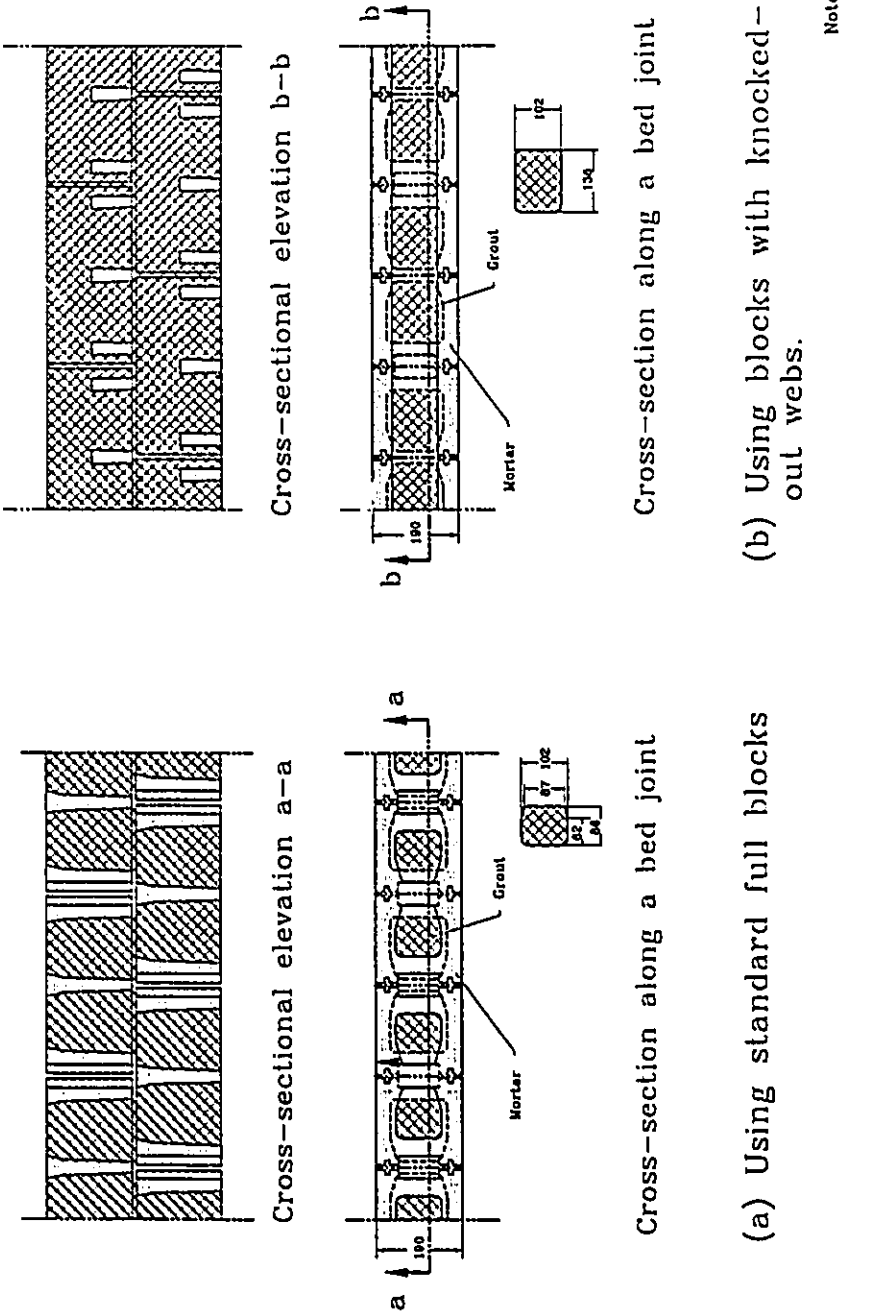

(a) Using standard full blocks (b) Using blocks with knocked-out webs.

Fig. 4.38 Cross-sections in grouted concrete masonry assemblages.

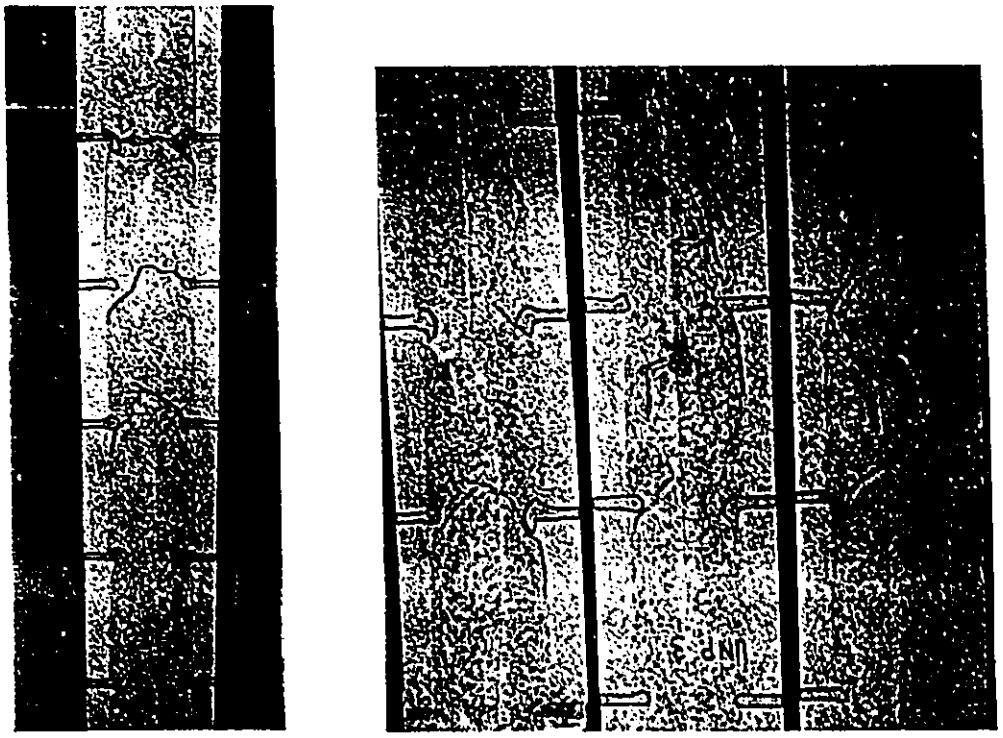

(a) Panel UNP2 (b) Panel UNP3

Fig. 4.39 Longitudinal saw cuts along the grout cores.

were extended inward and tended to hang over the lower blocks, as the panel was laid. These mortar fins result in smaller minimum grout core cross-sections. The mortar joints along with the flared tops of the blocks also provide a horizontal platform which tend to restrain additional settlement of the grout as water is absorbed from the grout. This leads to the formation of grout bridges similar to the ones identified before by Hegemier el al. (1978). In addition to significantly reducing the minimum area of the grout cores normal to the bed joints, the flaws

resulting from the mortar fins would be expected to influence the strength of the remaining section. The plane of fracture along the bed joint of panel UNP15 is shown in Fig. 4.40 after having the flaw-free grout areas marked. The ratio between this area and the gross area was measured and found to be in the order of approximately 15%, instead of the expected ratio of 22.6%. The situation was better in the RP series where the grout could flow both horizontally and vertically. Also the flared ends of the blocks were tri...med to a thickness of 44 mm.

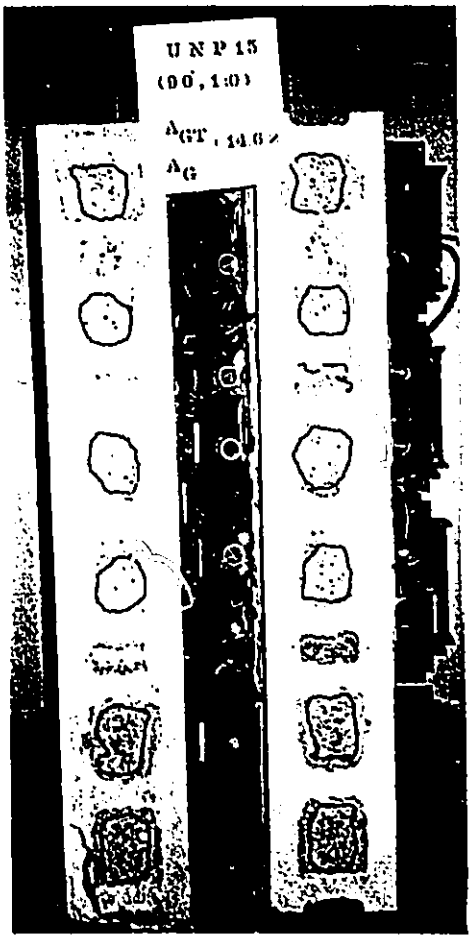

Fig. 4.40 The plane of fracture of panel UNP15.

4.5 CLOSING REMARKS

All possible modes of failure were observed and there was complete agreement between the modes of failure of the panels of series UNP tested under uniaxial compression and the corresponding prisms of series UCU. This finding, in conjunction with the observed uniform well developed crack patterns of the reinforced panels of series RP, demonstrate the effectiveness and the reliability of the panel dimensions and loading arrangement chosen to study the macro-behaviour of grouted concrete masonry. This test technique was developed to study the macro-behaviour of grouted concrete masonry under in-plane stresses without the need to adopt assumptions of elastic or isotropic behaviour to analyze the test results. The experimental results reported in this chapter have, by themselves, provided a body of test data which helps in the understanding of the in-plane behaviour of grouted concrete masonry. In the following chapters the results are also used in the development and verification of analytical models.

The following remarks are based on the observations and the results of the tests of series UNP;

1. The different modes of failure observed in the unreinforced panel tests can be classified under two major categories; failure along mortar joint planes and failure along planes normal to the principal stress directions. The first category covers the modes of failure that take place either separately along the bed joints and the head joints or as combined in a stepped pattern. This category confirms the anisotropic characteristic of grouted masonry. The second category covers

failures along planes normal to principal tensile stress (or strain) directions. This category defines the states of stress under which grouted concrete masonry has properties more closely resembling an isotropic material.

2. The behaviour of grouted concrete masonry under uniaxial compression is dependent on the bed joint orientation θ. Under this state of stress, the modes of failure, the strength characteristics, and the deformation characteristics change significantly with θ. A reduction in the ultimate compressive stress, compared to the value obtained for $\theta=0°$, was found to be about 36% for $\theta=67.5°$, corresponding with a shear failure mode along the bed joint plane.

3. The behaviour of grouted concrete masonry under uniaxial tension is also dependent on the bed joint orientation θ. The configuration of the fracture pattern changes with θ. The fracture plane does not always occur along a plane normal to the principal tensile stress; rather it can follow the mortar joint planes resulting in different strengths and different deformation characteristics depending on θ.

4. The tensile strengths of the unreinforced masonry assemblages considered in this investigation were found to be in the range of 5.0 to 14.5% of the corresponding compressive strengths obtained for the same bed joint orientations.

5. The behaviour of grouted concrete masonry and its dependence on the bed joint orientation change with the ratio between the principal stresses. A change in the applied stresses from uniaxial tension to a state of $\sigma_1/\sigma_2=1/-1$

resulted in a reduced dependence of the masonry strength on the bed joint orientation. In the latter case, the principal compressive stress, σ_2, counteracted part of the tensile stresses acting along the mortar joints and forced the failure to take place along planes normal to the principal tensile stress (or strain) directions. With further increase in the algebraic ratio of σ_1/σ_2 (moving towards the state of uniaxial compression), the compression modes of failure dominate the response. In this range of stresses, the effect of θ on the behaviour of grouted masonry becomes more pronounced because the ultimate compressive stress of the assemblage depends on the shear capacities of the mortar joint planes.

6. It is advisable not to use blocks with frogged ends and flared tops for grouted concrete masonry. The use of this kind of block results in grout cores with small cross-sections along the bed joint planes which limit the beneficial effects of the grout in strengthening the masonry and reducing its anisotropic characteristics.

The following additional remarks can be based on the results obtained in the biaxial tests of series RP.

1. Before cracking, the existence of grout cores both normal and parallel to bed joints reduces the anisotropic characteristics of masonry. Depending on the principal stress ratio, this behaviour could change after cracking. In the cases where the principal tensile stress σ_1 predominates and the modes of failure are characterized by yielding of reinforcement, the bed joint orientation does not have a noticeable effect on the failure stresses. Conversely, the bed joint orientation

θ plays a significant role on both strength and mode of failure when the principal compressive stress σ_2 dominates. In the latter case, depending on the bed joint orientation θ, the mode of failure could change from a compression mode of failure, after yielding of the reinforcement, to a compression mode of failure before the reinforcement reaches the yield point or to a shear mode of failure along the mortar joints. For the last two modes of failure, the effectiveness of the reinforcement is reduced and results in less ductile behaviour.

2. Similar to unreinforced masonry, the behaviour of reinforced masonry changes with the principal stress ratio σ_1/σ_2. In the cases where the principal tensile stress σ_1 predominates, the modes of failure are characterized by yielding of reinforcement. An increase in the algebraic ratio of σ_1/σ_2 results in reductions in both cracking and ultimate stresses, as the modes of failure change to compression modes of failure characterized by spalling of the block face shells.

3. The mean value of the cracking stresses for the panels tested under a state of pure shear along the mortar joints was found to be reasonably close to the empirical formula $(\sigma_1)_{cr}=0.303\sqrt{f'_m}$, which is similar to but slightly lower than the formula of $(\sigma_1)_{cr}=0.33\sqrt{f'_m}$ which is adopted in the ACI code (1989) for predicting the diagonal tensile strength of the webs of reinforced concrete beams (Vecchio and Collins 1982).

4. Relating the effectiveness of shear reinforcement only to its total percentage is incorrect. Increasing the amount of shear reinforcement can be beneficial to both shear strength and ductility, but this cannot be achieved unless

attention is paid to the details of reinforcement. First, it is important to distribute the shear reinforcing parallel and normal to bed joints in order to be able to resist the excess of forces that cannot be carried by masonry after the formation of diagonal cracks. This implies that the vertical reinforcement in a masonry shear wall may have to be designed to resist part of the shear force in addition to the tensile forces due to a bending moment. Second, using ductile steel bars is essential especially in the direction of the lower percentage of shear reinforcement. If this condition is not satisfied, premature failure is likely to take place along the first diagonal crack before the steel bars in the direction of higher percentage of shear reinforcement achieve their full yield strength.

5. Properly detailed shear reinforcement, with total percentages up to 1.06%, were shown to increasingly help to avoid brittle shear failure and to improve both the strength and the ductility of the reinforced masonry assemblage.

CHAPTER 5

MACRO-BEHAVIOUR MODEL

5.1 INTRODUCTION

Several attempts have been made to predict the in-plane behaviour of masonry walls. Some of these attempts were conducted at a microscopic level, while others were concerned with the response of masonry at the macroscopic level. The wide variation in the properties of the masonry constituent materials, on one hand, and the difficulties associated with using some of the previously developed models, on the other hand, put serious limitations on the application of these models. It is the main purpose of this chapter to introduce a model that can be described as reasonably simple, yet accurate and capable of capturing the different aspects of the in-plane behaviour of both unreinforced and reinforced grouted concrete masonry.

The in-plane behaviour of grouted concrete masonry is discussed in the next section, followed by the main assumptions adopted in the proposed macro-behaviour model. The procedures involved in formulating the model are also presented. This model is based on the multi-laminate model, developed by Zienkiewicz and Pande (1977) for jointed rock masses. Several modifications have been introduced in the proposed model to accommodate the differences

associated with the behaviour of grouted concrete masonry.

The multi-laminate model has been used extensively in research and design of jointed rock masses (Pande and Xiong, 1982). Pande and Gerrard (1983 and 1985) extended its application to cover reinforced jointed rock masses. It was also used by Gerrard and Macindoe (1985) in a qualitative investigation of the response of reinforced brickwork under in-plane tensile loading.

5.2 IN-PLANE BEHAVIOUR OF MASONRY

The modelling of grouted concrete masonry is a difficult task. In addition to the effects of creep, shrinkage and loading rate, which are associated with many structural materials, the behaviour of grouted concrete masonry is complicated by the following factors:

1. Grouted concrete masonry is a highly structured, composite material. It involves different constituents (masonry unit, mortar, grout, and steel bars), each having its own physical, mechanical, and geometrical characteristics. The behaviour of this assemblage, even under the simple condition of uniaxial compression reveals some aspects of the complexity associated with modelling grouted concrete masonry. It was reported by Hamid and Drysdale (1979) that, with increases in the applied compressive stress, both grout and mortar exhibit large lateral strains as they approach their ultimate stresses. These lateral strains, in turn, impose lateral tensile stresses on the masonry units which act under a state of triaxial stress; vertical compression and lateral biaxial tension as illustrated in Fig. 5.1. The failure of the masonry units, and consequently the

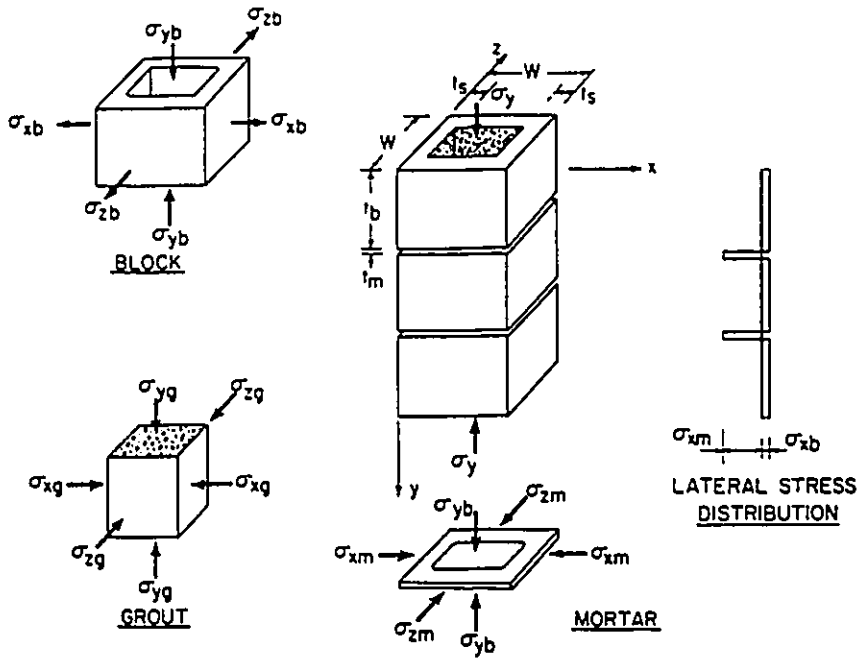

Fig. 5.1 Stress distribution in a grouted concrete prism under uniaxial compression (Hamid and Drysdale 1979).

masonry assemblage, is then related to the induced tension-compression state of stress, rather than the uniaxial compressive strength. Based on this argument, Hamid and Drysdale (1979) explained the reduction in the strength of grouted masonry, in comparison with that of ungrouted masonry, and proposed failure criteria for predicting the former.

2. Even for a particular assemblage, the interactions between the masonry constituents and their effects on global behaviour do not remain the same. They depend on the principal stress ratio and the orientation of the mortar joints with respect to the principal stress directions. As clearly shown in the literature review (Chapter 1) and by the experimental results obtained in this investigation,

masonry assemblages exhibit distinct directional properties due to the existence of the mortar joints acting as planes of weakness. This characteristic, which will be referred to hereafter as "inherent anisotropy", dominates the behaviour when failure follows the mortar joints. Its influence diminishes when failures take place along planes normal to the principal stress (or strain) directions, regardless of the bed joint orientation.

3. The formation of cracks in a masonry assemblage introduces another degree of anisotropy that will be referred to hereafter as "induced anisotropy". How the anisotropic characteristics (inherent and induced) interact and which one dominates, impose additional difficulty in modelling grouted concrete masonry. It should be kept in mind that, although modelling masonry using one of the models developed for simulating the behaviour of concrete may account for the induced anisotropy characteristics, the inherent part of the anisotropic characteristics is overlooked.

4. The contribution of reinforcement in resisting the stresses induced on the planes of weakness (mortar joints and cracking planes) is associated with different shear resisting mechanisms (friction, aggregate interlock, and dowel action) along with the tension stiffening effect.

5.3 MACRO-BEHAVIOUR MODEL

5.3.1 Introduction

Although the use of a micro-level analysis facilitates study of the influence of different parameters on the behaviour of masonry, there are serious limitations

on its general usefulness. First, the geometric characteristics of the masonry units and the mortar joints can lead to ill-conditioning of the algebraic system and/or instability of the numerical solution (Pietruszczak and Niu, 1992). Second, very sophisticated and detailed information is required about the characteristics of all of the materials and their interactions under various stress states and stress histories. Third, this kind of analysis becomes impractical for masonry shear walls and even large test assemblages.

From a consideration of the above factors, it was decided to model the behaviour of grouted concrete masonry at a macroscopic level. This technique has the advantages of being able to rationally explain the different aspects of masonry behaviour while remaining a relatively simple alternative to facilitate the modelling of the large masonry structures. In the macro-behaviour model described herein, certain considerations are also given to the micro-behaviour along the planes of weakness (mortar joints and crack planes) which yield a general and more realistic simulation of the anisotropic characteristics (inherent and induced) of the masonry assemblage.

As shown in Fig. 5.2, the reinforced masonry assemblage is replaced by an "equivalent material" which consists of a homogenous medium intersected by two sets of planes of weakness (along the head joint and bed joint planes) and two sets of reinforcement. Each set has its own characteristics and is described as an elastic-viscoplastic material. The macro-behaviour of the "equivalent material" is determined by smearing the influence of these sets throughout the respective

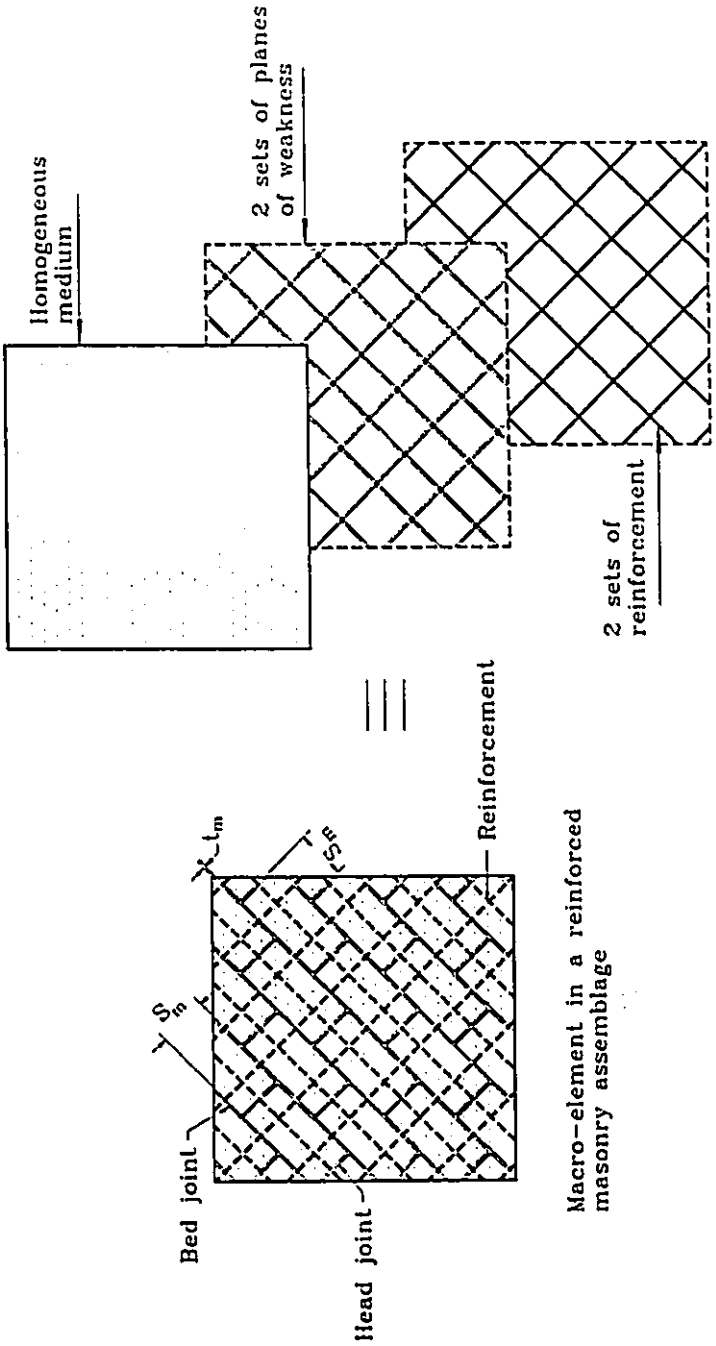

Fig. 5.2 Macro-element idealization

volumes that they occupy. This idealization provides a means of predicting highly anisotropic behaviour and is utilized to realistically model the inherent part of the anisotropic characteristics of masonry assemblages. The behaviour of the homogeneous medium is also described by an orthotropic model, originally developed by Darwin and Pecknold (1977), to account for the induced part of the anisotropic characteristics.

5.3.2 Assumptions and the Rheological Analogue of the Macro-Behaviour Model

The main assumptions adopted in the development of the macro-behaviour model are:

1. The planes of weakness and the reinforcement are uniformly distributed with spacings that are much smaller than the dominant dimensions describing the external geometry of a particular masonry structure.

2. Each set of planes of weakness and each set of reinforcement is modelled as an elastic-viscoplastic material, in which the strength is determined according to the Mohr-Coulomb failure criterion with a tension cut-off. Figure 5.3(a) shows the rheological analogue of an elastic-viscoplastic material (Zienkiewicz and Cormeau, 1972). It consists of a spring connected in series with a viscoplastic unit formed by a slider and a viscous dashpot connected in parallel. The slider, representing the plastic component, can only become active if the stresses go outside the yield surface. The instantaneous response of this material, symbolized by the spring, is elastic. If the stresses go outside the yield surface, the plastic

strains, symbolized by the slider, take place with time as the dashpot does not respond instantaneously. In this manner, the elastic-viscoplastic idealization can account for the elastic and inelastic strain components along with the time dependence of the latter.

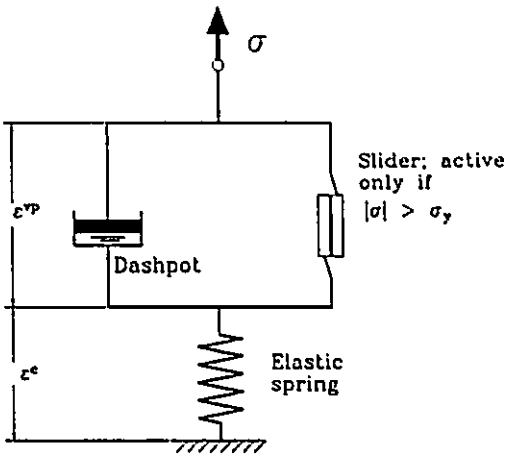

(a) Elastic–viscoplastic model for the planes of weakness and reinforcement.

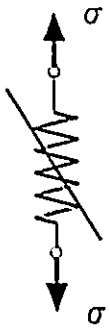

(b) Incrementally elastic model for the homogeneous medium.

Fig. 5.3. Rheological analogues for the macro-element components.

3. The homogenous medium, modelled as stress-induced orthotropic material according to the model proposed by Darwin and Pecknold (1977), is treated as an incrementally linear elastic material with the stiffness and strains being corrected during each load increment to reflect the latest changes. The failure of the homogeneous medium is described by the biaxial envelope developed by Kupfer and Grestel (1973). This failure envelope is defined in terms of the

uniaxial compressive strength of the masonry assemblage at $\theta=0°$ (i.e. compression is normal to bed joints), rather than the separate strengths of grout, mortar, or masonry units. In this manner, the failure envelope accounts for the influence of mortar and grout on the compressive strengths of the masonry assemblage under biaxial compression-compression states of stress when a splitting failure occurs parallel to the plane of the assemblage (Page 1981). The rheological analogue of the homogeneous medium is shown in Fig. 5.3(b) as a dashed spring, to be distinguished from the linear elastic material.

4. Following the work of Zienkiewicz and Pande (1977), the mortar joints comprising each set of planes of weakness are considered to occupy a negligible volumetric portion of the masonry assemblage (5 % in the masonry assemblage under consideration). Consequently, the same global stress vector is assumed to be experienced by the homogeneous medium and each set of planes of weakness.

5. The reinforcement is assumed to be perfectly bonded to the masonry assemblage at the macroscopic level. This assumption, however, does not exclude the possibility of bond failure at a microscopic level (see Sec. 6.3.2).

6. As a part of the orthotropic model used to simulate the behaviour of the homogeneous medium, the orientations of the principal stresses and principal strains of the homogeneous medium are assumed to coincide. It should be kept in mind that this assumption does not mean that the orientations of the principal stresses and principal strains of the masonry assemblage coincide. As stated before, the masonry assemblage comprises, in addition to the homogeneous

medium, two sets of planes of weakness and two sets of reinforcement.

According to assumptions 1 to 4, the homogeneous medium and the two sets of planes of weakness can be considered, in rheological terms, to be connected in series as shown in Fig. 5.4. Referenced to the global coordinates, the series connection assures that they are subjected to the same stress increment and the resultant incremental strains are additive to produce the macro-strain increment for an unreinforced masonry assemblage.

Adoption of the fifth assumption of perfect bond implies that the masonry assemblage and each set of reinforcement undergo the same global strain increment. In rheological terms, a reinforced masonry assemblage can be represented by three strings connected in parallel as illustrated in Fig. 5.5. The first string represents the masonry assemblage and the other two strings represent the two sets of reinforcement normal and parallel to bed joints. The parallel connection, in this case, means that the same global strain increment is experienced by the three stings upon which the applied stress increment is distributed according to their stiffnesses.

5.4 CONSTITUTIVE EQUATIONS FOR UNREINFORCED AND REINFORCED MASONRY ASSEMBLAGES

The constitutive equations presented in this section are developed in terms of global coordinates. The transformation between global and local coordinates is addressed in the following section.

Considering a set "i", representing one of the sets of the planes of

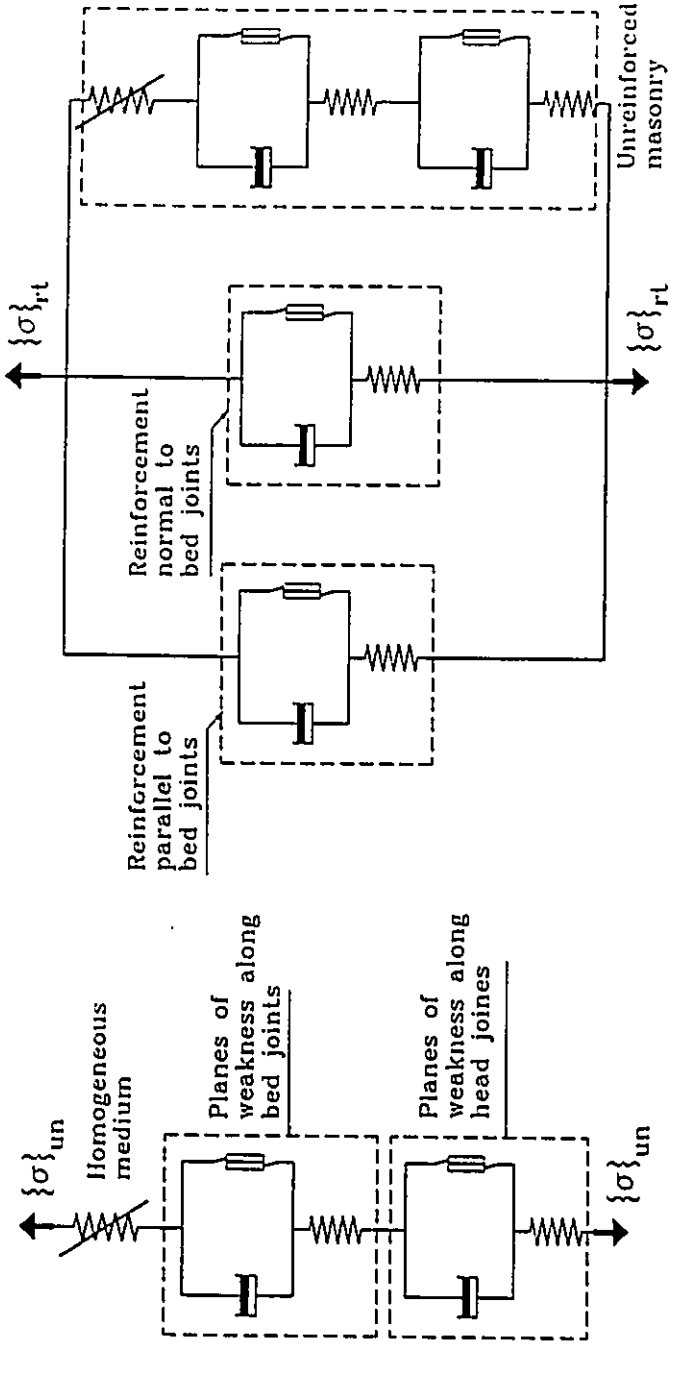

Fig. 5.5 Rheological analogue for reinforced masonry.

Fig. 5.4 Rheological analogue for unreinforced masonry.

weakness or of the reinforcement, the total strain increment can be separated into elastic and viscoplastic components, or in general terms, elastic and inelastic components that can be written in the form of:

$$\{\Delta\epsilon\}_i = \{\Delta\epsilon\}_i^e + \{\Delta\epsilon\}_i^{ne} \qquad \ldots(5.1)$$

where $\{\Delta\epsilon\}_i$ is the vector of total strain increment,

$\{\Delta\epsilon\}_i^e$ is the vector of the elastic strain increment, and

$\{\Delta\epsilon\}_i^{ne}$ is the vector of the inelastic strain increment.

The elastic strain increment is related to the applied stress increment through:

$$\{\Delta\epsilon\}_i^e = [D]_i^{-1} \{\Delta\sigma\}_i \qquad \ldots(5.2)$$

where $[D]_i$ is the tangential elasticity matrix for set "i" and

$\{\Delta\sigma\}_i$ is the vector of the stress increment.

The tangential elasticity matrices for the different sets of planes of weakness and the sets of reinforcement are kept constant and equal to the initial values throughout the analysis. In contrast, the tangential elasticity matrix of the homogeneous medium is updated at the end of each increment as illustrated schematically in Fig. 5.6. The total strain increment experienced by the homogeneous medium under a stress increment can also be separated into an elastic strain increment, induced in the first iteration, and inelastic strain increments, added during the following iterations until convergence is achieved. In this manner, Eqs. 5.1 and 5.2 can be used to relate the stress and strain increments experienced by the different parts of the masonry assemblage. The

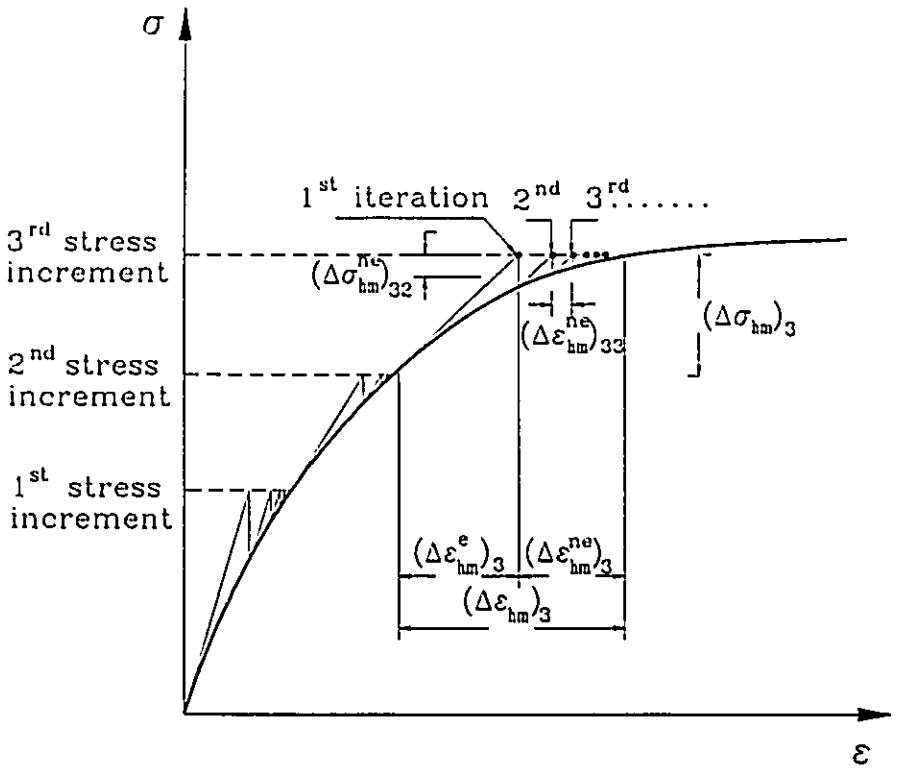

Fig. 5.6 Elastic and inelastic strain components for the homogeneous medium.

procedures followed to define the tangential elasticity matrices and the nonlinear strain increments are discussed in more details in the following sections.

As shown before in Fig 5.4, the unreinforced masonry assemblage can be presented, in rheological terms, by series connections between the homogenous medium and the two sets of planes of weakness. This idealization implies that the same stress increment experienced by the masonry assemblage is experienced by these three components, i.e.

$$\{\Delta\sigma\}_{un} = \{\Delta\sigma\}_{hm} = \{\Delta\sigma\}_{b} = \{\Delta\sigma\}_{h} \qquad \ldots(5.3)$$

The subscripts un, hm, b, and h are used in this equation to refer to the unreinforced assemblage, the homogeneous medium, the planes of weakness along the bed joints and the planes of weakness along the head joints, respectively. The macro-strain vector experienced by the unreinforced masonry assemblage can then be determined by summing up the strain vectors induced in the three components of the masonry assemblage, in terms of global coordinates, as follows:

$$\{\Delta\epsilon\}_{un} = \frac{s_m - t_m}{s_m} \{\Delta\epsilon\}_{hm} + \frac{t_m}{s_m} (\{\Delta\epsilon\}_b + \{\Delta\epsilon\}_h) \qquad \ldots(5.4)$$

where t_m and s_m are the thickness and spacing of the mortar joints as indicated in Fig. 5.2. Substituting Eqs. 5.1 and 5.2 into Eq. 5.4 and making use of Eq. 5.3 yield the following relationships:

$$\begin{aligned} \{\Delta\epsilon\}_{un} &= [D]_{un}^{-1} \{\Delta\sigma\}_{un} + \{\Delta\epsilon\}_{un}^{ne} \\ \{\Delta\sigma\}_{un} &= [D]_{un} (\{\Delta\epsilon\}_{un} - \{\Delta\epsilon\}_{un}^{ne}) \end{aligned} \qquad \ldots(5.5)$$

in which the global elasticity matrix $[D]_{un}$ and the inelastic strain increment $\{\Delta\epsilon\}_{un}^{ne}$ experienced by the unreinforced assemblage can be evaluated by

$$\begin{aligned} [D]_{un}^{-1} &= \frac{s_m - t_m}{s_m} [D]_{hm}^{-1} + \frac{t_m}{s_m} ([D]_b^{-1} + [D]_h^{-1}) \\ \{\Delta\epsilon\}_{un}^{ne} &= \frac{s_m - t_m}{s_m} \{\Delta\epsilon\}_{hm}^{ne} + \frac{t_m}{s_m} (\{\Delta\epsilon\}_b^{ne} + \{\Delta\epsilon\}_h^{ne}) \end{aligned} \qquad \ldots(5.6)$$

In a similar manner, a reinforced masonry assemblage can be represented

in rheological terms by three strings connected in parallel as shown in Fig. 5.5. The parallel connection implies that the masonry assemblage and each of the sets of reinforcement experience the same vector of strain increment, defined in the global coordinates. This equality can be written as

$$\{\Delta\epsilon\}_{rt} = \{\Delta\epsilon\}_{un} = \{\Delta\epsilon\}_{p} = \{\Delta\epsilon\}_{n} \qquad \ldots(5.7)$$

where the subscripts rt, un, p, and n refer to the reinforced masonry assemblage, the unreinforced masonry, the reinforcement parallel to bed joint and the reinforcement normal to bed joint, respectively. To satisfy equilibrium conditions, the applied stress increment should be distributed between the masonry assemblage and the reinforcement according to the following relationship:

$$\{\Delta\sigma\}_{rt} = \{\Delta\sigma\}_{un} + \rho_p \{\Delta\sigma\}_{p} + \rho_n \{\Delta\sigma\}_{n} \qquad \ldots(5.8)$$

where ρ_p and ρ_n are the percentages of reinforcement provided parallel and normal to the bed joints. The reduction in the cross-section of the unreinforced masonry assemblage due to the existence of reinforcement is usually small enough (in the range of 1%) to be neglected as expressed by the first term in the above equation. Substituting Eqs. 5.1, 5.2 and 5.5 into Eq. 5.8 and making use of Eq. 5.7 result in the following relationships:

$$\begin{aligned} \{\Delta\sigma\}_{rt} &= [D]_{rt} \left(\{\Delta\epsilon\}_{rt} - \{\Delta\epsilon\}_{rt}^{ne}\right) \\ \{\Delta\epsilon\}_{rt} &= [D]_{rt}^{-1} \{\Delta\sigma\}_{rt} + \{\Delta\epsilon\}_{rt}^{ne} \end{aligned} \qquad \ldots(5.9)$$

where the global elasticity matrix $[D]_{rt}$ and the inelastic strain increment $\{\Delta\epsilon\}_{rt}^{ne}$

of the reinforced assemblage can be evaluated as

$$[D]_{rt} = [D]_{un} + \rho_p [D]_p + \rho_n [D]_n$$

$$\{\Delta\epsilon\}_{rt}^{ne} = [D]_{rt}^{-1} ([D]_{un} \{\Delta\epsilon\}_{un}^{ne} + \rho_p [D]_p \{\Delta\epsilon\}_p^{ne} + \rho_n [D]_n \{\Delta\epsilon\}_n^{ne}) \quad \ldots(5.10)$$

5.5 COORDINATE TRANSFORMATION

Two kinds of coordinate axes (global and local) are required to formulate the macro-behaviour model. A set of global coordinate axes is used to define the overall properties and the mechanical response of the masonry assemblage. On the other hand, several sets of local coordinate axes are used in the orientations of the planes of weakness, the reinforcement, and the principal directions of the homogeneous medium. Appropriate transformations are required to transform vectors and matrices such as stress, strain and stiffness from the local to the global coordinates and vice versa.

Different sets of coordinate axes are shown in Fig. 5.7, where the X-Y axes represent the global coordinate axes. The two sets of axes x_b-y_b and x_h-y_h are the local coordinate axes for the planes of weakness along the bed and the head joints, respectively. The homogenous medium is idealized as an orthotropic material in the principal directions which are indicated by the local coordinates 1_{hm}-2_{hm}. The relationships between the local coordinate axes x_b-y_b and the global axes X-Y are discussed here as an example. However, the same transformation rules are applicable between any local axis and the global axes.

The global vectors of stresses and strains can be converted to the local

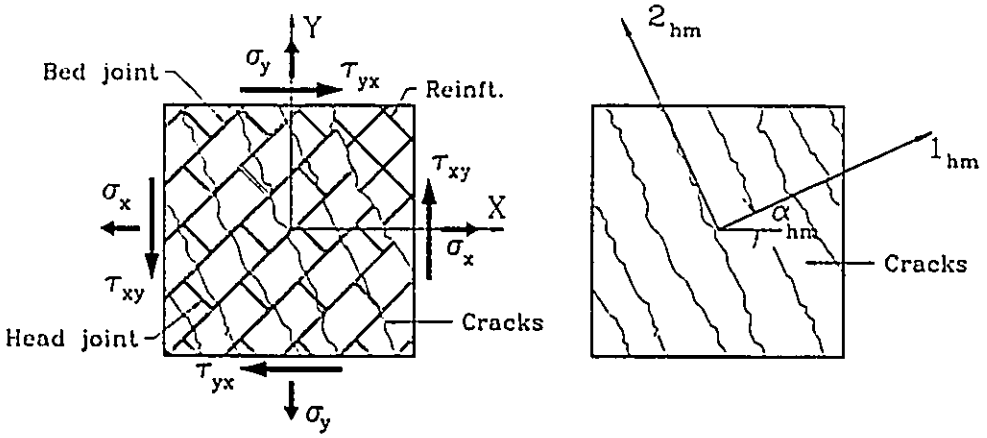

(a) Global coordinates

(b) Local coordinates of the homogeneous medium.

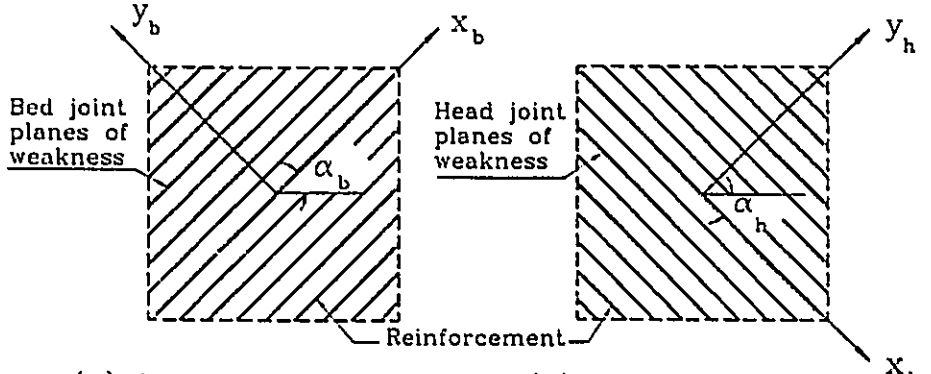

(c) Local coordinates for planes of weakness and reinforcement parallel to bed joints.

(d) Local coordinates for planes of weakness and reinforcement parallel to head joints.

Fig. 5.7 Local and global axes.

coordinates x_b-y_b using the following relationships:

$$\{\Delta\sigma\}_{bL} = [T_{sr}]_{LG}\ \{\Delta\sigma\}_{bG} \qquad \ldots(5.11)$$

$$\{\Delta\epsilon\}_{bL} = [T_{sn}]_{LG}\ \{\Delta\epsilon\}_{bG} \qquad \ldots(5.12)$$

where $\{\Delta\sigma\}_{bL}$ and $\{\Delta\epsilon\}_{bL}$ are the stress and strain vectors defined in the local coordinate axes x_b-y_b,

$\{\Delta\sigma\}_{bG}$ and $\{\Delta\epsilon\}_{bG}$ are the stress and strain vectors defined in the global coordinate axes X-Y,

$[T_{sr}]_{LG}$ is the stress transformation matrix from the global to the local coordinate axes which is given by

$$[T_{sr}]_{LG} = \begin{bmatrix} c^2 & s^2 & 2sc \\ s^2 & c^2 & -2sc \\ -sc & sc & c^2-s^2 \end{bmatrix} \qquad \ldots(5.13)$$

$[T_{sn}]_{LG}$ is the strain transformation matrix from the global to the local coordinate axes which is given by

$$[T_{sn}]_{LG} = \begin{bmatrix} c^2 & s^2 & sc \\ s^2 & c^2 & -sc \\ -2sc & 2sc & c^2-s^2 \end{bmatrix} \qquad \ldots(5.14)$$

$c=\cos\alpha_b$ and $s=\sin\alpha_b$

where α_b is the angle between the bed joint planes of weakness and axis X as indicated in Fig. 5.7(c).

It is interesting to note that the stress and strain transformation matrices are related by

$$[T_{sr}]_{LG} = [T_{sn}]^T_{GL} \qquad \ldots(5.15)$$

where $[T_{sn}]_{GL}$ is the strain transformation matrix from the local to the global coordinate axes (i.e. c=cos ($-\alpha_b$) and s=sin ($-\alpha_b$)).

Both the elasticity matrix [D] and its inverse can be transformed to the global coordinate axes in the form of

$$[D]^{-1}_{bG} = [T_{sn}]_{GL}\,[D]^{-1}_{bL}\,[T_{sr}]_{LG} = [T_{sr}]^T_{LG}\,[D]^{-1}_{bL}\,[T_{sr}]_{LG}$$
$$[D]_{bG} = [T_{sn}]^T_{LG}\,[D]_{bL}\,[T_{sn}]_{LG} \qquad \ldots(5.16)$$

It should be kept in mind that the constitutive equations presented in Sec. 5.4 were developed in terms of the global coordinates, but in that instance, for clarity, the subscript "G" was not included.

5.6 IDEALIZATION OF JOINTS

5.6.1 Introduction

Two sets of planes of weakness are used to simulate the bed and head joint planes. The deformations and the failure conditions for these planes were described in terms of the average normal and average shear stresses (σ and τ) acting on them. However, in modelling a grouted concrete masonry assemblage, two difficulties are encountered in the idealization of the mortar joints by separate sets of planes of weakness. First, the planes along bed and head joints intersect more than one material; mortar, grout and block face shells. Second, the possibility of developing a stepped failure pattern through bed and head joints

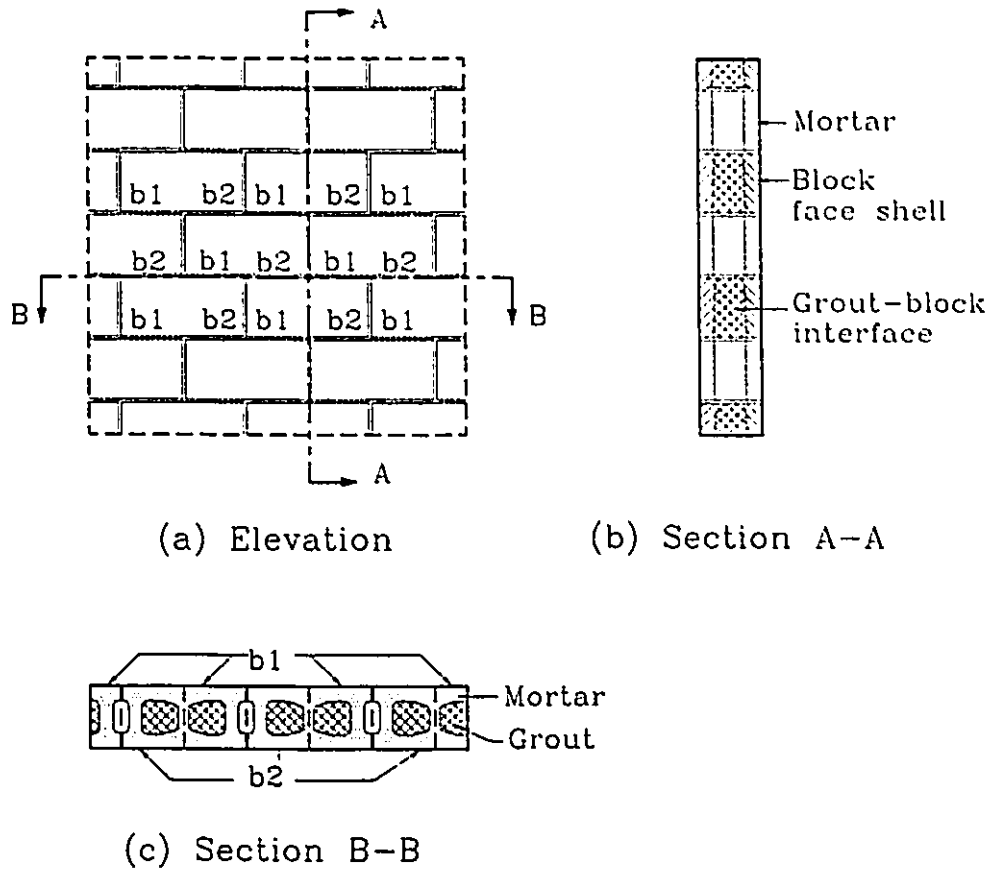

Fig. 5.8 Material components along the planes of weakness.

cannot be addressed unless the interaction between the two sets of planes of weakness is considered. The procedures followed to overcome these difficulties along with the modelling of the different constituent materials along the joints are discussed in the following sub-sections.

5.6.2 Head Joints

As shown in Fig. 5.8(b), the planes of weakness along the head joint planes pass through three different components; mortar joints, blocks and the grout-block interface. This figure represents the case of a masonry assemblage

with continuous grout cores normal to bed joints only. An additional grout component will be required in cases where the masonry assemblages have also continuous grout cores parallel to the bed joints. Studying the problem at a macroscopic level, the average normal and average shear stress increments ($\Delta\sigma_h$ and $\Delta\tau_h$) acting on these planes can be determined in terms of the global stress increments using Eq. 5.11. These stresses should be in equilibrium with the internal stress increments induced in the three components of mortar, blocks and grout-block interface so that they satisfy the following equilibrium relationship:

$$\begin{Bmatrix}\Delta\sigma_h\\ \Delta\tau_h\end{Bmatrix} = \frac{A_{mh}}{A_h}\begin{Bmatrix}\Delta\sigma_{mh}\\ \Delta\tau_{mh}\end{Bmatrix} + \frac{A_k}{A_h}\begin{Bmatrix}\Delta\sigma_k\\ \Delta\tau_k\end{Bmatrix} + \frac{A_{in}}{A_h}\begin{Bmatrix}\Delta\sigma_{in}\\ \Delta\tau_{in}\end{Bmatrix} \qquad \ldots(5.17)$$

where A_h is the cross-sectional area of the masonry assemblage along the head joint planes of weakness. The subscripts "mh", "k" and "in" are used here to refer, respectively, to the mortar, the block and the grout-block interface along the head joint planes of weakness. In addition, compatibility of the deformations along the planes of weakness implies that the same average strain increments are experienced by these three components at the macroscopic level. This can be written as

$$\begin{Bmatrix}\Delta\epsilon_h\\ \Delta\gamma_h\end{Bmatrix} = \begin{Bmatrix}\Delta\epsilon_{mh}\\ \Delta\gamma_{mh}\end{Bmatrix} = \begin{Bmatrix}\Delta\epsilon_k\\ \Delta\gamma_k\end{Bmatrix} = \begin{Bmatrix}\Delta\epsilon_{in}\\ \Delta\gamma_{in}\end{Bmatrix} \qquad \ldots(5.18)$$

The above two equations can be represented in rheological terms by three elastic-viscoplastic units connected in parallel as shown in Fig. 5.9. This combination can then be used to replace the single elastic-viscoplastic unit which

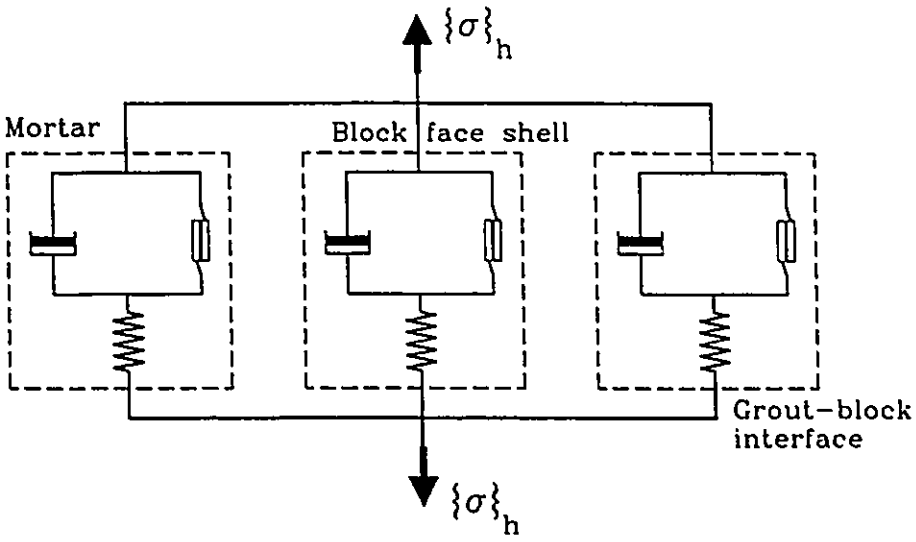

Fig. 5.9 Rheological analogue for the head joint planes of weakness.

represents the planes of weakness along the head joints in Fig. 5.4. The same procedures are used as in the case of the parallel connection between masonry and reinforcement to define the average elasticity matrix and the inelastic strain vector of a reinforced masonry assemblage (Sec. 5.4). Thus, the average elasticity matrix and the inelastic strain vector of the head joint planes of weakness can be defined in terms of the corresponding matrices and vectors of the three component materials along these planes of weakness as follows:

$$[D]_h = \frac{A_{mh}}{A_h}[D]_{mh} + \frac{A_k}{A_h}[D]_k + \frac{A_{in}}{A_h}[D]_{in} \qquad \ldots(5.19.a)$$

$$\{\Delta\epsilon\}_h^{ne} = [D]_h^{-1}\left(\frac{A_{mh}}{A_h}[D]_{mh}\{\Delta\epsilon\}_{mh}^{ne} + \frac{A_k}{A_h}[D]_k\{\Delta\epsilon\}_k^{ne} + \frac{A_{in}}{A_h}[D]_{in}\{\Delta\epsilon\}_{in}^{ne}\right) \qquad \ldots(5.19.b)$$

Adopting the assumption of uniform strain distribution along the head joint planes of weakness implies that the failure of any component along these planes is followed by stress redistribution between this component and the surrounding components until a complete failure of the plane of weakness occurs. This behaviour is in agreement with the test observations since no cracks were detected in the mortar head joints until the complete failure along a head joint plane occurred.

5.6.3 Bed Joints

Similar to the head joint planes of weakness, the planes of weakness along the bed joints pass through both the mortar and the grout components, as illustrated in Fig 5.8(c). However, it was decided to break the planes of weakness into four components; two identical mortar components and two identical grout components. The main reason behind this decision was to allow prediction of the stepped mode of failure as well as failure along the bed joint planes.

As illustrated in Fig 5.8(c), the bed joints can be divided into two series of elements which are identical in their constitution but different in their location with respect to the mortar head joint. The first series of elements lies on the upper left side of the mortar head joints and is referred to by "b1". In between the elements of this series, the second series of elements that falls on the upper right side of the mortar head joints is referred to by "b2". Both series,

identically, consist of 50% of the grout and the mortar components along the bed joints.

The relationships developed for the planes of weakness along the head joints are applicable to each series of elements. Consequently, the elasticity matrix and the inelastic strain vector for each series of elements can be determined as follows:

$$[D]_{b1} = [D]_{b2} = \frac{A_{mb}}{2A_b}[D]_{mb} + \frac{A_g}{2A_b}[D]_g \qquad \ldots(5.20.a)$$

$$\{\Delta\epsilon\}^{ne}_{b1} = \{\Delta\epsilon\}^{ne}_{b2} = [D]^{-1}_{b1}\left(\frac{A_{mb}}{2A_b}[D]_{mb}\{\Delta\epsilon\}^{ne}_{mb} + \frac{A_g}{2A_b}[D]_g\{\Delta\epsilon\}^{ne}_g\right) \qquad \ldots(5.20.b)$$

Applying the same equilibrium and compatibility requirements again to the two series of elements, the average characteristics of the planes of weakness along the bed joints can be defined as

$$\begin{aligned} [D]_b &= [D]_{b1} + [D]_{b2} \\ \{\Delta\epsilon\}^{ne}_b &= \frac{1}{2}(\{\Delta\epsilon\}^{ne}_{b1} + \{\Delta\epsilon\}^{ne}_{b2}) \end{aligned} \qquad \ldots(5.21)$$

According to the above relationships, the planes of weakness along the bed joints can be presented in rheological terms by a parallel connection between two identical series as shown in Fig. 5.10. Each series consists of two elastic-viscoplastic units connected in parallel; one for the mortar component and the

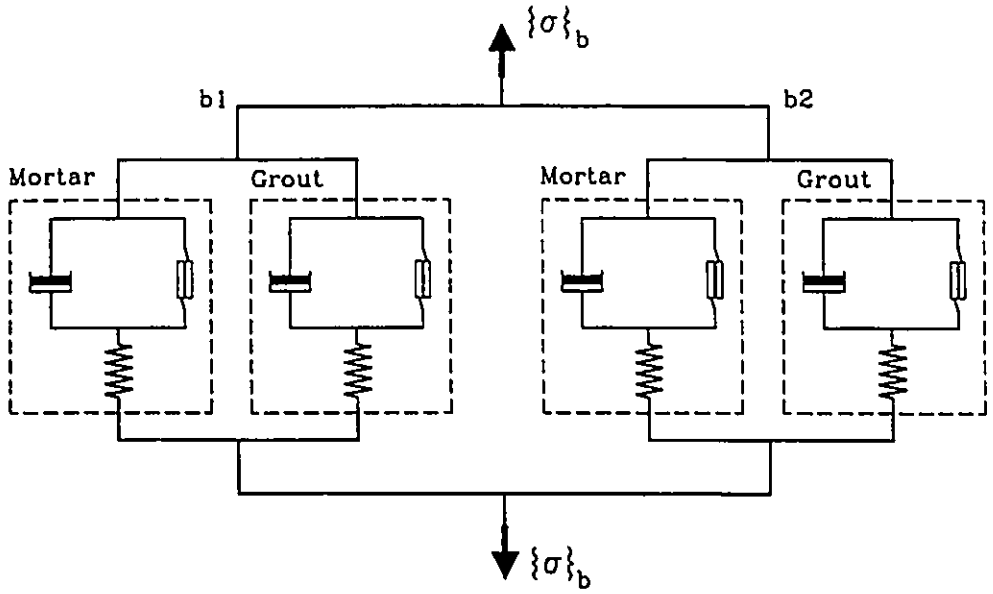

Fig. 5.10 Rheological analogue for the bed joint planes of weakness.

other for the grout component. This connection can then be used to replace the single elastic-viscoplastic unit used to represent the bed joint planes of weakness in Fig. 5.4.

5.6.4 Stepped Modes of Failure

Classification of the bed joints into the two series "b1" and "b2" accommodates prediction of the different possible modes of failure along the mortar joints. A simultaneous failure of the two series, before failure of the mortar component along the head joint planes of weakness, indicates a complete failure along the bed joints as shown in Fig. 5.11(a). On the other hand, failure of the mortar component along the head joint planes of weakness could lead to different modes of failure depending on the relative strengths of the components along the bed and the head joint planes. Failure of the mortar component along

the head joint planes results in stress redistributions not only along the head joint planes but also along the bed joint planes. The process of stress redistribution

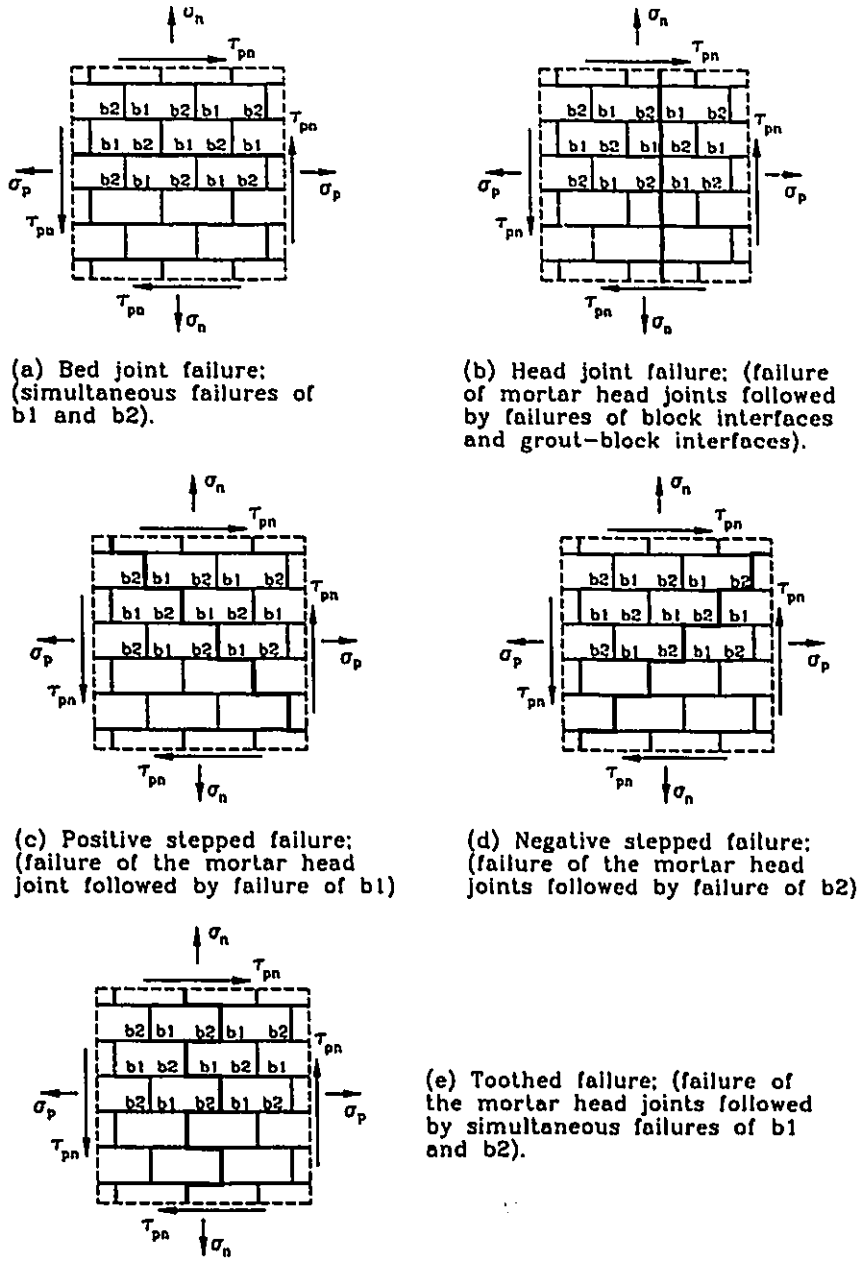

Fig. 5.11 Different modes of failure along the mortar joint planes.

continues until a complete failure takes place either along the head joint planes alone (Fig. 5.11(b)) or in a stepped pattern through both head and bed joints, as demonstrated in Figs. 5.11(c) to (e).

A typical macro-element in a masonry assemblage is shown in Fig. 5.12(a). When the stresses acting on the mortar component of the head joint planes of weakness exceed their maximum values (σ^*_{mh} and τ^*_{mh}), defined by the yield surface, the excess of stresses ($\Delta\sigma'_{mh}$ and $\Delta\tau'_{mh}$) that cannot be resisted by this component have to be redistributed to the surrounding components. Figure 5.12(b) shows the forces acting along section A-A before and after the stress redistribution takes place. Consideration of the equilibrium conditions in the two directions parallel and normal to bed joints, shown in the free body in Fig. 5.12(b), yields the following two equations:

$$\begin{aligned}(t\times L)\,\sigma_p &= A_{mh}(\sigma^*_{mh}+\Delta\sigma'_{mh})+A_k\sigma_k+A_{in}\sigma_{in} \\ &= A_{mh}\sigma^*_{mh}+A_k(\sigma_k+\Delta\sigma'_k)+A_{in}(\sigma_{in}+\Delta\sigma'_{in})\end{aligned} \qquad \ldots(5.22.a)$$

$$\begin{aligned}(t\times L)\,\tau_{pn} &= A_{mh}(\tau^*_{mh}+\Delta\tau'_{mh})+A_k\tau_k+A_{in}\tau_{in} \\ &= A_{mh}\tau^*_{mh}+A_k(\tau_k+\Delta\tau'_k)+A_{in}(\tau_{in}+\Delta\tau'_{in})\end{aligned} \qquad \ldots(5.22.b)$$

These two equations can be simplified in the forms of

$$A_{mh}\Delta\sigma'_{mh} = A_k\Delta\sigma'_k+A_{in}\Delta\sigma'_{in} \qquad \ldots(5.23.a)$$

$$A_{mh}\Delta\tau'_{mh} = A_k\Delta\tau'_k+A_{in}\Delta\tau'_{in} \qquad \ldots(5.23.b)$$

where $\Delta\sigma'_k$ and $\Delta\sigma'_{in}$ are the changes in the normal stresses acting, respectively, on the block and the grout-block interface components along the head joint planes of weakness after the stresses acting on the

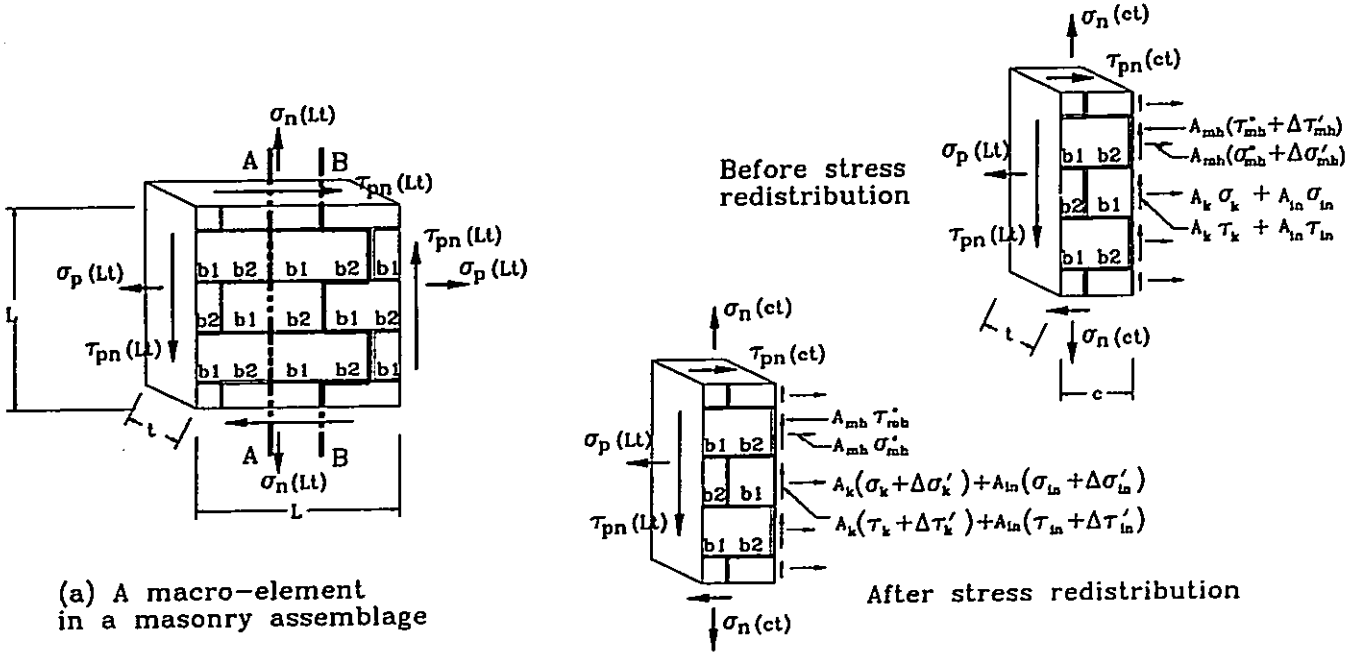

(a) A macro-element in a masonry assemblage

(b) Equilibrium conditions along section A–A after the stresses acting on the mortar component of the head joint planes of weakness reach their yield surface.

Fig. 5.12 Equilibrium conditions after the failure of the mortar component of the head joint planes of weakness.

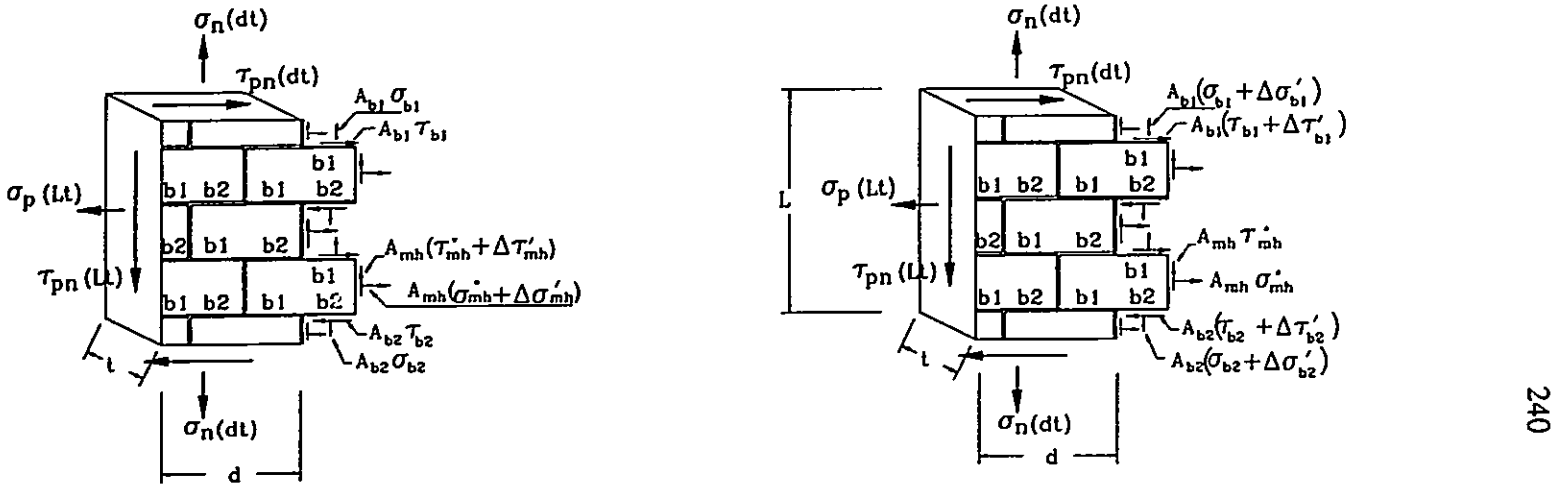

Before stress redistribution

After stress redistribution

(c) Equilibrium conditions along section B–B after the stresses acting on the mortar component of the head joint planes of weakness reach their yield surface.

Fig. 5.12 Continued.

mortar component reach its yield surface, and

$\Delta\tau'_k$ and $\Delta\tau'_{in}$ are the changes in the shear stresses acting, respectively, on the block and the grout-block interface components along the head joint planes of weakness after the stresses acting on the mortar component reach their yield surface.

Equations 5.23(a) and (b) describe the process of stress redistribution among the different components along the head joint planes of weakness after the stresses acting on the mortar component reach their yield surface.

The process of stress redistribution between the mortar component of the head joint planes of weakness and the components along the bed joint planes of weakness, can be studied using a toothed section b-b made through both bed and head joints as shown in Fig. 5.12(a). Figure 5.12(c) shows the forces resisted by the different components crossed by section b-b before and after the stress redistribution takes place. Consideration of the equilibrium conditions of the free body shown in Fig. 5.12(c), in the two directions parallel and normal to bed joints, yields the following two equations:

$$\begin{aligned}(t\times L)\,\sigma_p &= 2A_{mh}(\sigma^*_{mh}+\Delta\sigma'_{mh})+A_{b1}\tau_{b1}-A_{b2}\tau_{b2}\\ &= 2A_{mh}\sigma^*_{mh}+A_{b1}(\tau_{b1}+\Delta\tau'_{b1})-A_{b2}(\tau_{b2}-\Delta\tau'_{b2})\end{aligned} \qquad \ldots(5.24.a)$$

$$\begin{aligned}(t\times L)\,\tau_{pn} &= 2A_{mh}(\tau^*_{mh}+\Delta\tau'_{mh})+A_{b1}\sigma_{b1}-A_{b2}\sigma_{b2}\\ &= 2A_{mh}\tau^*_{mh}+A_{b1}(\sigma_{b1}+\Delta\sigma'_{b1})-A_{b2}(\sigma_{b2}-\Delta\sigma'_{b2})\end{aligned} \qquad \ldots(5.24.b)$$

where $\Delta\sigma'_{b1}$ and $\Delta\sigma'_{b2}$ are the changes in the normal stresses acting respectively on series b1 and b2 of the bed joint planes of weakness after the stresses

acting on the mortar component of the head joint planes of weakness reach their yield surface, and

$\Delta\tau'_{b1}$ and $\Delta\tau'_{b2}$ are the changes in the shear stresses acting respectively on series b1 and b2 of the bed joint planes of weakness after the stresses acting on the mortar component of the head joint planes of weakness reach their yield surface.

Because the two series of elements, b1 and b2, have identical constituent materials and stiffnesses, the changes in the stresses acting on these series should be equal as expressed by

$$\Delta\sigma'_{b1} = \Delta\sigma'_{b2} \qquad \ldots(5.25.a)$$

$$\Delta\tau'_{b1} = \Delta\tau'_{b2} \qquad \ldots(5.25.b)$$

Using Eq. 5.25, the equilibrium equations expressed by Eq. 5.24 can be simplified as

$$A_{mh}\Delta\sigma'_{mh} = A_{b1}\Delta\tau'_{b1} = A_{b2}\Delta\tau'_{b2} \qquad \ldots(5.26.a)$$

$$A_{mh}\Delta\tau'_{mh} = A_{b1}\Delta\sigma'_{b1} = A_{b2}\Delta\sigma'_{b2} \qquad \ldots(5.26.b)$$

It is worth noting that two stepped modes of failure, differing in their orientation, can be predicted if the stresses acting on the mortar component of the head joint planes of weakness and subsequently the stresses acting on the bed joint planes of weakness reach their respective yield surfaces. As illustrated in Fig. 5.11(c), a positive stepped mode of failure occurs when the stresses acting on elements of series "b1" reach their yield surfaces after the stresses acting on the mortar component of the head joint planes of weakness reach their yield

surfaces. Alternatively, if the stresses acting on the elements of series "b2" reach their failure surfaces after the stresses acting on the mortar component of the head joint planes of weakness reach their yield surfaces, a negative stepped mode of failure takes place as shown in Fig. 5.11(d). A toothed mode of failure, as sketched in Fig. 5.11(e), is expected to take place, if the stresses acting on both series b1 and b2 reach their respective yield surfaces subsequent to the stresses acting on the mortar component of the head joint planes of weakness reaching its yield surface.

5.6.5 Elasticity Matrix

A plane strain elasticity matrix [*D*] is used to define the elastic responses of the different components along the planes of weakness. This plane strain idealization is used to account for the confining effect of the blocks on the mortar joint and the grout along the joint planes where high stress and strain concentrations are likely to occur. The relationship between the stresses and the elastic strains of component material "i", in terms of the local coordinates along the planes of weakness, is given by

$$\begin{Bmatrix} \Delta\sigma_i \\ \Delta\tau_i \end{Bmatrix} = \frac{E_i}{(1+\nu_i)(1-2\nu_i)} \begin{bmatrix} 1-\nu_i & 0 \\ 0 & \frac{1-2\nu_i}{2} \end{bmatrix} \begin{Bmatrix} \Delta\epsilon_i^e \\ \Delta\gamma_i^e \end{Bmatrix} \qquad \ldots(5.27)$$

where E_i and ν_i are, respectively, the Young's modulus and the Poisson's ratio for the component material "i".

Because of the small thickness of the mortar joints compared to their lengths, the effect of the normal strains parallel to the orientation of the planes of weakness on $\Delta\sigma_i$ is neglected in Eq. 5.27. However, the interaction between the normal stresses (and strains), acting parallel and normal to the bed joints, is considered in the homogeneous medium.

5.6.6 Yield Surfaces and Flow Rules

The inelastic responses as well as failures of the different material components across the planes of weakness are modelled using the elastic-viscoplastic idealization. The Mohr-Coulomb criterion along with a tension cut-off are used to describe the yield surface of a component material "i".

As indicated by the solid line in Fig. 5.13, the failure in zone I is dominated by the shear stress. In the absence of sufficient information, the yield surface adopted for this zone is expressed as a function of stresses only, which implies an elastic-perfectly plastic response. This assumption is in agreement with the experimental results obtained in this investigation and by Guo (1991) in direct shear tests under the effect of compressive normal stress. The adopted yield surface is defined as

$$F_I = F_I(\sigma,\tau) = [|\tau| + \sigma \tan\Phi - c]_i = 0 \qquad \ldots(5.28)$$

where Φ and c are the angle of friction and coefficient of cohesion, respectively.

For zone II, where the failure is dominated by the tensile stress, three different criteria are used in the analyses reported in Chapter 7. As shown by the solid lines in Fig. 5.13(a), the first criterion adopted is a straight tension cut-off,

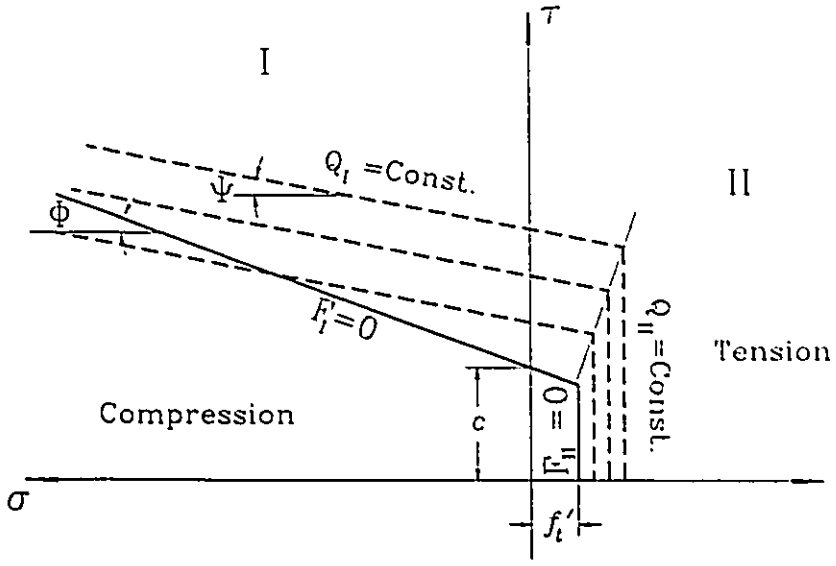

(a) Mohr–Coulomb criterion with vertical tension cut–off.

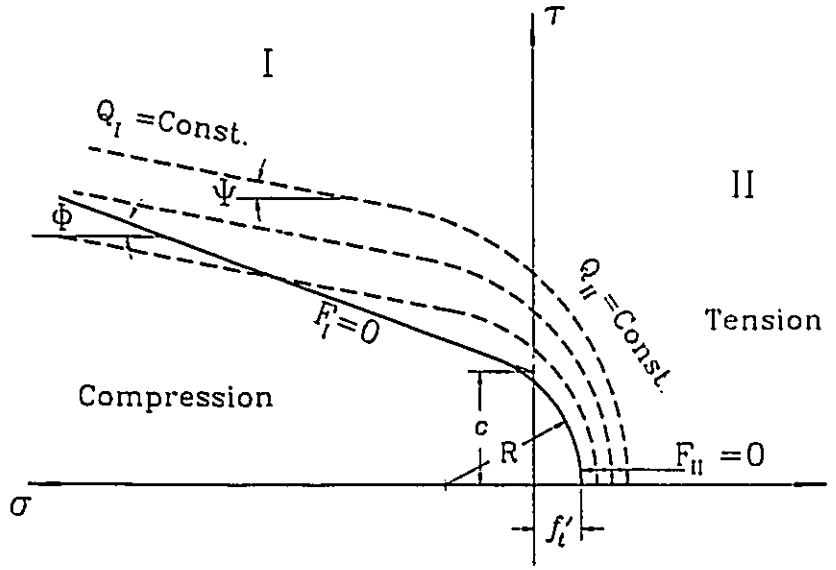

(b) Mohr–Coulomb criterion with circular tension cut–off.

Fig. 5.13 Yield and plastic potential surfaces for a typical component material along the planes of weakness.

which is described as a function of stress only in the form of

$$F_{II} = F_{II}(\sigma) = [\sigma - f_t']_i = 0 \qquad \ldots(5.29)$$

where f_t' is the uniaxial tensile strength of component material "i". The second criterion adopted for zone II is a circular tension cut-off as shown by the solid lines in Fig. 5.13(b). It is also expressed only as a function of stress in the following form:

$$F_{II} = F_{II}(\sigma,\tau) = [\sqrt{\tau^2+(\sigma+R-f_t')^2}-R]_i = 0 \qquad \ldots(5.30)$$

where $$R = c\,\tan(\frac{\pi}{4}+\frac{\Phi}{2}) - f_t'\,\frac{\sin\Phi}{1-\sin\Phi}$$

Adoption of yield surfaces which are functions of stresses only (Eqs. 5.29 and 5.30) implies the assumption of elastic-perfectly plastic response in zone II, which does not seem to be adequate for describing the brittle nature of the tension failure. Therefore, for zone II, a third criterion is adopted in the form of a circular tension cut-off, but having the tensile strength f_t' defined as a function of the normal tensile strain according the strain softening model proposed by Massicotte et al. (1990) and shown in Fig. 5.14(a). According to the third criterion, the yield surface of zone II contracts with the increase in the normal tensile strain. This idealization, as shown in Fig. 5.14(b), introduces a transition zone between the tension brittle failure, indicated by point A', and the more ductile behaviour in the existence of compressive normal stress along line B'-C.

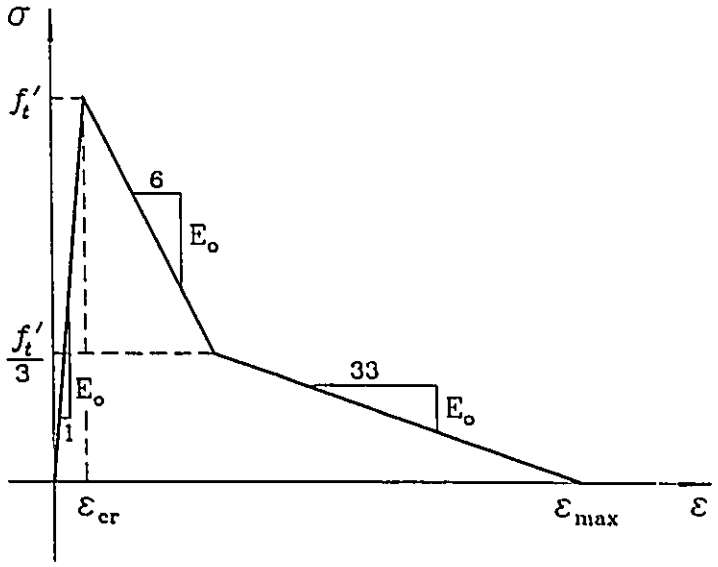

(a) Tension softening stress–strain relationship

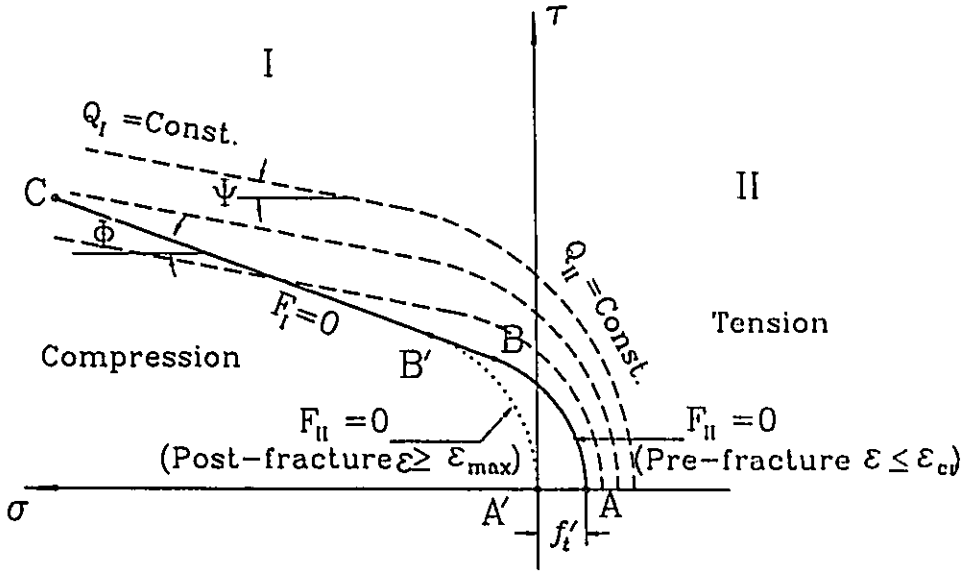

(b) Mohr–Coulomb criterion with a moving circular tension cut–off.

Fig. 5.14 Circular tension cut-off with tension softening idealization of a typical component material along the planes of weakness.

The inelastic strain increment experienced by a material "i" is determined by the viscoplastic strain increment. The response of the material remains elastic as long as the state of stress lies inside the yield surface. Once the state of stress is on or outside the yield surface, a viscoplastic strain increment, $\Delta\epsilon_i^{vp}$, takes place according to:

$$\Delta\epsilon_i^{ne} = \Delta\epsilon_i^{vp} = [\gamma \langle F \rangle \frac{\delta Q}{\delta \sigma}]_i \qquad \ldots(5.31)$$

in which

$$\begin{aligned} \langle F \rangle &= 0 \qquad && \text{if } F \leq 0 \\ \langle F \rangle &= F \qquad && \text{if } F > 0 \end{aligned} \qquad \ldots(5.32)$$

γ is the fluidity parameter which is commonly adopted as unity when time dependence is not real, and

Q is the plastic potential function.

A non-associated flow rule is adopted in zone II to account for the dilation of the joints after failure in shear. This is achieved by specifying a plastic potential function Q_I different than the yield surface F_I, as shown by the dashed lines in Figs. 5.13 and 5.14. This potential function can be expressed in the following form:

$$Q_I = [|\tau| + \sigma \tan\psi - constant]_i = 0 \qquad \ldots(5.33)$$

Non-dilatant behaviour can be represented by $\psi=0$, while $0<\psi<\Phi$ results in varying dilation. Plastic potential functions Q_{II}, similar to those of the yield surfaces F_{II} adopted in zone II, are used when failure is dominated by tensile stress, i.e. via an associated flow rule.

5.7 IDEALIZATION OF THE HOMOGENEOUS MEDIUM

5.7.1 Constitutive Relationships

The homogeneous medium is modelled, as indicated before, as a stress-induced orthotropic material according to the model proposed by Darwin and Pecknold (1977) for plain concrete. In this model, the principal axes "1_{hm}" and "2_{hm}" of the material are considered to coincide with the principal stress axes of the homogeneous medium. The material is treated as incrementally linear elastic according to the following stress-strain relationship:

$$\{\Delta\sigma\}_{hm} = [D]_{hm}\ \{\Delta\epsilon\}_{hm}$$

or

$$\begin{Bmatrix} \Delta\sigma_1 \\ \Delta\sigma_2 \\ \Delta\tau_{12} \end{Bmatrix}_{hm} = \frac{1}{1-\nu} \begin{bmatrix} E_1 & \nu\sqrt{E_1E_2} & 0 \\ & E_2 & 0 \\ Sym. & & (1-\nu^2)G \end{bmatrix}_{hm} \begin{Bmatrix} \Delta\epsilon_1 \\ \Delta\epsilon_2 \\ \Delta\gamma_{12} \end{Bmatrix}_{hm} \quad \ldots(5.34)$$

where $G = \frac{1}{4}(E_1 + E_2 - 2\nu\sqrt{E_1E_2})$

The subscript "hm", referring to the homogeneous medium, is moved outside the matrices for simplicity. The next step is to determine the material constants; E_1, E_2 and ν for each load increment. Darwin and Pecknold developed the concept of the "equivalent uniaxial strain" which allows actual biaxial stress-strain curves

to be duplicated from the uniaxial curve. The same technique was discussed and used by Elwi and Murray (1979) to develop three-dimensional stress-strain relationships for concrete. They pointed out that Eq. 5.34 can be rewritten in the form of

$$\begin{Bmatrix} \Delta\sigma_1 \\ \Delta\sigma_2 \\ \Delta\tau_{12} \end{Bmatrix}_{hm} = \begin{bmatrix} E_1 & 0 & 0 \\ & E_2 & 0 \\ Sym. & & G \end{bmatrix}_{hm} \begin{Bmatrix} \Delta\epsilon_{1u} \\ \Delta\epsilon_{2u} \\ \Delta\gamma_{12} \end{Bmatrix}_{hm} \qquad \ldots(5.35)$$

where the vector on the right side can be defined as the vector of equivalent uniaxial strains after removing the effects of Poisson's ratio. The values of the incremental equivalent uniaxial strains can be determined as

$$\Delta\epsilon_{hmiu} = \frac{\Delta\sigma_{hmj}}{E_{hmj}} \qquad (j = 1, 2) \qquad \ldots(5.36)$$

Integrating this equation, at the end of each iteration, yields the total equivalent uniaxial strains as

$$\epsilon_{hmiu} = \int \frac{d\sigma_{hmj}}{E_{hmj}} = \sum \frac{\Delta\sigma_{hmj}}{E_{hmj}} = \sum \frac{\sigma_{hmj\,new} - \sigma_{hmj\,old}}{E_{hmj\,old}} \qquad \ldots(5.37)$$

The constitutive relationship given by Eq. 5.34 and based on the equivalent uniaxial strain can then be summarized as

$$\{\Delta\sigma\}_{hm} = g\,(\{\Delta\epsilon\}_{hm}, \int\{d\sigma\}_{hm}) \qquad \ldots(5.38)$$

in which g implies a functional relationship. This relationship is path dependent and was described by Elwi and Murray (1979) and Chen (1982) as a hypoelastic

constitutive relationship.

At the end of each load increment, the elasticity matrix of the homogeneous medium is updated to reflect the latest changes in the material characteristics. This matrix is kept constant during the same load increment as illustrated in Fig. 5.6. The strains induced in the first iteration of each load increment represent the elastic part of the strain corresponding to this load increment. Following the "initial strain" solving technique, the inelastic strain increments for the next iterations are required. They are determined by evaluating the difference between the current stresses and the true stresses corresponding to the current strain (for example, $\{\Delta\sigma^{ne}_{hm}\}_{32}$ for the 2nd iteration of the 3rd increment as indicated in Fig.5.6). This vector of stress differences can then be substituted into Eq. 5.34 to determine the inelastic strain increment for the next iteration $\{\Delta\epsilon^{ne}_{hm}\}_{33}$, as illustrated graphically in Fig. 5.6. This strain increment is later assembled with the inelastic strain increments of the planes of weakness and the reinforcement to determine the inelastic strain increment of the assemblage according to the relationships derived before in Sec. 5.4. Dividing the inelastic strain into increments, rather than applying the total value, allows for tracing the nonlinear behaviour of the assemblage especially during the propagation of cracks.

5.7.2 Pre-failure Stress-Strain Relationships

The stress-strain relationship of the homogeneous medium under uniaxial

compression is described by Saenz's equation (Saenz 1964) in the form of

$$\sigma_{hmj} = \frac{\epsilon_{hmju}\, E_o}{1 + \left(\frac{E_o}{E'_s} - (1+A)\right)\left(\frac{\epsilon_{hmju}}{\epsilon_o}\right) + \left(\frac{\epsilon_{hmju}}{\epsilon_o}\right)^2} \qquad \ldots(5.39)$$

where E_o is the initial tangential modulus of elasticity,
E'_s is the secant modulus of elasticity at peak stress, and
ϵ_o is the strain associated with the peak stress, σ_{jp}, in the principal stress direction j, under uniaxial compression.
A is a constant usually taken equal to one for concrete. Different values were determined for the masonry assemblages considered in this investigation using the experimental results of two series of prisms tested under uniaxial compression (Chapter 6).

The value of peak stress σ_{hmjp} under uniaxial compression is defined as the compressive strength of the masonry assemblage, f'_m, rather than that of the different constituent materials. In this manner, the local effects of the differential lateral deformations of mortar, grout and blocks on the failure load of the assemblage are taken into consideration at the macroscopic level. The uniaxial compressive strength f'_m can be determined simply by testing four course prisms or by using one of the available theoretical failure criteria.

The values of the peak stresses, σ_{hmlp} and σ_{hm2p}, under different biaxial states of stress are defined by the failure envelope shown in Fig. 5.15. This failure envelope was developed by Kupfer and Grestel (1973) to fit the experimental results for plain concrete. Adopting this failure envelope for the homogeneous medium implies having equal uniaxial compressive strengths normal and parallel to bed joints. The test results of the panels of series UNP, which

were prepared with grout cores normal to bed joints, as well as the prisms of series UCR, which were prepared with grout cores normal and parallel to bed joints, are in agreement with this assumption. However, it is relatively simple to modify the failure envelope to account for any difference between the uniaxial compressive strengths normal and parallel to bed joints, if such a situation exists for other masonry assemblages.

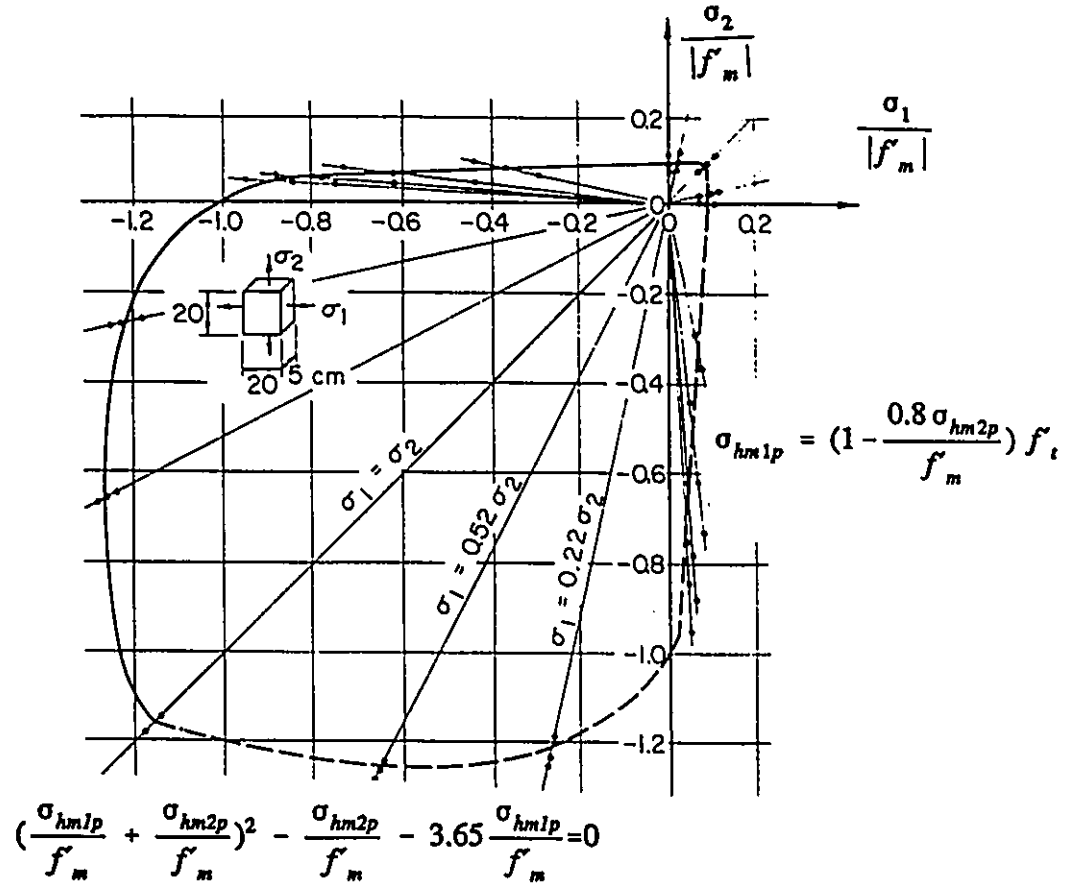

Fig. 5.15 Biaxial failure envelope for the homogeneous medium (Kupfer and Grestel 1973).

The uniaxial tensile strength of the homogeneous medium is defined by the following equation:

$$f'_t = 0.33\sqrt{f'_m} \qquad \ldots(5.40)$$

which was adopted in the ACI code (1989) and was used by Vecchio and Collins (1986) and Massicotte et al. (1988) for modelling plain concrete. The cracking stresses determined by this equation, along with the failure envelope shown in Fig. 5.15, agree with the experimental values of the panels of series RP, which were tested under the biaxial state of stress of $\sigma_{hm1}/\sigma_{hm2}=1/-1$. These panels exhibited cracks normal to the direction of the principal tensile stress, rather than following the mortar joints.

The next step in defining the equivalent uniaxial stress-strain curves is to determine the values of strain, ϵ_{hmjp}, associated with the peak stresses, σ_{hmjp}, which are different than the uniaxial compressive strength f'_m. Darwin and Pecknold (1977) suggested the following equation:

$$\epsilon_{hmjp} = \epsilon_o\left(3.15\frac{\sigma_{hmjp}}{f'_m} - 2.15\right) \quad ; |\sigma_{hmjp}| \geq |f'_m|$$

$$\epsilon_{hmjp} = \epsilon_o\left(-1.6\left(\frac{\sigma_{hmjp}}{f'_m}\right)^3 + 2.25\left(\frac{\sigma_{hmjp}}{f'_m}\right)^2 + 0.35\left(\frac{\sigma_{hmjp}}{f'_m}\right)\right) \quad ; |\sigma_{hmjp}| < |f'_m| \qquad \ldots(5.41)$$

The values of ϵ_{hmjp} are constrained to insure that E_o/E'_s in Eq. 5.39 is always greater than or equal to A+1. This procedure is adopted to ensure convexity of the stress-strain curve.

Similar to the assumption made by Darwin and Pecknold, a constant value for the Poisson's ratio ν is used under the biaxial tension-tension and compression-compression states of stress. However, a constant value of ν does not agree with the strain measurements obtained, in the experimental part of this investigation, for masonry under uniaxial compression or as reported by Kupfer et al. (1969) in their tests on plain concrete. A significant increase in the value of ν was observed as the compressive stresses approach the peak values. To account for this effect, the formula suggested by Massicotte et al. (1988) was fitted to the experimental results obtained for the tests of masonry assemblages with continuous grout in one or two directions. The equation used to define ν took the form of

$$\nu = \nu_o + \xi \left(\frac{\sigma_2}{f'_m}\right)^4 (1-\alpha_s) \qquad \ldots(5.42)$$

where α_s is the absolute principal stress ratio $|\sigma_{hm1}/\sigma_{hm2}|$,
ν_o is the initial Poisson's ratio, and
ξ is a constant determined by the regression analyses.

The values of the different parameters required in the above equation along with the experimental results are presented in Chapter 6.

5.7.3 Post-failure Stress-Strain Relationships

The homogeneous medium can fail either in tension or in compression according to the applied states of stress. The stress-strain relationships adopted

after the formation of cracks or compression failure are presented in the following sections.

5.7.3.1 Crack Formation

The homogeneous medium is considered to be cracked once the tensile stress reaches the ultimate tensile strength defined by the failure envelope. The cracks in the homogeneous medium are assumed to occur normal to the direction of the principal tensile stress. Cracking is modelled here in a smeared manner in which the cracked homogeneous medium is treated as a continuum, but with different average stress-average strain relationships. After cracking, Poisson's ratio is set equal to zero. The Young's modulus in the principal tensile stress direction E_1 is also reduced close to zero. An artificially small value of $E_1/1000$ was used to avoid numerical difficulty during the cracking response. The Young's modulus, E_2, parallel to the crack direction was determined according to the stress-strain curve in this direction.

The biaxial test results from the reinforced panels of series RP were used to establish average stress-average strain relationships for cracked masonry. The relationships are briefly presented here. More details on the experimental results and the regression analyses involved in defining these relationships are described in Chapter 6.

Principal compressive stress-strain relationships

The experimental results reported in Chapter 4 along with those obtained

by Vecchio and Collins (1982) indicate a significant degradation of the compressive strength and stiffness parallel to the crack direction as the tensile strain increases normal to it. Vecchio and Collins accounted for this effect by a damage parameter λ defined in terms of the tensile strain normal to the crack direction. This parameter was used to modify the compressive stress-strain relationships after cracking. The same procedure is followed herein to define the following formulae, which are shown in Fig. 5.16:

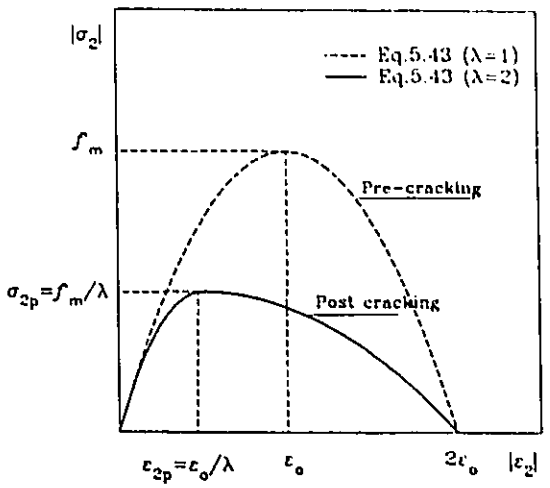

Fig. 5.16 Average stress-average strain relationship in the principal compressive stress direction for the homogeneous medium.

$$\sigma_{hm2} = f'_m \left[2\left(\frac{\varepsilon_{hm2}}{\varepsilon_o}\right) - \lambda\left(\frac{\varepsilon_{hm2}}{\varepsilon_o}\right)^2 \right] \quad ; \quad |\varepsilon_{hm2}| \le |\varepsilon_{hm2p}|$$

$$\sigma_{hm2} = \sigma_{hm2p}\left[1 - \frac{(\varepsilon_{hm2} - \varepsilon_{hm2p})^2}{(2\varepsilon_o - \varepsilon_{hm2p})^2} \right] \quad ; \quad |\varepsilon_{hm2p}| < |\varepsilon_{hm2}| \le |2\varepsilon_o| \qquad \ldots(5.43)$$

$$\sigma_{hm2} = 0 \quad ; \quad |\varepsilon_{hm2}| > |2\varepsilon_o|$$

where $\sigma_{hm2p} = \dfrac{f'_m}{\lambda}$, $\varepsilon_{hm2p} = \dfrac{\varepsilon_o}{\lambda}$, *and* $\lambda = \sqrt{\dfrac{\varepsilon_{hm1}}{\varepsilon_{hm2}}} - 0.3$

Tensile stress-strain relationships.

The stress-strain relationship obtained for the principal tensile stress direction, as shown in Fig. 5.17, is given by

$$\sigma_{hm1} = \frac{f_{cr}}{1 + 400\ \epsilon_{hm1}} \qquad \ldots(5.44)$$

where f_{cr} is the cracking stress defined by the failure envelope according to the ratio of $\sigma_{hm1}/\sigma_{hm2}$.

This relationship deals with the average values and does not provide information about the local behaviour. At a crack, the tensile stresses in the reinforcement are higher than average, whereas midway between two cracks they are lower than average. The stresses resisted by the homogeneous medium, on the other hand, are zero at the cracks and higher than average midway between cracks. The ability of the reinforcement to transmit the local stresses could govern the ultimate capacity of a cracked macro-element. Considering the equilibrium requirements along sections a-a and b-b in Fig. 5.18, Vecchio and Collins (1982) derived the following equation

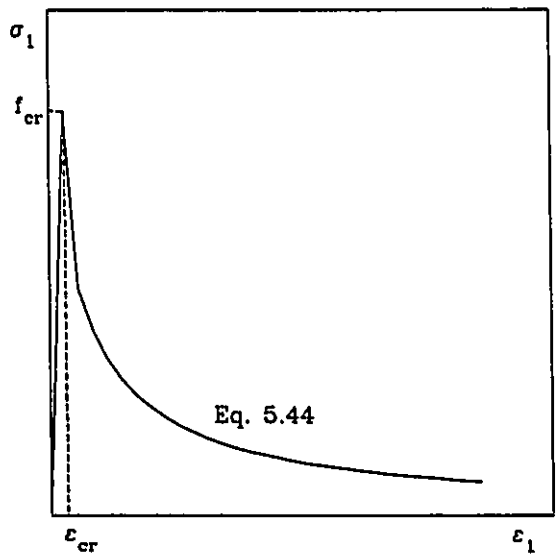

Fig. 5.17 Average stress-average strain relationship in the principal tensile stress direction for the homogeneous medium after cracking.

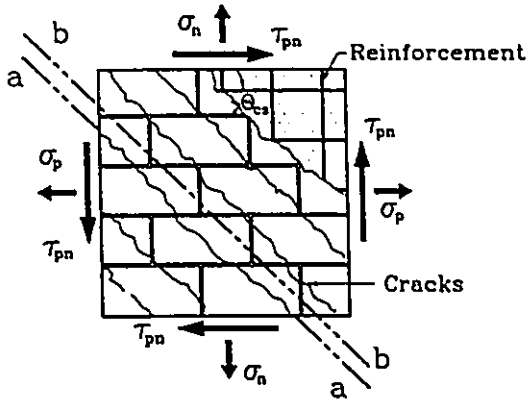

(a) Macro-element in a cracked masonry assemblage.

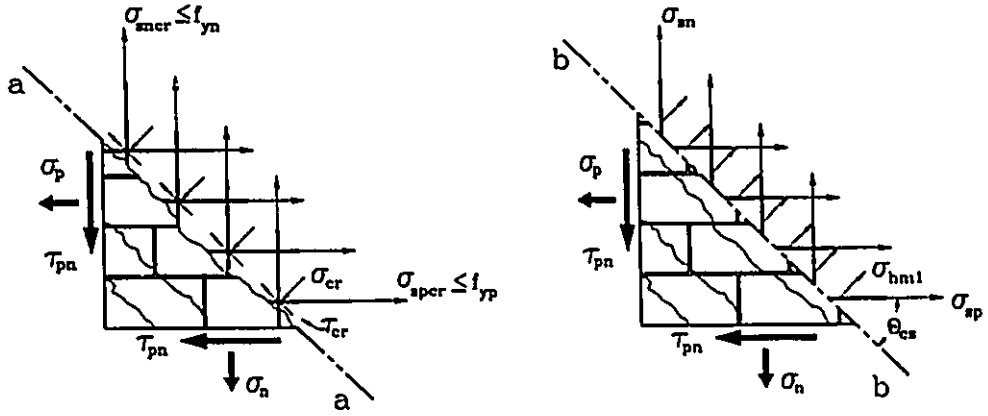

(b) Equilibrium conditions along sections a-a and b-b.

Fig. 5.18 Average stresses versus local stresses along a crack (adapted from Vecchio and Collins 1986).

which provides an upper limit for the average tensile stress when the reinforcement in the two orthogonal directions yield.

$$\sigma_{hm1} \leq \rho_p(f_{yp} - \sigma_{sp})\cos^2\theta_{cs} + \rho_n(f_{yn} - \sigma_{sn})\sin^2\theta_{cs} \quad \ldots(5.45)$$

where θ_{cs} is the crack angle measured from the reinforcement parallel to the bed joint plane as indicated in Fig. 5.18,

σ_{sp} and σ_{sn} are the stresses in reinforcement parallel and normal to bed joint planes, respectively, and

f_{yp} and f_{yn} are the yield stress of the reinforcement parallel and normal to bed joint planes, respectively.

5.7.3.2 Compression Failure

In the case of biaxial compression-compression states of stress, compression failure is defined according to the failure envelope. After failure, the Young's moduli in the two principal directions are reduced to $E_o/1000$ and Poisson's ratio is set equal to zero. Under biaxial tension-compression states of stress, on the other hand, the compression failure occurs after the formation of cracks. The failure stress in this case is defined in terms of the damage parameter λ as indicated by Eq. 5.43. The remaining Young's modulus parallel to the cracks is then dropped to $E_o/1000$ and the behaviour is described by the descending branch of Eq. 5.43.

5.8 IDEALIZATION OF REINFORCEMENT

Each set of reinforcement is assumed, at the macroscopic level, to resist the average axial stress acting parallel to its direction. This assumption does not

account for the local dowel action of reinforcement crossing the cracks and consequently implies that the total average shear stress has to be resisted by the masonry assemblage. The elasticity matrix for a set of reinforcement "i" in its local coordinates can be written as

$$[D]_i = \begin{bmatrix} E_s & 0 & 0 \\ & 0 & 0 \\ Sym. & & 0 \end{bmatrix}_i \qquad \ldots(5.46)$$

where E_s is the Young's modulus of steel.

Yielding of the set of reinforcement "i" is described by the yield function

$$F_i(\sigma) = \sigma - f_{yi} = 0 \qquad \ldots(5.47)$$

A constant yield stress f_{yi}, which represents an elastic-perfectly plastic response, is adopted in the case of steel bars that exhibited a definite yield point. However, the 6 mm diameter steel bars did not exhibit a definite yield point. The yield stress, in this case, is defined as a function of the axial strain ϵ in the following form:

$$f_{yi} = 32.22 + \frac{E_s \epsilon}{\sqrt{1 + \left(E_s \frac{\epsilon}{f_u}\right)^2}} \qquad \ldots(5.48)$$

where f_u is the ultimate strength of the steel expressed in MPa.

5.9 PREDICTION OF THE MODES OF FAILURE

Modelling the masonry assemblage as a homogeneous medium, intersected

by two sets of planes of weakness, allows prediction of the different possible modes of failure, whether the planes of failure follow the mortar joints or not. Once the stresses induced in one of the component materials along the planes of weakness or in the homogeneous medium reach the values defined by its failure surface, it begins to shed stresses to the surrounding components. This process of stress redistribution continues until the final failure takes place. In this manner, the macro-behaviour model is capable of predicting the initiation and progress of the different modes of failure that may occur in the bed joint planes of weakness, the head joint planes of weakness, or the homogeneous medium in a separate or a combined manner.

The different modes of failure that can be predicted along the planes of weakness, which represent the failures of the mortar joints, are summarized in Fig. 5.11. They include failure of the bed joints, failure of the head joints, positive or negative stepped failure as well as toothed failure. Depending on the dominant stresses acting along the planes of failure, these modes of failure can be categorized as shear or tension failure. When the Mohr-Coulomb failure criterion (zone I in Fig. 5.13) is violated, the failure is identified as a shear failure, whereas the tensile failure can be identified when the tension cut-off criterion (zone II in Fig. 5.13) is violated.

A failure in the homogeneous medium symbolizes a failure of the masonry assemblage along planes normal to the principal stress directions, regardless of the bed joint orientation. According to the principal stresses ratio σ_1/σ_2, several

modes of failure can be recognized for the homogeneous medium as indicated in Fig. 5.19. The results obtained by Kupfer et al. (1969) in their biaxial tests on plain concrete are used herein to classify these modes of failure. A tensile mode of failure, characterized by a tensile crack normal to the principal tensile stress direction, is expected to occur under biaxial tension-compression states of stress

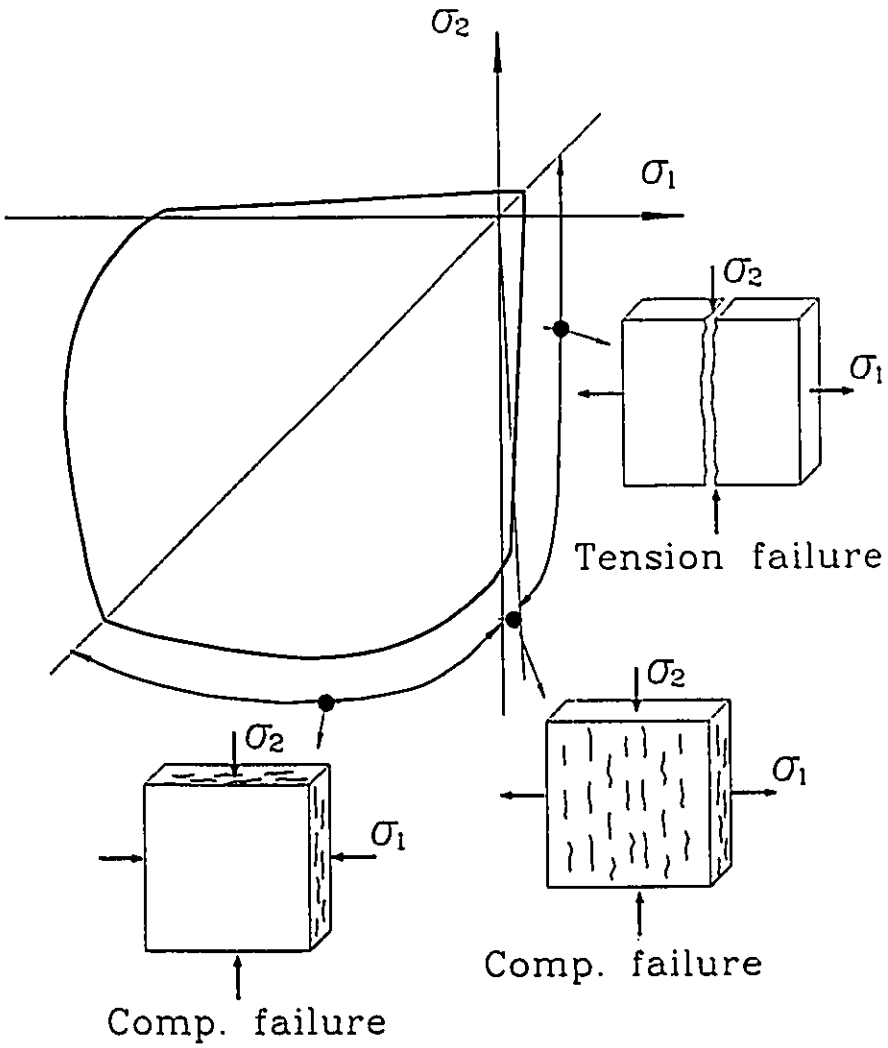

Fig. 5.19 Modes of failure of the homogeneous medium.

with $\sigma_1/\sigma_2 < 1/-15$ and under biaxial tension-tension states of stress. A compression mode of failure in the homogeneous medium is considered to occur under the biaxial compression-compression states of stress. This mode of failure was characterized by the formation of numerous micro-cracks in the longitudinal planes parallel to the plane of the masonry assemblage, as shown in Fig. 5.19, until complete crushing took place (Kupfer et al. 1969). Under uniaxial compression or biaxial tension-compression states of stress with $\sigma_1/\sigma_2 > 1/-15$, a compression mode of failure is expected to occur. Under these states of stress, micro-cracks were reported by Kupfer et al. to occur along the longitudinal and the transverse planes parallel to the direction of σ_2 as indicated in Fig. 5.19.

5.10 COMPUTATIONAL PROCEDURE

The formulation and the solution for the proposed macro-behaviour model are obtained using the initial strain method for nonlinear analysis. A brief discussion of the steps involved in this technique is presented below. For more information, the readers can refer to Zienkiewicz and Cormeau (1972 and 1974) and Higgins (1989).

1. The elasticity matrices of the different components of the masonry assemblage are defined in their local coordinates;

   $[D]_{hm}$ for the homogeneous medium,

   $[D]_b$ and $[D]_h$ for the planes of weakness, and

   $[D]_p$ and $[D]_n$ for the reinforcement.

2. The elasticity matrices are then transferred to the global coordinates and assembled to define the masonry assemblage elasticity matrix [*D*].
3. Under the effect of the applied stress increment, the elastic strain increments of the assemblage are determined. The strains induced in each part of the assemblage can then be evaluated.
4. The strains and stresses of each part of the assemblage are used separately to check the failure criteria and to evaluate the inelastic strain increments for the next iteration.
5. Stress increments, equivalent to the inelastic strain increments, are then determined for each component of the masonry assemblage. These stresses are assembled to define the stress increment for the next iteration.
6. If the convergence criteria are not satisfied, steps 3 to 5 have to be repeated.
7. If the convergence criteria are satisfied, the elasticity matrix of the homogeneous medium is updated and steps 2 to 6 under the effect of a new load increment are repeated.

In the proposed model, the convergence is checked by comparing the square root of the sum of the squares "RRS" of the change in the assemblage strains for the last iteration "m" to the RRS of the total strain. The RRS of the change in the strains of the last iteration "m" is also compared to the RRS of the strain increment induced in the first iteration of the current load increment "1".

The adopted convergence criteria can be expressed as

$$\frac{RRS(\Delta \epsilon^{lm})}{RRS(\epsilon)} \leq 0.01 \quad or \quad \frac{RRS(\Delta \epsilon^{lm})}{RRS(\Delta \epsilon^{ll})} \leq 0.001 \qquad \ldots(5.49)$$

where $RRS(\epsilon) = \sqrt{\epsilon_X^2 + \epsilon_Y^2 + \gamma_{XY}^2}$

A Fortran language program "MACROM" was developed, verified and used to predict the macro-behaviour of the masonry assemblages tested in this investigation and by others. In Chapter 7, the results obtained are discussed and compared to the experimental results.

5.11 CLOSING REMARKS

The macro-behaviour model presented in this chapter was developed to predict the response of grouted concrete masonry under the effect of in-plane stresses. Although the proposed model is formulated at a macroscopic level, certain considerations are also given to the micro-behaviour along the mortar joints and the cracks. This helps to provide a more realistic simulation of the anisotropic characteristics (inherent and induced) of the masonry assemblage.

In the proposed macro-behaviour model, the masonry assemblage is replaced by an "equivalent material" which consists of a homogenous medium intersected by two sets of planes of weakness (along the head joint and bed joint planes) and two sets of reinforcement. Each set has its own characteristics and is described as an elastic-viscoplastic material. The macro-behaviour of the "equivalent material" is determined by smearing the influence of these sets

throughout the respective volumes which they occupy. This idealization provides a means of predicting highly anisotropic behaviour. Thus it can be expected to realistically model the inherent part of the anisotropic characteristics of a masonry assemblage.

The average characteristics of each set of the planes of weakness are defined in terms of the characteristics of the different components (block, mortar, grout and grout-block interface) along these planes. In addition, the interactions of the behaviours of the different components along the bed and the head joint planes of weakness are taken into consideration. These interactions permit prediction of the separate failures of the bed or the head joint planes as well as the stepped failure patterns through both of them.

The failure of the homogeneous medium is described by the biaxial envelope developed by Kupfer and Grestel (1973). This failure envelope is defined in terms of the uniaxial compressive strength of the masonry assemblage at $\theta=0°$, rather than that of grout, mortar or masonry unit. In this manner, the local effects of the differential lateral deformations in mortar, grout and block on the failure loads of the assemblage are taken into consideration at a macroscopic level. Once the tensile stress reaches the ultimate value defined by the failure envelope, the homogeneous medium is considered to be cracked. Cracking is modelled in the proposed model in a smeared manner in which the cracked homogeneous medium is treated as a continuum, but with different average stress-average strain relationships in the directions of the principal stresses.

CHAPTER 6

AVERAGE STRESS-AVERAGE STRAIN RELATIONSHIPS

6.1 INTRODUCTION

Moving towards the limit state design approach, more research effort has been devoted to establishing stress-strain relationships for masonry under different states of stress. With this approach, unlike the current Canadian design Code (CAN3-S304-M84) which is based on working stress design, masonry structures have to be designed at the ultimate load level and their responses have to be checked at the service load level. To be able to predict the response of these structures, particularly beyond the elastic range, it is necessary to have detailed information about the stress-strain characteristics of masonry before and after cracking. The characteristics required to define complete stress-strain relationships extend beyond the compressive strength and the initial Young's modulus of masonry to include the strain value associated with the peak stress, the falling branch, the ultimate strain, the Poisson's ratio as well as the influence of cracking on these characteristics. Such information is essential for modelling masonry structures and for developing a unified design procedure for masonry under the effects of the different internal forces (compression, tension, bending, and shear).

Until recently, there was very limited experimental data on the stress-stain relationships of masonry, particularly in the post-peak stress range and after cracking. It has been a common practice to assume that grouted concrete masonry is sufficiently similar to concrete to justify adopting the concrete stress-strain relationships for masonry. However, the question of "how realistic is this assumption?" remains to be answered. The uniaxial compression tests on grouted concrete masonry assemblages reported by Priestley and Elder (1983) and Hart et al. (1988 and 1989) suggested the need for some modification of the concrete stress-strain relationship, especially the descending branch. For cracked masonry, there has not been sufficient experimental data, obtained under uniform well defined stress conditions, to establish stress-strain relationships. The biaxial tests performed in this investigation, on the reinforced masonry panels, provide a unique opportunity to study the response of grouted masonry after cracking.

It is the main purpose of this Chapter to answer the question addressed earlier. In the next section, the compressive stress-strain relationships proposed in earlier investigations are summarized, followed by comparisons of them with the experimental results of two series of prisms tested under uniaxial compression to evaluate the required parameters. The macro-behaviour of masonry after cracking is discussed in conjunction with the results of the biaxial tests of series RP. These results were then used to judge the validity of the existing stress-strain relationships, originally developed for concrete, and to identify the necessary modifications.

It is important to point out that all of the average stress-average strain relationships proposed in this chapter are based on specimens that exhibited failures along planes normal to the directions of the principal stresses, regardless of the bed joint orientation. These relationships are meant to be used in modelling the response of the homogeneous medium, which constitutes a major element in the macro-behaviour model presented in Chapter 5. The adoption of these stress-strain relationships accounts for the stress-induced anisotropic characteristics due to cracking in the homogeneous medium, whereas the planes of weakness introduced along the mortar joints simulate the inherent anisotropic characteristics of masonry.

6.2 STRESS-STRAIN RELATIONSHIPS FOR MASONRY UNDER UNIAXIAL COMPRESSION

6.2.1 Existing Stress-Strain Relationships

Among the other stress-strain relationships proposed for concrete, the two formulae developed by Hognestad (1951) and Saenz (1965) are the most widely used. Hognestad used a parabolic equation to describe the ascending branch in the form of

$$\sigma = f'_c \left[2\left(\frac{\epsilon}{\epsilon_o}\right) - \left(\frac{\epsilon}{\epsilon_o}\right)^2 \right] \qquad ; \quad |\epsilon| \le |\epsilon_o| \qquad \ldots(6.1)$$

where ϵ_o is the strain associated with the peak compressive stress of concrete f'_c. Saenz included the initial Young's modulus E_o as a third parameter, in addition

to ϵ_o and f'_c, in the following formula:

$$\sigma = \frac{\epsilon E_o}{1 + (\frac{E_o}{E_s} - (1+A))\frac{\epsilon}{\epsilon_o} + A\left(\frac{\epsilon}{\epsilon_o}\right)^2} \qquad \ldots(6.2)$$

in which E_s is the secant modulus at the peak compressive stress, and
A is a constant equal to 1.

Although the formula proposed by Hognestad is a simpler alternative, inclusion of the third parameter in the formula, suggested by Saenz, improves its ability to fit the experimental results.

Priestley and Elder (1983) investigated experimentally the effects of confinement and loading rate on the complete stress-strain relationship. They performed tests on five-course prisms with continuous grout cores normal to bed joints only. They modified the stress-strain relationship originally proposed by Kent and Park (1971) for concrete, to fit the experimental results of grouted concrete masonry. As described in the following equation, the final relationships for unconfined masonry consisted of a parabolic ascending branch, a linear descending branch and a plateau at $0.2 f'_m$:

$$\sigma = 1.067 f'_m \left[2\left(\frac{\epsilon}{0.002}\right) - \left(\frac{\epsilon}{0.002}\right)^2 \right] \quad ; \ |\epsilon| \le |0.0015|$$

$$\sigma = f'_m [\, 1 - Z\,(\epsilon - 0.0015)] \ge 0.2 f'_m \quad ; \ |\epsilon| > |0.0015| \qquad \ldots(6.3)$$

$$\textit{where} \quad Z = \frac{0.5}{\left(\frac{3 + 0.29 f'_m}{145 f'_m - 1000}\right) - 0.002}$$

In these relationships, the compressive strain ϵ_o, corresponding to the peak compressive stress of masonry f'_m, was taken equal to 0.0015. It is also interesting to note the similarity between the equation used for the ascending branch and the formula suggested by Hognestad (Eq. 6.1). Different relationships were also proposed for confined grouted concrete masonry, which is outside the scope of this investigation.

As a part of a finite element analysis, Ewing (1988) used the formula proposed by Hognestad, with ϵ_o equal to 0.002, to describe the ascending branch of the compressive stress-strain relationship for uncracked masonry. The descending branch was described by an exponential curve in the form of

$$\sigma = f'_m \exp\left[- \Omega \frac{(\epsilon - \epsilon_o)}{\epsilon_o} \right] \geq 0.1 f'_m \quad ; \quad |\epsilon| > |\epsilon_o| \qquad ...(6.4)$$

where Ω is the parameter used to ensure that the ascending and descending branches are tangential at the peak stress. The descending branch was followed by a plateau at $0.1 f'_m$.

Hart et al. (1988 and 1989) reported on 107 tests on grouted concrete prisms having different confinement schemes. The four blocks high prisms were laid in a stack pattern with continuous grout cores normal to bed joints. They used the test results to check the stress-strain relationships proposed by Priestley and Elder (1983) and by Ewing (1988). The former relationships, given by Eq. 6.3, were found to overestimate the strength and to underestimate ϵ_o in the case of unconfined prisms. The predicted descending branch also did not match the

experimental results. The relationships proposed by Ewing were in better agreement with the results, except that the descending branch was not as steep as found in the tests. As a result, Hart et al. suggested two new stress-strain relationships, defined as the "acceptable fit model" and the "best fit model". The acceptable fit model consists of a linear ascending branch followed by an exponential function for the descending branch as follows:

$$\begin{aligned} \sigma &= f'_m \left(\frac{\epsilon}{\epsilon_o}\right) && ; \quad |\epsilon| \le |\epsilon_o| \\ \sigma &= f'_m \exp\left[-B_1 (\epsilon - \epsilon_o)\right] && ; \quad |\epsilon| > |\epsilon_o| \end{aligned} \qquad \ldots(6.5)$$

This relationships includes one constant B_1 to be determined using the experimental results. On the other hand, three constants B_2, B_3, and B_4 are required to define the best fit model which can be written as

$$\begin{aligned} \sigma &= f'_m \left(B_2\, \epsilon_o^2 + \left(\frac{1}{\epsilon_o} - B_2 \epsilon_o\right) \epsilon \right) && ; \quad |\epsilon| \le |\epsilon_o| \\ \sigma &= f'_m \left[B_3 + (1 - B_3) \exp\left[-B_4 (\epsilon - \epsilon_o)\right]\right] && ; \quad |\epsilon| > |\epsilon_o| \end{aligned} \qquad \ldots(6.6)$$

Several values for the four constants, B_1 to B_4, were reported for the test prisms. They also proposed the following equation to determine ϵ_o in terms of f'_m:

$$\epsilon_o = 0.01 \left[0.042 + 7.68 \left(\frac{f'_m}{1000}\right)\right] \qquad \ldots(6.7)$$

where f'_m is measured in MPa.

6.2.2 Proposed Stress-Strain Relationships

The experimental program described in Chapter 2 includes a large number of prisms tested under uniaxial compression to define the masonry compressive strength f'_m for the different panels. The prisms were four units high and were laid in the running-bond pattern. Strain measurements were recorded, as shown in Fig. 2.21, on seven of the prisms prepared with continuous grout cores normal to the bed joints only (series NG). The strain measurements included both normal and lateral strains. The same strain measurements were also recorded on fourteen of the prisms that had continuous grout cores normal and parallel to the bed joints (series NPG). The experimental results of series NG and NPG are summarized, respectively, in Tables 6.1 and 6.2 in terms of f'_m, ϵ_o, E_o, and the initial Poisson's ratio ν_o. It is important to note that the first three prisms in Table 6.1 were constructed along with the first batch of unreinforced panels, including UNP1-UNP5, whereas the last four prisms were constructed with the second batch, including UNP6-UNP16. This explains the significant change in the observed compressive strengths. The prisms reported in Table 6.2 were all constructed at the same time as the reinforced panels of series RP. Lacking the facilities required to perform these tests under displacement control, the following discussion is limited to the ascending branch of the stress-strain relationship.

The stress-strain data obtained in the tests of series NG and NPG were normalized by dividing the stresses by f'_m and the strains by ϵ_o, as shown in

Table 6.1 Summary of the test results of series NG.

PRISM	f'_m (MPa)	ϵ_o (mm/m)	E_o (GPa)	ν_o
NG1	11.3	1.51	16.1	0.12
NG2	10.3	1.47	16.0	0.44
NG3	12.4	1.37	16.2	0.23
NG4	14.4	1.66	21.0	0.13
NG5	17.7	1.48	25.1	0.41
NG6	15.1	1.91	25.1	0.42
NG7	15.7	1.78	26.7	0.22

Table 6.2 Summary of the test results of series NPG.

PRISM	f'_m (MPa)	ϵ_o (mm/m)	E_o (GPa)	ν_o
NPG1	16.9	1.95	24.7	0.27
NPG2	19.5	1.61	25.1	0.26
NPG3	17.3	1.93	26.7	0.26
NPG4	14.6	1.81	25.5	+
NPG5	15.9	2.17	25.7	+
NPG6	14.6	2.38	18.3	0.15
NPG7	14.5	2.07	20.9	0.26
NPG8	17.4	2.30	27.0	0.41
NPG9	17.1	1.32	26.0	0.14
NPG10	15.1	2.00	20.9	0.37
NPG11	19.7	2.06	26.2	0.38
NPG12	13.8	2.36	19.8	0.17
NPG13	15.1	1.88	21.9	0.18
NPG14	17.0	1.68	20.8	0.31

\+ No lateral deformation was recorded during the test.

Figs. 6.1 and 6.2, respectively. Regression analyses were then performed to determine the constant A in Saenz's equation given by Eq. 6.2. Constant values of 0.78 and 0.98 were determined for series NG and NPG, respectively. The value of constant A determined for series NPG is very close to the unity value normally used for concrete. This could be attributed to having continuous grout cores both normal and parallel to the bed joints. The modified Saenz's equation along with Hognestad's parabolic equation are compared to the experimental results in Figs. 6.1 and 6.2. The two equations fall in the range of the obtained results, but the modified Saenz's equation is much closer to the mean of the results.

The test results of series NG and NPG were used herein to evaluate the equation proposed by Hart et al. (1989) to predict the value of ϵ_o. A comparison

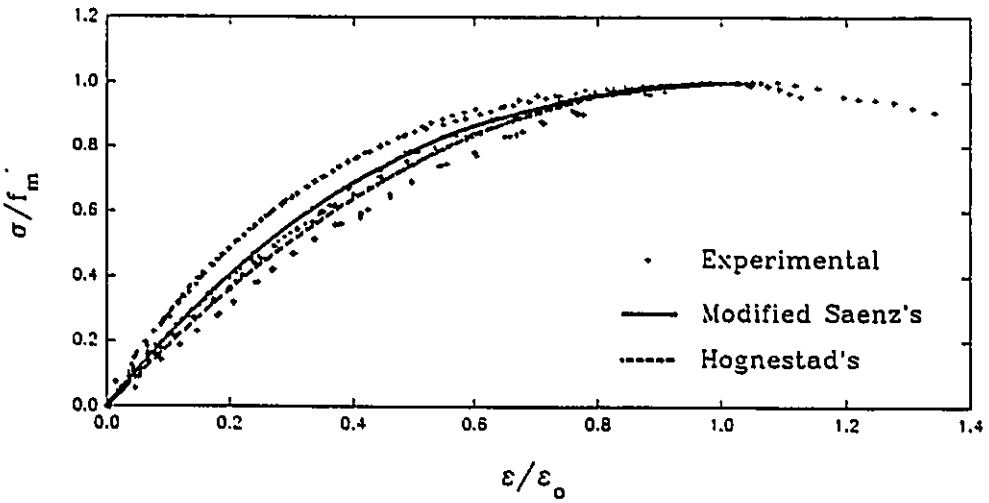

Fig. 6.1 Compressive stress-strain relationships for masonry with continuous grout cores normal to the bed joints only (Series NG).

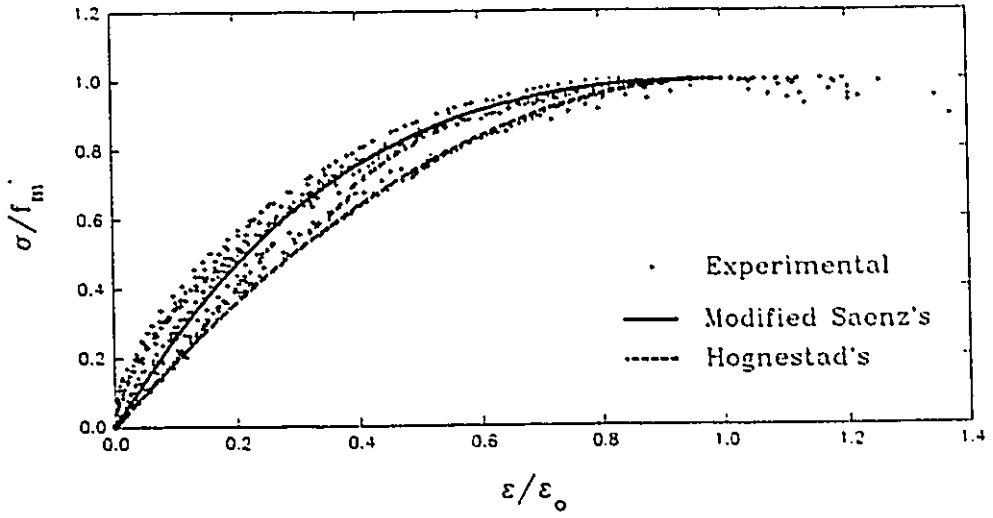

Fig. 6.2 Compressive stress-strain relationships for masonry with continuous grout cores normal and parallel to the bed joints (Series NPG).

of the predicted values with the experimental results is shown in Fig. 6.3(a) which reveals a significant scatter in the ratios between the observed and the predicted values of ϵ_o. Equation 6.7 seems to underestimate the value of ϵ_o especially for series NPG. Linear regression analyses were performed to re-evaluate the constants involved in this equation which can be rewritten as

$$\epsilon_o = 0.01 \left[C_1 + C_2 \left(\frac{f'_m}{1000} \right) \right] \qquad \ldots(6.8)$$

where C_1 = 0.116 and 0.30 for series NG and NPG, respectively,

and C_2 = 3.17 and -6.47 for series NG and NPG, respectively.

The predicted values of ϵ_o using this equation reflects better agreement (see Fig. 6.3(b)). The prisms of series NG exhibited a mean value of ϵ_o=0.0016 with a C.O.V. of 12.0%. The corresponding value for series NPG was 0.0019, with a C.O.V. of 14.4%, which is very close to the value of 0.002 usually used

for concrete. However, the dramatic changes in the values of C_1 and C_2 for the different set of data raises questions about the usefulness of the equation.

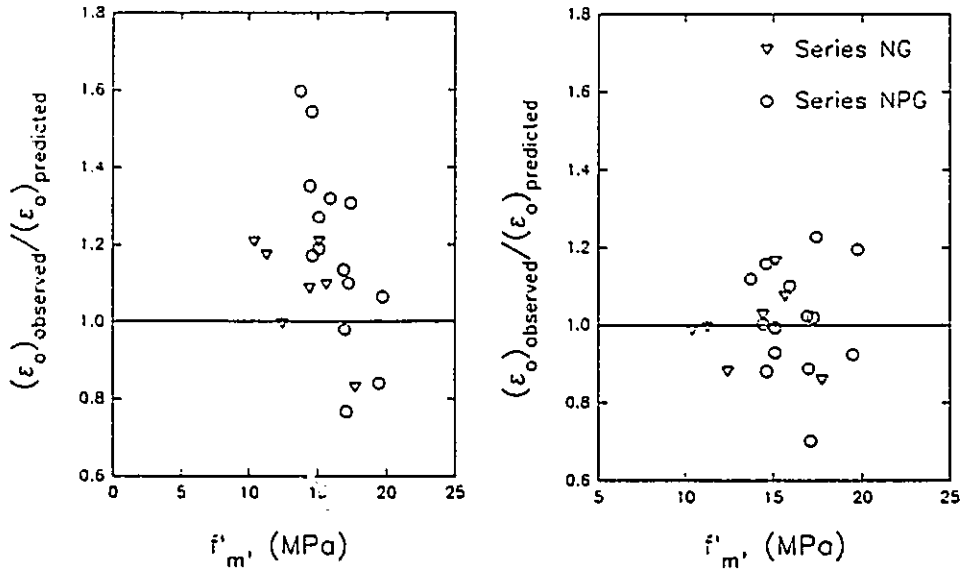

(a) Using Eq. 6.7 (b) Using Eq. 6.8

Fig. 6.3 Comparison of the observed and the predicted values of ϵ_o.

The lateral strain measurements recorded in the tests of series NG and NPG were used to determine the variations of Poisson's ratio ν with uniaxial compressive stress. As shown in Figs. 6.4 and 6.5, the Poisson's ratios remain almost constant up to compressive stresses in the range of $0.6 f'_m$, after which they begin to increase to reach values even higher than 0.5 in the unstable crushing phase. Similar behaviour was indicated for plain concrete (Chen, 1982 and Darwin and Pecknold, 1977), but at a higher compressive stress of about 0.8 of the concrete compressive strength. These results were used to determine the constant values in the following equation which was suggested by Massicotte et

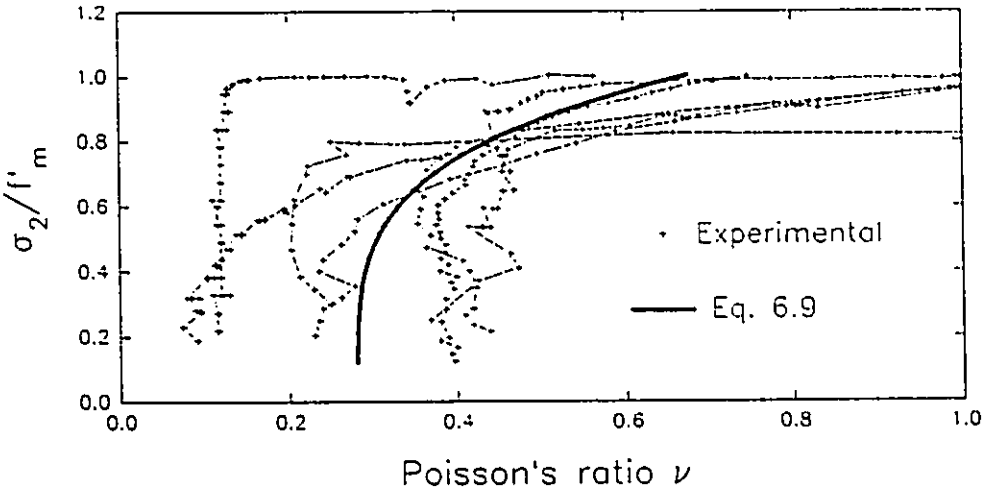

Fig. 6.4 Variation of Poisson's ratio with the uniaxial compressive stress for masonry with continuous grout cores normal to bed joints only (Series NG).

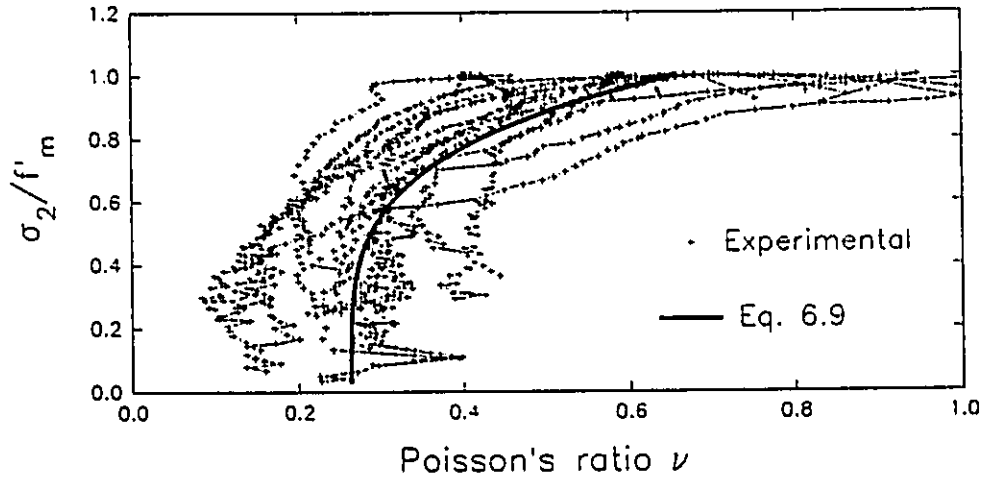

Fig. 6.5 Variation of Poisson's ratio with the uniaxial compressive stress for masonry with continuous grout cores normal and parallel to the bed joints (Series NPG).

al. (1988):

$$\nu = \nu_o + \xi \left(\frac{\sigma}{f'_m}\right)^4 (1-\alpha_s) \qquad \ldots(6.9)$$

where α_s is the absolute principal stress ratio $|\sigma_1/\sigma_2|$,

ν_o = 0.28 and 0.26 for series NG and NPG respectively, and

ξ = 0.39 for both series.

The curves defined by this equation are shown in Figs. 6.4 and 6.5 along with the experimental results.

6.3 MACRO-BEHAVIOUR OF CRACKED MASONRY UNDER BIAXIAL TENSION-COMPRESSION

6.3.1 Introduction

One of the major objectives of the biaxial tests performed on the reinforced panels of series RP is to achieve a better understanding of the macro-behaviour of grouted concrete masonry after cracking. Before cracking, the applied stresses are distributed between masonry and reinforcement according to their stiffnesses, which results in only a small contribution by the latter. After the reinforced assemblage has cracked, the ability of masonry to resist the principal tensile stress drops significantly, transferring more stresses to the reinforcement. The cracked masonry continues to help in resisting the principal compressive stresses, but with lower stiffness and ultimate capacity, depending on the crack orientation, the crack width, and the crack spacing.

Cracking of the masonry assemblage could take place along the mortar joints and/or on planes normal to the principal stresses (or strains), as indicated

in Fig. 6.6. The appearance of cracks along the mortar joints identifies those cases where the inherent anisotropic characteristics of masonry predominate. The post-cracking response of the masonry assemblages in these cases is accounted for in the proposed macro-behaviour model by the failures of the different components along the planes of weakness, as shown in Fig. 6.6(a) and described before in Chapter 5. On the other hand, the formation of cracks normal to the principal stress directions, as indicated in Fig. 6.6(b), is indicative of the induced anisotropic characteristics of the masonry assemblage. This part of the anisotropic characteristics is taken into consideration in the macro-behaviour model through the post-cracking response of the homogeneous medium. After cracking takes place in the homogeneous medium, as indicated in Fig. 6.6(b), the homogeneous medium is treated as a new material with its own stress-strain relationships in the principal stress directions. One of the main objectives of the following sections is to utilize the test results of series RP to define these relationships.

In the following sections, the assumption of perfect bond between the reinforcement and the masonry, adopted in the macro-behaviour model, is discussed. The experimental responses obtained after cracking, for the different reinforced panels of series RP, are also presented in terms of the stress-strain relationships in the principal directions. The results from panels that exhibited failures along planes normal to the principal stress directions, regardless of the bed joint orientation, are then used to define the average stress-average strain relationships required to describe the post-cracking behaviour of the homogeneous

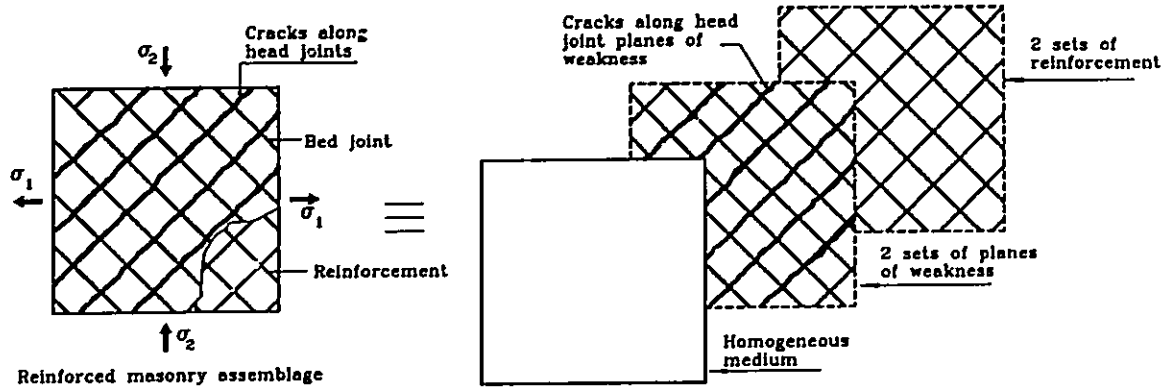

(a) Idealization of a masonry assemblage after cracking along the head joints.

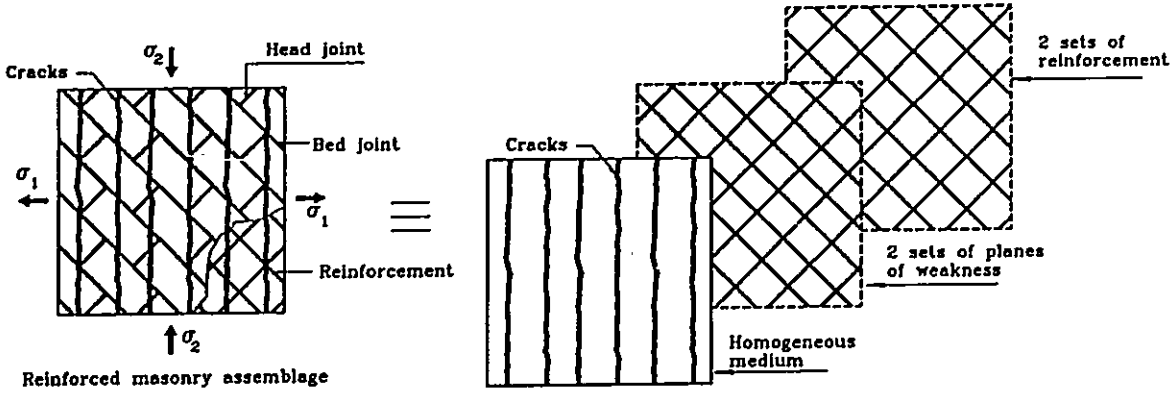

(b) Idealization of a masonry assemblage after cracking normal to σ_1.

Fig. 6.6 Modelling of cracked masonry assemblages.

medium of the macro-behaviour model.

6.3.2 The Assumption of Perfect bond at the Macroscopic Level

A longitudinal cross-section in a cracked reinforced masonry assemblage, subjected to a tension force T, along with a schematic illustration of the expected local stain and stress distributions are shown in Fig. 6.7. The stress and strain distributions shown in this Figure are adapted from the work by Somayaji and Shah (1981). At each crack, a short length of the bar is considered to be debonded from the masonry. Over this length, all of the tensile force has to be carried by the reinforcing bar, which in turn leads to different local strains in the masonry and the reinforcement in the vicinity of the cracks as shown in Figs. 6.7(b) and (c). Away from the cracks, where the masonry and the reinforcing bar are still bonded and experience the same local strain, a part of the tensile stress is transferred to masonry as indicated in Fig. 6.7(f). As the applied tensile force increases, the number of cracks increases and the length, along which local debonding takes place, increases.

As an alternative to the above, the macroscopic behaviour of a masonry assemblage can be described in terms of the average stresses and average strains in the masonry and the reinforcement. To complete the formulation of the macro-behaviour model presented in Chapter 5, it is necessary to relate the average strains in the masonry to those in the reinforcement. The macroscopic bond characteristics must be defined to describe this relationship.

An assumption of perfect bond between masonry and reinforcement, at

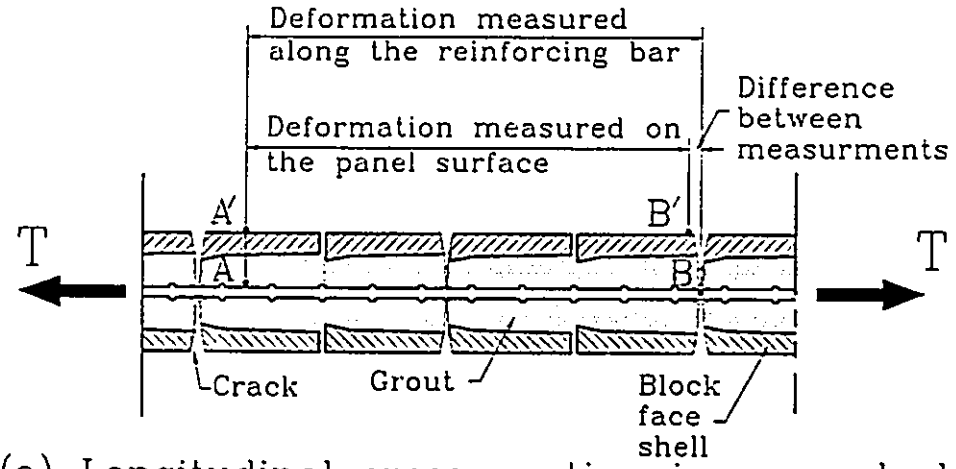

(a) Longitudinal cross–section in a cracked masonry assemblage.

(b) Strain distribution in reinforcement.

(c) Strain distribution in masonry.

(d) Stress distribution in reinforcement.

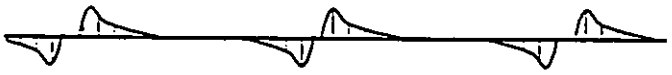

(e) Bond stress distribution.

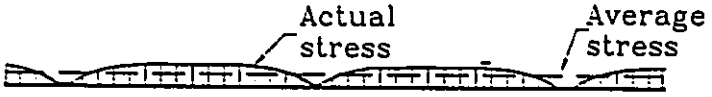

(f) Stress distribution in masonry.

Fig 6.7 Stress and strain distributions in a reinforced masonry assemblage after Cracking.

the macroscopic level, is adopted in the macro-behaviour model. This assumption requires that the same average strain components be experienced by both the masonry and the reinforcement but it does not rule out the possibility of local bond failures in limited zones along the masonry-reinforcement interface. Adoption of this assumption would not be reasonable if a bond failure took place in a global manner resulting in a significant difference between the average strains experienced by the masonry and the reinforcement.

In an attempt to verify the assumption of perfect bond between masonry and reinforcement at the macroscopic level, strain measurements were taken on both masonry and reinforcement as described before in Chapter 2. The measurements were taken on gage lengths of 900 mm, both parallel and normal to the bed joints. The strains recorded parallel and normal to bed joints (ϵ_p and ϵ_n) on panels RP1, RP4, and RP9 are shown in Fig. 6.8. These panels were chosen to represent different loading conditions and failure modes. Panel RP1 (θ=0°, σ_1/σ_2=1/-7.08, and $\rho_p=\rho_n$=0.26%) failed in compression after yielding of reinforcement parallel to bed joints. Panel RP4 (θ=67.5°, σ_1/σ_2=1/-7.7, and $\rho_p=\rho_n$=0.26%) exhibited a shear failure along the bed joints. Panel RP9 (θ=45°, σ_1/σ_2=1/0, and $\rho_p=\rho_n$=0.26%) failed by yielding of the reinforcement normal and parallel to bed joints. The results reveal good agreement between the strains experienced by the masonry and the reinforcement before and after cracking. The small differences in the observed values can be attributed to the different methods followed to attach the LPDTs to the masonry and the reinforcing bars. As

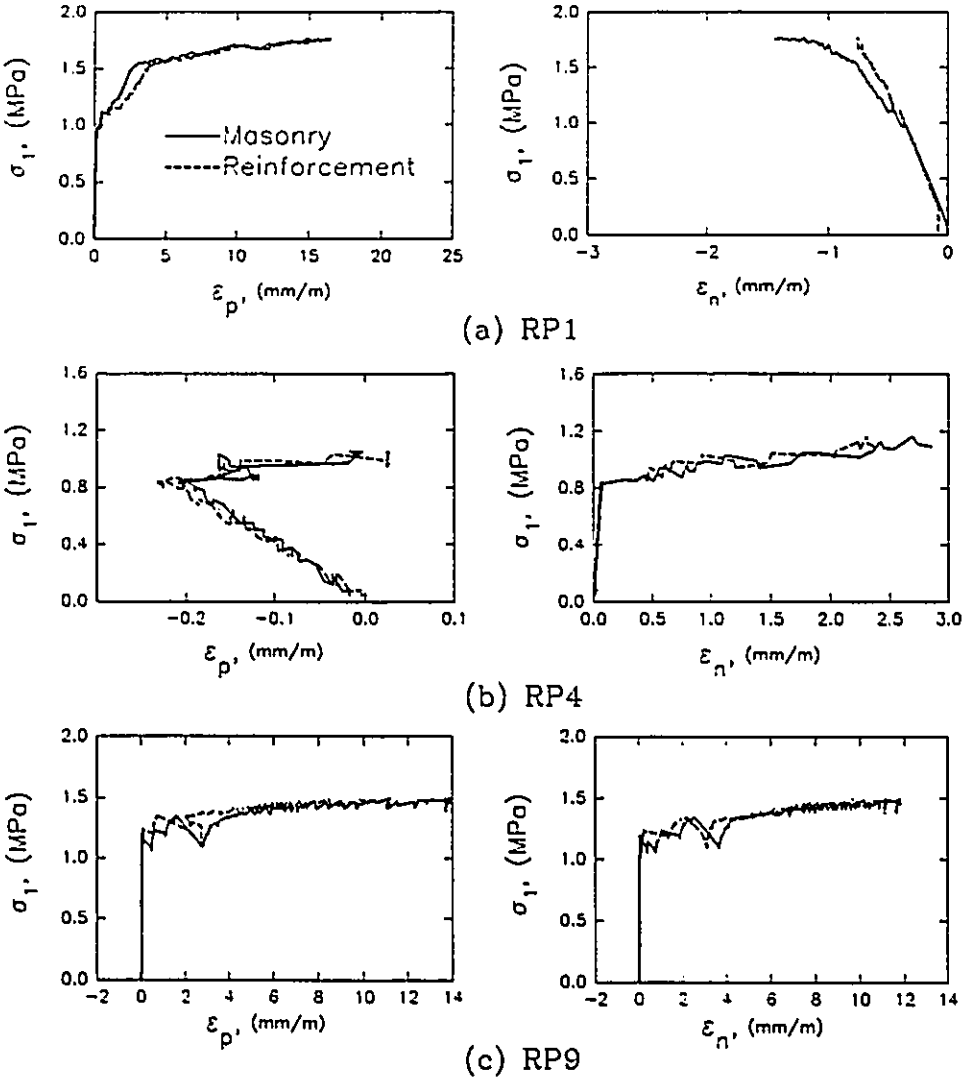

Fig. 6.8 Comparisons between the strains of masonry and reinforcement.

described in Sec. 2.2.5, the LPDTs used to measure the strains in the masonry were attached on the panel surfaces, whereas the LPDTs used to record the strains in reinforcement were attached to the reinforcing bars positioned in the centre of the wall cross-section. When a crack forms, the masonry in the vicinity of the crack is relieved of any tensile stress or strain as indicated in the local

stress and strain distributions in Fig 6.7(c) and (f). Due to the shear lag effect (i.e. plane section does not remain plane at or near a crack as shown in Fig. 6.7(a)), more deformation can be measured on the surface of the specimen compared to its centre. Therefore, the appearance of a crack near one of the points where the LPDTs are attached could result in a little difference between the deformations recorded on the panel surface and on the reinforcing bar as illustrated in Fig. 6.7(a).

The agreement found between the average stress-average strain relationships of the masonry and the reinforcement, along with the fact that no bond failures were observed in any of the panels tested, support the assumption of perfect bond at the macroscopic level.

6.3.3 Observed Response of Cracked Masonry

The deformations and the loads recorded during the biaxial tests of series RP were used to define the average stresses and strains experience by reinforced masonry as composite material and individually by the reinforcement as well as the masonry. These results were used to draw the average stress-average strain relationships for masonry in the principal directions. Figure 6.9 shows, as an example, the average stress and strain components experienced by panel RP8 at three different load levels. The analyses of the test results were performed according to the following steps:

1. The deformation measurements along with the applied loads were used to draw the Mohr's circles of average strain and average stress for the reinforced

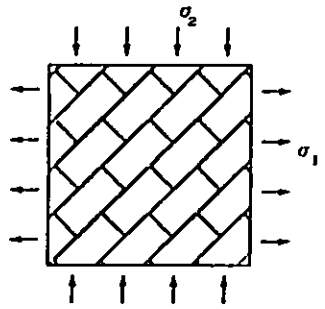

(a) Panel RP8
(θ=45°, σ_1/σ_2 =1/−1.08)

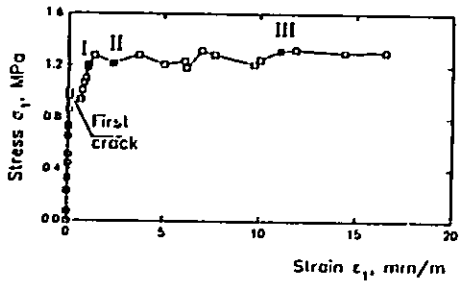

(b) $\sigma_1 - \varepsilon_1$ for RP8.

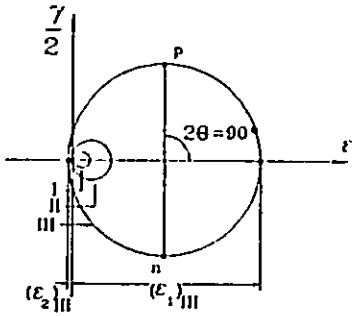

(c) Mohr's circles of average strains in the reinforced masonry assemblage, the reinforcement, and the masonry

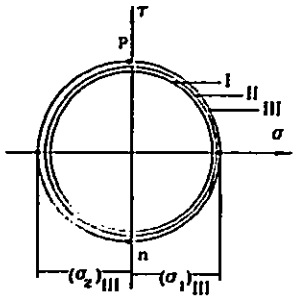

(d) Mohr's circles of average stresses in the reinforced masonry assemblage.

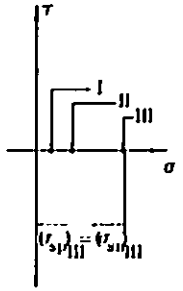

(e) Mohr's circles of average stresses in the reinforcement.

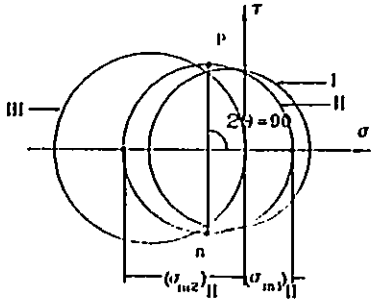

(f) Mohr's circles of average stresses in the masonry.

Fig. 6.9 Mohr's circles of average strains and average stresses for panel RP8.

masonry assemblage as shown in Figs. 6.9(c) and (d), respectively. This step is discussed in more details in Sec. 3.3.1.3. The adopted assumption of perfect bond between reinforcement and masonry, at the macroscopic level, implies that the same average strain components are experienced by the reinforced masonry assemblage, the reinforcement, and the masonry (see Fig. 6.9(c)).

2. According to the orientation of the reinforcement, the average axial strains experienced by the reinforcement parallel and normal to the bed joints (ϵ_p and ϵ_n) were determined from the Mohr's circles of strain obtained before in step 1, as indicated in Fig. 6.9(c). These strains, along with the stress-strain relationships determined for the reinforcing bars (Sec. 3.2.4), were used to define the average axial stresses resisted by reinforcement (σ_{sp} and σ_{sn}). These stresses were then used to draw the Mohr's circles of average stress for reinforcement as shown in Fig. 6.9(e). In the case of panel RP8, which was prepared with $\theta=45°$ and $\rho_p=\rho_n$, the average axial stresses resisted by the reinforcement were almost equal (i.e. $\sigma_{sp}=\sigma_{sn}$) resulting in circles with zero radii.

3. Subtracting the average stress components resisted by reinforcement from the corresponding total stresses resisted by reinforced masonry, the average stresses resisted by masonry alone were determined. These stresses were then used to draw Mohr's circles of average stress for masonry and to determine the average principal stresses (σ_{m1} and σ_{m2}), as shown in Fig. 6.9 (f).

4. Having defined the average principal strains (ϵ_{m1} and ϵ_{m2}) and the average principal stresses (σ_{m1} and σ_{m2}) at the different load levels allows the average

stress-average strain relationships for the masonry to be drawn.

The above steps are based on the assumption that only the reinforcing bars resist axial stresses at the macroscopic level. This implies that all of the average shear stresses have to be resisted by the masonry.

The average principal tensile strain ϵ_{m1} versus the average principal tensile stress σ_{m1} relationships determined for the different reinforced panels are presented in Fig. 6.10. It is obvious that masonry continues to resist a part of the applied tension after cracking due to the tensile stresses carried by masonry between the cracks. The masonry contribution, known as the "tension stiffening effect", decays with increasing tensile strain, as the number and the widths of cracks continue to increase.

A comparison of the relationships obtained for panels RP1 and RP2, Fig. 6.10(a), reveals the effect of the bed joint orientation (and the reinforcement orientation) θ on the contribution of masonry in resisting the tensile stress after cracking. Panel RP1, which was prepared with θ=0°, displays a steeper falling curve compared to RP2, which was prepared with θ=22.5°. The same difference can also be observed between the stress-strain relationships of panels RP7 (θ=0°) and RP8 (θ=45°) which were tested under states of almost equal and opposite principal stresses. The effect of the bed joint orientation on the post-cracking behaviour of masonry is presented schematically in Fig. 6.11, in which the Mohr's circles of strains for θ=0 and 22.5° are shown. As the total stresses increase after cracking, the tensile strains continue to increase while the tensile

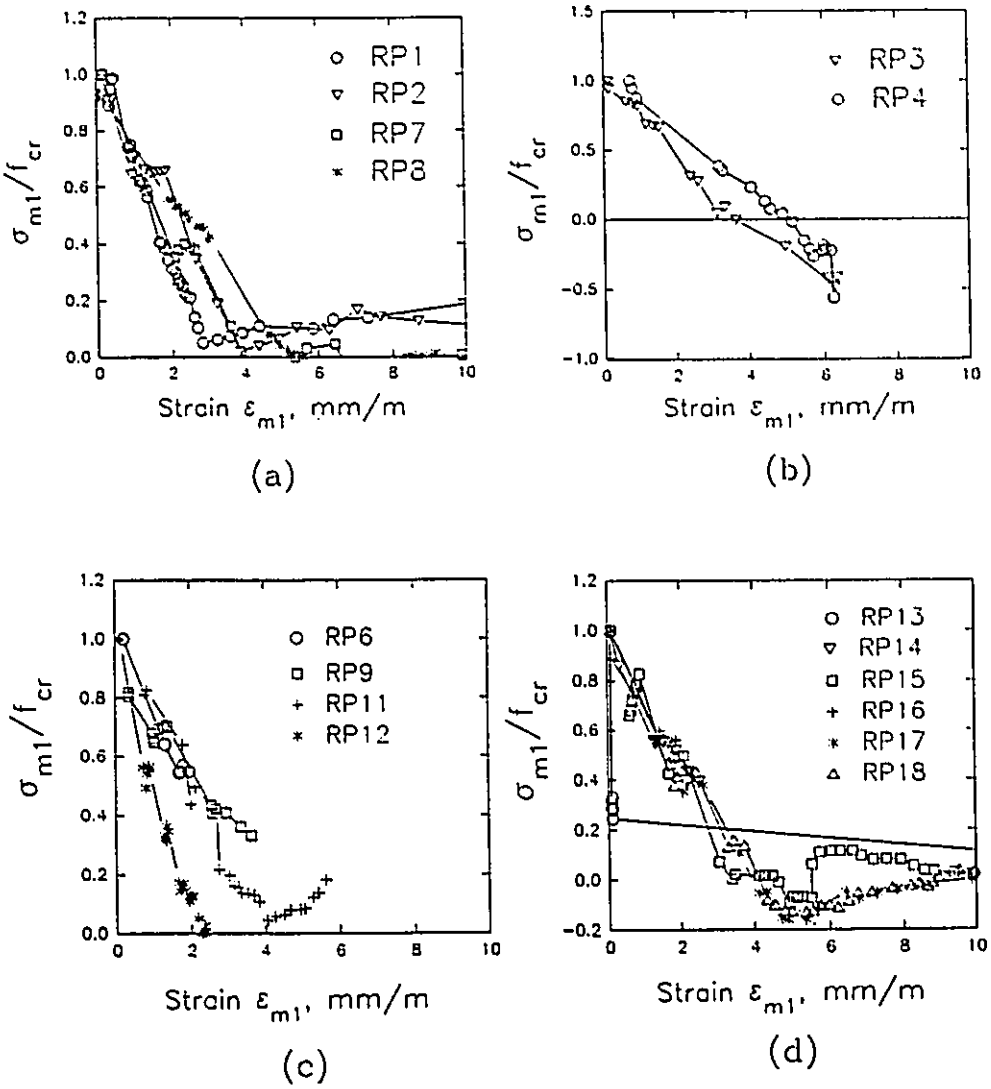

Fig. 6.10 Average stress-average strain relationships in the principal tensile directions of cracked masonry.

stresses resisted by the masonry continue to decrease. The contribution of the masonry is expected to decrease to close to zero when the reinforcement across the cracked sections reaches the yield stress. It is obvious, from the Mohr's circles of strains, shown in Figs. 6.11(a) and (b), that the reinforcement parallel to bed joints reaches the yield strain with θ=0° at a lower principal strain, ϵ_1,

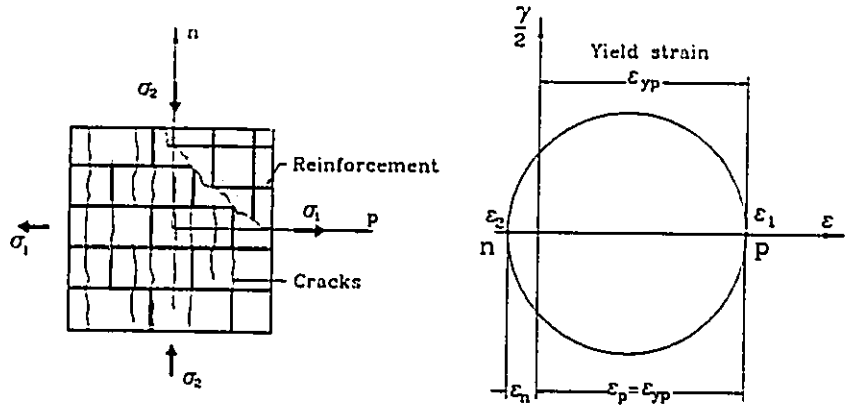

(a) Strain condition at yielding of the reinforcement with $\Theta=0^\circ$.

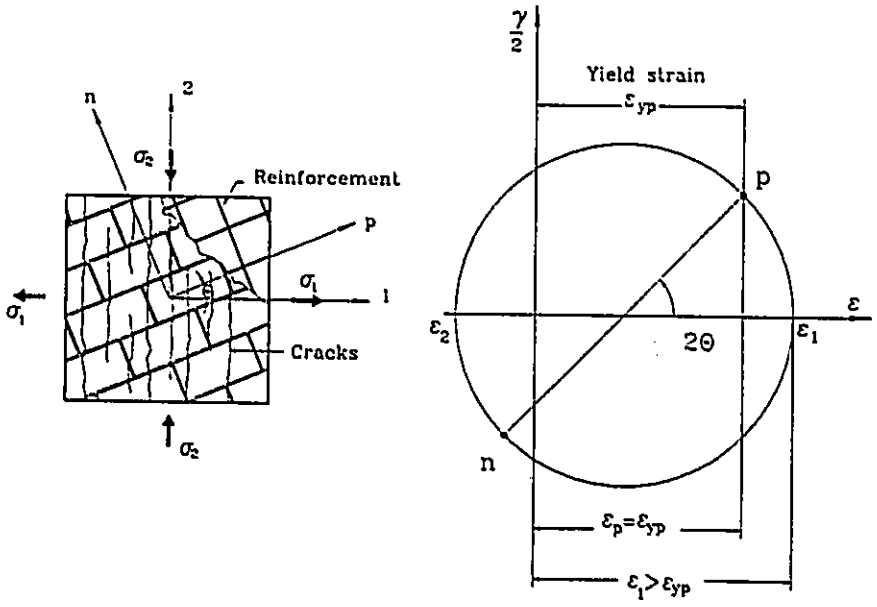

(b) Strain condition at yielding of the reinforcement with $\Theta=22.5^\circ$.

Fig. 6.11 Effect of the bed joint orientation θ on the principal tensile strain ϵ_1 at the stage of yielding of reinforcement.

than with θ=22.5°. This explains why the average principal tensile stress of cracked masonry drops to zero at a lower principal tensile strain for θ=0° compared to θ=22.5°.

As shown in Fig. 6.10(b), panels RP3 and RP4 exhibited a change in the principal tensile stress resisted by cracked masonry σ_{m1} from tension to compression, while the principal tensile strain ϵ_{m1} continued to increase. It is important to remember that these two panels, like the other panels, were tested under monotonic increasing loads applied in two orthogonal directions. This implies that the principal tensile stress resisted by cracked masonry σ_{m1} changed to compression while the principal tensile stress resisted by the reinforced assemblage remained in tension. The facts that panel RP4 (θ=67.5°, σ_1/σ_2=1/-7.7, and $\rho_p=\rho_n$=0.26%) failed in shear along the bed joints and panel RP2 (θ=22.5°, σ_1/σ_2=1/-6.22, and $\rho_p=\rho_n$=0.26%) exhibited a mixed mode of shear failure along the bed joints and spalling of the block face shells, as indicated in Sec. 4.3.1.1, could help explain the reasons behind this behaviour.

Cracks with rough surfaces result when they cross both the mortar and the grout along a bed joint. With the increase of the applied stresses, the slip along the cracked bed joints forces the rough surfaces of the cracks to separate. This deformation, known as "dilatancy", was noticed clearly in the shear tests of the couplet specimens especially in those that were grouted (Sec. 3.3.3.3). The dilation of the cracked bed joints induces additional tensile stress in any reinforcement crossing these joints. The induced tensile stress has to be balanced

by compressive stress in masonry normal to the cracked bed joints. Since panels RP3 and RP4 were tested with θ=45° and 67.5°, respectively, a component of the induced compressive stress in the masonry acts in the principal tensile stress direction. This component, along with the decreasing tensile stress resisted by the masonry after cracking, results in the change of the principal tensile stress from tension to compression. The induced tensile stresses due to the dilation of the cracked joints are added to the stresses from the externally applied load. These additional stresses could cause the reinforcement to yield at a lower applied load than predicted if masonry is modelled using one of the concrete models, neglecting the potential effect of shear slip along the mortar joints.

Figure 6.12 shows the Mohr's circles of average strains and average stresses measured at three loading levels for panel RP4. As indicated in Fig. 6.12(b), points I and II represent load levels after cracking, but before the shear failure took place along the bed joints. At these levels, increases in the applied stresses led to increases in the strains and the stresses experienced by the reinforced masonry assemblage and the reinforcement; Fig. 6.12(c),(d) and (e). Also, the principal compressive stress experienced by masonry increased with the increasing total stresses, whereas the principal tensile stress decreased but remained in tension. After the shear failure, the stresses resisted by the reinforced assemblage in the two principal directions decreased, as indicated in Fig. 6.12(d) by the Mohr's circle of stress III. At the same loading level, the tensile stress in the reinforcement normal to the bed joints continued to increase (Fig. 6.12(e))

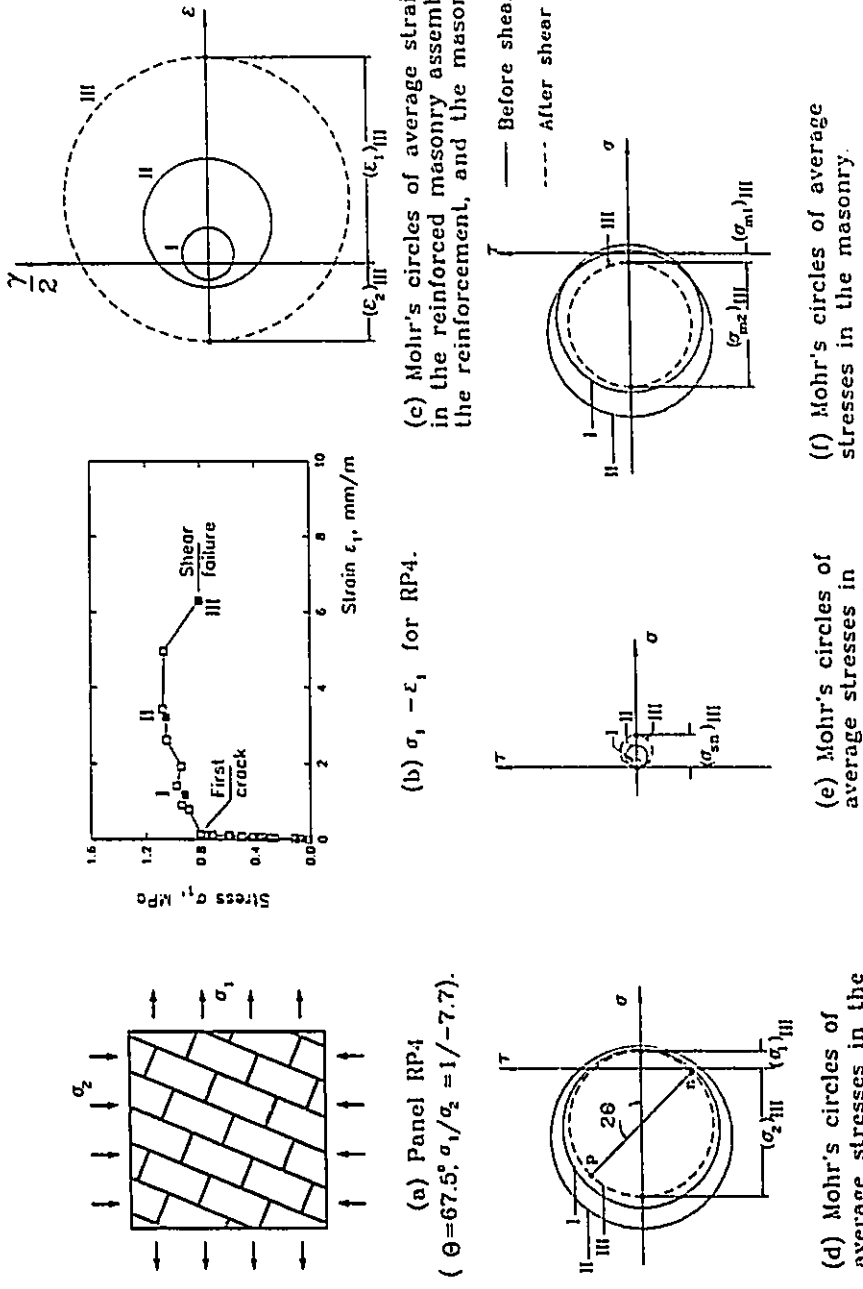

(a) Panel RP4 (θ=67.5°, σ_1/σ_2 =1/−7.7).

(b) $\sigma_1 - \varepsilon_1$ for RP4.

(c) Mohr's circles of average strains in the reinforced masonry assemblage, the reinforcement, and the masonry

(d) Mohr's circles of average stresses in the reinforced masonry assemblage.

(e) Mohr's circles of average stresses in the reinforcement.

(f) Mohr's circles of average stresses in the masonry.

Fig. 6.12 Mohr's circles of average strains and average stresses for panel RP4.

which resulted in a considerable reduction in the radius of the Mohr's circle III of the average stresses in masonry due to the change of the principal tensile stress σ_{m1} from tension to compression, Fig. 6.12(f).

Similar to the behaviour of panels RP3 and RP4, panels RP15, RP17 and RP18, with $\rho_p \neq \rho_n$, exhibited changes in the principal tensile stress in masonry from tension to compression, but only for small compressive stress values, as shown in Fig. 6.10(d). The main cracks in these panels were normal to the principal stress direction and not along mortar joints. However, during the process of stress redistribution between the reinforcement, shear deformations

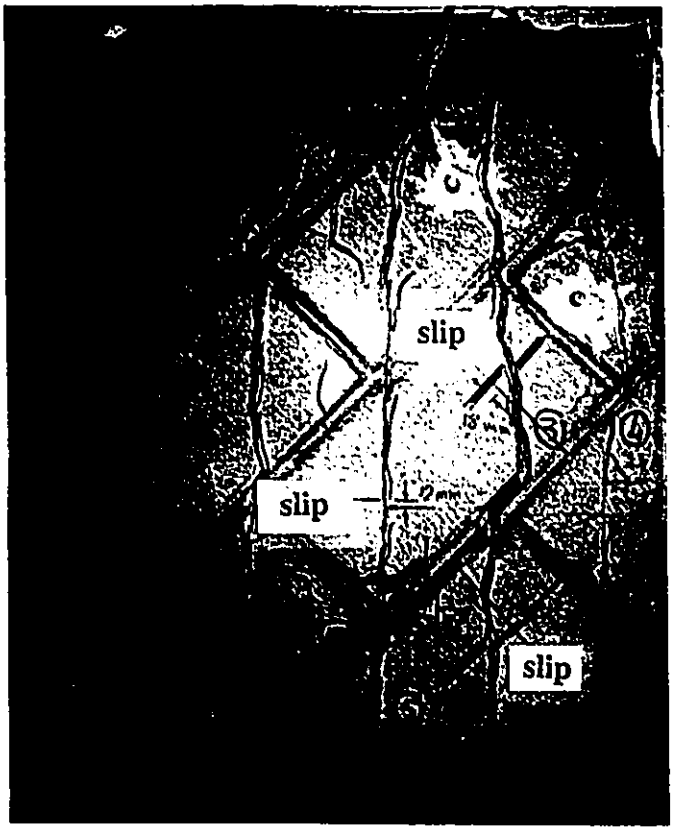

Fig. 6.13 Shear deformations along the cracks of panel RP18.

took place along the cracked sections as can be seen in Fig. 6.13. These deformations were accompanied by additional tensile stresses in the reinforcement along with compressive stresses in the masonry in the principal tensile stress direction. At large deformations (tensile strains), this effect tended to vanish as the crack widths increased moving the rough sides of the cracks apart.

The relationships of the average principal compressive strain ϵ_{m2} versus the average principal compressive stress σ_{m2}, obtained for the panels of series RP,

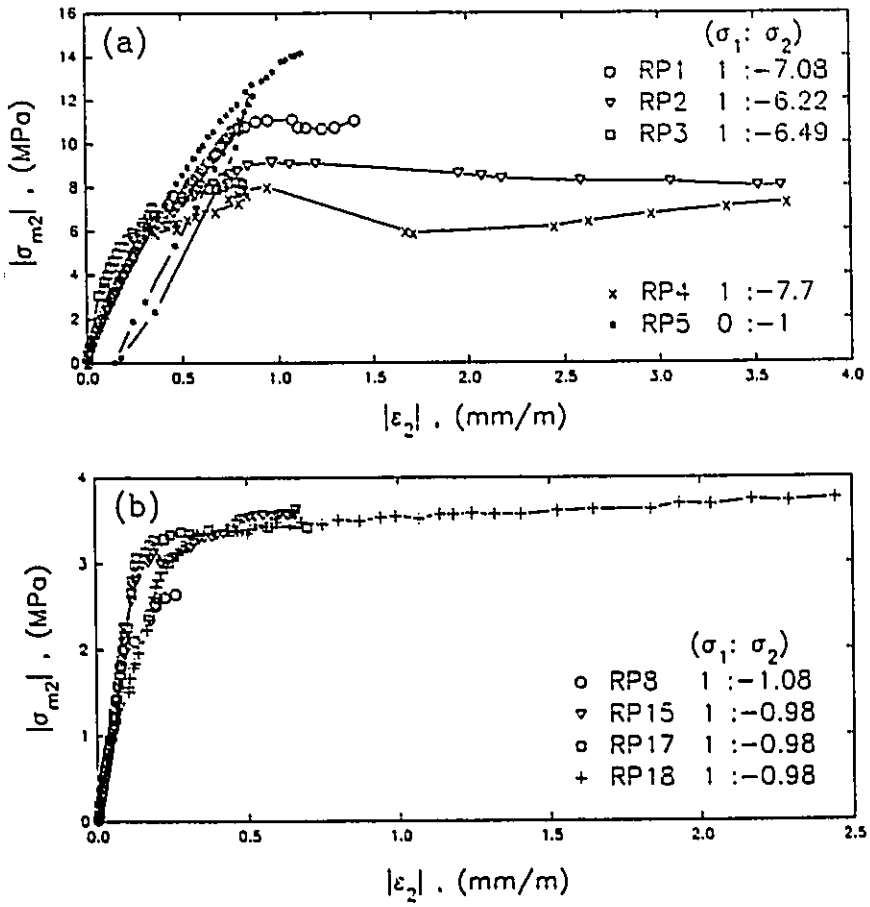

Fig. 6.14 Average stress-average strain relationships in the principal compressive directions of cracked masonry.

are presented in Fig 6.14. The results are arranged in two groups; the first group, shown in Fig. 6.14(a), were tested under states of stress in the range of σ_1/σ_2=1/-6.22 to 0/-1, whereas the second group, shown in Fig. 6.14(b), were tested under states of almost equal and opposite principal stresses. A comparison between the stress-strain relationships of RP5, which was tested under uniaxial compression, and the relationships for the other panels, which were tested under biaxial tension-compression, provides clear evidence of the reductions of the ultimate stress and the stiffness in the principal compressive stress direction after cracking. These reductions seem to increase as the algebraic ratio between the principal stresses σ_1/σ_2 decreases, corresponding to cases where the principal tensile stress dominates the behaviour leading to higher tensile strains. This trend can be confirmed by comparing the corresponding values of ultimate stress and stiffness of the panels tested under states of σ_1/σ_2 = 1/-1 with those from the panels tested under states of stress in the range of σ_1/σ_2=1/-6.22 to 1/-7.7, and with panel RP5 which was tested under uniaxial compression. Similar behaviour of reinforced concrete panels was reported by Vecchio and Collins (1982).

6.3.4 Average Stress-Average Strain Relationships for the Homogeneous Medium of the Macro-Behaviour Model after Cracking

6.3.4.1 Existing Stress-Strain Relationships

Based on their experimental results, Vecchio and Collins (1982) proposed average stress-average strain relationships for the principal stress directions of cracked concrete. The relationship proposed for the principal tensile stress

direction was:

$$\sigma_{c1} = \frac{f_{cr}}{1 + \sqrt{200\ \epsilon_1}} \qquad \ldots(6.10)$$

They also studied equilibrium of the cracked sections and sections between cracks as illustrated before in Fig. 5.18. As a result, Eq. 5.45 was proposed as an upper limit for the cases when yielding takes place in reinforcement which crosses cracked sections.

As indicated before, cracked concrete subjected to tensile strains in the direction normal to the compression was found to be weaker and develop larger strains than concrete under uniaxial compression. To account for this behaviour, Vecchio and Collins modified the parabolic equation of Hognestad (Eq. 6.1) using a damage parameter which was defined in terms of the tensile strain normal to the cracking direction. This is written as

$$\sigma_{c2} = f'_m \left[2\left(\frac{\epsilon_2}{\epsilon_o}\right) - \lambda \left(\frac{\epsilon_2}{\epsilon_o}\right)^2 \right] \qquad ;\ |\epsilon_2| \le |\epsilon_{2p}|$$

$$\sigma_{c2} = \sigma_{2p} \left[1 - \frac{(\epsilon_2 - \epsilon_{2p})^2}{(2\epsilon_o - \epsilon_{2p})^2} \right] \qquad ;\ |\epsilon_{2p}| < |\epsilon_2| \le |2\epsilon_o| \qquad \ldots(6.11)$$

$$\sigma_{c2} = 0 \qquad ;\ |\epsilon_2| > |2\epsilon_o|$$

where $\sigma_{2p} = \frac{f'_c}{\lambda}$, $\epsilon_{2p} = \frac{\epsilon_o}{\lambda}$, *and* $\lambda = 0.58 + 0.27\frac{\epsilon_1}{\epsilon_2}$ ...(6.12)

Thus, the principal compressive stress was defined, after cracking, as a function of both ϵ_1 and ϵ_2.

In the context of a finite element program for reinforced masonry walls, Ewing (1988) utilized Eq. 6.10 along with the following two other equations in the principal tensile stress direction:

$$\sigma_{ml} = 0 \qquad \ldots(6.13)$$

$$\sigma_{ml} = f_{cr}\left[K_1+(1-K_1)\exp\left(-\alpha 1\ \frac{\epsilon_1-\epsilon_{cr}}{\epsilon_1}\right)\right] \qquad \ldots(6.14)$$

Although Eq. 6.13 implies zero tension stiffening, the constants in Eq. 6.14 were used to control the shape of the falling branch. The values of these constants were given at different percentages of reinforcement. Ewing adopted the stress-strain relationships, proposed by Vecchio and Collins for the principal compressive stress direction, after replacing the descending branch by an exponential function as given in Eq. 6.4. Similar relationships were also adopted by Seible et al. (1990) in another finite element analysis for masonry assemblages. In the finite element analyses performed by Ewing and by Seible et al., the stress-induced anisotropic characteristics of masonry were considered, whereas the inherent anisotropic characteristics due to the mortar joints were not.

6.3.4.2 Proposed Stress-Strain Relationships

Because the uniaxial compression test results of the prisms of series PNG were similar to the stress-strain relationships used for concrete, it was decided to use the experimental results of series RP to verify and modify the equations proposed by Vecchio and Collins. The test results of panels RP3 and RP4, which exhibited shear failures along mortar joints, were not used because the average

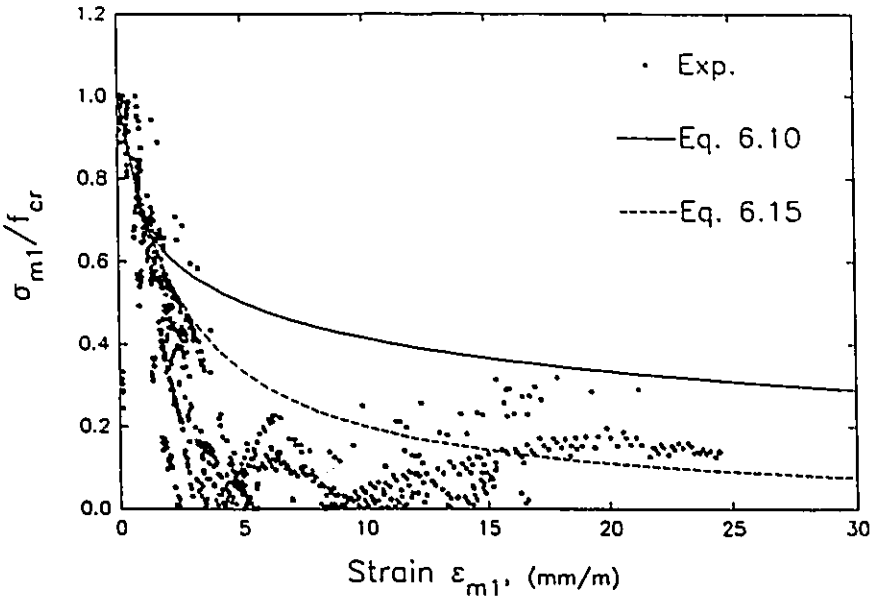

Fig. 6.15 Average stress-average strain relationships in the principal tensile stress direction.

stress-average strain relationships were meant to be used in modelling the homogeneous part of the macro-behaviour model.

The stress-strain relationship described by Eq. 6.10 is plotted along with the experimental results in Fig. 6.15. Equation 6.10 overestimates the contribution of masonry in resisting tensile stresses after cracking. This could be attributed to the significant difference between the relatively high percentages of reinforcement used in the reinforced concrete panels tested by Vecchio and Collins, compared to that used in the grouted masonry assemblages. To account for this difference, the following new equation is proposed.

$$\sigma_{ml} = \frac{f_{cr}}{1 + 400\ \epsilon_1} \qquad \ldots(6.15)$$

As can be seen in Fig. 6.15, this equation provides a better fit of the test results.

This equation should be used in conjunction with the upper limit proposed by Vecchio and Collins and given in Eq. 5.45 to account for the reduction in σ_1 as the reinforcement reaches its yield strain.

For the principal compressive stress direction, the values of the damage parameter λ, determined by Eq. 6.12, are plotted in Fig. 6.16 along with the experimental results. A continuous increase in the damage parameter λ (or in other words a continuous decrease in the peak value of the principal compressive stress σ_{2p}) with the increase in the absolute principal strain ratio $|\epsilon_1/\epsilon_2|$ is apparent. The rate of increase of the damage parameter λ also decreases with the increase of $|\epsilon_1/\epsilon_2|$. Whereas Eq. 6.12 seems to underestimate the peak value of the principal compressive stress σ_{2p} at high ratios of $|\epsilon_1/\epsilon_2|$, it is close to the experimental results at low ratios of $|\epsilon_1/\epsilon_2|$. In this regard, it should be noted that Eq. 6.12 was based on experimental results of reinforced concrete panels with a

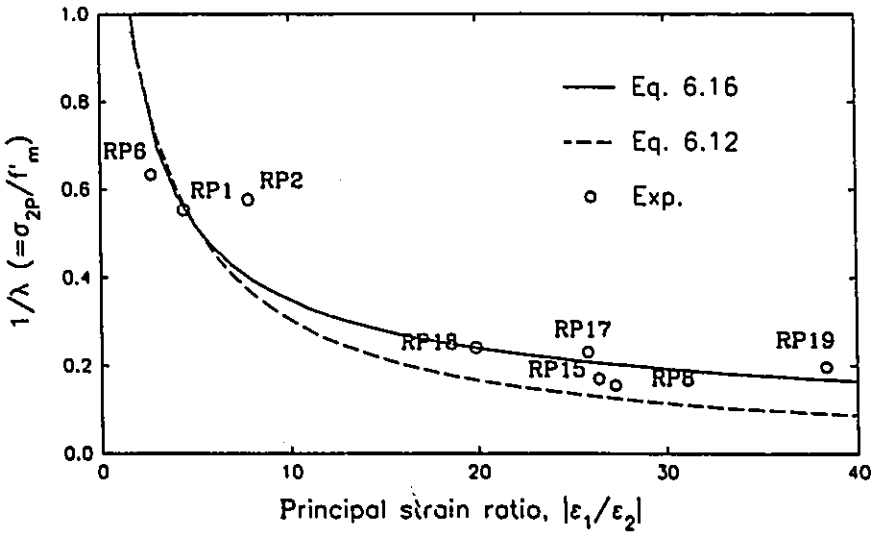

Fig. 6.16 Variation of $1/\lambda$ with the principal strain ratio $|\epsilon_1/\epsilon_2|$.

maximum value of $|\epsilon_1/\epsilon_2| = 20$. A regression analysis was performed to obtain an equation for the damage parameter λ, which better fits the results from series RP. This relationship is shown in Fig. 6.16 and takes the form of

$$\lambda = \sqrt{|\frac{\epsilon_1}{\epsilon_2}| - 0.3} \geq 1.0 \qquad \ldots(6.16)$$

6.4 CLOSING REMARKS

The following points summarize the main findings of this chapter:

1. Although the stress-strain relationships proposed by Hognestad (1951) and by Saenz (1965) for concrete fell within the range of the uniaxial compression test results, the relationship proposed by Saenz was found to be much closer to the mean of these experimental results.

2. Under uniaxial compression, the Poisson's ratio remains almost constant up to compressive stress in the range of $0.6f'_m$, after which it begins to increase to reach values even higher than 0.5 in the unstable crushing phase.

3. The strain measurements, recorded over gauge lengths of 900 mm in the biaxial tests of series RP, showed good agreement between the strains in the masonry and the reinforcement. This supports the assumption of perfect bond at the macroscopic level as was adopted in Chapter 5.

4. Before cracking, the stresses applied on a reinforced masonry assemblage are distributed between the masonry and the reinforcement according to their stiffnesses. After cracking, the ability of masonry to resist the principal tensile stress decreases significantly with increasing principal tensile strain ϵ_1. This leads

to transfer of more stress to reinforcement. The cracked masonry continues to help resist the principal compressive stresses, but with lower stiffness and lower ultimate capacity, depending on the principal strain ratio $|\epsilon_1/\epsilon_2|$.

5. Depending on the principal stress ratio and the bed joint orientation, cracking can occur along the mortar joints, rather than normal to the principal tensile stress direction. In this case, the shear deformation along the cracked joints is accompanied by dilation which induces additional tensile stresses in the reinforcing bars that cross these joints. These stresses can cause the reinforcement to yield at lower principal tensile stresses than would be predicted if masonry is modelled neglecting the potential for failure along the mortar joints. The induced tensile stresses in the reinforcement are balanced by compressive stresses in masonry, acting normal to the cracked joints. These could result in the principal tensile stress in cracked masonry changing from tension to compression.

6. Based on series RP, new formulae are proposed to describe the post-cracking behaviour of masonry when the cracks takes place along planes normal to the principal stress directions, regardless of the bed joint orientation. A damage parameter λ is used to account for the effect of tensile cracking on the stress-strain relationship in the principal compression stress direction. The relationships developed in this chapter are meant to be used for modelling the homogeneous medium in the macro-behaviour model presented in Chapter 5.

CHAPTER 7

PREDICTIONS OF THE MACRO-BEHAVIOUR MODEL

7.1 INTRODUCTION

The macro-behaviour model, presented in Chapter 5, together with the average stress-average strain relationships, proposed in Chapter 6, were used to analyze unreinforced and reinforced grouted concrete masonry assemblages subjected to different states of stress with different bed joint orientations θ. The predicted results were compared to the experimental test results from this study and elsewhere (Hamid (1978) and Guo (1990)). The wide ranges of masonry components and states of stress included in the tests provide a good background for assessing the potential of the macro-behaviour model to simulate the different aspects of the response of grouted masonry under in-plane stresses. The model also was used to predict responses to fill the gaps in the available test results and to provide a more complete picture of the macro-behaviour of grouted concrete masonry. Some observations regarding the shear response of grouted concrete masonry conclude this chapter.

7.2 MACRO-BEHAVIOUR OF UNREINFORCED MASONRY

In addition to the data presented in Chapters 2 to 4, results of two other series of prisms, tested under uniaxial compression with different θ (Hamid (1978) and Guo (1990)), were used to assess the reliability of the macro-

behaviour model. These tests include masonry assemblages built of blocks with different shapes and different percents solid, which consequently resulted in grout cores with different configurations. Whereas the prisms tested by Hamid were prepared using 140 mm block with flat ends; series UNP, series UCU and the series of prisms tested by Guo were built of 190 mm block with frogged ends. Furthermore, the webs of the blocks used to build series UCR were knocked out for a depth of 100 mm which resulted in continuous grout cores both normal and parallel to the bed joints. Added to this diversity in the geometric characteristics, a variety of material strengths were used.

The material properties used to model the homogeneous medium as well as the bed joint and the head joint planes of weakness in the analyses are summarized in Tables 7.1 and 7.2. As shown in Fig. 7.1(b), the head joint planes of weakness, for a masonry assemblage with grout cores normal to the bed joints, include the components of mortar, block face shells, and the block-grout interface. A forth component of grout is added for assemblages with grout cores both normal and parallel to the bed joints as shown in Fig. 7.2(b). The bed joint planes of weakness include grout and mortar in both cases, as indicated in Figs. 7.1(c) and Fig. 7.2(c). The area of each component along the planes of weakness was determined according to the dimensions and the configurations shown in Figs. 7.1 and 7.2. The areas of the grout and the mortar components along the bed joint planes of weakness were then altered to account for the effects of the shrinkage cracks and the mortar fins in reducing the minimum cross-sections

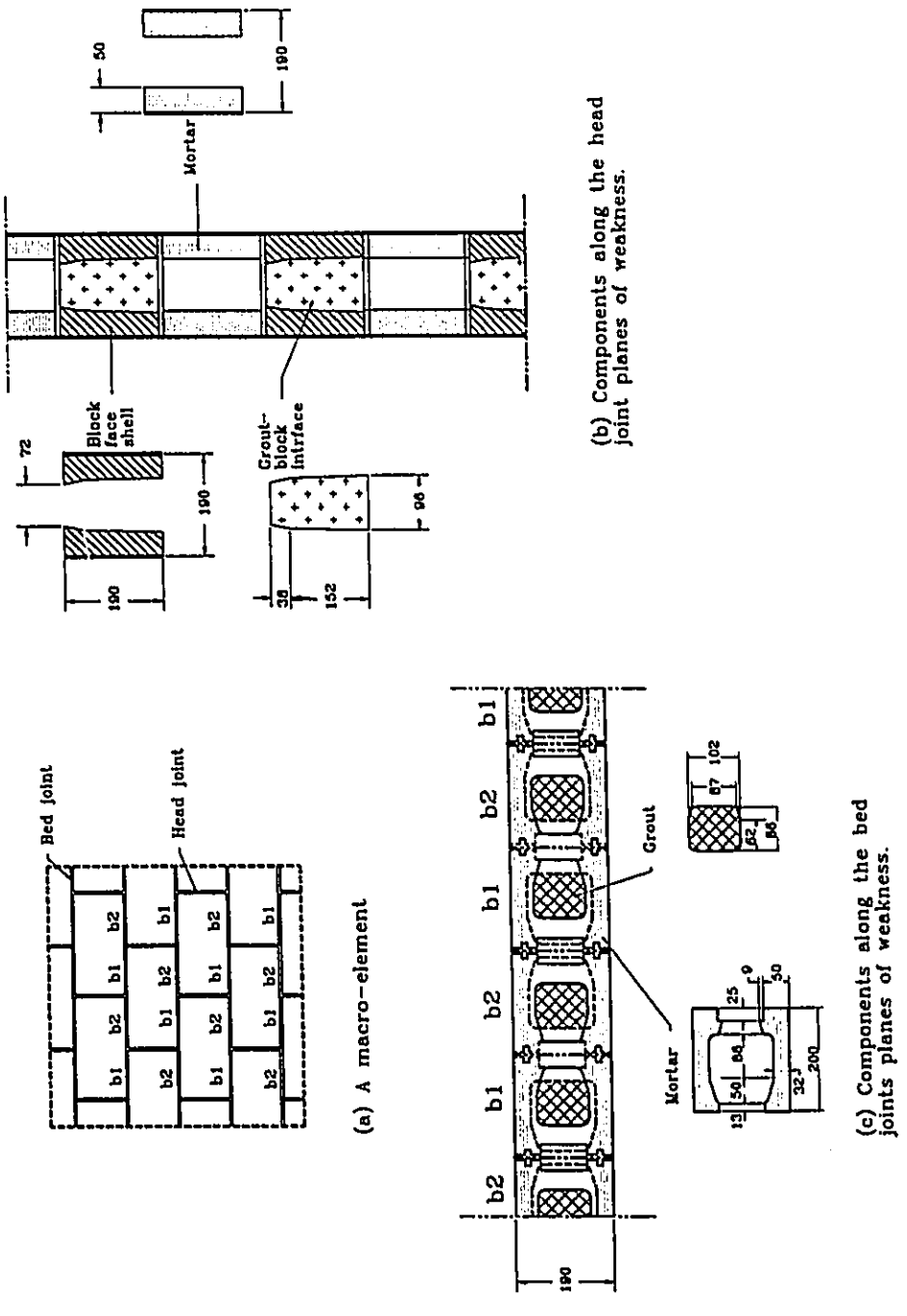

Fig. 7.1 Planes of weakness for a masonry assemblage with continuous grout cores normal to bed joints.

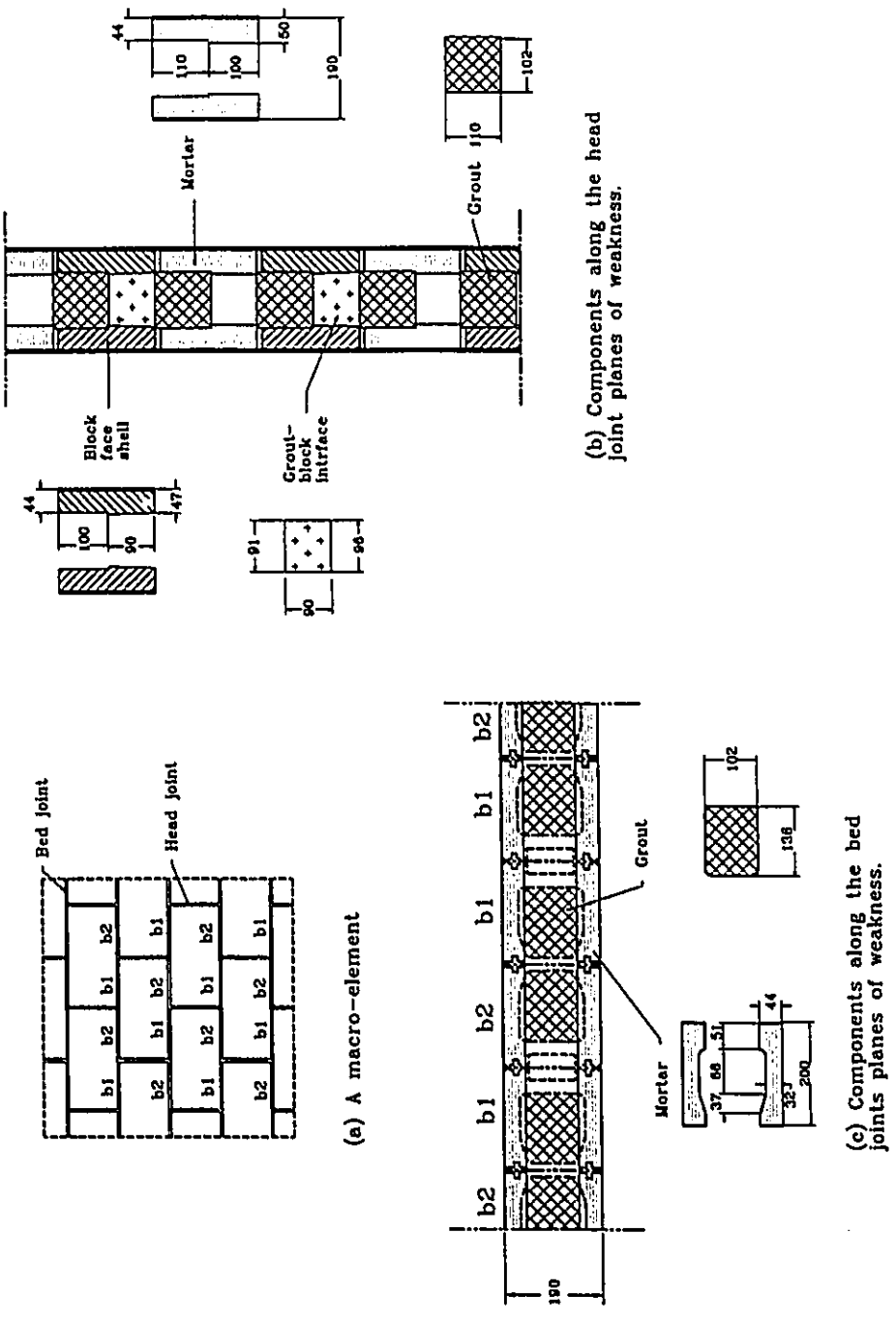

Fig. 7.2 Planes of weakness for a masonry assemblage with continuous grout cores normal and parallel to bed joints.

Table 7.1 Summary of the material properties used for analyzing specimens under uniaxial compression.

Component*		Item	Series			
			UNP and UCU	UCR	Hamid's	Guo's
Homogeneous medium		f_m' (MPa) f_t' (MPa) E_o (MPa) ϵ_o ν_o	11.1 1.1 15680 0.0015 0.2	17.4 1.4 24500 0.00194 0.26	13.6 1.2 25000 0.0015 0.2	13.6 1.2 25000 0.0015 0.2
Head joint planes of weakness	M	A_{mh}/A_h f_t' (MPa) c (MPa) Φ (deg.) ψ (deg.)	0.3 0.19 0.2 20 10	0.26 0.19 0.2 30 10	0.525 0.2 0.2 30 10	0.3 0.19 0.2 30 10
	B	A_b/A_h f_t' (MPa) c (MPa) Φ (deg.) ψ (deg.)	0.25 1.9 4.7 37 20	0.23 2.1 5.3 37 20	0.29 1.8 4.6 37 20	0.25 2.1 5.2 37 20
	G	A_{gh}/A_h f_t' (MPa) c (MPa) Φ (deg.) ψ (deg.)	--	0.29 4.3 7.9 37 37	--	--
	GBI	A_{in}/A_h f_t' (MPa) c (MPa) Φ (deg.) ψ (deg.)	0.23 -- 2.82 37 20	0.11 -- 3.18 37 20	0.19 -- 2.76 37 20	0.23 -- 3.12 37 20
Bed joint planes of weakness	M	A_{mb}/A_b f_t' (MPa) c (MPa) Φ (deg.) ψ (deg.)	0.45 0.25 0.23 33 15	0.45 0.25 0.35 43 15	0.55 0.5 0.52 46.9 15	0.45 0.25 0.35 43 15
	G	A_{gb}/A_b f_t' (MPa) c (MPa) Φ (deg.) ψ (deg.)	0.18 3.34 7.4 37 37	0.30 4.25 7.9 37 37	0.18 2.65 6.5 37 37	0.18 3.92 9.8 37 37

* M = Mortar, B = Block, G = Grout, and GBI = Grout Block Interface.

Table 7.2 Summary of the material properties used for analyzing specimens under uniaxial tension or biaxial states of stress.

Component*		Item	Series	
			UNP	UCR
Homogeneous medium		f_m' (MPa) f_t' (MPa) E_o (MPa) ϵ_o ν_o	14.0 1.23 18700 0.0015 0.2	17.4 1.4 24500 0.00194 0.26
Head joint planes of weakness	M	A_{mb}/A_b f_t' (MPa) c (MPa) Φ (deg.) ψ (deg.)	0.3 0.19 0.2 20 10	0.26 0.19 0.2 30 10
	B	A_b/A_b f_t' (MPa) c (MPa) Φ (deg.) ψ (deg.)	0.25 2.1 5.2 37 20	0.23 2.1 5.3 37 20
	G	A_g/A_b f_t' (MPa) c (MPa) Φ (deg.) ψ (deg.)	--	0.29 4.3 7.9 37 37
	GBI	A_{in}/A_b f_t' (MPa) c (MPa) Φ (deg.) ψ (deg.)	0.23 -- 3.12 37 20	0.11 -- 3.18 37 20
Bed joint planes of weakness	M	A_{mb}/A_b f_t' (MPa) c (MPa) Φ (deg.) ψ (deg.)	0.45 0.25 0.35 43 15	0.45 0.25 0.35 43 15
	G	A_g/A_b f_t' (MPa) c (MPa) Φ (deg.) ψ (deg.)	0.18 3.46 9.8 37 37	0.30 4.25 7.9 37 37

* M = Mortar, B = Block, G = Grout, and GBI = Grout Block Interface.

of the grout cores normal to bed joints (Sec. 4.4). Only 80% of the grout area was considered, whereas the other 20% was added to the mortar area to attain the same total area.

The parameters of the homogeneous medium were defined according to the relationships proposed in Chapter 6, utilizing the results of the auxiliary tests. The angles of friction "Φ" and the coefficients of cohesion "c" used for mortar were determined from the results of the direct shear tests reported with the corresponding series. The values of Φ and c used for the grout and the block face shell components were defined as $\Phi=37°$ and $c=f_c'/4.0$, in accordance with the values proposed by Johansen (1958) for plain concrete. The tensile strengths of the block and the grout components were taken equal to the splitting tensile strengths determined experimentally with each series. Following Johansen's recommendation (1975), in his analysis of plain construction joints, the coefficient of cohesion c at the grout-block interface was taken equal to 60% of the smaller of the values found for the grout and the block. The angle of friction, Φ, of the grout-block interface also was taken equal to the smaller of the values determined for the grout and the block, whereas the tensile strength of the grout-block interface was set equal to zero. In the absence of sufficient experimental information to define the angle of dilation ψ, the values used by Gerrard and Macindoe (1985) were used for guidance in this investigation.

In the next sections, the prediction using the model for various states of stress are presented and compared to the experimental results in terms of the

modes of failure, the strength characteristics and the deformation characteristics.

7.2.1 Uniaxial Compression

7.2.1.1 Modes of Failure

The modes of failure predicted for the specimens tested under uniaxial compression are summarized in Table 7.3, together with the observed modes. In agreement with the experimental results, the predicted modes of failure changed from compression failures in the homogeneous medium at $\theta=0°$ and 90° to shear failures along the head joints at $\theta=15$ and 22.5° and to shear failures along the bed joints at $\theta=67.5$ and 75°. At $\theta=45°$, where both the head joints and the bed joints were subjected to equal normal and shear stresses, a mixed mode of shear failure along the head joints, shear failure along the bed joints and compression failure of the homogeneous medium were predicted. The predicted modes of failure were consistently in agreement with those observed in the different series of tests. The prediction of the different modes of failure and their agreement with the experimental results demonstrate the ability of the macro-behaviour model to reproduce the different modes of failure that can be experienced by a grouted concrete masonry assemblage under uniaxial compression.

7.2.1.2 Strength Characteristics

For comparison purposes, the predicted strengths for the five series of specimens are presented in Table 7.3 together with the corresponding experimental results. The variations of the uniaxial compressive strengths, with

Table 7.3 Comparison between the predicted and the observed uniaxial compression behaviour.

Series	θ (deg.)	Predicted		Observed		Pre. $(\sigma_2)_{ult}$ / Obs. $(\sigma_2)_{ult}$
		Ultimate stress, $(\sigma_2)_{ult}$ (MPa)	Failure mode	Ultimate stress, $(\sigma_2)_{ult}$ (MPa)	Failure mode	
UNP	0	-11.1	CHM	-9.5	CHM	1.17
	22.5	-7.7	SHJ	-8.2	SHJ	0.94
	45	-9.4	Mixed	-9.5	Mixed	0.99
	67.5	-5.9	SBJ	-6.1	SBJ	0.97
	90	-11.1	CHM	-9.8	CHM	1.13
UCU	0	-11.1	CHM	-11.1	CHM	1.0
	22.5	-7.7	SHJ	-6.5	SHJ	1.18
	45	-9.4	Mixed	-7.8	Mixed	1.21
	67.5	-5.9	SBJ	-6.3	SBJ	0.94
UCR	0	-17.5	CHM	-17.0	CHM	1.03
	22.5	-15.4	SHJ	-13.9	SHJ	1.11
	45	-17.5	Mixed	-17.3	Mixed	1.01
	67.5	-11.6	SBJ	-14.5	SBJ	0.80
	90	-17.5	CHM	-18.8	CHM	0.93
Hamid's	0	-13.6	CHM	-13.4	CHM	1.01
	15	-9.6	SHJ	-9.8	SHJ	0.98
	45	-13.1	Mixed	-10.1	Mixed	1.30
	75	-8.4	SBJ	-8.3	SBJ	1.01
	90	-13.6	CHM	-13.7	CHM	0.99
Guo's	0	-13.6	CHM	-13.6	CHM	1.0
	30	-9.0	SHJ	-12.3	SHJ	0.73
	60	-9.4	SBJ	-8.5	SBJ	1.11
					Mean ratio	1.02
					C.O.V.	12.6%

CHM = Compression failure of the homogeneous medium,
C = Compression failure,
SHJ = Shear failure along head joints,
SBJ = Shear failure along bed joints, and
Mixed = Mixed mode of compression failure, shear failure along head joints, and shear failure along bed joints.

the bed joint orientation θ, are also shown in Fig. 7.3. Five distinct regions can be identified in the failure envelopes presented, with each region corresponding to a particular mode of failure. The straight lines marked by AB and EF correspond to conditions where the stress components acting along the planes of weakness were not large enough to cause shear failure along them. Compression failures were found to occur in the homogeneous medium regardless of the bed joint orientation. On the other hand, curves BC and DE represent the cases where shear modes of failure took place, separately, along the bed joint planes and head joint planes, respectively. Along these regions, the grouted concrete masonry assemblages exhibited a significant decrease in uniaxial compressive strength. The ratios between the minimum compressive strength and the compressive strength at $\theta=0°$ were predicted to be 0.52, 0.65, 0.54, and 0.65 for series UNP, series UCR, Hamid's prisms, and Guo's prisms, respectively. These ratios confirm the importance of considering the anisotropic characteristics of grouted concrete masonry under uniaxial compression.

At the bed joint orientations close to $\theta=45°$, a mixed mode of shear failure along the bed joint and the head joint planes was predicted for series UNP and UCU where points C and D coincide (Fig. 7.3(a)). In series UCR, which had grout cores both normal and parallel to the bed joints, the increases in the grout strength and in the minimum cross-sectional area of the grout cores helped strengthen the planes of weakness. As a result, a compression failure was predicted to occur in the homogeneous medium along line CD as shown in

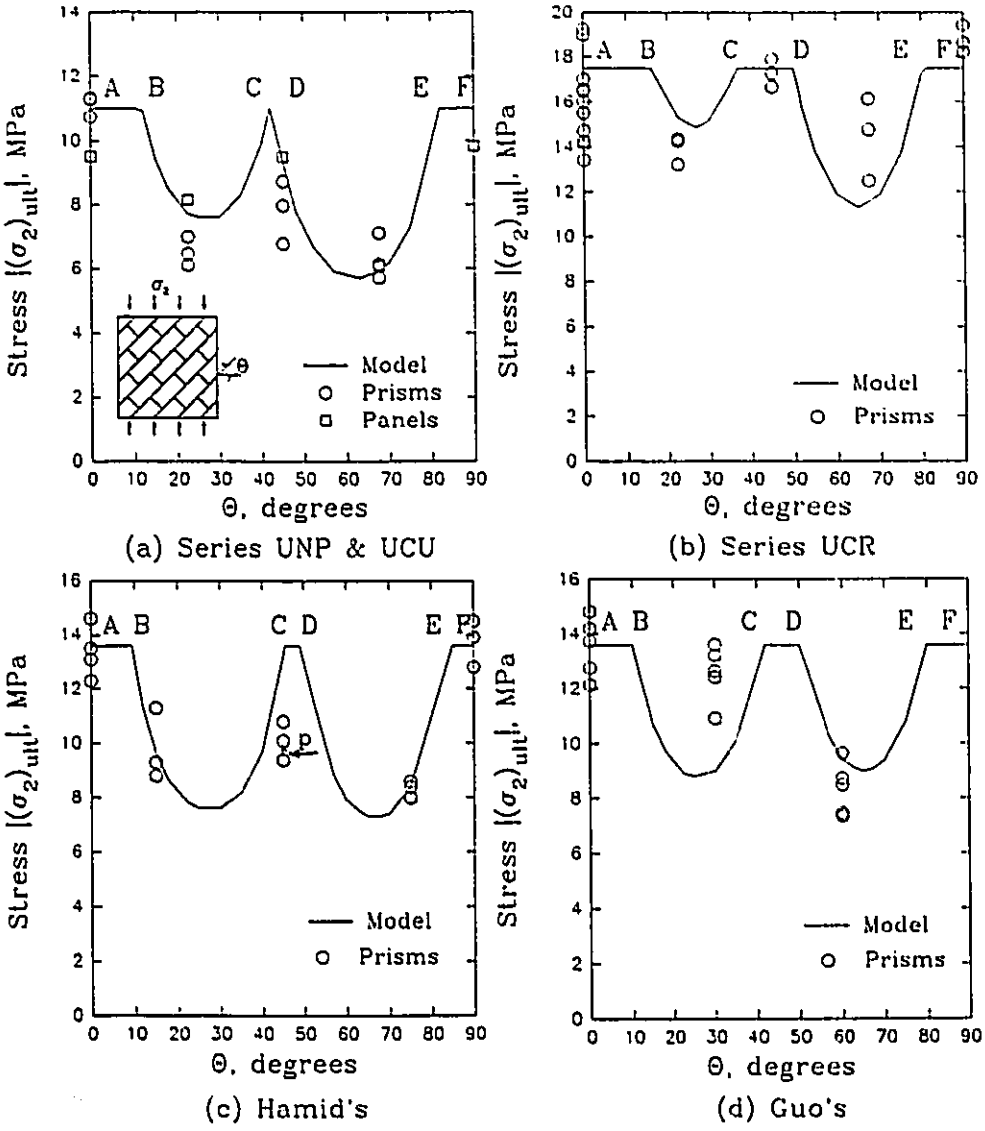

Fig. 7.3 Variation of compressive strength of grouted masonry with different bed joint orientations.

Fig. 7.3(b). This predicted behaviour is in agreement with the mode of failure observed at θ=45° for series UCR. Similar strengthening was also predicted, but over a narrow range of bed joint orientations, in Figs. 7.3(c) and (d).

The generally satisfactory agreement between the observed and predicted strengths is quantified by the mean ratio of 1.02, at a C.O.V. of 12.6%, found between the predicted and observed strengths. The predicted values tend to be closer to the results of the panels of series UNP rather than to the results of the prisms of series UCU, as shown in Fig. 7.3(a). This can be attributed to the cutting configuration of the prisms and their narrow widths which resulted in proportionally smaller grout areas along some mortar joints. In an attempt to investigate this effect, the actual cross-sectional areas of the grout cores, resulting from the cutting configuration for the prisms tested by Hamid at θ=45°, were calculated and used to determine the prism strengths. The predicted mean strength is represented in Fig. 7.3(c) by point "p" which is in much better agreement with the observed values. The cutting configuration in this case resulted in a 29% reduction in the compressive strength. These results confirm that panel tests are more representative of the macro-behaviour of grouted concrete masonry than are prism tests.

7.2.1.3 Deformation Characteristics

The average stress-average strain relationships predicted for the prisms of series UCU and panels UNP1 to UNP4 are plotted with the observed results in Fig. 7.4. The relationships are presented in terms of the variations of the

principal strains ϵ_1 and ϵ_2 with principal compressive stress σ_2 at different θ values. Similar comparisons are also possible in Fig. 7.5 for the prisms of series UCR.

The predicted relationships are in good agreement with the experimental

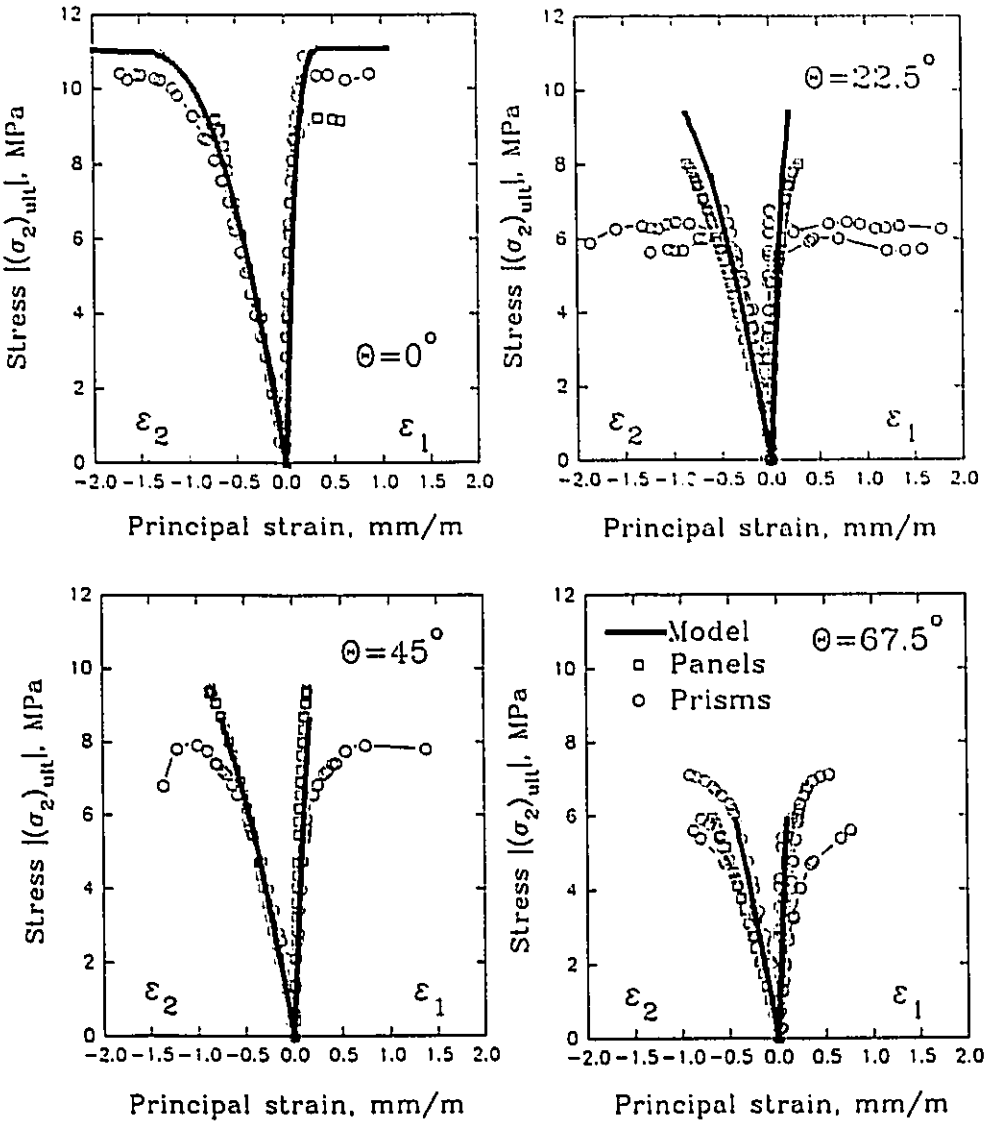

Fig. 7.4 Predicted and experimental stress-strain relationships for series UCU and panels UNP1-UNP4.

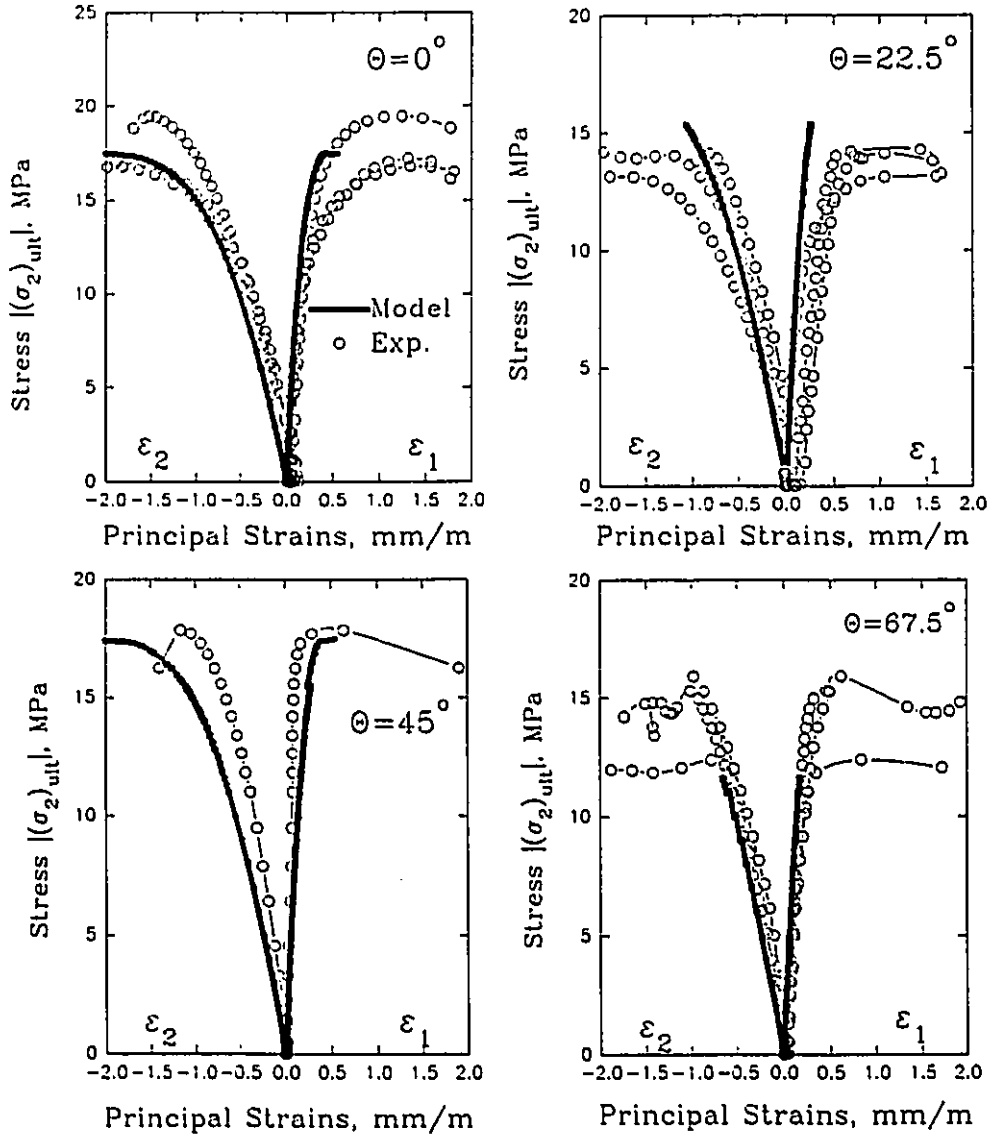

Fig. 7.5 Predicted and experimental stress-strain relationships for series UCR.

results. In all of the cases studied, the former lie within the range of the measured stress-strain relationships in the repeated tests at the same θ. Approaching the peak stresses, a significant inelastic increase in the principal compressive strains ϵ_2 was predicted for those specimens that failed in compression. The alternate

brittle response, predicted for the specimens that failed in shear along the mortar joints, also agreed with the experimental observations. No attempt was made to trace the descending branches of the stress-strain relationships after failure, because all of the specimens were tested under load control conditions.

7.2.2 Uniaxial Tension

7.2.2.1 Modes of Failure

Both the observed and predicted modes of failure for the five panels UNP11 to UNP15, tested under uniaxial tension at different θ's, are summarized in Table 7.4 to facilitate comparisons. Depending on θ, three different modes of

Table 7.4 Comparison between the predicted and the observed uniaxial tension behaviours for series UNP.

Panel	θ (deg.)	Predicted*		Observed		Pre. $(\sigma_1)_{ult}$ / Obs. $(\sigma_1)_{ult}$
		Ultimate stress, $(\sigma_1)_{ult}$ (MPa)	Failure mode	Ultimate stress, $(\sigma_1)_{ult}$ (MPa)	Failure mode	
UNP11	0	0.49	THJ	0.48	THJ	1.02
UNP12	22.5	0.57	THJ	0.53	THJ	1.08
UNP13	45	0.88	STEP	0.67	STEP	1.31
UNP14	67.5	0.75	STEP	0.80	TBJ	0.94
UNP15	90	0.80	TBJ	0.78	TBJ	1.03
					Mean ratio	1.08
					C.O.V.	13.0%

THJ = Tension failure along head joints,
TBJ = Tension failure along bed joints, and
STEP = Stepped mode of failure.
* Predicted according to case III.

failure were obtained; tension failure along the bed joint planes, tension failure along the head joint planes, and a stepped mode of failure. Except for panel UNP14, the predicted modes of failure were identical to those observed. At θ=67.5°, the observed mode of failure of panel UNP14 was a tension failure along the bed joint plane, whereas it was predicted to occur in a stepped manner. This discrepancy can be explained by the fact that, the predicted change from a stepped failure to a tension failure along the bed joint planes was close to θ=67.5°. The predicted results demonstrate the effect of the bed joint orientation on the mode of failure under uniaxial tension and demonstrate the ability of the macro-behaviour model to predict them.

7.2.2.2 Strength Characteristics

To study the effect of the material idealization of the planes of weakness on the predicted responses of grouted concrete masonry under uniaxial tension, the analyses were performed three times. The behaviours of the components along the planes of weakness were modelled under tensile stresses according to the following cases;

Case I; Straight tension cut-off criterion with an elastic-perfectly plastic stress-strain relationship,

Case II; Circular tension cut-off criterion with an elastic-perfectly plastic stress-strain relationship, and

Case III; Circular tension cut-off criterion with an elastic-strain softening stress-strain relationship.

These three cases are presented with more details in Chapter 5. The strengths, listed in Table 7.4, were predicted according to case III.

The macro-behaviour model was used to predict the variation of the masonry tensile strength with the bed joint orientation. As shown in Fig. 7.6, regardless of the material idealization, there are three distinct regions that can be identified in each of the three cases of analysis. Each region corresponds to a distinct mode of failure. Along curves AB and CD, tensile modes of failure were predicted to occur, respectively, along the head and the bed joint planes. Between these two regions, along BC, the failures were predicted to occur in a stepped manner along both head and bed joints.

The strengths predicted in the analysis designated by case III were the closest to the experimental results. As could be expected, the analyses performed

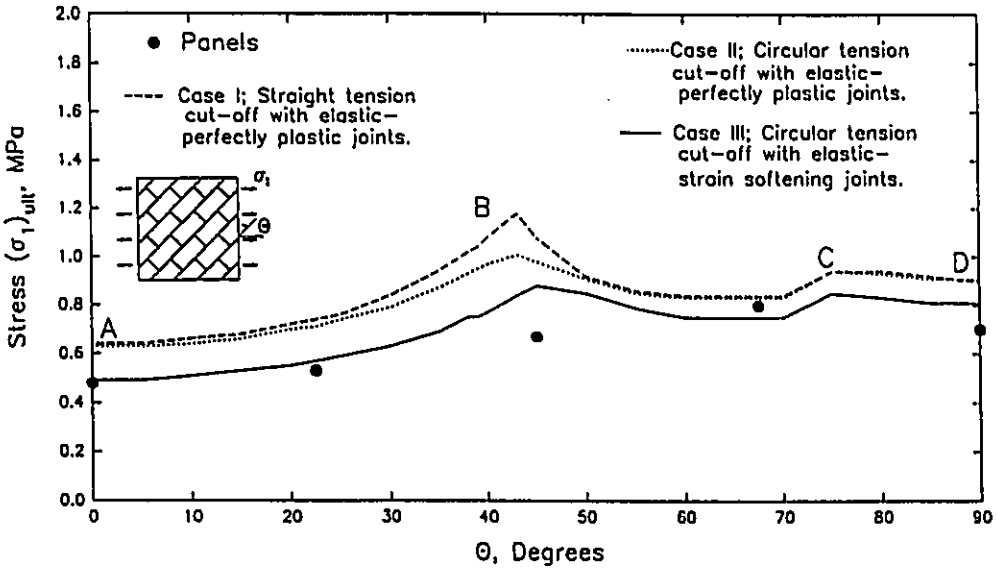

Fig. 7.6 Variation of uniaxial tensile strength of grouted masonry with the bed joint orientation.

according to cases I and II, assuming perfectly plastic responses after cracking, tended to overestimate the tensile strengths of the grouted assemblage. In these two cases, adoption of the straight cut-off or the circular cut-off as a tension failure criterion did not seem to affect the predicted strengths except at angles around $\theta=45°$. On the other hand, adoption of the strain softening response after cracking resulted in extensive stress redistribution from the cracked component to the surrounding ones, in case III, and gave lower strengths compared to the predictions of cases I and II. Considering the inherent variability in the properties of the materials used to build the specimens, the results obtained in case III agreed well with the experimental results. As indicated in Table 7.4, a mean ratio of 1.08, with a C.O.V. of 13.0%, was found between the predicted and the observed uniaxial tensile strengths.

Both the theoretical and the experimental results showed higher strengths when the failure occurred along the bed joints, in comparison with the cases when the failure took place along the head joints. This can be explained by the fact that the masonry assemblage under consideration had grout cores only normal to the bed joints.

7.2.2.3 Deformation Characteristics

The average stress-average strain relationships, obtained in the analyses designated by case III, are plotted in Fig. 7.7 along with the relationships obtained experimentally. Unlike the uniaxial compression case, the macro-behaviour model tended to predict almost linear stress-strain relationships under

uniaxial tension, whereas the experimental results showed softer responses approaching the failure stresses. This discrepancy between the predicted and observed behaviour can be attributed to the effect of modelling the masonry components as elastic materials before cracking. However, considering that the

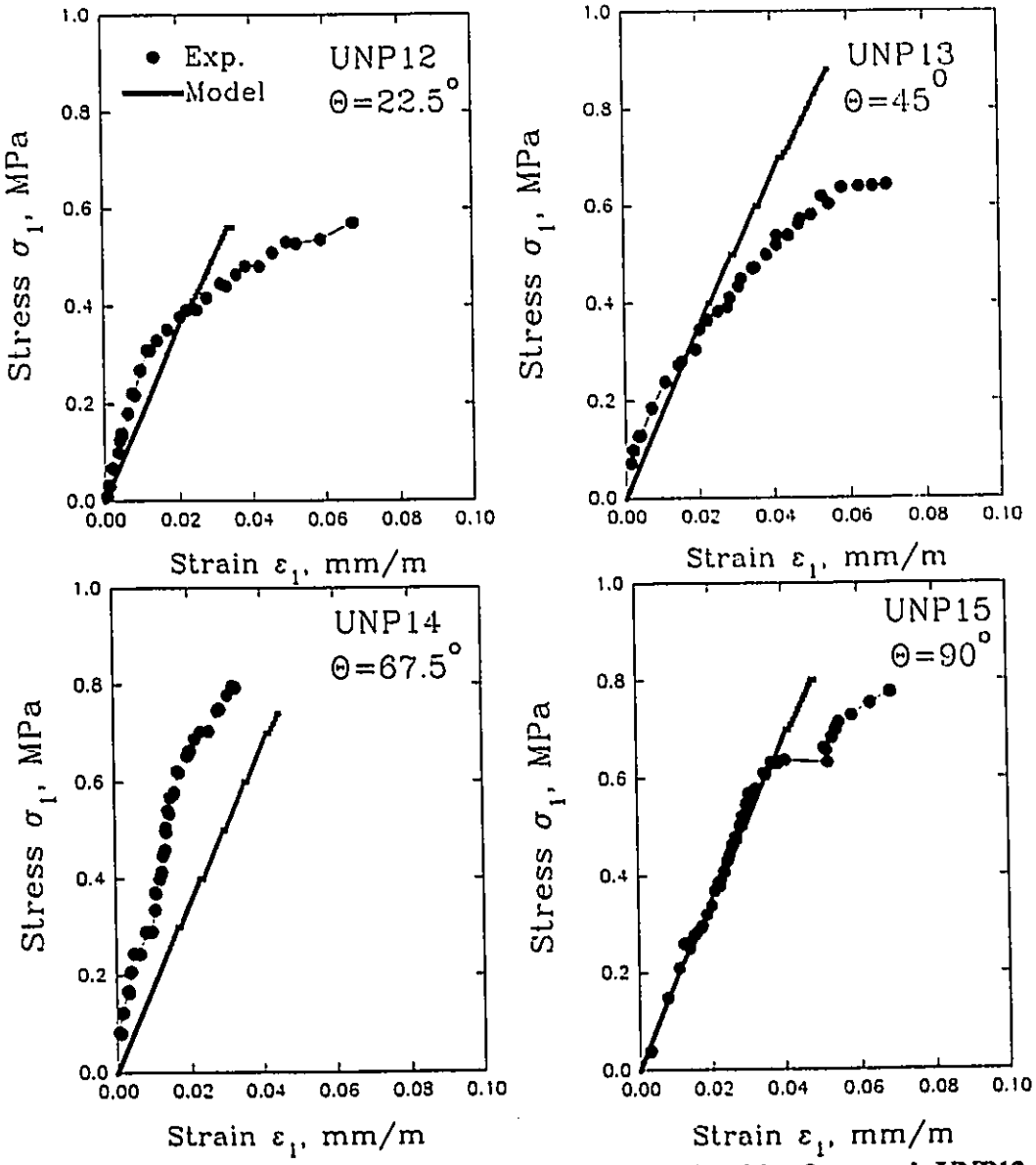

Fig. 7.7 Predicted and experimental stress-strain relationships for panels UNP12-UNP15.

strains experienced by masonry before cracking are very small, the accuracy of the predicted stress-strain relationships can still be considered to be satisfactory.

7.2.3 Biaxial Tension-Compression

7.2.3.1 Modes of Failure

As a part of series UNP, six panels were tested under biaxial tension-compression states of stress. For comparison purposes, both the predicted and observed modes of failure are presented in Table 7.5. Four of the six panels were tested under a biaxial state of stress of σ_1/σ_2=1/-1.09 at different bed joint orientations. The predicted and the observed modes of failure associated with

Table 7.5 Comparison between the predicted and the observed biaxial tension-compression behaviours.

Panel	θ (deg.)	Predicted*		Observed		Pre. $(\sigma_1)_{ult}$ / Obs. $(\sigma_1)_{ult}$
		Ultimate stress, $(\sigma_1)_{ult}$ (MPa)	Failure mode	Ultimate stress, $(\sigma_1)_{ult}$ (MPa)	Failure mode	
UNP6	45	0.84	THM	0.73	T	1.15
UNP7	45	0.97	THM	0.95	T	1.02
UNP8	22.5	0.64	THJ	0.70	THJ	0.91
UNP9	45	0.77	STEP	0.79	STEP	0.97
UNP10	67.5	0.79	STEP	0.72	STEP	1.10
UNP16	0	0.51	THJ	0.74	THJ	0.69
					Mean ratio	0.97
					C.O.V.	16.8%

THM = Tension failure of the homogeneous medium,
T = Tension failure normal to σ_1,
THJ = Tension failure along head joints,
SBJ = Tension failure along bed joints, and
STEP = Stepped mode of failure.
* Predicted according to the case III.

these panels changed from a tension failure along the head joint plane at $\theta=0°$ and 22.5° to a stepped mode of failure at $\theta=45°$ and 67.5°. The last two panels (UNP6 and UNP7) were both tested with $\theta=45°$, but under two different biaxial states of stress of $\sigma_1/\sigma_2=1/-3.86$ and 1/-6.6, respectively. With the increase in the absolute magnitude of the principal compressive stress σ_2, the failures of UNP6 and UNP7 were predicted to occur in the homogeneous medium rather than to follow the planes of weakness. This mode of failure was in agreement with the observed mode of failure where the cracks occurred along planes normal to σ_1 rather than following the mortar joints.

7.2.3.2 Strength Characteristics

Similar to the analyses performed for uniaxial tension, the masonry strengths under biaxial tension-compression were predicted using each of the three cases for tension indicated before. The strengths predicted according to case III, together with the corresponding experimental values, are summarized in Table 7.5 for the six panels. In addition, the variation of the masonry strength with respect to θ, under a biaxial state stress of $\sigma_1/\sigma_2=1/-1.09$, is shown in Fig. 7.8. Similar to the observations made earlier for the results obtained under uniaxial tension, the strengths predicted according to case III were the lowest and the closest to the experimental results.

In an attempt to better understand the response of grouted masonry, the macro-behaviour model was used to predict the failure envelopes under biaxial tension-tension and tension-compression states of stress for five bed joint

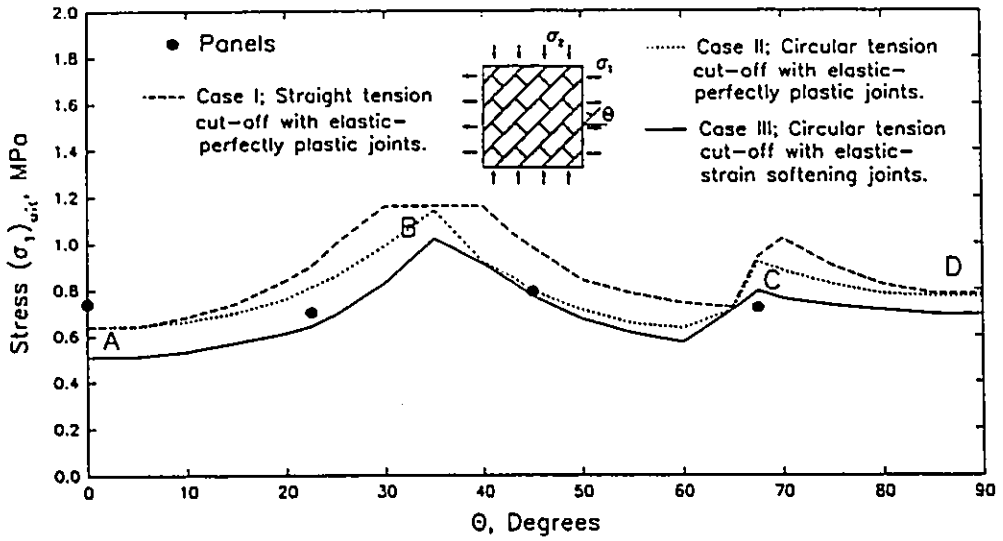

Fig. 7.8 Variation of grouted masonry strength with the bed joint orientation under biaxial tension-compression σ_1/σ_2=1/-1.09.

orientations. The values predicted along with the biaxial tension-compression experimental results are presented in Fig. 7.9 to facilitate comparisons. The results presented in this figure demonstrate clearly the significant change in the failure envelope with the bed joint orientation. The effect of the bed joint orientation on the strength of masonry does not remain constant, but varies with the principal stress ratio. Under biaxial tension-compression, these anisotropic characteristics are more pronounced as the absolute magnitude of the principal compressive stress σ_2 increases. On the other hand, the bed joint orientation does not play a significant role on the masonry strength when the effect of the principal tensile stress σ_1 predominates.

The differences between the analyses performed using the three different tension relationships tend to decrease as the algebraic ratio of σ_1/σ_2 increases

(moving towards the state of uniaxial compression) corresponding to failure in the homogeneous medium rather than following the planes of weakness. The

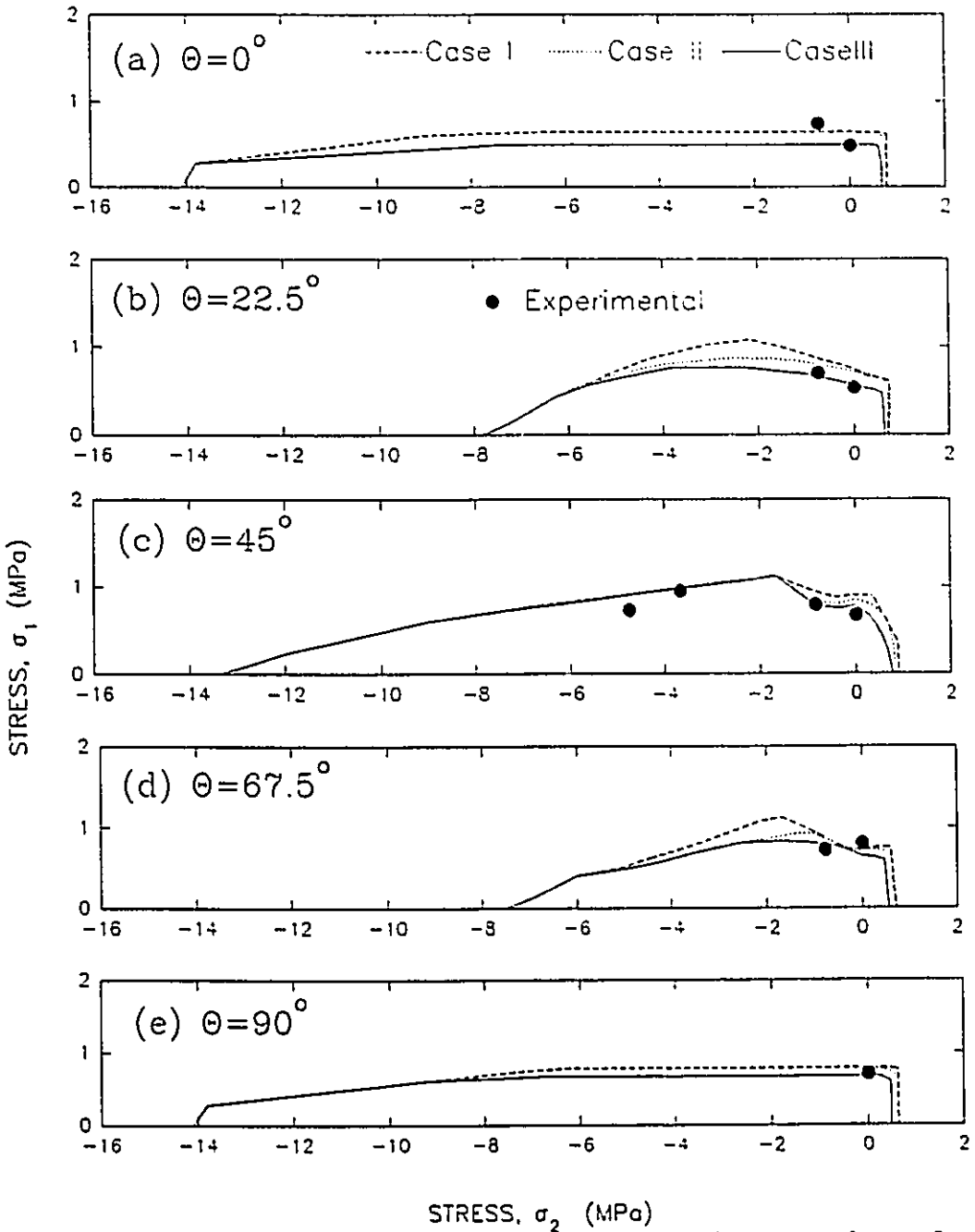

Fig. 7.9 Tension-tension and tension-compression failure envelopes for masonry assemblages with grout cores normal to bed joints.

predicted failure envelopes are consistently in good agreement with the experimental results which confirms the potential of the macro-behaviour model to reproduce the response of grouted masonry under different states of stress.

7.2.3.3 Deformation Characteristics

The average stress-average strain relationships predicted for panels UNP6 and UNP7, using the tensile relationships of case III, are plotted in Fig. 7.10 along with the experimental results. Similar data are also presented in Fig. 7.11 for the panels tested under a biaxial tension-compression ratio of σ_1/σ_2=1/-1.09. The good agreement between the experimental and theoretical stress-strain relationships is best in the cases when σ_2 is noticeably larger than σ_1. As indicated before, the idealization of the masonry components as elastic materials under

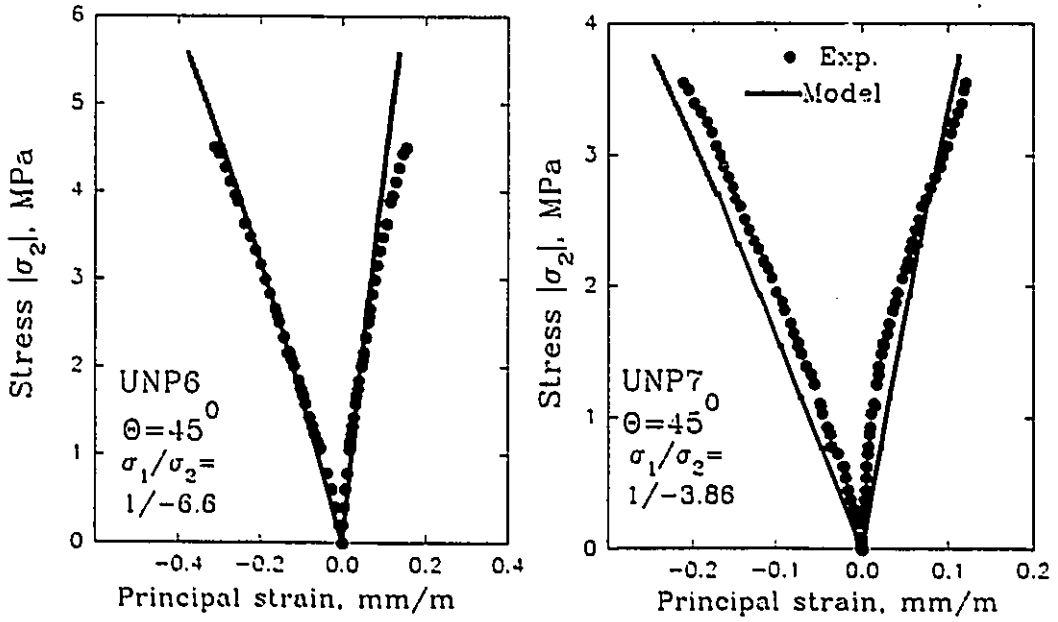

Fig. 7.10 Predicted and experimental stress-strain relationships for UNP6 and UNP7.

tension before cracking can explain the slightly poorer agreement in Fig. 7.11 related to tension dominated failures.

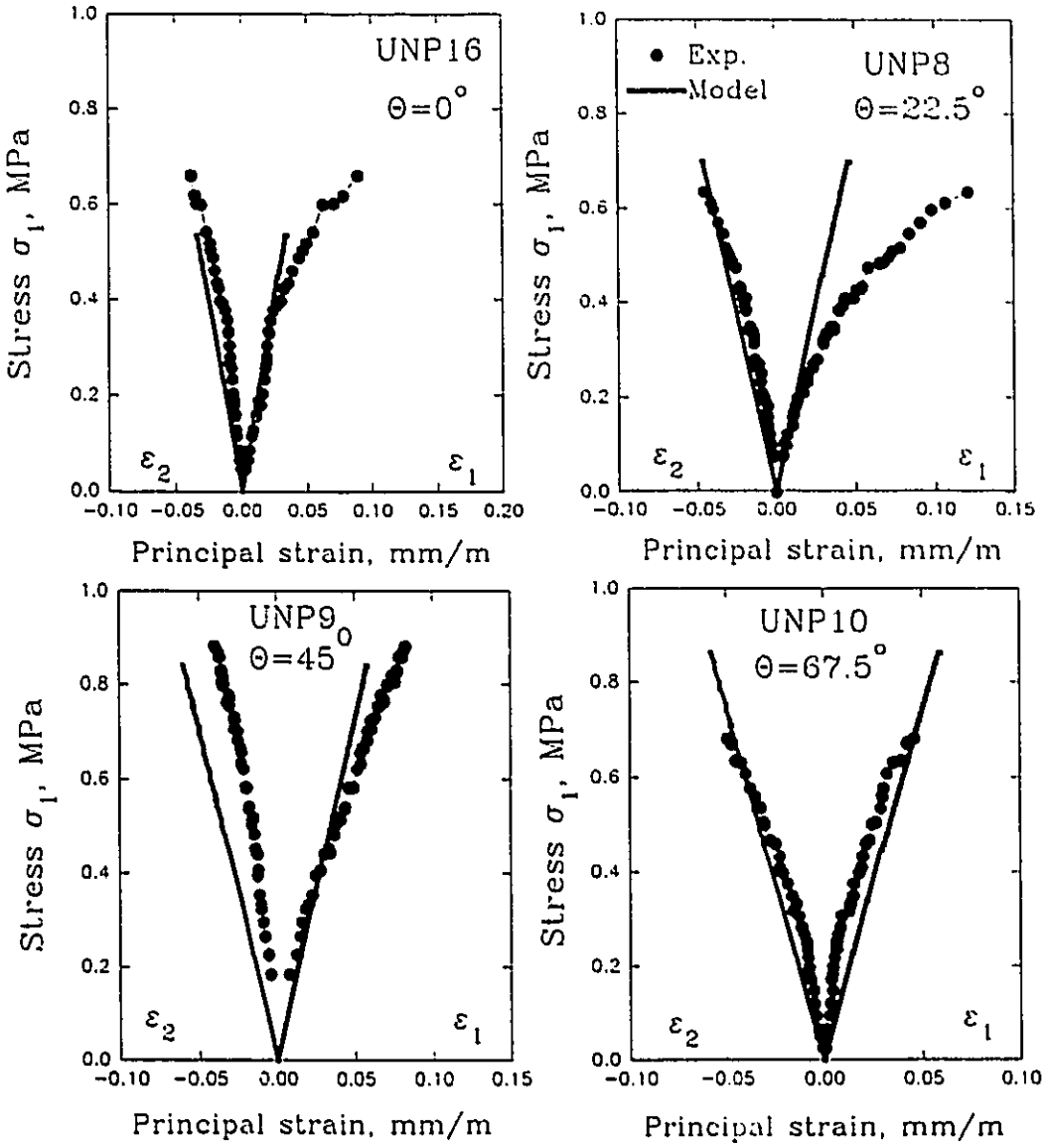

Fig. 7.11 Predicted and experimental stress-strain relationships for UNP8-UNP10 and UNP16.

7.2.4 The Complete Failure Envelopes

Although none of the tests performed in this investigation were conducted under the state of biaxial compression-compression, the macro-behaviour model was used to predict the behaviour of grouted masonry in this range. The analyses were performed on the masonry assemblage of series UNP, having the properties described in Table 7.2. Although predictions were made using the three tensile relationships described earlier, no differences were noticed between the results obtained because the masonry responses were dominated by the principal compressive stresses. The results obtained in these analyses, together with the results obtained before under the states of biaxial tension-compression and tension-tension, were used to develop the complete failure envelopes shown in Fig. 7.12 at θ=0°, 22.5°, and 45°. The failure envelopes at θ=90° and 67.5° can simply be defined by interchanging σ_1 and σ_2 in the envelopes at θ=0° and 22.5°, respectively.

Comparing the three failure envelopes predicted under biaxial compression-compression states of stress, three distinct regions can be distinguished. In the three envelopes in Fig. 7.12, the parts marked by A´A and CC´ correspond to the states of stress under which shear modes of failure occurred along the bed joints and the head joints, respectively. In these ranges, the anisotropic characteristics of masonry were very apparent as the failure stresses changed significantly with the bed joint orientation. On the other hand, the parts marked by ABC correspond to the states of stress under which

compression failures occurred in the homogeneous medium regardless of the bed joint orientation. These results are consistently in agreement with the observations made by Page (1981) as a result of his tests on brick masonry under biaxial compression-compression states of stress. He indicated that the bed joint

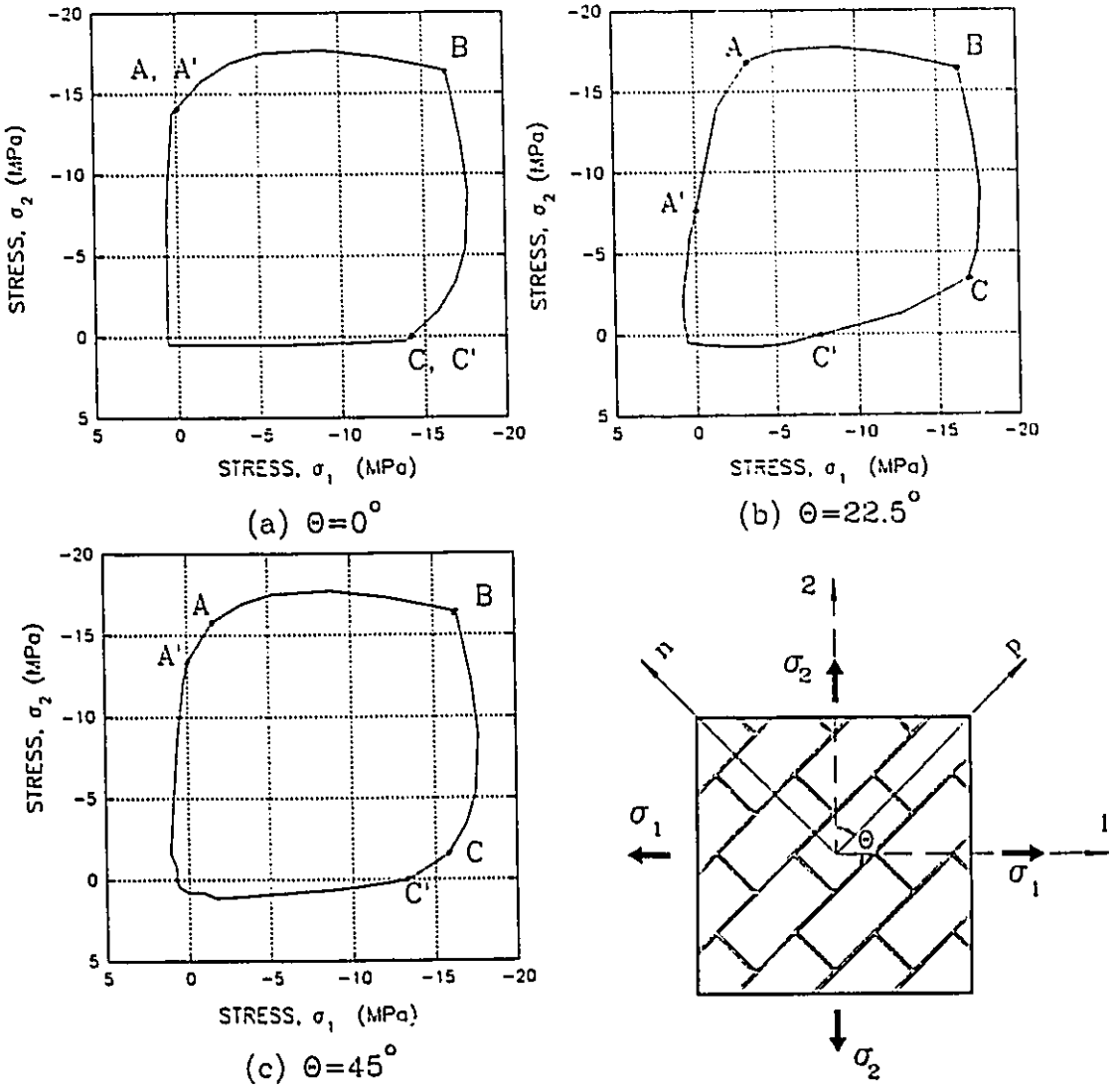

Fig. 7.12 Failure envelopes for masonry assemblages with grout cores normal to bed joints only.

orientation had a significant effect when one of the principal compressive stresses dominated and the failure in this case occurred along the mortar joints. It was also found that as the principal stresses got closer to being equal, the bed joint effect decreased and the failure took place along longitudinal planes parallel to the assemblage plane, rather than following the mortar joints.

A comparison of the complete failure envelopes in Fig. 7.12, reveals those cases where the anisotropic characteristics of the masonry assemblage play an important role. Although the bed joint orientation, as indicated before, affected both the mode of failure and the strength when the failure was governed by the principal tensile stress, its effect was more pronounced when the absolute value of the principal compressive stress was higher than the absolute value of the other principal stress. These situations occurred under both biaxial tension-compression and compression-compression states of stress where the failure stresses were governed by the capacities of the planes along the mortar joints.

Analyses were performed on the masonry assemblage of series UCR, using the properties listed in Table 7.2. The failure envelopes obtained for these assemblages, having continuous grout cores both normal and parallel to bed joints, are presented in Fig. 7.13. Comparisons of the changes in the failure envelopes for the different bed joint orientation, in this figure, with those in the corresponding envelopes in Fig. 7.12, shows the effect of having grout cores in the two directions on reducing the ranges marked by A′A and CC′, which correspond to anisotropic behaviour. The existence of grout cores normal and

parallel to bed joints were very effective in reducing the inherent anisotropic characteristics of grouted masonry.

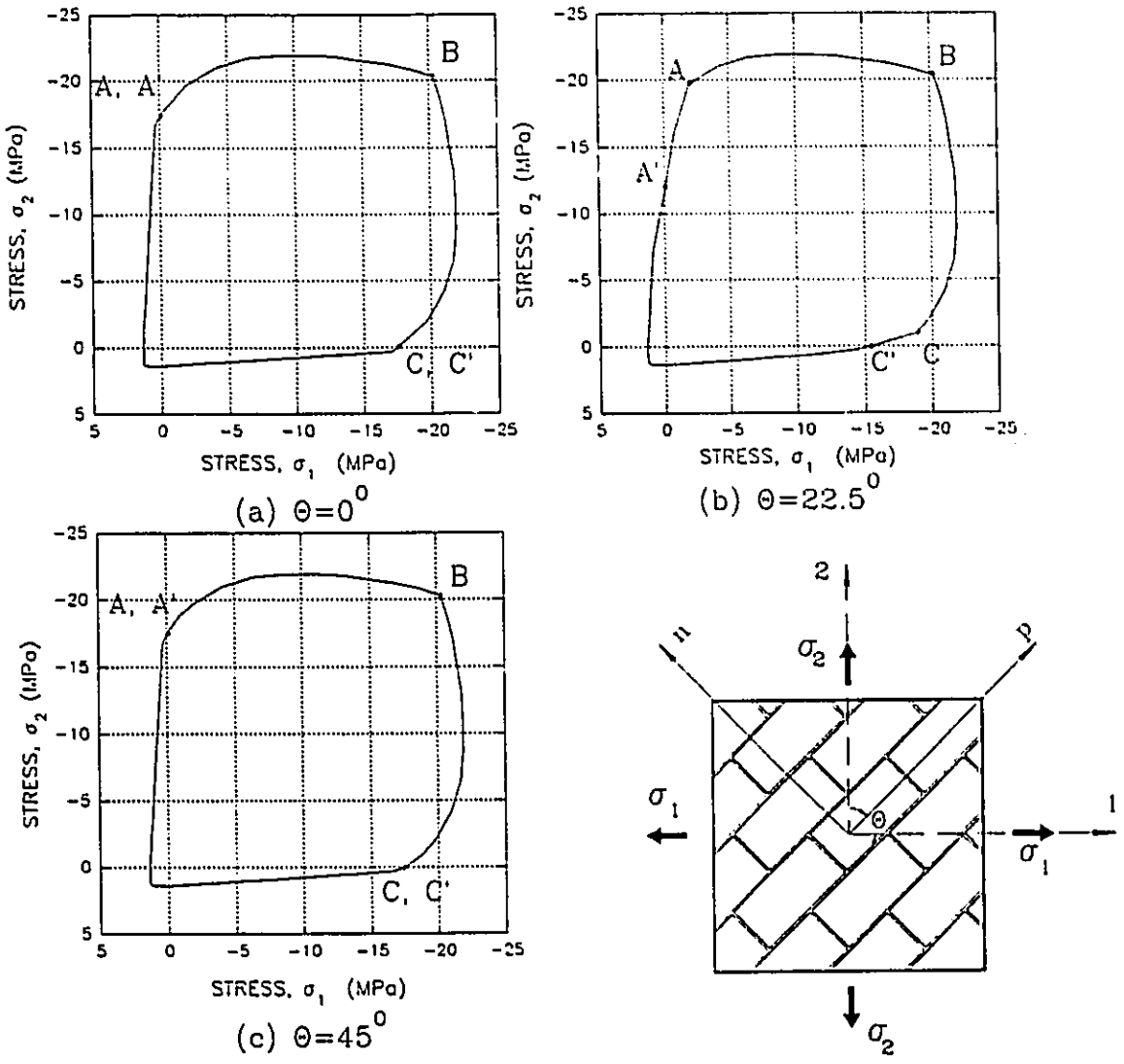

Fig. 7.13 Failure envelopes for masonry assemblages with grout cores both normal and parallel to bed joints.

7.3 MACRO-BEHAVIOUR OF REINFORCED MASONRY

The experimental data used to verify the ability of the macro-behaviour model to predict the behaviour of reinforced masonry consisted of the test results of series RP which was a part of the experimental program reported in Chapters 2 and 4. As mention before, all of the panels in this series were built using 190 mm blocks which had the webs knocked-out for a depth of 100 mm to facilitate placing the steel bars. Consequently, all the panels had continuous grout cores both normal and parallel to the bed joints. The material properties used to model these panels are summarized in Table 7.6. The analyses of the reinforced masonry assemblages were all performed using the tensile stress-strain relationships identified as case III in Sec. 7.2.2.2, which was found to result in the best agreement with the experimental results. The predictions of the macro-behaviour model are presented, discussed and compared with the experimental results, in the following sections. The effects of the bed joint orientation, the principal stress ratio, and the percentages of reinforcement on the response of reinforced masonry in terms of modes of failure, strength characteristics and deformation characteristics are studied.

7.3.1 Effect of Bed Joint Orientation

7.3.1.1 Modes of Failure

Seven panels were tested to study the effect of the bed joint orientation. They all were equally reinforced normal and parallel to the bed joints, so that $\rho_n=\rho_p=0.26\%$. The predicted and the observed modes of failure for these panels

Table 7.6 Summary of the material properties used for analyzing the panels of series RP.

Component	Item	Value	Component*		Item	Value
Homogeneous medium	f_m' (MPa) f_t' (MPa) E_o (MPa) ϵ_o ν_o	16.12 1.32 23500 0.0019 0.26	Head joint planes of weakness	M	A_{mh}/A_h f_t' (MPa) c (MPa) Φ (deg.) ψ (deg.)	0.26 0.19 0.2 30 10
Steel	E_s (MPa)	200000		B	A_t/A_h f_t' (MPa) c (MPa) Φ (deg.) ψ (deg.)	0.23 2.1 5.3 37 20
	f_y (MPa)	531 (ρ=0.17%) 568 (ρ=0.26%) 415 (ρ=0.53%) 420 (ρ=0.79%)		G	A_{gh}/A_h f_t' (MPa) c (MPa) Φ (deg.) ψ (deg.)	0.29 4.3 7.9 37 37
				GBI	A_{ig}/A_h f_t' (MPa) c (MPa) Φ (deg.) ψ (deg.)	0.11 -- 3.18 37 20
			Bed joint planes of weakness	M	A_{mb}/A_h f_t' (MPa) c (MPa) Φ (deg.) ψ (deg.)	0.45 0.25 0.35 43 15
				G	A_{gb}/A_h f_t' (MPa) c (MPa) Φ (deg.) ψ (deg.)	0.30 4.25 7.9 37 37

* M = Mortar, B = Block, G = Grout, and GBI = Grout Block Interface.

are presented in Table 7.7. The three panels tested under a biaxial state of stress of approximately $\sigma_1/\sigma_2 = 1/-1$ were panel RP7 at $\theta = 0°$ and panels RP8 and RP19 at $\theta = 45°$. The initial cracking, for the three panels, was predicted to occur in the homogeneous medium which is in agreement with the observed cracking normal to the direction of σ_1, regardless of the bed joint orientation. Failure of panel RP7 was characterized by yielding of the reinforcement parallel to the bed joints. In panels RP8 and RP19, the reinforcement normal and parallel to the bed joints were predicted to yield simultaneously. These predicted modes of failure were also similar to the observed modes of failure.

Table 7.7 Predicted and observed results for reinforced panels with different bed joint orientation, $\rho_p = \rho_n = 0.26\%$.

Panel	θ (deg.)	σ_1/σ_2	Predicted		Observed		Pre. $(\sigma_1)_{ult}$ / Obs. $(\sigma_1)_{ult}$
			Ultimate stress, $(\sigma_1)_{ult}$ (MPa)	Failure mode	Ultimate stress, $(\sigma_1)_{ult}$ (MPa)	Failure mode	
RP1	0	1/-7.08	1.48	YP+CHM	1.77	YP+C	0.84
RP2	22.5	1/-6.22	1.52	YP+CHM	1.45	YP+C	1.05
RP3	45	1/-6.49	1.28	CHM+SBJ	1.13	YN+C+SBJ	1.13
RP4	67.5	1/-7.70	1.09	SBJ	1.16	SBJ+YN	0.94
RP7	0	1/-0.98	1.5	YP	1.69	YP	0.89
RP8	45	1/-1.08	1.5	YP+YN	1.35	YP+YN	1.11
RP19	45	1/-1.08	1.5	YP+YN	1.55	YP+YN	0.97
						Mean ratio	0.99
						C.O.V. (%)	11.1

CHM = Compression failure of the homogeneous medium,
C = Compression failure,
SBJ = Shear failure along bed joints,
YP = Yield of reinforcement parallel to bed joints, and
YN = Yield of reinforcement normal to bed joints.

Panels RP1, RP2, RP3, and RP4 were tested at the four different bed joint orientations of θ=0°, 22.5°, 45°, and 67.5°, respectively. They were tested under biaxial states of stress with very similar ratios of σ_1/σ_2, having an average of σ_1/σ_2=1/-6.87. Similar to the observed behaviour, the initial cracks for panels RP1, RP2, and RP3 were predicted to occur in the homogeneous medium, whereas panel RP4 was predicted to crack first along the bed joint planes of weakness. The predicted post-cracking behaviours for the four panels were quite different from each other. Panels RP1 and RP2 failed after yielding of the reinforcement parallel to the bed joints which was followed by a compression failure in the homogeneous medium. The predicted failure of panel RP3 was characterized by a shear failure along the bed joint planes of weakness. The macro-behaviour model also predicted that a shear failure along the bed joint planes of weakness would govern the failure of panel RP4. No yielding of reinforcement was predicted to occur, at the macroscopic level, in panels RP3 and RP4. However, the predicted shear failure along the bed joint planes of weakness implied that the reinforcement across these planes reached the yield stress at a microscopic level. The behaviour of the last two panels is typical of those cases where failure of the mortar joints limits the effectiveness of the reinforcement in resisting the applied loads. The fact that the predicted modes of failure for RP1-RP4, and their dependence on the bed joint orientation, were consistently in agreement with the observed modes of failure confirms the suitability of the model for reinforced assemblages. The importance of considering the anisotropic

characteristics of reinforced grouted masonry, especially when the principal compressive stress predominates the behaviour, is documented.

7.3.1.2 Strength Characteristics

For comparison purposes, the predicted strengths for the seven panels discussed in the above section are presented, together with the experimental results, in Table 7.7. The results obtained under the effects of σ_1/σ_2=1/-1 and 1/-6.87 are shown in Figs. 7.14(a) and (b), respectively. The differences between the ultimate and the cracking stresses in these figures (expressed in terms of σ_1) reflect the effectiveness of the reinforcement in improving the capacity of reinforced masonry, compared to unreinforced masonry, at different θ values.

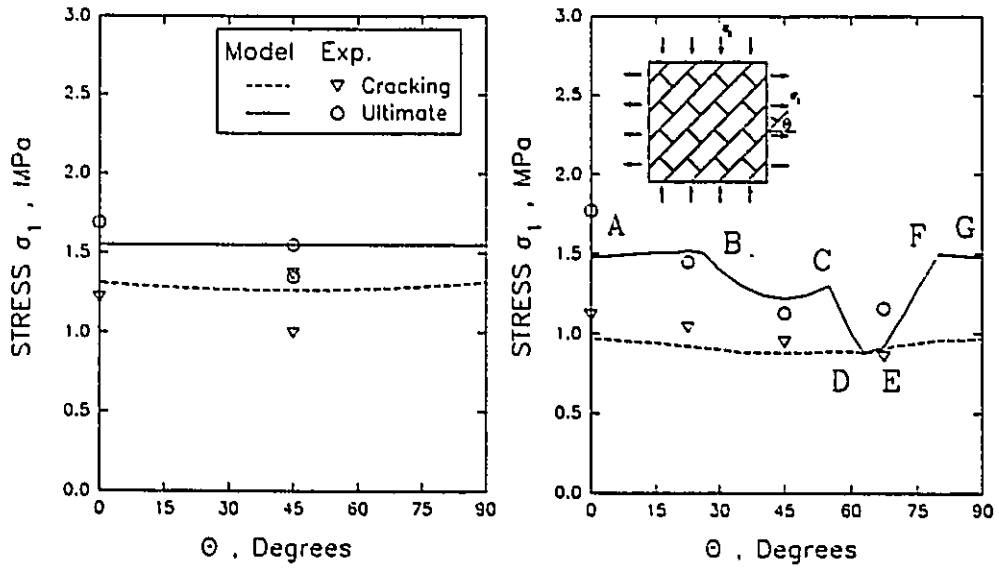

Fig. 7.14 Variations of cracking and ultimate stresses of reinforced masonry with the bed joint orientation ($\rho_p=\rho_a$=0.26%).

Under the effect of $\sigma_1/\sigma_2=1/-1$, the initial cracking was predicted to occur in the homogeneous medium regardless of the bed joint orientation which did not have a significant effect on the values of the cracking stress. Cracking was then followed by a dramatic increase in the principal tensile strain as stress redistribution took place between the cracked masonry and the reinforcement. The ultimate stresses in this case were governed by yielding of the reinforcement. The principal compressive stress in the homogeneous medium was far from reaching the ultimate value. Considering the equilibrium conditions of the cracked macro-element shown in Fig. 7.15(a), after the tensile stress in masonry, σ_{m1}, drops to zero, the ultimate value of σ_1 can be defined as:

$$(\sigma_1)_{ult} = f_{yp}\,\rho_p\cos^2\theta + f_{yn}\,\rho_n\sin^2\theta \qquad \ldots(7.1)$$

Accordingly, a constant value of $(\sigma_1)_{ult} = 1.48$ MPa can be determined for the masonry assemblage under consideration, with $\rho_p=\rho_n=0.26\%$. This value is 5% less than the values determined using the macro-behaviour model under the effect of $\sigma_1/\sigma_2=1/-1$ as shown in Fig. 7.15(a). This small difference can be attributed to the contribution of the cracked masonry which is neglected in Eq. 7.1. These results and their agreement with the experimental results, suggest that the equilibrium condition can be used alone to define the capacity of reinforced masonry when the failure takes place in the form of cracks normal to σ_1 followed by yielding of reinforcement. In this case, the bed joint orientation does not play a significant role on the cracking and the ultimate stresses.

Similar to the situation under $\sigma_1/\sigma_2=1/-1$, the bed joint orientation did not

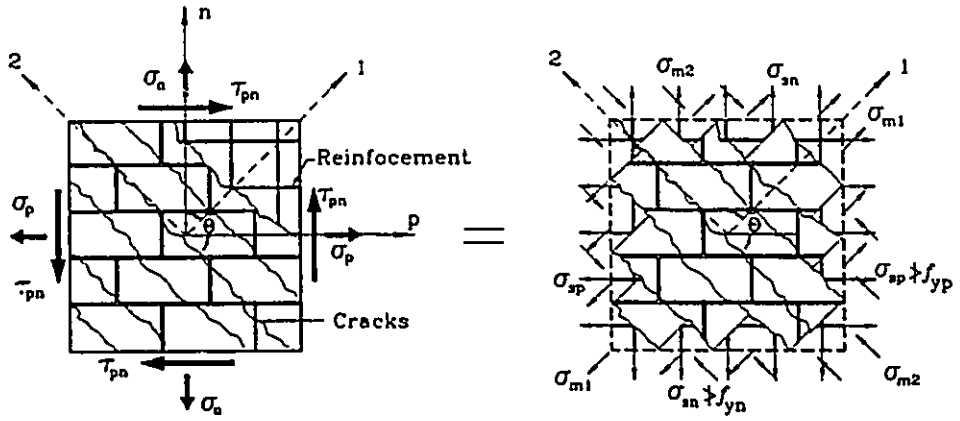

(a) Stress conditions of a reinforced macro-element after cracking.

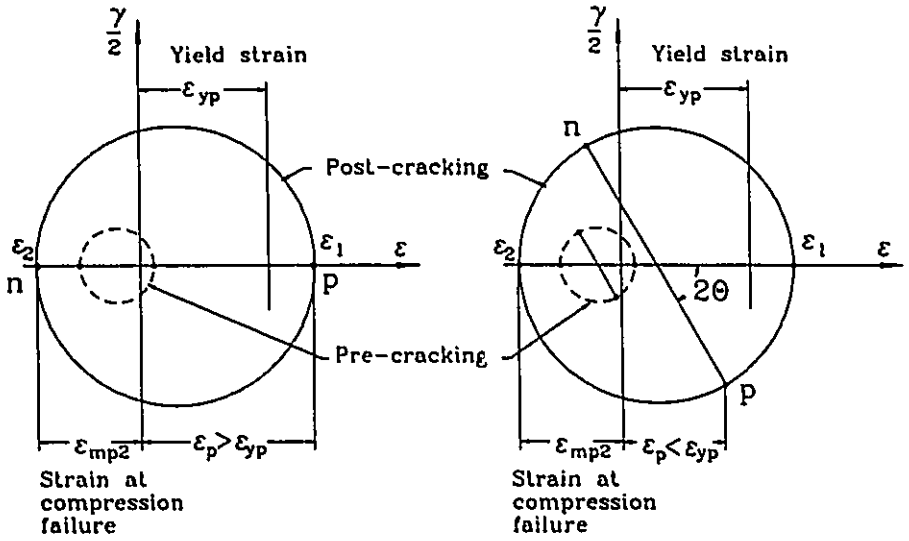

(b) Strain conditions of a reinforced macro-element with Θ =0° (Yield of parallel reinft. before the compression failure of masonry).

(c) Strain conditions of a reinforced macro-element with Θ =30° (Compression failure of masonry before the yield of reinforcement).

Fig. 7.15 Stress and strain conditions of a reinforced macro-element after cracking normal to σ_2.

significantly affect the cracking stress under $\sigma_1/\sigma_2=1/-6.87$. Conversely, both the ultimate stress and the contribution of the reinforcement after cracking under $\sigma_1/\sigma_2=1/-6.87$ were significantly influenced by the bed joint orientation. There are four distinct regions that can be identified in Fig. 7.14(b); each corresponding to a distinct mode of failure. Along AB and FG, the failures are characterized by yielding of the reinforcement which helped significantly in resisting the applied loads after cracking. In these cases, the principal compressive stress in the homogeneous medium also reached its peak value, but only after yielding of the reinforcement parallel and normal to the bed joints took place. The compatibility condition at failure can be presented at $\theta=0°$ by Mohr's circle of strains as shown in Fig. 7.15(b), in which $\epsilon_2=\epsilon_{mp2}$ (strain corresponding to the peak compressive stress), whereas $\epsilon_p>\epsilon_{yp}$ (yield strain).

With the increase in the bed joint orientation along curve BC in Fig. 7.14(b), the angle between the reinforcement and σ_1 increases, so that the masonry assemblage fails in compression prior to yielding of the reinforcement. The compression failure does not allow the reinforcement to achieve its full capacity which consequently leads to a reduction in the ultimate stress. The compatibility condition, presented by Mohr's circle of strains as shown in Fig. 7.15(c), can be used to explain the predicted behaviour as the increase in θ leads to a reduction in the strains of the reinforcement at compression failure of the masonry (i.e. $\epsilon_p<\epsilon_{yp}$ when $\epsilon_2=\epsilon_{mp2}$). Consequently the ultimate stress decreases continuously with θ to reach a minimum at $\theta=45°$. Consideration of the

equilibrium conditions only would not be enough to determine the capacity when compression failure dominates the behaviour. It is worth noting that the ultimate strength along curve BC depends on the bed joint orientation even though the failures did not follow the mortar joints.

Along the third region designated by CDEF in Fig 7.14(b), failure took place in the form of a shear failure along the bed joint planes. In this region, the contribution of reinforcement dropped significantly to the point that the ultimate stress values were equal to the cracking stress values over the region DE.

Even with large differences in the principal stress ratios and the effects of the inherent variation in the properties of the constituent materials of the masonry assemblages, the predicted and the experimental results were consistently in good agreement. An average ratio of 0.99 was found between the observed and the predicted strengths at a C.O.V. of 11.1%.

7.3.1.3 Deformation Characteristics

The predicted and the observed average stress-average strain relationships are plotted in Fig. 7.16 for panels RP7 and RP8. The relationships are presented in terms of the principal stresses and strains. The experimental stress-strain relationships for masonry were determined by extracting the contribution of reinforcement from the total stresses-strain relationships of the reinforced assemblage in accordance with the procedure discussed previously in Sec. 6.3.3. The solid lines in this figure correspond to the predicted responses of reinforced masonry, whereas the predicted responses of masonry are represented by the

dashed lines. This presentation demonstrates the process of stress redistribution between the masonry and the reinforcement after cracking and documents the contribution of reinforcement. Similar data for panels RP1 and RP4 are shown in Fig. 7.17.

In general, good agreement can be recognized between the predicted and the measured stress-strain relationships. Under the effect of $\sigma_1/\sigma_2=1/-1$, the reinforcement played a significant role in resisting the applied stresses after cracking and can be seen as providing the ductility for panels RP7 and RP8. The same effect can be observed for panels RP1 and RP2 where yielding of

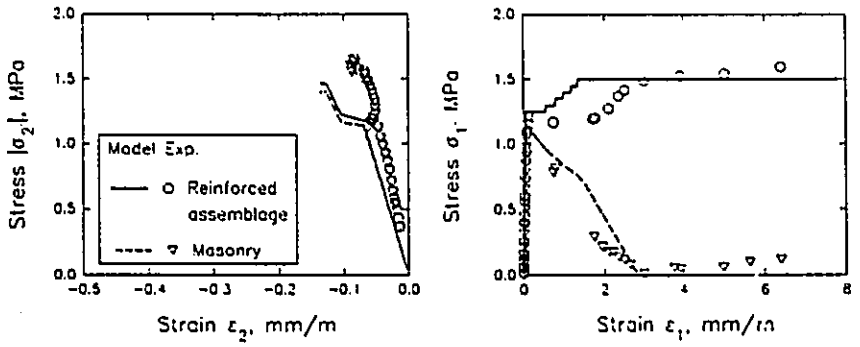

(a) Panel RP7 ($\Theta=0^\circ$, $\sigma_1/\sigma_2=1/-0.98$, and $\rho_p=\rho_n=0.26\%$).

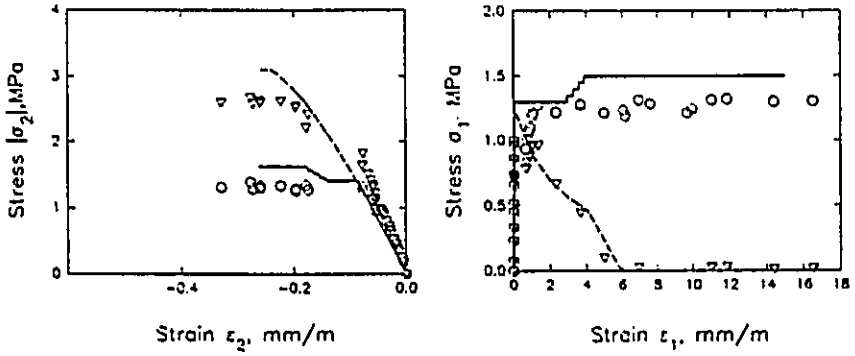

(b) Panel RP8 ($\Theta=45^\circ$, $\sigma_1/\sigma_2=1/-1.08$, and $\rho_p=\rho_n=0.26\%$).

Fig. 7.16 Predicted and experimental stress-strain relationships for panels RP7 and RP8.

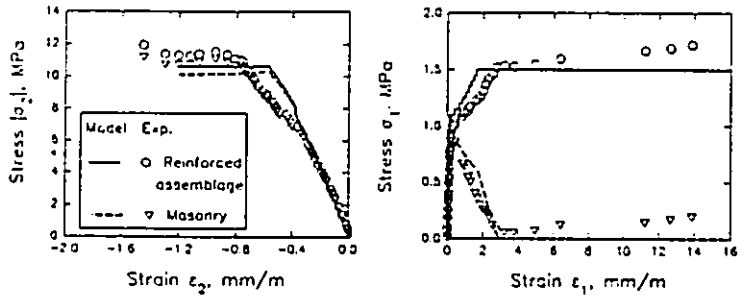

(a) Panel RP1 ($\theta=0^\circ$, $\sigma_1/\sigma_2=1/-7.08$, and $\rho_p=\rho_n=0.26\%$).

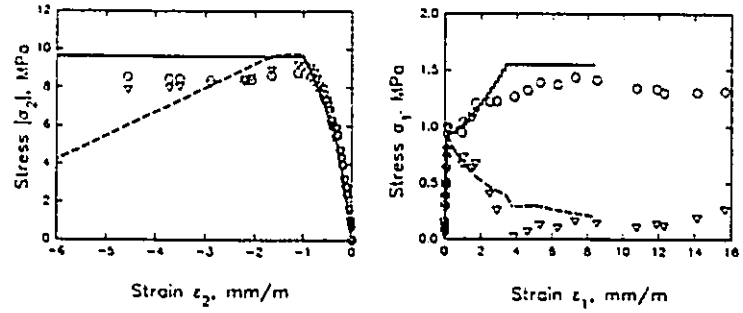

(b) Panel RP2 ($\theta=22.5^\circ$, $\sigma_1/\sigma_2=1/-6.22$, and $\rho_p=\rho_n=0.26\%$).

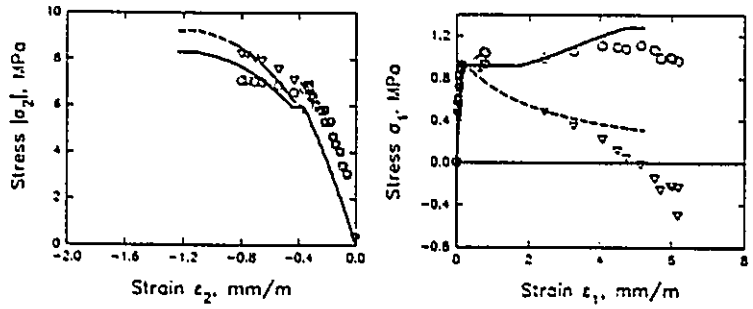

(c) Panel RP3 ($\theta=45^\circ$, $\sigma_1/\sigma_2=1/-6.49$, and $\rho_p=\rho_n=0.26\%$).

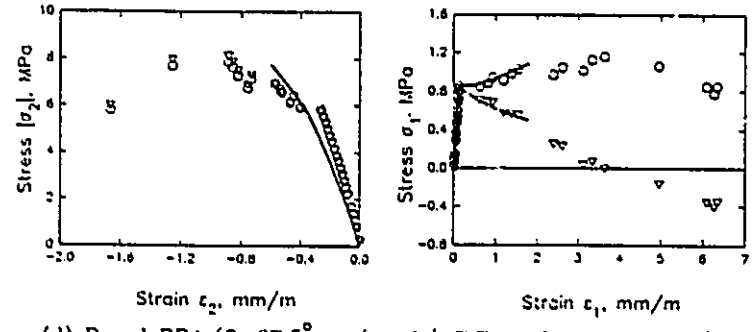

(d) Panel RP4 ($\theta=67.5^\circ$, $\sigma_1/\sigma_2=1/-7.7$, and $\rho_p=\rho_n=0.26\%$).

Fig. 7.17 Predicted and experimental stress-strain relationships for panels RP1-RP4.

reinforcement took place before the compression failure occurred in the homogeneous medium. Conversely, shear failures along the bed joint planes occurred in panels RP3 and RP4 which limited the effectiveness of the reinforcement. The predicted response of RP4 was less ductile than the experimental results showed. This difference could be attributed to modelling only the longitudinal resistance of the reinforcement, thus neglecting its dowel action in the macro-behaviour model.

Both the theoretical and the experimental results displayed the effect of the bed joint orientation on increasing the principal tensile strain associated with yielding of the reinforcement. This effect can be observed by comparing RP7 and RP8 or RP1 and RP2.

7.3.2 Effect of Principal Stress Ratio σ_1/σ_2

7.3.2.1 Modes of Failure

Six panels were tested with $\theta=45°$ to investigate the effect of the principal stress ratio σ_1/σ_2 on the response of reinforced masonry. All six panels were equally reinforced parallel and normal to the bed joints, so that $\rho_n=\rho_p=0.26\%$. Both the predicted and the observed modes of failure are listed in Table 7.8, along with the principal stress ratios.

The predicted modes of failure are identical to those modes of failure observed in the tests. The responses of panels RP8 and RP9, which were tested under $\sigma_1/\sigma_2=1/-1$ and 1/0, respectively, were similarly dominated by the principal tensile stress σ_1. The modes of failure, in these cases, were characterized by

yielding of the reinforcement after cracking of the homogeneous medium. Under the effect σ_1/σ_2=1/-6.49, the mode of failure of panel RP3 was governed by shear failure along the bed joints which took place simultaneously with the compression failure in the homogeneous medium. At higher principal stress ratios of σ_1/σ_2=1/-13.5 and 0/-1, panels RP6 and RP5, respectively, were predicted to fail in compression in the homogeneous medium without yielding of the reinforcement.

Table 7.8 Predicted and observed behaviours of reinforced panels with different principal stress ratios, ($\rho_p=\rho_n=0.26\%$).

Panel	θ (deg.)	σ_1/σ_2	Predicted		Observed		Pre.$(\sigma_1)_{ult}$ / Obs$(\sigma_1)_{ult}$
			Ultimate stress, $(\sigma_1)_{ult}$ (MPa)	Failure mode	Ultimate stress, $(\sigma_1)_{ult}$ (MPa)	Failure mode	
RP9	45	1.0/0	1.5	YP+YN	1.5	YP+YN	1.00
RP8	45	1/-1.08	1.5	YP+YN	1.35	YP+YN	1.11
RP19	45	1/-1.08	1.5	YP+YN	1.55	YP+YN	0.97
RP3	45	1/-6.49	1.28	CHM+SBJ	1.13	YP+C+SBJ	1.13
RP6	45	1/-13.5	0.83	CHM	0.76	C	1.09
RP5	45	0/-1.0	*	CHM	*	C	
						Mean ratio	1.06
						C.O.V. (%)	6.90

* The compressive strength of RP5 was higher than the capacity of the test rig, but it was predicted to fail at $(\sigma_2)_{ult}$=16.7 MPa.

CHM = Compression failure of the homogeneous medium,
C = Compression failure,
SBJ = Shear failure along bed joints,
YP = Yield of reinforcement parallel to bed joints, and
YN = Yield of reinforcement normal to bed joints.

7.3.2.2 Strength Characteristics

The values of the predicted and the observed cracking and ultimate stresses listed in Table 7.8 are plotted in Fig. 7.18 for conditions of $\theta=45°$ and $\rho_p=\rho_n=0.26\%$. The tension-compression failure envelope and the envelope of the cracking stress are both shown in this figure. The difference between the envelopes for the cracking and the ultimate stresses reflects the effectiveness of the reinforcement in improving the strength of reinforced masonry, compared to unreinforced masonry. Both the theoretical and the experimental results shown in Fig. 7.18 were normalized by dividing the stress values by the masonry compressive strength f'_m.

There are three distinct parts that can be identified along the ultimate stress envelope; each corresponding to a different mode of failure. Along AB, where the principal tensile stress dominates the behaviour, the mode of failure is characterized by yielding of the reinforcement. In this range of biaxial states of stress, the ultimate tensile stress remains almost constant, whereas the cracking stress value along A´B´ decreases slightly with the increase in the algebraic ratio of σ_1/σ_2.

Along the region designated by BC, compression failure in the homogeneous medium occurs prior to yielding of the reinforcement. As a result, not only the cracking stress, but also the ultimate stress decreases with the increase in the algebraic ratio of σ_1/σ_2. In spite of this, the difference between curves ABC and A´B´C´ shows that the effect of reinforcement to sustain more

stresses after cracking (for example to move from B´ to B) increases continuously with the increase in the algebraic ratio of σ_1/σ_2. This can simply be attributed to the steeper drop in the cracking stress with the increase of the ratio of σ_1/σ_2, compared to the change in the ultimate stress.

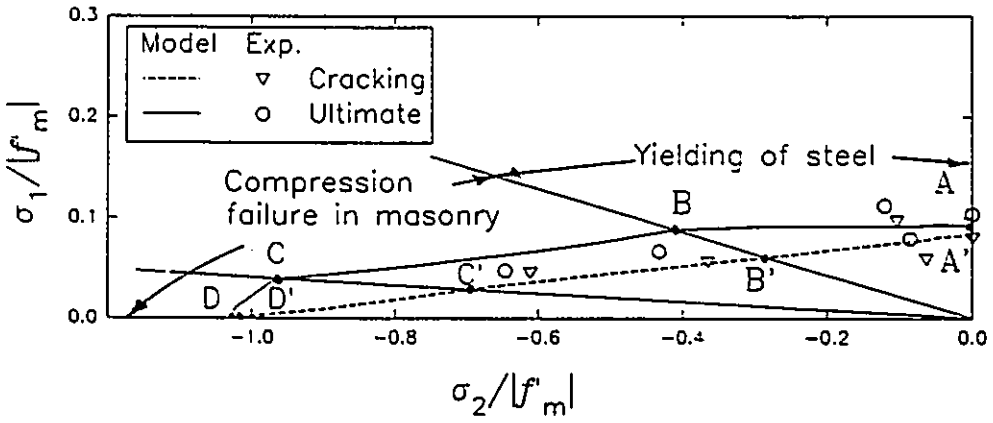

Fig. 7.18 Envelopes of the cracking and the ultimate stresses of a reinforced masonry assemblage with θ=45° and $\rho_p=\rho_n$=0.26%.

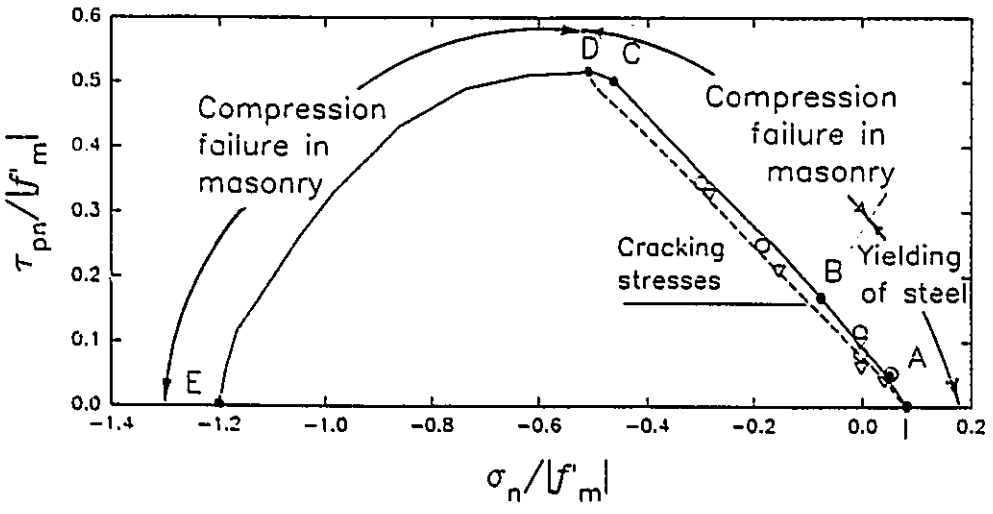

Fig. 7.19 Variation of shear stress with normal stress at failure, ($\sigma_p=\sigma_n$ and $\rho_p=\rho_n$=0.26%).

In the last region, marked by CD, a compression mode of failure occurs in the homogeneous medium. The difference between regions CD and BC is that the reinforcement under the biaxial states of stress defined by CD are subjected to compressive stresses rather than tensile stresses. In addition, the increase in the principal tensile strains after cracking, along CD, are not large enough to result in a significant reduction in the compressive strength, such as occurs along BC. It is interesting to note that the contribution of reinforcement after cracking, along CD, decreases with the increase in the algebraic ratio of σ_1/σ_2. The existence of the reinforcement resulted in an increase of only 3% in the uniaxial compressive strength, which can be measured by the distance between D´ and D.

The effect of the states of stress on the strength of reinforced masonry is illustrated in Fig. 7.19 in terms of the variation of the shear stress with the normal stresses along the mortar joint planes at failure. The predicted results used to draw this curve were obtained for the condition of $\sigma_p=\sigma_n$ which is equivalent to analyzing panels with $\theta=45°$ under the effect of different ratios of σ_1/σ_2. For example, the state of stress defined by point A in Fig. 7.19 corresponds to a principal stress ratio of $\sigma_1/\sigma_2=1/0$ at $\theta=45°$ which is marked by A in Fig. 7.18. In this manner, the three regions identified before in Fig. 7.18 by AB, BC, and CD correspond to the regions marked by the same letters in Fig. 7.19. The only differences are curves IA and DE which represent natural extensions of regions AB and CD, respectively. Along the regions marked by IABCD, increases in the applied normal stresses significantly enhance the shear strength of the masonry

assemblage, but at a slightly decreasing rate. The predicted maximum shear strength is about 0.51 f'_m which corresponds to the ratio of σ_p:σ_n:τ=-1.2:-1.2:1. Any increase of the normal stress beyond this point is accompanied by a decrease in the ultimate shear stress as the failure is characterized as a compression failure. It is worth noting that no cracking was predicted in region DE which corresponds to compression-compression states of stress at θ=45°.

The predictions provided in Table 7.8 and in Figs. 7.18 and 7.19, which cover various aspects of the possible responses of reinforced masonry, compare well with the available experimental results. An average ratio of 1.06 was found between the observed and the predicted strengths at a C.O.V. of 6.9%.

7.3.2.3 Deformation Characteristics

The average stress-average strain relationships predicted for panels RP5, RP6 and RP9 are plotted along with the experimental results in Fig. 7.20. The results for panels RP8 and RP3 were presented previously in Figs. 7.16 and 7.17, respectively. In agreement with the experimental results, the predicted stress-strain relationships reveal the effect of increasing the ratio of σ_1/σ_2 on reducing the ductility of the reinforced assemblage.

7.3.3 Effect of Percentage of Reinforcement

7.3.3.1 Modes of Failure

Eleven of the panels of series RP were tested under the stress ratio σ_1/σ_2=1/-1 at θ=45° to produce a state of pure shear stress along the mortar joint

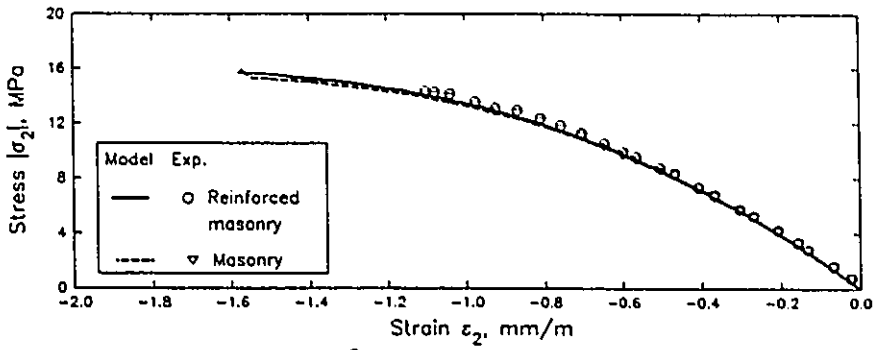

(a) Panel RP5 (Θ=45°, σ_1/σ_2=0/−1, and $\rho_p=\rho_n$=0.26%).

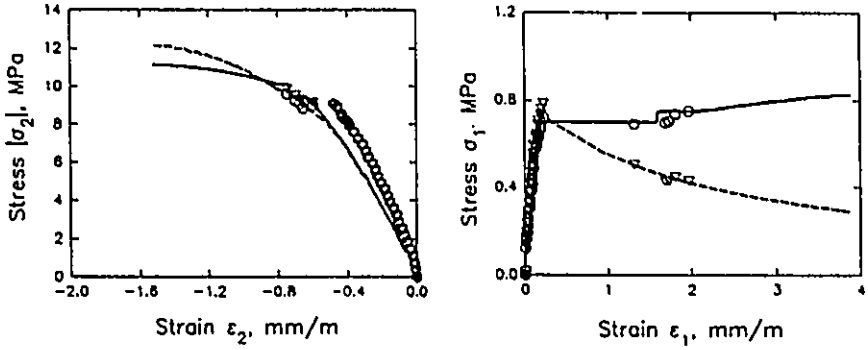

(b) Panel RP6 (Θ=45°, σ_1/σ_2=1/−13.5, and $\rho_p=\rho_n$=0.26%).

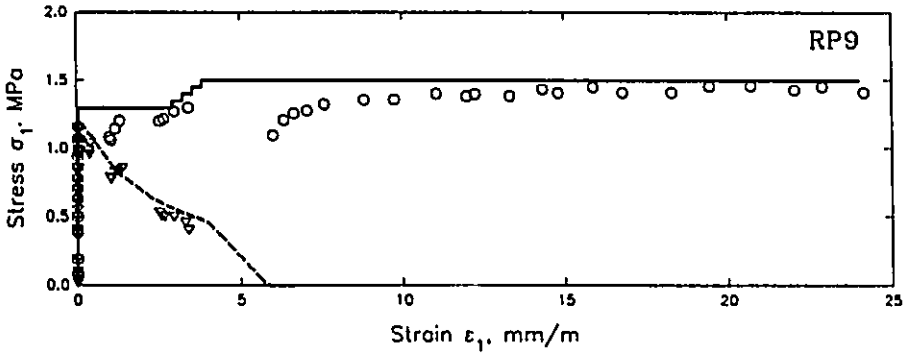

(c) Panel RP9 (Θ=45°, σ_1/σ_2=1/0, and $\rho_p=\rho_n$=0.26%).

Fig. 7.20 Prediction and experimental stress-strain relationships for panels RP5, RP6, and RP9.

planes. This state of stress permitted study of the effect of the percentage of reinforcement on the shear response without interference from any axial or flexural stress. Five of these panels; RP8, RP10, RP11, RP12, and RP19, were reinforced equally both normal and parallel to the bed joints, but with different percentages of reinforcement. Panels RP13, RP14, and RP15 were tested to study the effect of increasing ρ_p, with ρ_n constant and equal to 0.53%. Another group can be formed of panels RP8, RP16, RP17, and RP18 to investigate the effect of ρ_p, with ρ_n constant and equal to 0.26%. The eleven panels were analyzed using the macro-behaviour model and the predicted results are listed in Table 7.9 along with the experimental results.

In agreement with the experimental results, the macro-behaviour model predicted the initial cracking in the eleven panels to take place normal to σ_1 rather than to follow the mortar joints. Depending on the percentages of reinforcement used normal and parallel to the bed joints, the panels exhibited yielding of the reinforcement in one or two directions. The panels, reinforced in one direction only or reinforced in one of the two directions using steel with limited ductility, were observed experimentally to fail locally in a brittle manner with very limited numbers of cracks. The deformations recorded in these cases did not indicate yielding of the reinforcement in the direction of higher percentage of reinforcement at the macroscopic level. However the observed crack width was large enough to suggest that local yielding of the reinforcement took place across the failure plane. Because the macro-behaviour model is based on the assumption

Table 7.9 Predicted and observed behaviours of panels with different percentages of reinforcement, (θ=45° and σ_1/σ_2=1/-1).

Panel	ρ_p %	ρ_n %	Predicted		Observed		Pre. $(\sigma_1)_{ult}$ / Obs. $(\sigma_1)_{ult}$
			Ultimate stress, $(\sigma_1)_{ult}$ (MPa)	Failure mode	Ultimate stress, $(\sigma_1)_{ult}$ (MPa)	Failure mode	
RP8	0.26	0.26	1.50	YP+YN	1.35	YP+YN	
RP19	0.26	0.26	1.50	YP+YN	1.55	YP+YN	1.11
RP11	0.53	0.53	2.25	YP+YN	*	YP+YN	0.97
RP12	0.79	0.79	3.35	YP+YN	*	*	
RP13	0.0	0.53	1.40	YN	1.22	L	1.15
RP14	0.17	0.53	1.45	YP+YN	1.34	L	1.08
RP15	0.26	0.53	1.85	YP+YN	1.78	YP+YN	1.04
RP16	0.17	0.26	1.20	YP+YN	1.29	L	0.93
RP17	0.53	0.26	1.85	YP+YN	1.72	YP+YN	1.08
RP18	0.79	0.26	2.25	YP+YN	1.88	YP+YN	1.20
						Mean ratio	1.07
						C.O.V. (%)	8.28

* = Premature failure of steel bars
YP = Yield of reinforcement parallel to bed joints,
YN = Yield of reinforcement normal to bed joints, and
L = Local failure along one crack before yielding of reinforcement at the macroscopic level.

of a uniform distribution of cracks, it is not an easy task to clearly identify this kind of behaviour. However, as will be indicated later, a careful study of the predicted stress-strain relationships could provide implicit evidence on the occurrence of this brittle local mode of failure.

7.3.3.2 Strength Characteristics

The predicted strengths for the eleven panels are presented, together with the experimental results, in Table 7.9 to facilitate comparisons. The macro-

behaviour model was used to investigate the variation of the shear strength of the reinforced masonry assemblage with the increase in the percentages of reinforcement. The analyses covered the three different cases of $\rho_p=\rho_n$ and of $\rho_n=0.26\%$ and 0.53% with various values of ρ_p. The predicted and experimental results are presented in Fig. 7.21 in terms of $\rho_p f_y/f'_m$ and τ/f'_m. The maximum percentage of reinforcement used to prepare this figure was 1.13% which corresponds to $\rho_p f_y/f'_m=0.4$. This percentage of reinforcement could be impractical, although it satisfies the limitations stated in UBC (1991).

It is interesting to note that, in each of Figs. 7.21(a), (b), and (c), there are three rather distinct regions. For low percentages of reinforcement, along the regions marked by AB, the shear strengths are governed by the cracking stress regardless of the percentages of reinforcement. The percentages of reinforcement designated by points B can therefore be considered as the minimum percentages of reinforcement required to sustain the redistributed shear stresses after cracking. Any increase in the percentage of reinforcement beyond the amount corresponding to point B results in considerable increases in the shear strengths. In the range identified by BC, the failures take place after yielding of the reinforcement.

A comparison of the three curves BC in Figs. 7.21(a), (b), and (c) shows that the effectiveness of ρ_p as a means of increasing the shear strength improves with increased percentages of ρ_n. Using equal percentages of reinforcement parallel and normal to the bed joints results in the highest rate of increase. At high percentages of reinforcement over the range CD, the mode of failure

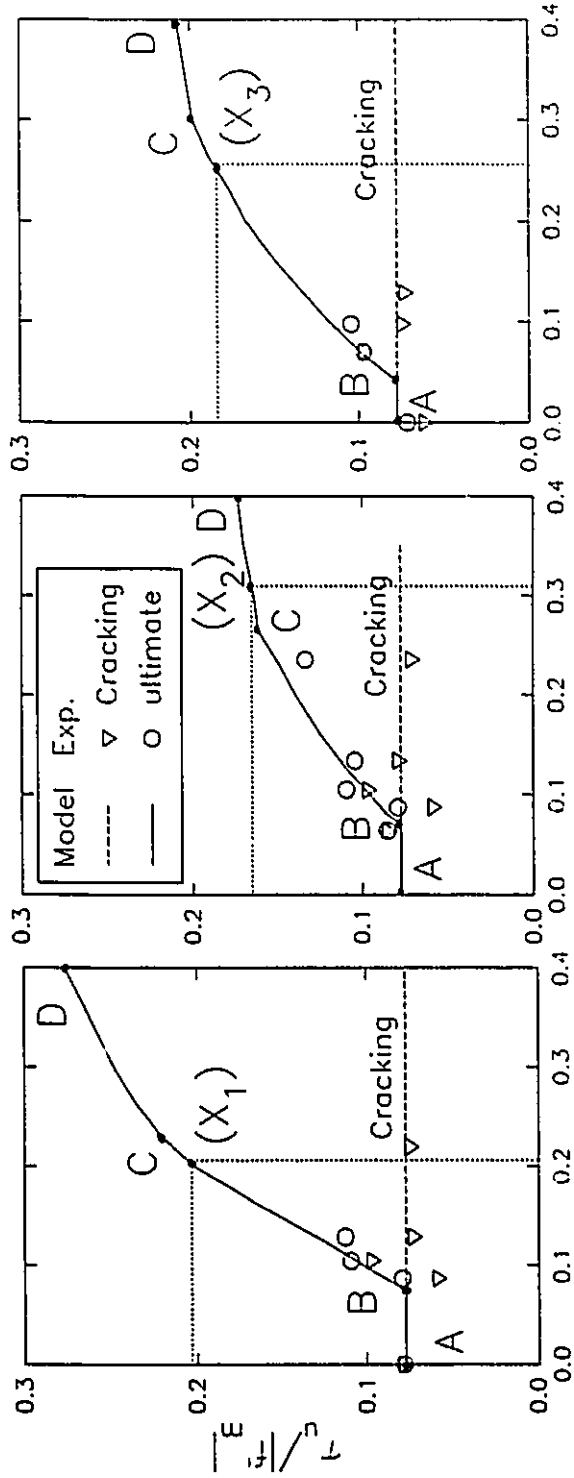

Fig. 7.21 The effect of percentages of reinforcement on shear stress at cracking and at failure.

changes to a compression failure in the masonry. The rate of increase in strength over this region is lower than it is along BC, especially in the cases of $\rho_p \doteqdot \rho_n$. The percentages of reinforcement designated by points C can be identified as limits beyond which the use of increased percentages of reinforcement are less beneficial. It is worth noting that the percentages of reinforcement, defined by points C in Figs. 7.21(a), (b), and (c), were predicted to be ρ_p=0.65%, 0.74% and 0.74%, respectively. Even though these percentages of reinforcement were predicted specifically for the masonry assemblage under consideration, it is significant that they are all considerably higher than the 0.2% and 0.3%, that were suggested by Schneider (1959) and Scrivener (1967), respectively, as upper limits for shear reinforcement.

To study the effect of the distribution of reinforcement, three points corresponding to the same total of 1.14% of reinforcement are marked as X1, X2 and X3 in Fig. 7.21. The percentages of reinforcement parallel and normal to the bed joints defined by each point are as follows:

At X1, $\rho_p=\rho_n=0.57\%$

At X2 $\rho_p=0.88\%$ and $\rho_n=0.26\%$

At X3 $\rho_p=0.61\%$ and $\rho_n=0.53\%$.

A comparison of the locations of X1, X2 and X3 on the curves, reveals how the distribution of reinforcement can affect the mode of failure as well as the strength. Also, the closer the percentages of reinforcement used normal and parallel to the bed joints are to being equal, the higher the shear strength is.

The model predictions presented in Table 7.9 and Fig. 7.21 are in good agreement with the available test results especially for those cases that did not suffer a premature failure. An average value of 1.07, at a C.O.V. of 8.28%, was found for the ratio of predicted versus observed strengths.

7.3.3.3 Deformation Characteristics

The average stress-average strain relationships for panels RP11 and RP12, which were reinforced equally normal and parallel to the bed joints, are shown in Fig. 7.22. The results obtained for RP8 were presented earlier in Fig. 7.16. Although the model tended to overestimate the stiffness of RP11 and RP12 in the principal tensile direction after cracking, the theoretical and experimental curves were in very good agreement in the principal compressive stress direction. The discrepancy in the tensile direction could be attributed to the fact that panels RP11 and RP12 suffered premature failures in some of the steel bars (see Sec. 4.3.3.1 for details).

Good agreement can be observed between the experimental and the theoretical results in Figs. 7.23(a) to (f) for panels RP13 to RP18 which were unequally reinforced normal and parallel to the bed joints. In the case of panel RP13, which was reinforced in one direction only, there was no increase in the capacity after cracking. The predicted sudden decrease in the masonry stresses for panel RP13 implies a brittle mode of failure. The tensile stress carried by the masonry dropped almost to zero in one iteration as the tensile strain increased

dramatically. While this behaviour is in agreement with the observed local brittle failure along a single crack, it is significantly different from the gradual stress redistributions predicted to occur between the masonry and the reinforcement (for example in panles RP15, RP17, and RP18) where the reinforcement was able to carry added stress after cracking. Being reinforced by steel bars with

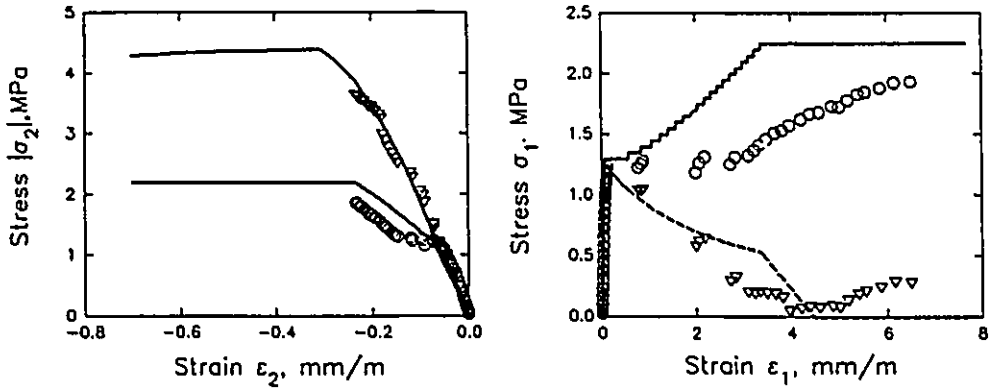

(a) Panel RP11 (Θ=45°, σ_1/σ_2=1/−0.98, and $\rho_p=\rho_n$=0.53%).

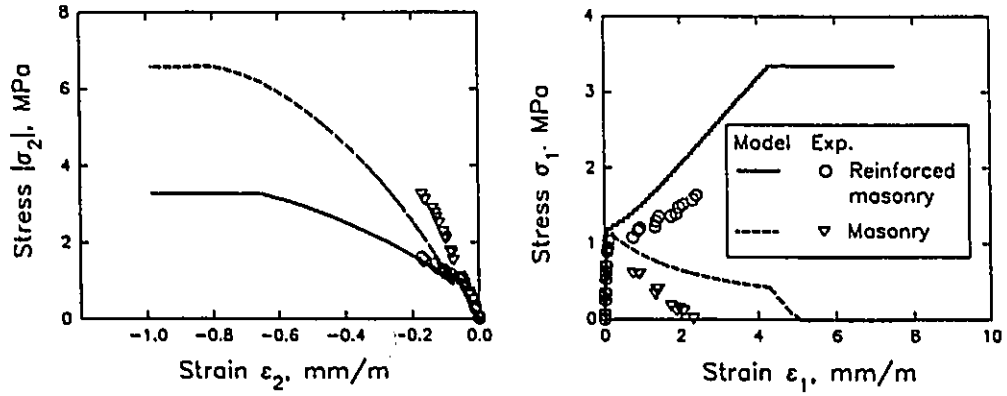

(b) Panel RP12 (Θ=45°, σ_1/σ_2=1/−0.98, and $\rho_p=\rho_n$=0.79%).

Fig. 7.22 Prediction and experimental stress-strain relationships for panels RP11 and RP12.

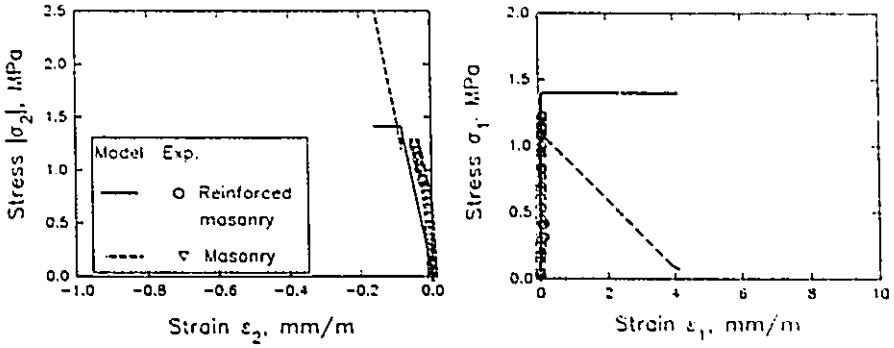

(a) Panel RP13 (θ=45°, σ_1/σ_2=1/−1.08, ρ_p=0, and ρ_n=0.53%).

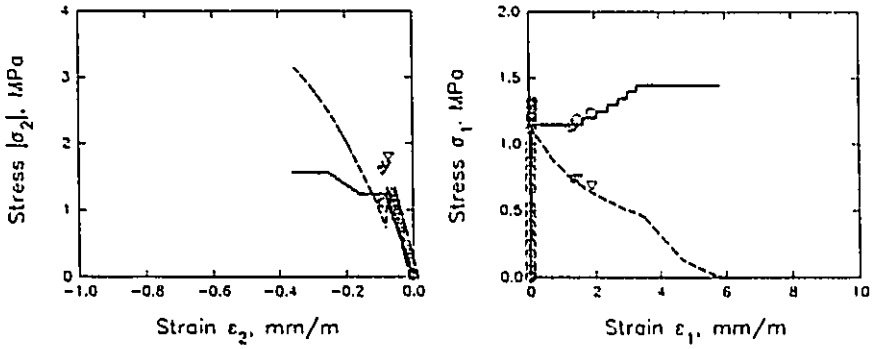

(b) Panel RP14 (θ=45°, σ_1/σ_2=1/−1.08, ρ_p=0.17, and ρ_n=0.53%).

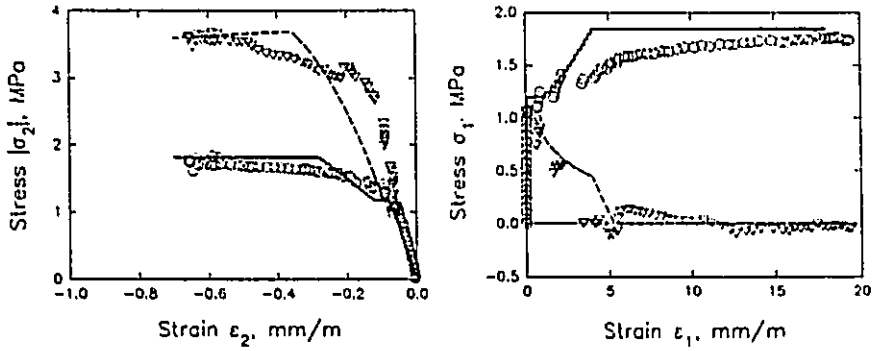

(c) Panel RP15 (θ=45°, σ_1/σ_2=1/−0.98, ρ_p=0.26, and ρ_n=0.53%).

Fig. 7.23 Prediction and experimental stress-strain relationships for panels with $\rho_p \neq \rho_n$.

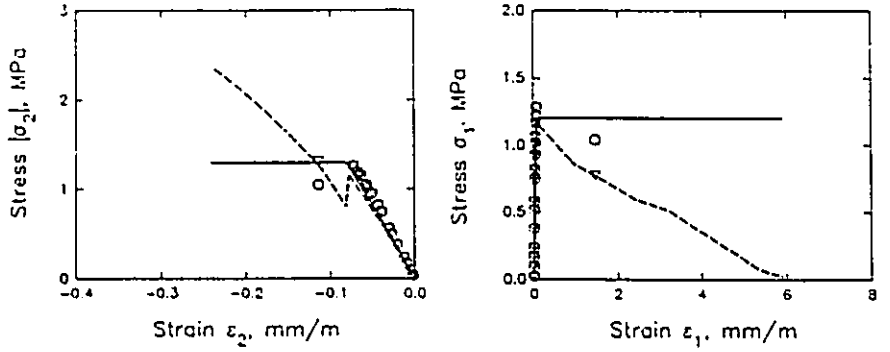

(d) Panel RP16 (Θ=45°, σ_1/σ_2=1/−1.02, ρ_p=0.17, and ρ_n=0.26%).

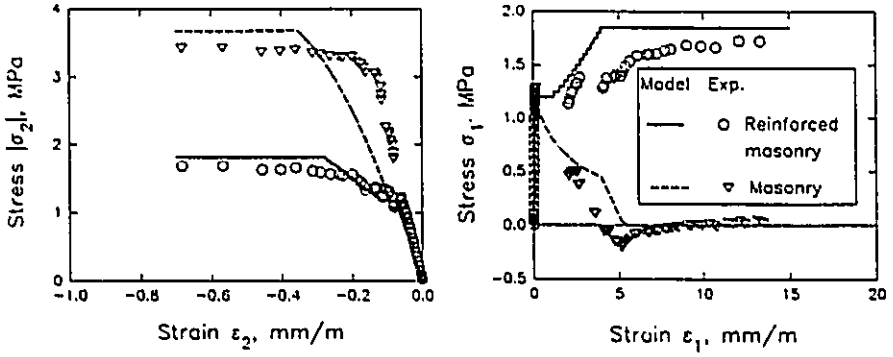

(e) Panel RP17 (Θ=45°, σ_1/σ_2=1/−0.98, ρ_p=0.53, and ρ_n=0.26%).

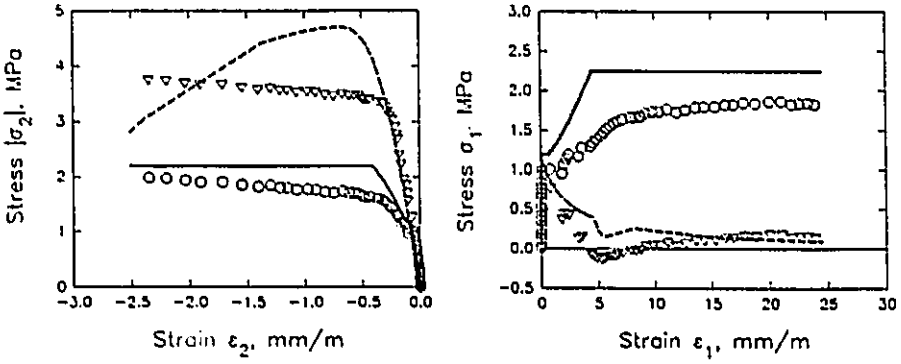

(f) Panel RP18 (Θ=45°, σ_1/σ_2=1/−0.98, ρ_p=0.79, and ρ_n=0.26%).

Fig. 7.23 (continued).

limited ductility in one of the two directions, panels RP14 and RP16 were predicted to undergo stress redistribution at a rate between those of panel RP13, on one side, and panels RP15, RP17, and RP18, on the other side.

As mentioned before and as shown in Fig. 7.24(a), a state of pure shear stress along the mortar joint planes (and along the reinforcement directions) can be replaced by a biaxial state of $\sigma_1/\sigma_2=1/-1$ at $\theta=45°$. Before cracking, the masonry resists stresses equally along the directions of the principal compressive and tensile stresses. At this stage, the effect of reinforcement in resisting part of the applied stresses is very limited because of its small area compared to the masonry cross-section. Consequently, the angle θ_m between the bed joints (and the parallel reinforcement) and σ_{1m} (the principal tensile stress of masonry) is equal to the bed joint orientation θ, which is 45° under pure shear stress. It is important to remember that θ is measured between the bed joint and σ_1 (the principal tensile stress of the reinforced masonry assemblage). With the formation of cracks normal to σ_1, the stress resisting mechanism begins to change. The tensile stress carried by the masonry decreases significantly, whereas the compressive stress continues to increase with increasing applied stresses. The reinforcement begins to take over the excess of stresses that cannot be resisted by the cracked masonry.

Mohr's circles for the stress conditions in reinforced masonry, reinforcement, and masonry are shown in Figs. 7.24(b) and (c). Figure 7.24(b) represents a case with equal percentages of reinforcement normal and parallel to

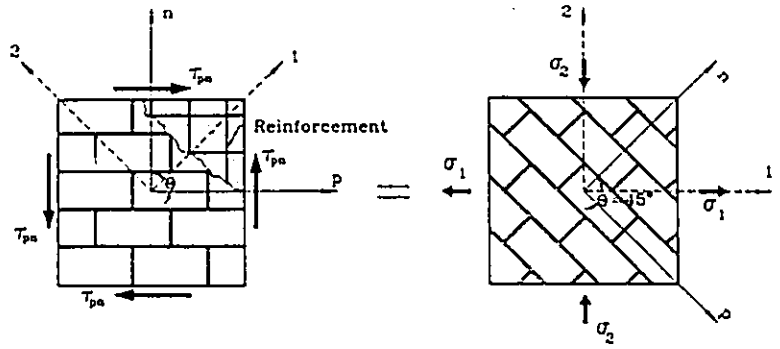

(a) A macro-element under pure shear.

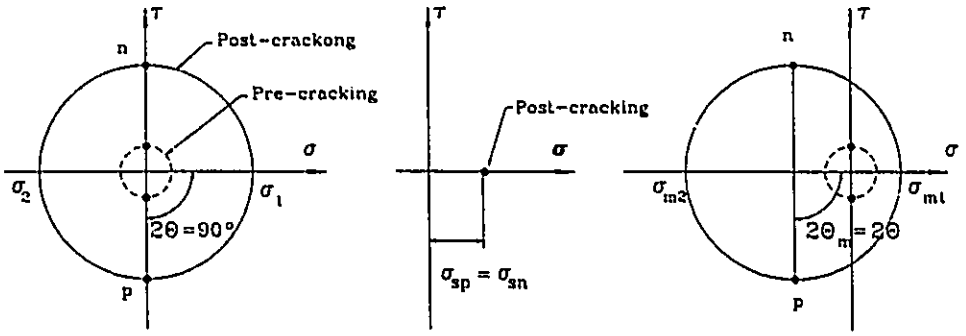

(b) Stress conditions in a macroelement with $\rho_p = \rho_n$.

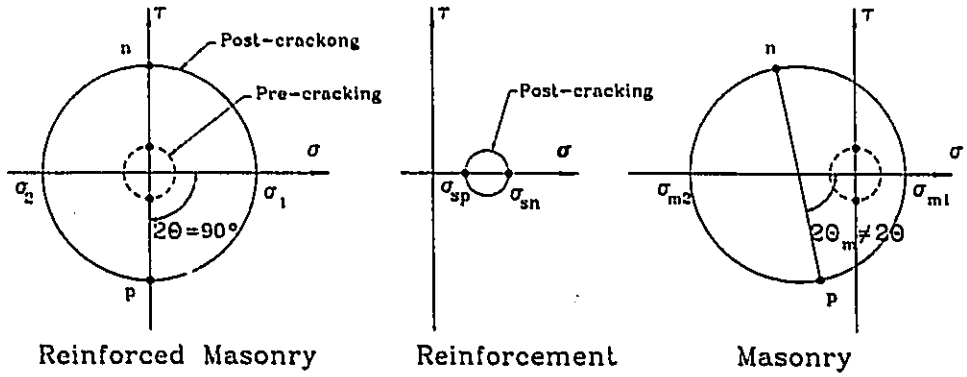

(c) Stress conditions in a macroelement with $\rho_p > \rho_n$.

Fig. 7.24 Effect of the percentages of reinforcement on the orientation of the principal stresses in masonry.

the bed joints, in which both sets of reinforcement resist equal stresses so that the angle θ_m remains constant and equal to θ even after cracking. The situation is different, as illustrated in Fig. 7.24(c), where the percentages of reinforcement, used parallel and normal to the bed joints, are unequal. Depending on the ratio of the percentages of reinforcement ρ_p/ρ_n, the stresses carried by the parallel and the normal reinforcement are also unequal. This stress distribution results in a deviation in the orientation of σ_{1m} with respect to the bed joints θ_m, which is no longer equal to θ. The difference between θ_m and θ is also expected to increase further when the reinforcement in one direction reaches the yield point while the reinforcement in the other direction continues to resist more stress. The angle θ_m is an essential parameter required to design for shear stress and to determine the percentages of shear reinforcement in the two directions (Collins and Mitchell, 1980 and Vecchio and Collins, 1986).

To display the potential of the macro-behaviour model to predict the behaviour described above, the predict values of θ_m versus σ_1 for panels RP15, RP17 and RP18 are presented in Fig. 7.25. The experimental values of θ_m obtained using the stress and strain measurements are also shown. It is suggested that a difference between the values of θ_m obtained using the stress versus the strain measurements reflects the effects of the anisotropic characteristics of grouted masonry. There is almost no sign of this difference before cracking, which supports the conclusion that having grout cores both normal and parallel to the bed joints reduces the anisotropic characteristics of masonry.

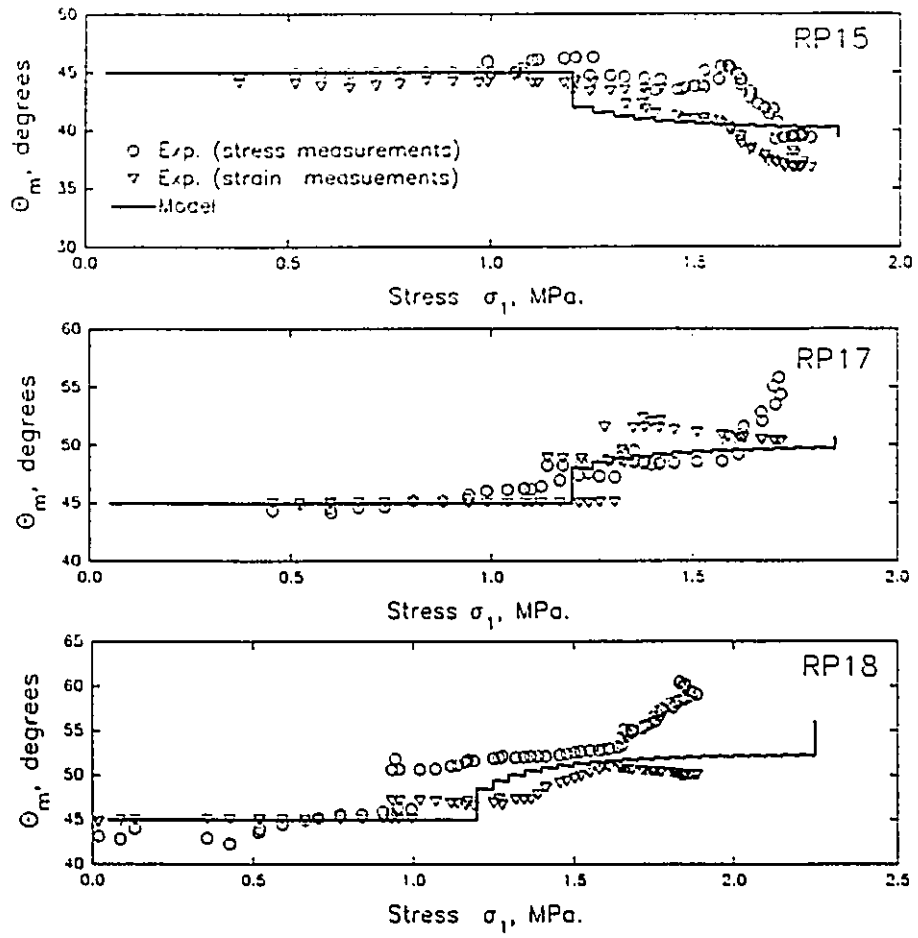

Fig. 7.25 Predicted and experimental values of θ_m for panels with $\rho_p \doteqdot \rho_n$.

The differences between θ_m values calculated using stress versus strain measurements began to appear after the formation of cracks but with small values less than 10° which is in the same order as the values reported in the test on reinforced concrete (Vecchio 1982). This finding supports the assumption that the directions of the principal stresses and the principal strains in the homogeneous medium coincide. The predicted angles for the three panels lay generally between the two sets of data calculated from the experimental results.

7.4 SHEAR STRENGTH OF GROUTED CONCRETE MASONRY

After confirming that the macro-behaviour model is able to accurately reproduce the different aspects of the in-plane behaviour of grouted and reinforced concrete masonry, the model was used to investigate the influence of several parameters on the shear strength of masonry. This investigation was performed in an attempt to discover the reasons for the discrepancies between the results obtained by the different investigators identified in Chapter 1, regarding the shear strength of masonry. The parameters considered in the investigation included normal stresses, tensile strength of the masonry assemblage and the percentage of reinforcement. The results obtained are reported in the following sections under the two categories of unreinforced and reinforced masonry. The properties of the materials adopted in the analyses of unreinforced and reinforced masonry assemblages are the same as those summarized, respectively, in Table 7.2 for series UNP and Table 7.6 for series RP.

7.4.1 Shear Strength of Unreinforced Masonry

7.4.1.1 Effect of Normal Stresses

The macro-behaviour model was used to predict the strength of a representative macro-element in a masonry shear wall under the effect of τ_{pn}, σ_p and σ_n as illustrated in Fig. 7.26. The results obtained for the masonry assemblage with grout cores normal to the beds joints only are presented in Fig. 7.27 in terms of the normalized shear strength τ_{pn}/f'_m and the associated normal stresses σ_n/f'_m under different ratios between σ_p and σ_n. The different

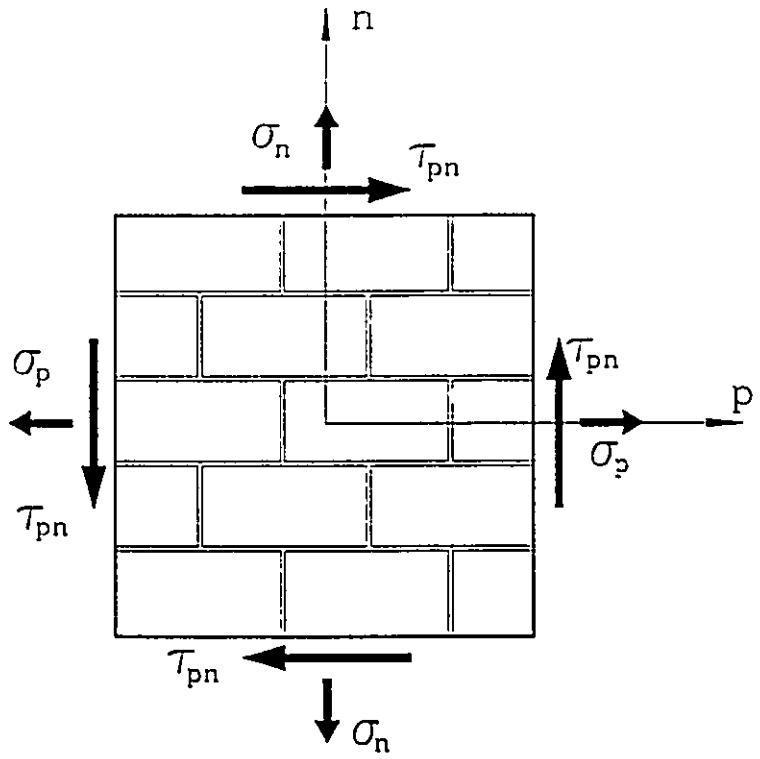

Fig. 7.26 Stress components along the mortar joint planes in a representative macro-element.

cases of failure predicted along the mortar joints, where the anisotropic characteristics of masonry dominated the shear strength, are marked in Fig. 7.27.

It is obvious that the normal stresses significantly affect the shear strength of the masonry assemblage. Considering the case where $\sigma_p=0$, the shear strength increases considerably with the change of σ_n from tension to compression. This increase continues, under the range of low normal compressive stress, until the shear strength reaches a maximum value. The failure of the masonry assemblage in this range of normal stresses was found to occur in a stepped manner. With further increase in the applied normal stress, the shear strength remains almost

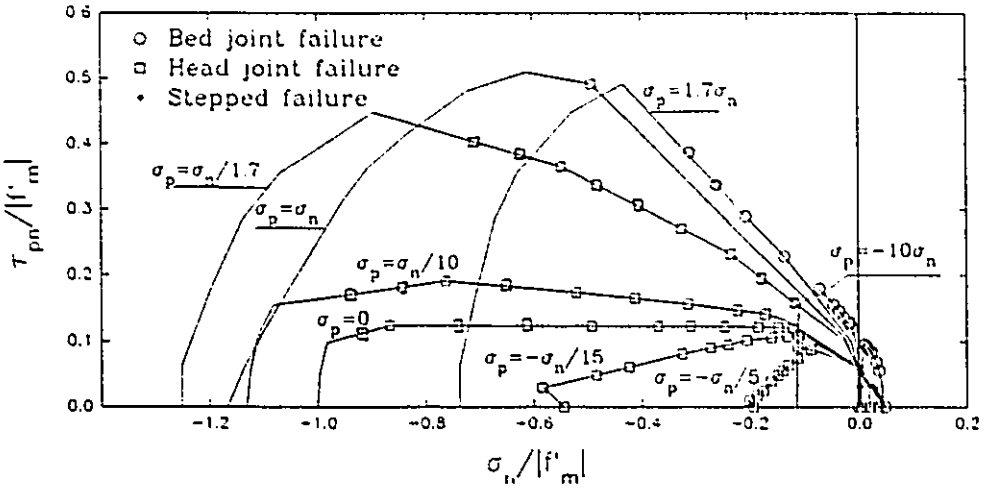

Fig. 7.27 Variation of shear strength with normal stresses for a masonry assemblage with grout cores normal to the bed joints.

constant as the failure occurs along the head joint planes. Eventually, as the normal stress approaches the compressive strength of the assemblage, the failure occurs in the homogeneous medium with the shear strength dropping to zero. The shape of the shear strength-normal stress interaction diagram, the maximum strength, as well as the modes of failure predicted at $\sigma_p=0$ change significantly for different σ_p values. The existence of tensile stresses normal or parallel to the bed joints results in a large reduction in the shear strength of the assemblage (i.e. for cases of $\sigma_p=-\sigma_n/15$ and $\sigma_p=-\sigma_n/5$). Conversely, the existence of compressive stresses normal and parallel to the bed joints improves the shear strength. The maximum shear strength predicted for the masonry assemblage under consideration was about $0.5f'_m$ under the effect of $\sigma_p=\sigma_n$.

The variations of the shear strengths with the applied normal stresses for a masonry assemblage grouted both normal and parallel to the bed joints are

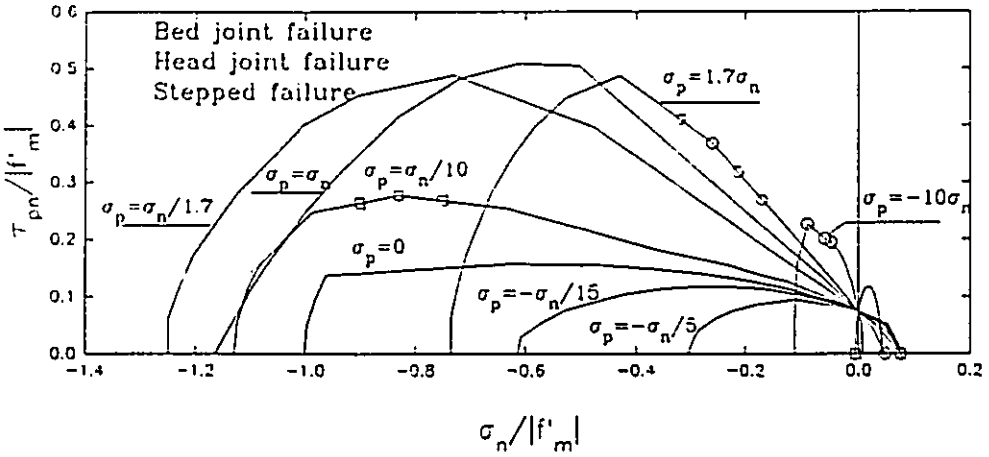

Fig. 7.28 Variation of shear strength with normal stresses for a masonry assemblage with grout cores both normal and parallel to the bed joints.

shown in Fig. 7.28. A comparison between this figure and Fig. 7.27 reveals the effect of the added continuity of the grout in reducing the cases where the failure is governed by the capacity of the mortar joints. The improved shear strength resulting from having grout cores both normal and parallel to bed joints is more apparent in the cases having tensile stress normal or parallel to the bed joints (for example under σ_p=-σ_n/5 and -σ_n/15). This effect is not as evident under high compressive stresses.

7.4.1.2 Effect of Masonry Tensile Strength

It is stated in the current Canadian design code (CAN3-S304-M84, 1984) that "a plain masonry shear wall shall be designed so that no part in the wall is in tension". In an attempt to investigate the implication of this statement on the shear strength, the macro-behaviour model was used to predict the variation of the shear strength with the normal stresses for the representative macro-element modelled as having zero tensile strength for the different components in the

unreinforced masonry assemblage. The results obtained for the masonry assemblages with grout cores in one and two directions are shown in Figs. 7.29 and 7.30, respectively. Also, in the same figures, the results obtained by including the masonry tensile strength are presented to facilitate comparisons.

The results shown on the left sides in Figs. 7.29 and 7.30 represent the

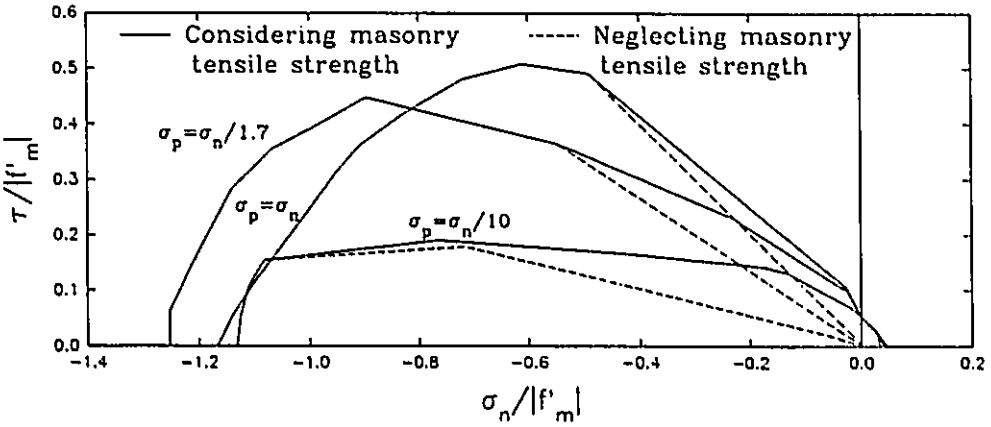

Fig. 7.29 Effect of masonry tensile strength on the shear strength of masonry assemblage with grout cores normal to the bed joints.

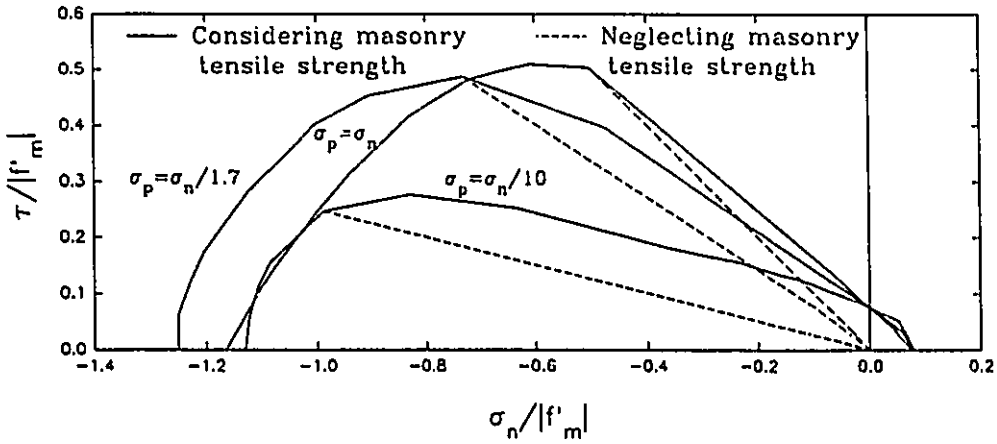

Fig. 7.30 Effect of masonry tensile strength on the shear strength of masonry assemblage with grout cores both normal and parallel to the bed joints.

capacities under the effects of normal compressive stresses. Utilizing the tensile strength of the masonry assemblage seems to have a significant role under the effect of low compressive stress. This effect gradually decreases with the increased normal compressive stresses and is not a factor where the compression mode of failure governs the behaviour. The reduction in the shear strength, in the absence of tensile strength in the masonry is more apparent for the masonry assemblage with grout cores in two directions.

7.4.2 Shear Strength of Reinforced Masonry

The effects of the normal stresses and the percentages of reinforcement on the shear strength of reinforced masonry have been discussed separately in previous sections. To avoid repetition, the following sections are directed mainly towards investigating the possible reasons behind the discrepancies noticed among the results reported by different researchers, regarding the contribution of reinforcement to improving the shear strength. These reasons include the interaction between the effects of the normal stresses and the percentage of reinforcement, and the effect of the tensile strength of the masonry assemblage. All of the results presented here were obtained for a masonry assemblage with grout cores both normal and parallel to the bed joints.

7.4.2.1 Combined Effects of Normal Stresses and Percentage of Reinforcement

The macro-behaviour model was used to predict the shear strengths of a macro-element reinforced by three different percentages of reinforcement;

$\rho_p=\rho_n=0.0$, 0.26, and 0.53%. The interaction curves for the shear strength versus the normal stress σ_n were determined for each percentage of reinforcement under three different ratios between σ_p and σ_n. The results are presented in Fig. 7.31. The differences between the interaction curves for a certain percentage of reinforcement and that for zero percentage of reinforcement can be considered as an index for the effectiveness of reinforcement in improving the shear strength.

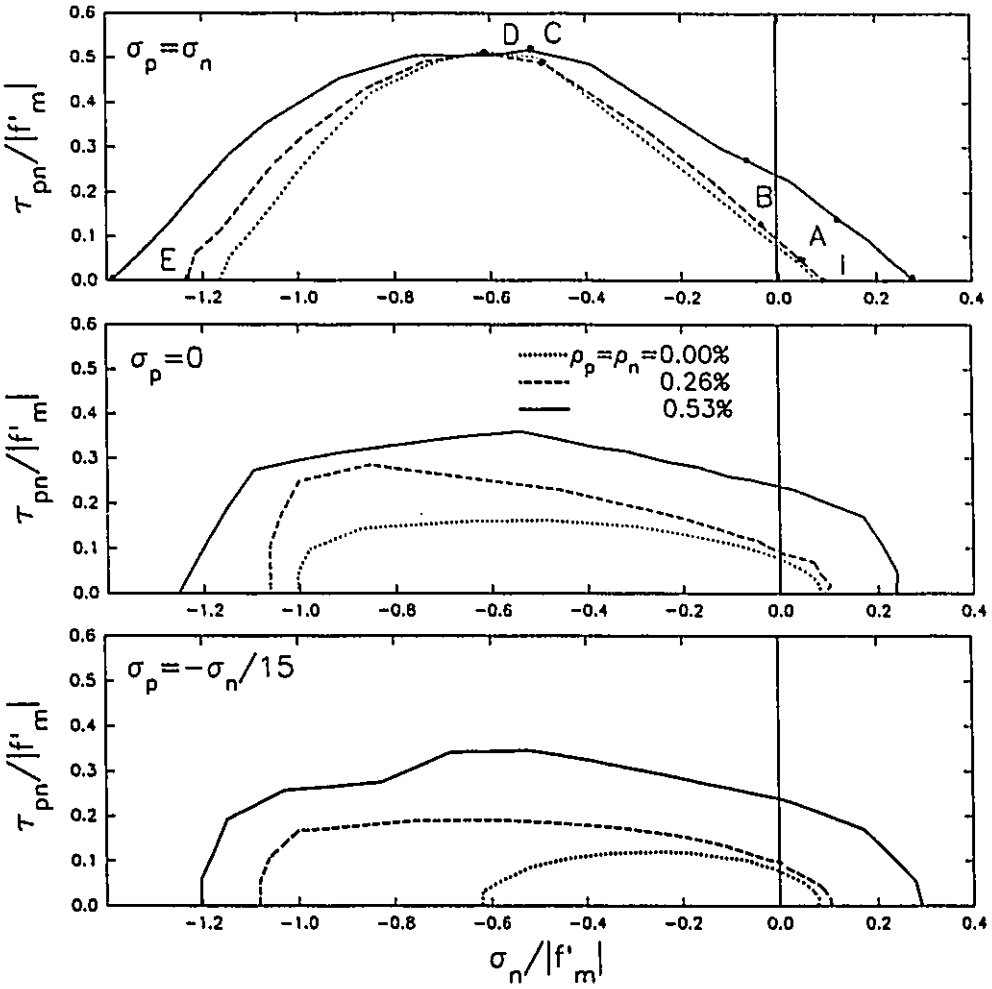

Fig. 7.31 Combined effects of the percentages of reinforcement and the normal stress on masonry shear strength.

The results indicate the dependence of the effect of the reinforcement on the level of the normal stress. Under the effect of $\sigma_p=\sigma_n$, the contribution of reinforcement is very apparent in the range marked by IAB where the assemblage is subjected to tensile or low normal compressive stress. Over this range, failure was predicted to occur by yielding of reinforcement after cracking. Thereafter, the contribution of reinforcement continues to decrease gradually with the increase in the normal compressive stresses over the range marked by BCD. At the maximum shear strength marked by D, the effect of the reinforcement almost vanishes. Further increases in the normal compressive stresses over the range marked by DE result in compression failure before cracking, which implies that the reinforcement was subjected to compressive stresses and strains. Over this range, the effectiveness of reinforcement continues to increase with increased normal compressive stresses.

It is not only the level of the normal stresses that affects the contribution of reinforcement, but also the ratio between σ_p and σ_n. A comparison between the results obtained under the effects of $\sigma_p=\sigma_n$, $\sigma_p=0$, and $\sigma_p=-\sigma_n/15$ demonstrates that the reinforcement is more effective under the effect of normal tensile stresses acting parallel or normal to the bed joint as indicated in the case of $\sigma_p=-\sigma_n/15$.

In addition to the dependence of the effectiveness of reinforcement on the level of the normal stress and the ratio of stresses, the contribution of the reinforcement does not always increase in proportion with the percentage of

reinforcement. This trend is obvious along the range marked by IABCD under $\sigma_p=\sigma_n$, where the capacity of the reinforced assemblage with $\rho_p=\rho_n=0.26\%$ is very close to the cracking stress of the plain masonry. Larger percentages of reinforcement along this range seem to be more effective. Unlike this behaviour, under the effect of $\sigma_p=-\sigma_n/15$, the increase of the percentage of reinforcement from zero to 0.26%, under high compressive stress σ_n, is more effective than the further increase from 0.26% to 0.53%. This finding, which is in agreement with the conclusions drawn by Sveinsson et al. (1985) and Shing et al. (1989 and 1990) regarding the inconsistent effect of reinforcement on improving the shear capacity of masonry shear walls, reveals the complicated interactive effects of the reinforcement and the normal stresses. This in turn necessitates the use of a rational design procedure to replace the empirical or semi-empirical formulae adopted in the design provision for shear in CAN3-S304-M84.

7.4.2.2 Effect of Masonry Tensile Strength

The macro-behaviour model was used to investigate the effect of the masonry tensile strength on the shear strength of the representative macro-element. The predicted variations of the shear strength with the percentage of reinforcement for an assumed zero tensile strength are shown in Fig. 7.32. The results obtained using the previously established tensile strength of the masonry material are also shown in the same figure to facilitate comparison.

As indicated before, there are three regions that can be recognized in each of the three cases under consideration. The effect of the masonry tensile strength

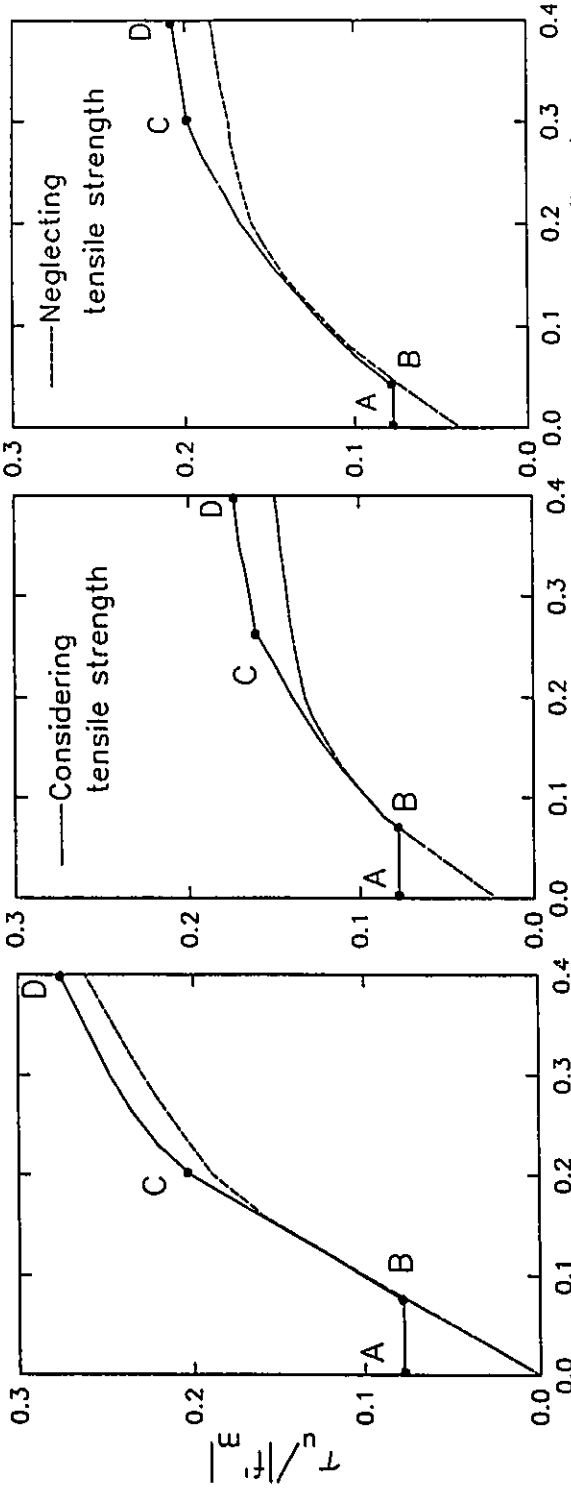

Fig. 7.32 Effect of masonry tensile strength on the shear strength of reinforced masonry.

changes from one region to another. Neglecting the masonry tensile strength along the ranges marked by AB underestimates the shear strength, which could be attributed to the fact that the shear strength of the assemblage in this range is govern by the cracking stresses. Along the ranges marked by BC, failure is characterized by yielding of the reinforcement which implies that most of the tensile stress carried by masonry is transferred to the reinforcement. As a result, neglecting the tensile strength along this range does not play a significant role in the shear strength prediction. Conversely, the failures along the ranges marked by CD take place in compression before the tensile stress in masonry decreases to zero. This argument explains the reason for the reduction in the shear strength, along CD, when the tensile strength is neglected.

7.5 CLOSING REMARKS

From the foregoing discussions regarding unreinforced masonry assemblages, the following remarks can be made:

1. Grouted concrete masonry is an anisotropic material which exhibits behavioural changes, according to the bed joint orientation θ, even under the same state of stress. The effect of the bed joint orientation on the strength and the failure mode of the assemblage also changes with changes in the principal stress ratio σ_1/σ_2. Consequently, there is no way to accurately predict the behaviour of grouted masonry without considering the effects of the mortar joints on the anisotropic properties. The macro-behaviour model, presented in Chapter 5, provides an accurate, yet reasonably simple, approach for modelling the

behaviour of grouted concrete masonry under in-plane stresses. In this model, the masonry assemblage is simulated as a homogeneous medium intersected by two sets of planes of weakness along the mortar joints. The agreement between the model predictions and the available test results confirms the potential of the model to realistically predict the full range of behaviour of grouted concrete masonry under in-plane stresses.

2. Under biaxial tension-compression, the bed joint orientation θ has a significant effect on both strength and mode of failure. The effect is more apparent for increased algebraic ratios between the principal stresses σ_1/σ_2 (i.e. moving towards the state of uniaxial compression). Under these states of stress, where σ_2 dominates the behaviour, the mode of failure changes with θ from a compression failure to a shear failure along the mortar joints resulting in a significant drop in the ultimate stresses. With a decrease in the algebraic ratio σ_1/σ_2, the tension modes of failure occur along the mortar joints or normal to σ_1, depending on θ. In spite of the effect of θ on the tensile modes of failure, its relative lack of effect on the strength could be attributed to the low tensile strength of masonry.

3. Under biaxial tension-tension, although the bed joint orientation has a significant effect on the modes of failure its relative lack of effect on the strength of the assemblage is in agreement with the previous remark.

4. Under biaxial compression-compression, the effect of the bed joint orientation changes with the ratio between the principal stresses. In the cases

where one of the principal stresses is significantly higher than the other, the anisotropic characteristics of masonry prevail as the failure takes place along the mortar joints. The behaviour of the masonry assemblage tends to resemble an isotropic behaviour as the principal stresses get closer to being equal. In this case, compression failure occurs in the homogeneous medium, rather than following the mortar joint planes of weakness.

5. Defining the tensile responses of the components along the mortar joints by a circular tension cut-off failure criterion along with an elastic-strain softening stress-strain relationship led to the best agreement between the theoretical and the experimental results. This material idealization was compared to two other cases based on a straight tension cut-off failure criterion along with an elastic-perfectly plastic stress-strain relationship or a circular tension cut-off failure criterion along with an elastic-perfectly plastic stress-strain relationship.

6. Compared to the masonry assemblage with grout cores normal to the bed joints only, having grout cores both normal and parallel to the bed joints helped reduce the anisotropic characteristics of masonry, due to the mortar joints.

7. The capacity of a masonry assemblage to resist the shear stresses acting along the mortar joints changes significantly with the magnitude of the normal stresses acting normal or parallel to the bed joints. This could be attributed to the anisotropic characteristics of the masonry, which require the failure to be defined in terms of three parameters; σ_1, σ_2, and θ or σ_p, σ_n, and τ_{pn}. The shear strength of a masonry assemblage decreases with increased normal tensile stresses.

8. The tensile strength of masonry has a significant effect on the shear capacity of masonry subject to tensile stress or low compressive stress.

Based on the results obtained regarding the behaviour of reinforced masonry, the following additional remarks can made:

9. Before cracking, the presence of grout cores both normal and parallel to the bed joints reduces the anisotropic characteristics of masonry. Depending on the principal stress ratio, this behaviour can change after cracking. In the cases where the effects of principal tensile stress σ_1 dominates and the failure takes place in the form of yielding of reinforcement, the bed joint orientation does not have a noticeable effect on the failure stresses. Conversely, the bed joint orientation θ plays a significant role on both strength and mode of failure when the effects of principal compressive stress σ_2 prevail. In the latter case, the mode of failure can change from a compression failure with yielding of the reinforcement to a compression failure before the reinforcement reaches the yield point or to a shear failure along the mortar joints. For the last two modes of failure, the effectiveness of reinforcement is limited, resulting in less ductile behaviour. It is worth noting that θ represents the angle between the bed joint (or the parallel reinforcement) and σ_1. As a result, the dependence of the response of the assemblage on θ could be due to the mortar joints and/or the reinforcement.

10. The contribution of reinforcement in resisting the shear stresses changes with percentages of reinforcement and their distribution between the parallel and the normal directions. Up to the percentage of reinforcement with strengths

equivalent to the cracking stress, the reinforcement has almost no effect in improving the shear strength. However, additional reinforcement results in a significant increase in the shear strength of the assemblage because the failure is characterized by yielding of reinforcement. This increase continues until the percentages of reinforcement reaches a limit, beyond which compression failure occurs before the reinforcement reaches the yield point. Therefore, further increases in the percentages of reinforcement have less significant effects on improving the shear strength.

11. The normal stresses, acting normal and parallel to bed joints, have very significant effects on the shear strength of reinforced masonry as well as on the effectiveness of the reinforcement in improving its shear strength. The contribution of the reinforcement is more apparent under the effect of normal tensile stress.

12. The shear capacity of reinforced masonry depends on the tensile strength of masonry in the cases where the shear strength is governed by the cracking stress or where the compression failure occurs before the reinforcement yields. The effect of the tensile strength of masonry vanishes as the reinforcement reaches the yield point before the masonry fails in compression.

13. The consistent agreement between the model predictions and the experimental results of reinforced masonry provides additional evidence of the suitability of the model to predict the behaviour of reinforced masonry.

CHAPTER 8

SUMMARY, CONCLUSIONS, AND RECOMMENDATIONS

1.1 SUMMARY

The available literature on the in-plane behaviour of masonry was categorized and reviewed under one of three research approaches; experimental investigation of the behaviour of masonry walls, microscopic modelling of masonry, and macroscopic modelling of masonry. Significant differences were found between the results obtained in different research programs which may leave a wrong impression about the potential of masonry as a structural material. The literature review also pointed out the lack of experimental data on the macro-behaviour of grouted concrete masonry, particularly for reinforced assemblages. Therefore, this investigation was initiated to explore the macro-behaviour of grouted concrete masonry, both unreinforced and reinforced, and to provide a body of test data for North American conditions (practice and material) that forms the basis of a macro-behaviour model.

The experimental program in this investigation included two major parts; biaxial tests and auxiliary tests. The biaxial tests involved a total of 36 full scale unreinforced or reinforced panels tested under uniform states of biaxial tension-compression. A biaxial test rig was specially devised to perform these tests. The

panel dimensions were chosen to exhibit the macro-behaviour of concrete masonry by including several blocks, grout cores, mortar joints and steel bars with the panel dimensions of 1200 mm square by 190 mm thick. The variables considered covered the bed joint orientation θ, the ratio between principal stresses σ_1/σ_2 and the percentages of reinforcement used parallel and normal to the bed joints.

The auxiliary tests included a large number of component material tests and assemblage tests performed before and during the biaxial test program. The component material tests were used to determine the physical and mechanical properties of each material used and served as control tests. The assemblage tests comprised 33 prisms tested under uniaxial compression, 27 prisms tested under uniaxial tension and 15 couplets tested under direct shear. The prisms were tested for comparison with the biaxial tests and to provide more information about the effects of the bed joint orientation θ and the grout configuration. In addition to these prisms, a four course prism was constructed in running bond pattern with each biaxial panel. All of the specimens were built using standard normal weight 190 mm autoclaved hollow concrete blocks, type S mortar, and coarse grout.

The results of the different tests were presented and discussed in terms of modes of failure, strength characteristics, and deformation characteristics. These, together with the analysis of the influence of various parameters, have provided well documented evidence of the macro-behaviour of grouted concrete masonry and have provided a sound foundation for numerical modelling.

Based on the experimental results and the literature review, a macro-model

was developed to predict the in-plane behaviour of grouted concrete masonry. In this model, the masonry assemblage was replaced by an "equivalent material" which consisted of a homogenous medium intersected by two sets of planes of weakness (along the head joint and bed joint planes) and two sets of reinforcement. The macro-behaviour of the "equivalent material" was determined by smearing the influence of these sets, which provided a means of modelling the inherent part of the anisotropic characteristics of masonry assemblages. On the other hand, the behaviour of the homogeneous medium was described by an orthotropic model to account for the induced part of the anisotropic characteristics. The reliability of the proposed model was confirmed using the experimental results from this investigation and elsewhere. The model was also used to fill the gaps in the available test results and to provide a more complete picture of the in-plane behaviour of grouted concrete masonry.

8.2 CONCLUSIONS

Specific conclusions regarding the test methods, the experimental results, the macro-behaviour model, and the stress-strain relationships were presented at the end of Chapters 2 to 7. However, general conclusions are also reported in this section to provide a consolidated overview of the in-plane behaviour of grouted concrete masonry. These conclusions are as follows:

1. Testing of masonry assemblages under uniform well defined stress conditions has the advantage, over testing full masonry shear walls, of explicitly defining the stresses and strains without the need to adopt any assumption of isotropic or elastic behaviour. Use of uniform stresses simplifies interpretation of

failure modes where stress redistribution to less highly loaded areas is not possible. This test technique also provides an opportunity to study the behaviour of masonry under a state of pure shear without any interference from flexural or axial stresses.

2. The facts that all possible modes of failure were observed in the tests of the unreinforced panels and that they were in complete agreement with those of the prisms tested under uniaxial compression, in conjunction with the observed uniform well developed crack patterns in the reinforced panels, demonstrate the effectiveness and the reliability of the panel dimensions and loading arrangement chosen to study the macro-behaviour of grouted concrete masonry. The experimental results reported in this investigation provide a body of test data which helps define the in-plane behaviour of grouted concrete masonry and which can be used to assess the validity of analytical methods.

3. Grouted concrete masonry is an anisotropic material with behavioral characteristics which depend on the bed joint orientation θ. For example, under a state of uniaxial compression, the modes of failure, the strength characteristics, and the deformation characteristics change significantly with the bed joint orientation. The reductions in the ultimate compressive stresses, compared to the values obtained for $\theta=0°$, were found to range from 15% to 43% for $\theta=67.5°$ corresponding with shear failures along the bed joints.

4. The anisotropic characteristics of grouted concrete masonry do not remain constant. They rather change significantly with changes in the principal stress ratio σ_1/σ_2. Under uniaxial tension, where the tensile modes of failure

dominate the behaviour, the fracture planes follow the mortar joints in different patterns depending on the bed joint orientation. With an increase in the algebraic ratio of σ_1/σ_2 (moving towards the state of uniaxial compression), the effect of the bed joint orientation decreases because the fracture occurs normal to the principal tensile stress direction, regardless of the bed joint orientation. With further increases in the algebraic ratio of σ_1/σ_2, where the compression modes of failure dominate the behaviour, the effect of the bed joint orientation becomes more apparent.

5. Under biaxial tension-tension, although the bed joint orientation has a significant effect on the mode of failure, the fact that its effect on the strength is not very significant could be attributed to the low tensile strength of masonry. On the other hand, under biaxial compression-compression, where one of the principal stresses is significantly higher than the other, the anisotropic characteristics of masonry prevail as the failure takes place along the mortar joints. The behaviour of the masonry assemblage tends to resemble an isotropic material as the principal stresses get closer to being equal.

6. Using two-cell blocks with frogged ends results in unaligned webs in the running bond pattern. The unaligned webs, along with the flared tops of the blocks, lead to small grout areas along the bed joint planes, which in turn limit the effectiveness of the grout in reducing the anisotropic characteristics of masonry. Therefore, use of blocks designed to provide uniform continuous cores of grout should result in less anisotropic behaviour. Use of blocks with knocked-out webs helped significantly to reduce the anisotropic characteristics of masonry

because of the resulting continuous grout cores parallel to the bed joints. These horizontal cores helped improve the flow of the grout inside the walls, which consequently reduces the potential of having flaws or unfilled head joints.

7. In case of the reinforced masonry assemblages built of blocks with knocked-out webs, the existence of continuous grout cores both normal and parallel to bed joints reduces the anisotropic characteristics of masonry before cracking. Depending on the principal stress ratio, this behaviour could change after cracking. In the cases where the principal tensile stress dominates and the modes of failure are characterized by yielding of reinforcement, the bed joint orientation does not have a noticeable effect on the failure stresses. Conversely, the bed joint orientation θ plays a significant role on both strength and mode of failure when the principal compressive stress dominates. In the latter case, depending on the bed joint orientation θ, the mode of failure could change from a compression mode of failure, after yielding of the reinforcement, to a compression mode of failure before the reinforcement reaches the yield point, or to a shear mode of failure along the mortar joints. The last two modes of failure reduce the effectiveness of reinforcement and result in less ductile behaviours.

8. The mean value of the cracking stresses for the reinforced panels, built using blocks with knocked-out webs and tested under a state of pure shear along the mortar joints, was found to be reasonably close to the empirical formula $(\sigma_1)_{cr}=0.303\sqrt{f'_m}$. This formula is similar to but slightly lower than the formula of $(\sigma_1)_{cr}=0.33\sqrt{f'_m}$ which is adopted in the ACI concrete code (1989) for predicting the diagonal tensile strength of the webs of reinforced concrete beams

(Vecchio and Collins 1982).

9. In the case where cracks follow the mortar joints, the shear deformations along the cracked joints are accompanied by dilation which induces additional tensile stresses in the reinforcing bars that cross these joints. These stresses can cause the reinforcement to yield at lower principal tensile stresses than would be predicted if masonry is modelled neglecting the potential for failure along the mortar joints.

10. The strain measurements, recorded over gauge lengths of 900 mm in the biaxial tests of the reinforced panels, showed good agreement between the strains in the masonry and the reinforcement. This finding supports the assumption of perfect bond between the masonry assemblage and the reinforcement at the macroscopic level.

11. Relating the effectiveness of shear reinforcement only to its total percentage is incorrect. Increasing the amount of shear reinforcement can be beneficial to both shear strength and ductility, but this cannot be achieved unless attention is paid to the details of reinforcement. First, it is important to distribute the shear reinforcing parallel and normal to the bed joints in order to be able to resist the excess of forces that cannot be carried by masonry after the formation of diagonal cracks. This implies that the vertical reinforcement in a masonry shear wall may have to be designed to resist part of the shear force in addition to the tensile forces due to the bending moment. Second, use of ductile steel bars is essential, particularly in the direction of the lower percentage of shear reinforcement. If this condition is not satisfied, premature failure is likely to take

place along the first diagonal crack before the steel bars in the direction of higher percentage of shear reinforcement achieve their full yield strength.

12. Properly detailed shear reinforcement, with total percentages up to 1.06%, were shown to increasingly help to avoid brittle shear failure and to improve both the strength and the ductility of the reinforced masonry assemblage.

13. Increasing the amount of reinforcement up to the percentage of reinforcement with strengths equivalent to the cracking stress has almost no effect on increasing the shear strength. Any further increase in the percentage of reinforcement results in a significant increase in the shear strength of the assemblage in the range where the failure is characterized by yielding of reinforcement. This increase continues until the percentage of reinforcement reaches a limit, beyond which compression failure occurs before the reinforcement reaches the yield point. In this range, additional increases in the percentages of reinforcement have less significant effect on improving the shear strength.

14. The axial stresses, acting normal and parallel to bed joints, have very significant effects on the shear strength of reinforced masonry as well as on the effectiveness of the reinforcement in improving its shear strength. The contribution of the reinforcement is more apparent under the effect of tensile stress.

15. Before cracking, the stresses applied on a reinforced masonry assemblage are distributed between the masonry and the reinforcement according to their stiffnesses. After cracking, the ability of masonry to resist the principal

tensile stress decreases significantly with increasing principal tensile strain ϵ_1. This leads to transfer of more stress to reinforcement. The cracked masonry continues to help resist the principal compressive stresses, but with lower stiffness and ultimate capacity, depending on the principal strain ratio $|\epsilon_1/\epsilon_2|$.

16. Because of its anisotropic characteristics, grouted concrete masonry cannot realistically be modelled without considering the effect of the mortar joints. The macro-behaviour model, proposed in this investigation, provides an accurate, yet reasonably simple, approach for modelling the behaviour of grouted concrete masonry under in-plane stresses. This model accounts for both the inherent and induced anisotropic characteristics of masonry. The consistent agreement between the model predictions and the available test results confirms the potential of the model to realistically predict the full range of behaviour of unreinforced and reinforced grouted concrete masonry under in-plane stresses.

17. Having achieved the main objectives stated before in Sec. 1.3, it is the next step to utilize the results obtained in this investigation to provide a rational design procedure for evaluating the shear strength of masonry shear walls. Such a design procedure is needed to replace the empirical or semi-empirical formulae adopted in recent design codes. In brief, the shear resistance of a masonry wall can be determined by considering an admissible stress field which satisfies the conditions of equilibrium and compatibility of strains, using the average stress-average strain relationships developed in this investigation. Then the cross-section dimensions can be chosen to ensure that the diagonally cracked masonry is capable of resisting the inclined compressive stresses. The

resistance of the diagonally cracked masonry should be defined in terms of its orientations with respect to the mortar joints which, in turn, account for the anisotropic characteristics of masonry. Vertical and horizontal reinforcement must be provided to maintain equilibrium with the diagonal compressive forces. This procedure can be used to design regular masonry shear walls consisting of a single rectangular element. For irregular masonry shear walls, the designer may need to perform a more detailed Finite Element analysis incorporating the macro-behaviour model proposed herein.

8.3. RECOMMENDATIONS FOR FURTHER RESEARCH

The following related areas are recommended for future investigations:

1. A repetition of the biaxial tension-compression tests performed in this investigation, but using masonry assemblages built of different material components, would help confirm the general validity of the results reported here.

2. An experimental investigation should be undertaken to investigate the behaviour of grouted concrete masonry under biaxial states of compression-compression and tension-tension. These test data are needed to confirm the validity of the proposed macro-behaviour model under the effects of these states of stress.

3. The possibility of employing or modifying the macro-behaviour model to simulate the in-plane behaviour of ungrouted and partially grouted concrete block masonry assemblages should be investigated. Such a step is essential towards providing a unified design method for masonry walls.

4. Development of a rational design procedure for shear, based on the

results presented in this investigation, is required to replace the empirical or semi-empirical formulae adopted in the current design code

5. Development and verification of a Finite Element model that incorporates the macro-behaviour model are needed to be able to predict the behaviour of masonry shear walls having different configurations and unusual loading conditions.

REFERENCES

A.C.I. Committee 318, (1989),"Building Code Requirements for Reinforced Concrete - ACI 318M-89/ACI 318R-89", American Concrete Institute, Detroit, 353 pages.

Ali, S., Page, A.W. and Kleeman, P.W., (1986),"Non-Linear Finite Element Model For Concrete Masonry with Particular Reference to Concentrated Loads", Proc. 4th. Canadian Masonry Symp., Fredericton, Canada, June 1986, pp. 137-148

Anderson, D.L. and Priestley, (1992),"In Plane Shear Strength of Masonry Walls", Proceedings 6th. Canadian Masonry Symposium, Saskatoon, Canada, June 1992, pp. 223-234.

Antonucci, R., Carboni, M. and Cocchi, G., (1989),"On the Subject of Numerical Modelling of the Structural Behaviour of Masonry walls under Plane Stress: An Application on Shear Walls", Proc. 5th. Canadian Masonry Symposium, Canada, June 1989, pp. 263-272.

Arya, S.k. and Hegemier, G.A., (1978)"On Non-Linear Response Predictions of Concrete Masonry Assemblies", Proc. North American Conf., Boulder, U.S.A., Aug. 1978, pp. 4-1 to 4-22.

A.S.T.M., (1991),"C42-90: Standard Test Method for Obtaining and Testing Drilled Cores and Sawed Beams of Concrete", Annual book of A.S.T.M. Standards, Philadelphia, Vol. 4.02, pp. 27-30.

A.S.T.M., (1991),"C67-90a: Standard Methods for Sampling and Testing Brick and Structural Clay Tile", Annual book of A.S.T.M. Standards, Philadelphia, Vol. 4.05, pp. 37-45.

A.S.T.M., (1991),"C109-90: Standard Test Methods for Compressive Strength of Hydraulic Cement Mortars", Annual book of A.S.T.M. Standards, Philadelphia, Vol. 4.01, pp. 59-63.

A.S.T.M., (1991),"C140-90: Standard Methods for Sampling and Testing Concrete Masonry Units", Annual book of A.S.T.M. Standards, Philadelphia, Vol. 4.05, pp. 87-88.

A.S.T.M., (1991),"C404-87: Standard Specification for Aggregates for Masonry Grout", Annual book of A.S.T.M. Standards, Philadelphia, Vol. 4.05, pp. 214-215.

Atkinson, R.H., Amadei, B., Sture, S. and Saeb, S., (1987),"Deformation and Failure Characteristics of Masonry Bed Joints under Shear Loading", Proceedings 4th. North American Masonry Conference, Los Angeles, U.S.A., August 1987, pp. 61/1-61/14.

Benjamin, J.R. and Williams, H.A., (1958),"The Behaviour of One Storey Brick Shear Walls" J. Struct. Eng. Div., Vol. 84, No. ST4, 1958.

Bernardini, A. Casellato, A., Modena, C. and Vitaliani, R., (1985),"Post-Elastic Behaviour of Plain Masonry Shear Walls", the 7th. International Brick Masonry Conference, Melbourne, Feb. 1985, pp. 489-500.

Bhide, S.B. and Collins, M.P., (1987),"Reinforced Concrete Elements in Shear and Tension", Publication No. 87-02, Department of Civil Engineering, University of Toronto, Jan. 1987, 308 pages.

Blume, J.A. and Proulx, J., (1968),"Shear in Grouted Brick Masonry Wall Elements", Western States Clay Products Association, San Francisco, Cal., 1968.

Borchelt, J.G., (1970),"Analysis of Brick Walls Subject to Axial Compression and In-Plane Shear", Proceedings of 2nd. International Brick Masonry Conference, Stoke-on-Trent, April 1970.

Chahine, G.N., (1989),"Behaviour Characteristics of Face Shell Mortared Block Masonry under Axial Compression", M.Eng. Thesis, McMaster University, Hamilton, Canada, 1989, 423 pages.

Chen, S.W., Hidalgo, P.A., Mayes, R.L., Clough, R.W. and McNiven, H.D., (1978),"Cyclic Loading Tests of Masonry Single Piers, Vol.2-Height to Width Ratio of 1", EERC Report No. UCB/EERC-78/28, University of California, Berkeley, California, 1978.

Chen, W.F., (1982),"Plasticity in Reinforced Concrete", McGraw-Hill Book Company, 474 pages.

CSA (1984), "CAN3-S304-M84: Masonry Design for Buildings", Rexdale, Ontario, Nov. 1984, 70 pages.

CSA (1976),"A179M-1976: Mortar and Grout for Unit Masonry", June 1976, 20 pages.

CSA (1976),"A82.56M-1976: Aggregate for Masonry Mortar", June 1976, 8 pages.

Darwin, D. and Pecknold, D.A., (1977),"Nonlinear Biaxial Stress-Strain Law for Concrete", J. Eng. Mech. Div., ASCE, Vol. 103, No. EM2, April 1977, pp.229-241.

Dhanasekar, M., Page A.W. and Kleeman, P.W., (1982),"The Elastic Properties of Brick Masonry", Int. J. of Masonry Construction, Vol.2, No.4, 1982, pp. 155-160.

Dhanasekar, M., Page A.W. and Kleeman, P.W., (1985-a),"The Failure of Brick Masonry under Biaxial Stresses", Proc. Instn. Civ. Engrs., Part 2, Vol.79, June 1985, pp. 295-313.

Dhanasekar, M., Kleeman, P.W., and Page A.W. (1985-b),"Biaxial Stress-Strain Relations for Brick Masonry", J. Struct. Eng. Div., ASCE, Vol. 111, No. ST5, May 1985, pp. 1085-1100.

Dickey, W.L., (1982),"Adhered Veneer in Earthquake, Storm and Prefabrication", Proc. 2nd. North American Masonry Conf., Maryland, USA, Aug. 1982, pp.4-1 to 4-25

Draper, N.R. and Smith, H.,"Applied Regression Analysis", John Wiley and Sons. Inc., 1966, 407 pages.

Drysdale, R.G., Hamid, A.A. and Heidebrecht, A.C., (1979),"Tensile Strength of Concrete Masonry", J. Struct. Eng. Div., ASCE, Vol. 105, No. ST7, July 1979, pp.1261-1276.

Elwi, A.A. and Murray, D.W., (1979),"A 3D Hypoelastic Concrete Constitutive Relationship", J. Eng. Mech. Div., ASCE, Vol. 105, No. EM4, Aug. 1979, pp.623-641.

Essawy, A.S., (1986),"Strength of Hollow Concrete Block Masonry Walls Subjected to Lateral (Out-of-Plane) Loading", Ph.D. Thesis, McMaster University, Hamilton, Canada, Sep. 1986, pp. 426.

Ewing, R.D., El-Mustapha and Kariotis, J.C., (1988),"A Finite Element Computer Program for the Nonlinear Analysis of Reinforced Masonry Walls", Proc. of the 8th. International Brick/Block Masonry Conference, Dublin,Ireland, Sep. 1989, pp. 1119-1129.

Ewing, R.D., Kariotis, J.C. and El-Mustapha, (1989),"Nonlinear Finite Element Analysis of Experiments on Two-Story Coupled Reinforced Masonry Shear Walls", Proc. 5th. Canadian Masonry Symposium, Canada, June 1989, pp. 319-328.

Ganz, H.R. and Thürlimann, B., (1983),"Strength of Brickwalls under Normal Force and Shear", Proc. 8th. Int. Symp. Load Bearing Brickworck, London, 1983.

Ganz, H.R. and Thürlimann, B., (1985),"Plastic Strength of Masonry Shear Walls", the 7th. International Brick Masonry Conference, Melbourne, Feb. 1985, pp. 837-846

Ganz, H.R. (1989),"Failure Criteria for Masonry", Proc. 5th. Canadian Masonry Symposium, Canada, June 1989, pp. 65-77.

Gazzola, E., Bagnariol, D., Toneff, J. and Drysdale, R.G., (1985),"Influence of Mortar Materials on the Flexural Tensile Bond Strength of Block and Brick Masonry", American Society for Testing and Materials, Philadelphia, 1985, pp. 15-26.

Gerrard, C. and Macindoe, L, (1985),"Predicted Response of Reinforced Brickwork to In-Plane Tensile Loading", the 7th. International Brick Masonry Conference, Melbourne, Feb. 1985, pp. 1075-1083.

Guo, P., (1991),"Investigation and Modelling of the Mechanical Properties of Masonry", Ph.D. Thesis, McMaster University, Hamilton, Canada, Feb. 1991, pp. 338.

Guo, P. and Drysdale, R.G., (1989),"Stress-Strain Relationship for Hollow Concrete Block in Compression", Proc. 5th. Canadian Masonry Symposium, Canada, June 1989, pp. 599-608.

Haller, P., (1969),"Load Capacity of the Brick Masonry", Designing Engineering and Construction with Masonry Products, Gulf Publishing Co., USA, May 1969, pp.129-149.

Hamid, A.A., (1978),"Behaviour Characteristics of Concrete Masonry", Ph.D. Thesis, McMaster University, Hamilton, Canada, Sep. 1978, pp. 445.

Hamid, A.A., Drysdale, R.G. and Heidebrecht, A.C., (1979),"Shear Strength of Concrete Masonry Joints", J. Struct. Eng. Div., ASCE, Vol. 105, No. ST7, July 1979, pp.1227-1240.

Hamid, A.A., and Drysdale, G.R., (1979),"Suggested Failure Criteria for Grouted Concrete Masonry under Axial Compression", ACI Journal, Proceedings V. 76, No. 10, October 1979, pp. 1047-1062.

Hamid, A.A., and Drysdale, G.R., (1980)," Concrete Masonry Under Combined Shear and Compression along The Mortar Joints", ACI Journal, Proceedings V. 77, No. 5, September-October 1980, pp. 314-320.

Hamid, A.A. and Drysdale, R.G. (1981),"Proposed Failure Criteria for Concrete Block Masonry Under Biaxial Stress", J. Struct. Eng. Div., ASCE, Vol. 107, No. ST8, Aug. 1981, pp.1675-1687.

Hart, G.C., Noland, J.L., Kingsley, G.R., Englekirk, R.E. and Sajjad, N.A., (1988),"The Use of Confinement Steel to Increase the Ductility in Reinforced Concrete Masonry Shear Walls", The Masonry Society Journal, Vol. 7, No.2, July-Dec. 1988, pp. T19-T42.

Hart, G.C., Sajjad, N.A., Kingsley, G.R., Englekirk, R.E. and Noland, J.L., (1989),"Analytical Stress-Strain Curves for Grouted Concrete Masonry", The Masonry Society Journal, Vol. 7, No.2, Jan.-June 1989, pp. T21-T34.

Hegemier, G.A., (1975),"Mechanics of Reinforced Concrete Masonry: A Literature Survey", Report No. AMES-NSF TR-75-5, University of California, San Diego, 1975.

Hegemier, G.A., Nunn, R.O., and Arya S.K., (1978-a),"Behaviour of Concrete Masonry Under Biaxial Stresses", Proceedings of The North American Masonry Conference, University of Colorado, Boulder, August 1978, paper 1.

Hegemier, G.A., Arya, S.K., Krishnamoorthy, G., Nachbar, W. and Furgerson, R., (1978-b),"On the Behaviour of Joints in Concrete Masonry", Proc. North American Masonry Conf., Boulder, USA, Aug. 1978, pp. 4-1 to 4-22.

Hidalgo, P.A., Mayes, R.L., McNiven, H.D. and Clough, R.W., (1978),"Cyclic Loading Tests of Masonry Single Piers, Vol.1-Height to Width Ratio of 2", EERC Report No. UCB/EERC-78/27, University of California, Berkeley, California, 1978.

Hidalgo, P.A., Mayes, R.L., McNiven, H.D. and Clough, R.W., (1979),"Cyclic Loading Tests of Masonry Single Piers, Vol.3-Height to Width Ratio of 0.5", EERC Report No. UCB/EERC-79/12, University of California, Berkeley, California, 1979.

Higgins, J.E., (1989),"Criteria for Numericai Stability of Explicit Time-stepping Elastic-Viscoplasticity", M. Eng. Thesis, McMaster University, Hamilton, Canada, June 1989, pp. 95.

Hodgkinson, H.R. and West, H.W.H., (1982),"The Shear Resistance of Some Damp-Proof-Course Materials", Proc. Bri. Ceram. Soc., No. 30, Load-Bearing Brickwork (7), Sept. 1982, pp.13-22.

Hofbeck, J.A., Ibrahim, I.O. and Mattock, A.H., (1969), "Shear Transfer in Reinforced Concrete", ACI Journal, Proceedings Vol. 66, No. 2, Feb. 1969, pp. 119-168.

Hognestad, E.A., (1951),"A Study of Combined Bending and Axial Load in Reinforced Concrete Members", Bulletin No. 399, Engineering Experiment Station, University of Illinois, Urbana, Illinois, Vol. 49, No. 22, Nov. 1951.

Jamal, B.D., Bennett, R.D. and Flanagan, R.D., (1992),"Numerical Analysis for In-Plane Behaviour of Infilled Frames", Proc. 6th. Canadian Masonry Symposium, Canada, June 1992, pp. 609-631.

Johnson, F.B. and Thompson, J.N., (1967),"The Development of Diametral Testing Procedures to Provide a Measure of Strength Characteristics of Masonry Assemblages", First International Conference on Masonry Structural Systems, Texas, Nov. 1967.

Johansen, K.W. (1958)"Failure Criteria for Concrete and Rock", Bygningsstatiske Meddelelser, Vol. 29, No.2, pp. 25-44.

Jensen, B.C. (1975)"Lines of Discontinuity for Displacements in the Theory of Plasticity of Plain and Reinforced Concrete", Magazine of Concrete Research, Vol. 27, No.92, pp. 143-150.

Kent, D.C. and Park, R., (1971),"Flexural Members with Confined Concrete", ASCE Journal of the Structural Division, Vol. 97, No. ST7, July 1971.

Khalaf, F.M., (1988),"An Investigation into the Capacity and Behaviour of Concrete Block Specimens Loaded Parallel to the Bed Face", Proc. 8th. Int. Brick/Block Masonry Conference, Ireland'88, 1988, pp. 752-763.

Khoo, C.L. and Hendry, A.W., (1973),"Strength Tests on Brick and Mortar under Complex Stresses for the Development of a Failure Criterion for Brickwork in Compression", Proc. Brit. Ceram. Soc., 21, 1973.

Kirschner, U. and Collins, M.P., (1986),"Investigating the Behaviour of Reinforced Concrete Shell Elements", Publication No. 86-09, Department of Civil Engineering, University of Toronto, Sep. 1986, 209 pages.

Kupfer, H., Hubert, K.H., and Rusch, H., (1969),"Behaviour of Concrete Under Biaxial stresses", ACI Journal, Proceedings V.66, No.8, August 1969, pp 656-666.

Kupfer, H. and Grestel, K.H., (1973),"Behaviour of Concrete Under Biaxial Stresses", J. Eng. Mech. Div., ASCE, Vol. 99, No. em4, Aug. 1973, pp. 852-866.

Maksoud, A.A. and Drysdale, R.G., (1992),"Numerical Modelling of Masonry Walls", Proc. 6th. Canadian Masonry Symposium, Canada, June 1992, pp. 801-811.

Mann, W. and Müller, H., (1982),"Failure of Shear-Stressed Masonry-An Enlarged Theory, Tests and Application to Shear Walls", Proc. Brit. Ceram. Soc., No.30, Load-bearing Brickwork (7), Stroke-on-Trent, Great Britain, Sep. 1982, pp. 223-235.

Massicotte, B., Elwi, A.E. and MacGregor, J.G., (1990),"Tension-Stiffening Model for Planner Reinforced Concrete Members",J. Struct. Eng. Div., ASCE, Vol. 116, No. 11, Nov. 1990, pp.3039-3057.

Massicotte, B., Elwi, A.E. and MacGregor, J.G., (1988),"Analysis of Reinforced Concrete Panels Loaded Axially and Transversely", Structural Eng. Report 161, University of Alberta, Dept. of Civil Eng., July 1988, 255 pages.

Matsumura, A., (1987),"Shear Strength of Reinforced Hollow Unit Masonry Walls", Proceedings 4th. North American Masonry Conference, Los Angeles, U.S.A., August 1987, pp. 50/1-50/16.

Matsumura, A., (1990),"Planar Shear Loading Test on Reinforced Fully Grouted Hollow Clay Masonry Walls", Proceedings 5th. North American Masonry Conference, Illinois, U.S.A., June 1990, pp. 347-358.

Mayes, R.L. and Clough, R.W., (1975-a),"A Literature Survey- Compressive, Tensile, Bond and Shear Strength of Masonry", EERC Report No. 75-15, University of California, Berkeley, July 1975.

Mayes, R.L. and Clough, R.W., (1975-b),"State-of-the-Art in Seismic Shear Strength of Masonry-An Evaluation and Review", EERC Report No. 75-21,

University of California, Berkeley, Oct. 1975, 137 pages.

Mayes, R.L., Omote, R.L., and Clough R.W., (1976-a),"Cyclic Shear tests of Masonry Piers, Volume I-Test Results", EERC Report No. 76-8, University of California, Berkeley, May 1976, 84 pages.

Mayes, R.L., Omote, R.L., and Clough R.W., (1976-b),"Cyclic Shear tests of Masonry Piers, Volume II-Test Results", EERC Report No. 76-16, University of California, Berkeley, May 1976.

Meli, R., (1972),"Behaviour of Masonry Walls Under Lateral Loads", Proceedings of 5th. World Conference on Earthquake Engineering, Rome, 1972.

Motta, F. and D'Amore, E., (1985),"Numerical Modelling of the Structural Behaviour of Masonry Buildings", the 7th. International Brick Masonry Conference, Melbourne, Feb. 1985, pp. 809-518.

Nawy, E.G., (1983),"Shear Transfer in Concrete Two Layer Systems", Advances in Structural Concrete Design, Proceeding of NJIT-ASCE-ACI, Structural Concrete Design Conference, March 1983, pp. 105-133.

Page, A.W., (1978),"Finite Element Model for Masonry', J. Struct. Eng. Div., ASCE, Vol. 104, No. ST8, Aug. 1978, pp. 1267-1285.

Page, A.W., (1980),"A Biaxial Failure Criterion for Masonry in the Tension-Tension Range", Int. J. Masonry Construction, Vol.1, No. 1, March 1980, pp. 26-29.

Page, A.W., (1981),"The Biaxial Compressive Strength of Brick Masonry", Proc. Instn Civ. Engrs, Part 2, 71, September 1981, pp. 893-906.

Page, A.W., (1983),"The Strength of Brick Masonry Under Biaxial Tension-compression", International Journal of Masonry Construction, V. 3, No. 1, March 1983, pp. 26-31.

Page, A.W., Samarasinghe, W. and Hendry, A.W., (1980),"The In-Plane Failure of Masonry-A Review", Proc. British Ceramic Soc., Load Bearing BrickWork, No. 30, Sep. 1980, pp. 90-100.

Pande, G.N. and Xiong, W., (1982),"An improved multi-laminated Model of Rocks", Numerical Models in Geomechanics, Eds, Dungar, Pande and Studer, A.A. Balkema, Rotterdam, 218-226.

Pande, G.N. and Gerrard, C.M., (1983),"The behaviour of Reinforced Jointed Rock Masses under Various Simple Loading States", Proc.
Fifth Congress Int. Society for Rock Mechanics, Vol. F, Melbourne, Australia, 1983, pp.217-224.

Gerrard, C.M. and Pande, G.N., (1985),"Numerical Modelling of Reinforced Jointed Rock Masses, I. Theory", Computer and Geotechnics, Vol. 1, 1985, pp.293-318.

Pearson, J.C., (1963),"Measurement of Bond between Bricks and Mortar", Proceedings American Society for Testing Materials, 43,1963.

Pieper, K. and Trautsch, W., (1970),"Shear Tests on Walls", Proc. 2nd. IBMaC, Stoke-on-Trent, Great Britain, April 1970, pp. 140-143.

Pietruszczak, S. and Niu, X., (1992),"A Mathematical Description of Macroscopic Behaviour of Brick Masonry", Int. J. Solids Structures Vol. 29, No. 5, 1992, pp. 531-546.

Pluijm, R. (1992),"Material Properties of Masonry and Its Components under Tension and Shear", Proc. 6th. Canadian Masonry Symposium, Canada, June 1992, pp. 675-686.

Priestley, M.J.N. and Bridgeman, D.O., (1974),"Seismic Resistance of Brick Masonry Walls", Bulletin of the New Zealand National Society for Earthquake Engineering, Vol. 7, No. 4, Dec. 1974, pp. 167-187.

Priestley, M.J.N. and Elder, D.M., (1983),"Stress-Strain Curves for Unconfined and Confined Concrete Masonry", ACI Journal, Proceedings V.80, No.3, May-June 1983, pp 192-201.

Priestley, M.J.N., (1986-b),"Flexural Strength of Rectangular Unconfined Masonry Shear Walls with Distributed Reinforcement", TMS Journal, V.5, No.2, July-Dec. 1986, pp T1-T20.

Priestley, M.J.N., (1986-a),"Seismic Design of Concrete Masonry Shearwalls", ACI Journal, Proceedings, Jan.-Feb. 1986, pp 58-63.

Qamaruddin, M., Qadeer, A., Usmani. S.A. and Kumar, P., (1989-a),"Displacement and Stress Analysis Shear Wall Panels with Openings", Proc. 5th. Canadian Masonry Symposium, Canada, June 1989, pp. 301-407.

Qamaruddin, M., Qadeer, A., Ali. S.M. and Saxena, A., (1989-b),"Dynamic

Response Analysis of Multistorey Masonry Building subjected to Earthquake", Proc. 5th. Canadian Masonry Symposium, Canada, June 1989, pp. 395-404.

Rizkalla, S.H., Hwang, L.S., and El Shahawi,M.,(1983),"Transverse Reinforcement Effect on Cracking Behaviour in R.C. Members", Canadian Journal of Civil Engineering, Vol. 10, No.4, Dec.1983, pp. 566-581.

Saenz, L. P., (1964), Discussion of "Equation for the Stress-Strain Curve of Concrete", ACI Journal, Vol. 61, No.9, Sep. 1964, pp. 1229-1235.

Sakr, K.,M. and Neis, V.V., (1989),"Some Studies on the Stress-Strain Behaviour of Grouted Concrete Masonry Block Units", Proc. 5th. Canadian Masonry Symposium, Canada, June 1989, pp. 619-628.

Samarasinghe, W., and Hendry, A.W., (1982),"The Strength of Brickwork Under Biaxial Tensile and Compressive stress", Proc. Brit. Ceram. Soc., No. 30, Load-Bearing Brickwork (7), September 1982, pp. 129-139.

Schneider, R.R., (1956),"Tests on Reinforced Grouted brick Masonry Shear Walls", Report issued by California state Division of Architecture, Los Angeles, 1956.

Schneider, R.R., (1959),"Lateral Load Tests on Reinforced Grouted Masonry Shear Walls", University of Southern California Engineering Centre, Report No. 70-101, 1959.

Schneider, R.R. and Dickey, W.L., (1980),"Reinforced Masonry Design", Prentice-Hall, Inc., U.S.A., 1980, 619 pages.

Scrivener, J.C., (1966),"Concrete Masonry Wall Panel Tests - Static Racking Tests with Predominant Flexural Effect", New Zealend Concrete Construction, July 1966.

Scrivener, J.C., (1969),"Static Racking Tests on Masonry Walls", Designing, Engineering and Constructing with Masonry Products, Edited by F.B. Johnson, Gulf Publishing Co., Houston, Texas, May 1969.

Seible, F., LaRovere, H.L. and Klingsley, G.R., (1990),"Nonlinear Analysis of Reinforced Concrete Masonry Subassemblages", Proceedings 5th. North American Masonry Conference, Illinois, U.S.A., June 1990, pp. 261-274.

Self, M.W.,"Structural Properties of Loadbearing Concrete Masonry", Masonry: Past and Present, ST9, A.S.T.M., Philadelphia. PA, 1975.

Shing, P.B., Noland, M., Klamerus, E., and Spaeh, H., (1989),"Inelastic Behaviour of Concrete Masonry Shear Walls", ASCE, Journal of Structural Engineering, Vol. 115, No. 9, September 1989, pp. 2204-2225.

Shing, P.B., Schuller, M. and Hoskere, V.S., (1990),"In-Plane Resistance of Reinforced Masonry Shear Walls", ASCE, Journal of Structural Engineering, Vol. 116, No. 3, March 1990, pp. 619-640.

Shrive, N.G., (1982),"The Failure Mechanism of Face-Shell Bedded (Ungrouted and Unreinforced) Masonry", Int. J. Masonry Construction, Vol. 2, No.3, 1982, pp. 115-128.

Simbeya, K.W., McMullen, A.E., Jessop, E.L. and Shrive, N.G., (1986),"Stress Distributions on Hollow Masonry Due to Concentrated Loading", Masonry Soc. J., Vol. 5, No. 2, 1986, pp. T25-T38.

Sinha, B.P. and Hendry, A.W., (1969),"Racking Tests on Storey-Hight Shear Wall Structures with Openings, Subjected to Precompression",Designing, Engineering and Constructing with Masonry Products, Gulf Publicating Company, Houston, USA, May 1969, pp. 192-199.

Somayaji, S. and Shah, S.P., (1981),"Bond Stress Versus Slip Relationship and Cracking Response of Tension Member", ACI Journal, Proceedings V.78, No.20, May-June 1981, pp 217-225.

Stafford-Smith, B., Carter, C., and Choudhury, H.R., (1970),"The Diagonal Tensile Strength of Brickwork", The Structural Engineer, Vol. 48, No. 6, June 1970, pp. 219-225.

Stafford-Smith, B. and Carter, C., (1971),"Hypothesis for Shear Failure of Brickwork", The Structural Engineer, Vol. 94, No. ST4, April 1971, pp.1055-1062.

Sveinsson, B.I., Mayes, R.L. and McNiven, H.D., (1981),"Evaluation of Seismic Design Provisions for Masonry in the United States", EERC Report No. UCB/EERC-81/10, University of California, Berkeley, California, 1981.

Sveinsson, B.I., McNiven, H.D. and Sucuoglu, H., (1985), "Cyclic Loading Tests of Masonry Single Piers, Vol.4-Height to Width Ratio of 1", EERC Report No. UCB/EERC-85/15, University of California, Berkeley, California, 1985.

Tomazevic, M. and Zarnic, R., (1985),"The Effect of Horizontal Reinforcement on The Strength and Ductility of Masonry Walls at Shear Failure", Proceedings

7th. International Brick Masonry Conference, Melbourne, Australia, Feb. 1985, pp. 1291-1302.

Uniform Building Code, (1988), International Conference of Building Officials, Whittier, CA.

Uniform Building Code, (1991), International Conference of Building Officials, Whittier, CA.

Vecchio, F.J. and Collins, M.P., (1982),"The Response of Reinforced Concrete to In-Plane Shear and Normal Stresses", Publication No. 82-03, Department of Civil Engineering, University of Toronto, March 1982, 332 pages.

Vecchio, F.J. and Collins, M.P., (1986),"The Modified Compression Field Theory fro Reinforced Concrete Elements Subjected to Shear", ACI Journal, Proceedings V.83, No.2, March-April 1986, pp. 219-231.

Williams, D., (1971),"Seismic Behaviour of Reinforced Masonry Shear Walls", Ph.d. Thesis, University of Canterbury, New Zealand, 1971.

Zienkiewicz, O.C. and Pande, G.N., (1977),"Time-Dependent Multilaminate Model of Rocks- a Numerical Study of Deformation and Failure of Rock Masses", Int. J. of Numerical and Analytical Methods in Geomechanics, Vol. 1, 1977, pp. 219-247.

Zienkiewicz, O.C. and Cormeau, I.C., (1972),"Visco-plasticity Solution by Finite Element Process", Archives of Mechanics (Warszawa), 24, 5-6, pp. 873-889.

Zienkiewicz, O.C. and Cormeau, I.C., (1974),"Visco-Plasticity-Plasticity and Creep in Elastic Solids-A Unified Numerical Solution Approach", Int. J. Num. Meth. Eng., Vol. 8, 1974, pp. 821-845.

Yokel, F.Y. and Fattal, S.G., (1976),"Failure Hypothesis for Masonry Shear Walls", J. Struct. Eng. Div., ASCE, Vol. 102, No. ST3, 1976, pp. 515-532.